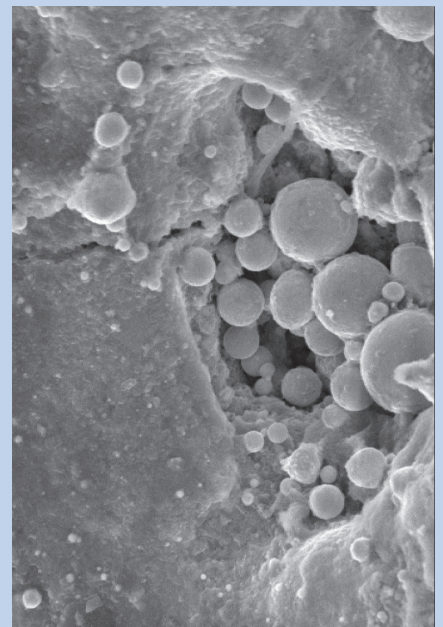
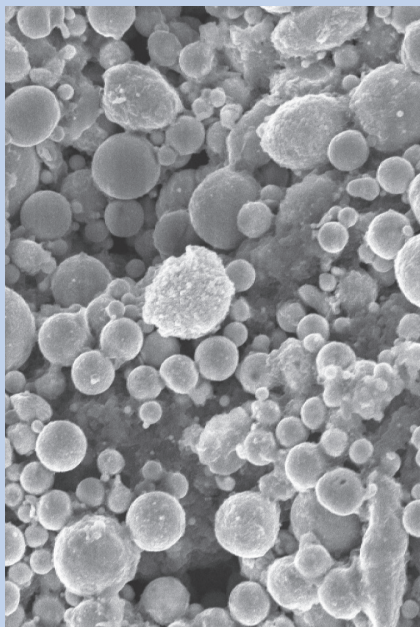
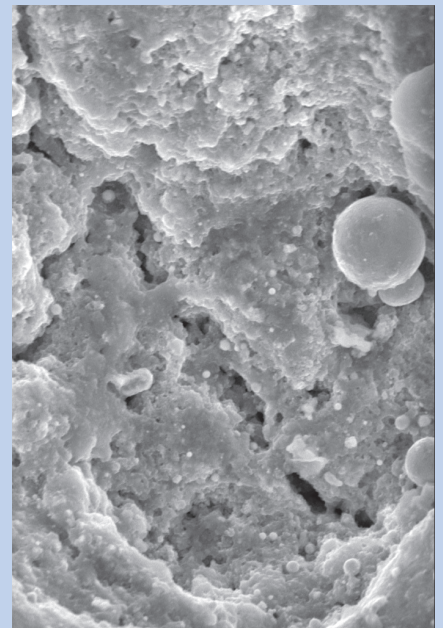
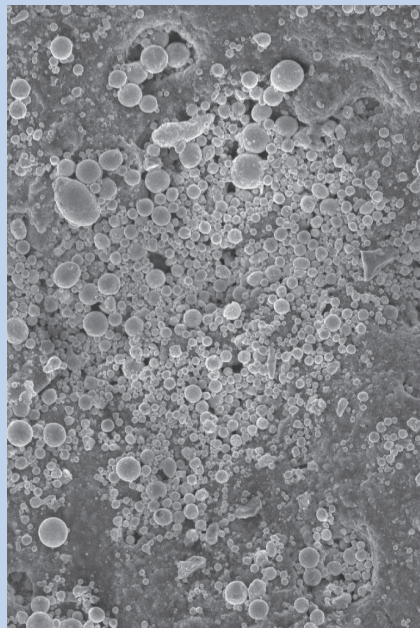




# Strojniški vestnik

## Journal of Mechanical Engineering



no. **11**  
year **2021**  
volume **67**

## Aim and Scope

The international journal publishes original and (mini)review articles covering the concepts of materials science, mechanics, kinematics, thermodynamics, energy and environment, mechatronics and robotics, fluid mechanics, tribology, cybernetics, industrial engineering and structural analysis.

The journal follows new trends and progress proven practice in the mechanical engineering and also in the closely related sciences as are electrical, civil and process engineering, medicine, microbiology, ecology, agriculture, transport systems, aviation, and others, thus creating a unique forum for interdisciplinary or multidisciplinary dialogue.

The international conferences selected papers are welcome for publishing as a special issue of SV-JME with invited co-editor(s).

## Editor in Chief

Vincenc Butala

University of Ljubljana, Faculty of Mechanical Engineering, Slovenia

## Technical Editor

Pika Škraba

University of Ljubljana, Faculty of Mechanical Engineering, Slovenia

## Founding Editor

Bojan Kraut

University of Ljubljana, Faculty of Mechanical Engineering, Slovenia

## Editorial Office

University of Ljubljana, Faculty of Mechanical Engineering

SV-JME, Aškerčeva 6, SI-1000 Ljubljana, Slovenia

Phone: 386 (0)1 4771 137

Fax: 386 (0)1 2518 567

info@sv-jme.eu, <http://www.sv-jme.eu>

**Print:** Demat d.o.o., printed in 250 copies

## Founders and Publishers

University of Ljubljana, Faculty of Mechanical Engineering, Slovenia

University of Maribor, Faculty of Mechanical Engineering, Slovenia

Association of Mechanical Engineers of Slovenia

Chamber of Commerce and Industry of Slovenia,

Metal Processing Industry Association

## President of Publishing Council

Mitjan Kalin

University of Ljubljana, Faculty of Mechanical Engineering, Slovenia

## Vice-President of Publishing Council

Bojan Dolšak

University of Maribor, Faculty of Mechanical Engineering, Slovenia

## International Editorial Board

Kamil Arslan, Karabuk University, Turkey

Hafiz Muhammad Ali, King Fahd U. of Petroleum & Minerals, Saudi Arabia

Josep M. Bergada, Politechnical University of Catalonia, Spain

Anton Bergant, Litostroj Power, Slovenia

Miha Boltežar, University of Ljubljana, Slovenia

Filippo Cianetti, University of Perugia, Italy

Janez Diaci, University of Ljubljana, Slovenia

Anselmo Eduardo Diniz, State University of Campinas, Brazil

Igor Emri, University of Ljubljana, Slovenia

Imre Felde, Obuda University, Faculty of Informatics, Hungary

Imre Horvath, Delft University of Technology, The Netherlands

Aleš Hribernik, University of Maribor, Slovenia

Soichi Ibaraki, Kyoto University, Department of Micro Eng., Japan

Julius Kaplunov, Brunel University, West London, UK

Iyas Khader, Fraunhofer Institute for Mechanics of Materials, Germany

Jernej Klemenc, University of Ljubljana, Slovenia

Milan Kljajin, J.J. Strossmayer University of Osijek, Croatia

Peter Krajnik, Chalmers University of Technology, Sweden

Janez Kušar, University of Ljubljana, Slovenia

Gorazd Lojen, University of Maribor, Slovenia

Darko Lovrec, University of Maribor, Slovenia

Thomas Lübben, University of Bremen, Germany

George K. Nikas, KADMOS Engineering, UK

Tomaž Pepelnjak, University of Ljubljana, Slovenia

Vladimir Popović, University of Belgrade, Serbia

Franci Pušavec, University of Ljubljana, Slovenia

Mohammad Reza Safaei, Florida International University, USA

Marco Sortino, University of Udine, Italy

Branko Vasić, University of Belgrade, Serbia

Arkady Voloshin, Lehigh University, Bethlehem, USA

## General information

Strojniški vestnik – Journal of Mechanical Engineering is published in 11 issues per year (July and August is a double issue).

Institutional prices include print & online access: institutional subscription price and foreign subscription €100,00 (the price of a single issue is €10,00); general public subscription and student subscription €50,00 (the price of a single issue is €5,00). Prices are exclusive of tax. Delivery is included in the price. The recipient is responsible for paying any import duties or taxes. Legal title passes to the customer on dispatch by our distributor. Single issues from current and recent volumes are available at the current single-issue price. To order the journal, please complete the form on our website. For submissions, subscriptions and all other information please visit: <http://www.sv-jme.eu>.

You can advertise on the inner and outer side of the back cover of the journal. The authors of the published papers are invited to send photos or pictures with short explanation for cover content.

We would like to thank the reviewers who have taken part in the peer-review process.

The journal is subsidized by Slovenian Research Agency.

Strojniški vestnik - Journal of Mechanical Engineering is available on <https://www.sv-jme.eu>.



**Cover:** The machining of components with complex features, as well as those constructed of difficult-to-cut and machining materials, is commonly done with an electrical discharge machine (EDM). Traditional machining processes, on the other hand, need an excessive amount of tool creation time for the EDM process, which has a significant effect on the machining rate. As a result, the tool electrode in this experiment is made using the powder metallurgy (PM) approach. During deformation, the load can efficiently move from the matrix to the evenly distributed reinforcement particles. The pictures reveal that once the TiC particle was removed, there were maybe a few voids remaining on the composite's surface.

*Image Courtesy:* S. Duraisivam & P. Suresh, Department of Mechatronics Engineering, Sona College of Technology, Tamilnadu, India

**ISSN 0039-2480, ISSN 2536-2948 (online)**

© 2021 Strojniški vestnik - Journal of Mechanical Engineering. All rights reserved. SV-JME is indexed / abstracted in: SCI-Expanded, Compendex, Inspec, ProQuest-CSA, SCOPUS, TEMA. The list of the remaining bases, in which SV-JME is indexed, is available on the website.

# Contents

**Strojniški vestnik - Journal of Mechanical Engineering**  
**volume 67, (2021), number 11**  
**Ljubljana, November 2021**  
**ISSN 0039-2480**

**Published monthly**

## **Papers**

Duraisivam Saminatharaja, Suresh Periyakgounder, Mahalingam Selvaraj, Jamuna Elangandhi: Performance Study of EDM Process Parameters Using TiC/ZrSiO <sub>4</sub> Particulate-Reinforced Copper Composite Electrode	547
Changbin Dong, Yongping Liu, Gang Zhao: A Method for Calculating Elliptic Gear Transmission Efficiency Based on Transmission Experiment	557
Govindaraj Periasamy, Senthilkumar Mouleeswaran, Prabhu Raja Venugopal, Chellapandi Perumal: Investigation of Hydrodynamic Flow Characteristics in Helical Coils with Ovality and Wrinkles	570
Mingjun Du, Yongjun Hou, Tong Tang, Lian Tang, Jialong Wang, Hongbo Gao: Synchronization and Stability of a Three Co-Rotating Rotor System Coupled with Springs in a Non-Resonance System	580
Andrzej Kosucki, Łukasz Stawiński, Adrian Morawiec, Jarosław Goszczak: Electro-Hydraulic Drive of the Variable Ratio Lifting Device under Active Load	599
Paul Gregory Felix, Velavan Rajagopal, Kannan Kumaresan: Applicability of MCDM Algorithms for the Selection of Phase Change Materials for Thermal Energy Storage Heat Exchangers	611



# Performance Study of EDM Process Parameters Using TiC/ZrSiO<sub>4</sub> Particulate-Reinforced Copper Composite Electrode

Duraisivam Saminatharaja<sup>1,\*</sup> – Suresh Periyakgounder<sup>2</sup> – Mahalingam Selvaraj<sup>3</sup> – Jamuna Elangandhi<sup>1</sup>

<sup>1</sup>The Kavery Engineering College, Department of Mechanical Engineering, India

<sup>2</sup>Sona College of Technology (Autonomous), Department of Mechatronics Engineering, India

<sup>3</sup>Sona College of Technology (Autonomous), Department of Mechanical Engineering, India

Electrical discharge machines (EDM) are widely employed in machining components containing complex profiles of hard-to-cut and machining materials. However, the fabrication-of-tool time for the EDM process is excessively high in the traditional machining method, which significantly affects the machining rate. Therefore, in this paper, a powder metallurgy (PM) technique is employed to fabricate the tool electrode using copper (Cu), titanium carbide (TiC), and zirconium silicate (ZrSiO<sub>4</sub>) for different combinations. An L18 orthogonal array (OA) is planned using the following input parameters: three types of tools (Cu, Cu<sub>90</sub>, Cu<sub>80</sub>), peak current (PC) [A], pulse on time (PT) [μs], and gap voltage (GV) [V]. The performance of EDM is evaluated through the material removal rate (MRR), tool wear rate (TWR), and surface roughness (SR). The process parameters are optimized using two different techniques: the technique for order of preference by similarity to the ideal solution (TOPSIS) and grey relational analysis (GRA). TOPSIS and GRA optimization techniques produce the same optimal parametric solution for less TWR, SR, and higher MRR with the combination of the Cu<sub>90</sub> tool, E8 APC, 15 μs pulse PT, and 75 V GV. Based on the ANOVA table of TOPSIS, pulse on time plays a major role, contributing 46.8 % of the machining performance; peak current shows the most significant contribution of 39.3 % of the machining performance using GRA values. Furthermore, the scanning electron microscope (SEM) image analyses are carried out on the machined workpiece surface to understand the effect of tools on machining quality.

**Keywords:** powder metallurgy, composite tool, copper, electrical discharge machine, technique for order of preference by similarity to ideal solution, grey relational analysis

## Highlights

- EDM process parameters (Gap voltage, current, pulse on time) were optimized through the L18 orthogonal experimental design method, GRA method, and the TOPSIS method considering responses, such as MRR, TWR, and SR.
- Based on the experiment, MRR and TWR were increased by increasing the reinforcement percentage of composite electrodes.
- It was revealed that the MRR value of the Cu<sub>90</sub> tool electrode was 0.0319 g/min, which is 1.9 times higher than the other tool electrode.
- Pulse on time and peak current have major contribution values (46.8 % and 39.3 %) from the ANOVA table of TOPSIS and GRA.

## 0 INTRODUCTION

EDM is a widely accepted and promising process used in non-traditional machining processes. Due to its unique nature of machining characteristics, the usage of EDM has been increasing enormously in manufacturing sectors, including forging, automobile, aviation, and the biomedical and medical industries. Moreover, an excellent surface finish and precision can be made by means of EDM, in cases in which the conventional machining method fails. The stainless steel (SS) SS304 has been employed in various manufacturing sectors due to its high toughness, wear resistance, and corrosion resistance. In the EDM process, apart from electrical parameters, other parameters, such as tool modification, dielectric medium changes, tool rotational assistances and tool vibration, play vital roles in improving machining performances. Therefore, various research attempts were undertaken in the previous decade by researchers. In line with that, Sivakumar et al. [1] investigated

the EDM process parameters for oil-hardening, non-deforming tool steel (OHNS) using copper and titanium die boride composite electrodes. They developed the electrode using a powder metallurgy process and optimized the process through response surface methodology. Chakmakchi et al. [2] used a titanium alloy (Ti) as an electrode for machining the cobalt-chromium (Co-Cr) alloy and Ti6Al7Nb through the EDM process. The EDM process parameters were analysed using the evaluations of morphological and electrochemical changes in the workpiece, and the results were validated with copper electrodes. They identified that Ti electrodes have less degradation effect on the workpiece than copper electrodes did. Yadav et al. [3] used geometry-modified electrodes (e.g., slotted, helical, and tubular) in the EDM process. The influences of process parameters on the EDM performance were studied with the electrodes. They noted that the removal of machined products from the inter-electrode gap (IEG) for all tools had increased the machining rate and surface roughness

\*Corr. Author's Address: The Kavery Engineering College, Department of Mechanical Engineering, Salem, Tamil Nadu, India, sduraisivam26@gmail.com

of work materials. Taherkhani et al. [4] investigated the EDM process parameters using  $Al_2O_3$  particles mixed dielectrically in various concentration ranges on titanium alloy. The significant enhancement in machining surface was due to the prevention of oxides layer formation in the dielectric medium. Also, the presence of oxygen and carbon elements leads to uniform power distributions, which control crack formations over the machining surface. Phan et al. [5] experimented with an aluminium electrode in EDM process to determine its suitability on the titanium alloy. They optimized the process parameters using Taguchi method and obtained the maximum MRR 0.0239 g/min with less error. Ilani et al. [6] and [7] fabricated a tool in the technique of fused deposition modelling and employed EDM to improve the machining performance. The result was a tool using the surfactant stirred dielectrics such as with powder mixed and non-powder mixed electrolyte. They noted a 77 % improvement in surface roughness with this novel electrode. Also, this type of electrode is cost effective and makes the EDM functions easier for the production of complex geometries. Phan et al. [8] coated aluminium chromium nickel on an aluminium electrode to investigate the EDM parameters for titanium alloy. The experiments' results of a coated electrode are compared with a non-coated aluminium electrode. The coating of the aluminium in the electrode increases the material removal rate significantly; the coated electrode produces 24 % less TWR than the uncoated electrode does. Shaikh and Ahuja [9] conducted the experiments with electrodes, such as silver coated tungsten and electroless nickel coated electrodes, in the EDM process. They noted that the electroless nickel-coated electrode has a 20 % higher machining rate than the silver-coated tool, which is because the electroless nickel coating increases the current distribution on the electrode. Walia et al. [10] studied the influences of a copper and titanium carbide mixed composite electrode on EDM with EN31 die steel. The copper composite electrode result reveals that the roundness of the hole was reduced around 25 % due to the electrode's conductance change. They mentioned that significant performance results in terms of MRR and surface roughness were obtained with the composite electrode than the plain copper electrode. Sahuand Mahaptra [11] prepared a aluminium, silicon, and magnesium mixed composite electrode through selective laser sintering method. They considered titanium as a workpiece and conducted the experiments using various tools, including composite, graphite, and copper electrodes. They obtained higher TWR and excellent surface

roughness with the composite electrode than other tools. Mahipal Reddy et al. [12] employed a 3D printing (i.e., direct metal laser sintering) to fabricate the aluminium composite electrode used in the EDM of steel alloy. The experiment results were compared with the commercial electrodes and performances were evaluated by means of MRR, TWR, and Servient et al. [13] used a rotary type tool in EDM of work material: high-speed steel through air mixed glycerine dielectric medium. The tool rotation speed, gas pressure, current, and dielectric flow rate were considered for the process parameters on the study of machining rate, overcut and surface roughness. They noted the improvement in the machining rate and surface roughness with the rotary tool electrode. Padhi et al. [14] used the additive manufacturing tool for machining the D2 steel using EDM. They coated the electrode with acrylonitrile-based polymer by fusion deposition method, which increased the electrical conductance of the electrode and increased the machining rate significantly. Mathai et al. [15] adopted the planetary tool movement on EDM to investigate the process parameters for titanium alloy. Along with this planter movement, they fabricated square holes with two types of electrodes materials (i.e., copper and graphite). Also, they noted that the copper tool produced better machining rate and surface finish than the graphite electrodes did. Wang et al. [16] tried two types of electrodes (i.e., cylindrical and helical) in a micro-EDM process on titanium alloy. The helical electrode increases the debris removal passage between tool and electrode, which increases the current flowability. This phenomenon ensures the high machining rate and better surface finish on the micro holes. Vincent and Kumar [17] used copper and brass rotary electrodes with EDM on En41b steel. They have noted less tool wear rate on the copper electrode than the brass electrode due to the current fluctuation on the IEG. Also, based on the analyses of variance, pulse on time and pulse off time played major role on the machining performance. Singh et al. [18] investigated the EDM performance using an air-assisted rotary tool on high chromium die steel. They compared the experimental results with non-air assisted EDM under the same parameter setup. According to this, a high machining rate and less overcut was found on the air-assisted tool than the normal tool. Along with various techniques employed in EDM to enhance its performances (e.g., powder mixed dielectric [19], tool coating [20] and optimization of process parameters), using various techniques such as TOPSIS, Taguchi-data envelopment analysis-based ranking, Taguchi-grey relational analysis by the researchers [21] to [24].

The aforementioned literature clearly indicates that the various research methodologies have been followed by the researchers to enhance the EDM process. However, research on powder metallurgy-based tools on the EDM process is sparse. Although some researchers have considered PM tools in EDM, all the methods show poor surface finish and machining rate due to the improper reinforcements with Cu [25] to [27]. Titanium carbide and zirconium silicate particles possess an excellent affinity with Cu material due to their crystallographic nature. Hence, in this research, two electrodes in different reinforcement combinations (i.e., 90 % Cu, 5% TiC 5 % ZrSiO<sub>4</sub>(Cu<sub>90</sub>) and 80 % Cu, 5% TiC 5 % ZrSiO<sub>4</sub>(Cu<sub>80</sub>)) are prepared using PM technique. The results of these tools are compared with plain Cu electrodes. With these three tools, EDM and its process parameters are optimized using TOPSIS and GRA methods. Furthermore, scanning electron microscope (SEM) image analyses are carried out for the better understanding of the effect of PM-based tools on machining performances.

## 1 EXPERIMENTAL SETUP

The experiments are conducted using a ZNC EDM machine, shown in Fig. 1. The tool electrode was prepared based on the powder metallurgy technique and hot extrusion method employed to diminish the porosity of the composite. The materials Cu- TiC-ZrSiO<sub>4</sub> are used for the tool electrode preparation with various weight ratios, as shown in Table 1. The procedures for producing tool electrodes are followed from the literature [28] and explored in Fig. 2. The grain sizes of reinforcement particles are considered lower than 75 μm for all electrode samples. The composite electrodes of diameter 10 mm and 5

cm length are prepared. When considering various application of SS, in this attempt 5 mm thick SS 304 materials are used as work material.



Fig. 1. EDM setup

The machining parameters levels and experimental planning with outcomes are shown in Tables 2 and 3. L18 OA is planned with three tool electrodes: PC, PT, and GV. The SEM pictures of PM-based electrodes (i.e., Cu, Cu<sub>90</sub>, and Cu<sub>80</sub>) are shown in Figs. 3 to 5. The performances of EDM are estimated in terms of MRR, TWR, and SR. The commercially available dielectric medium kerosene is used for flushing between the tool and electrode. The machining times fixed as 30 minutes for all experiments, and levels of parameters are selected based on the literature [28]. Every completion of experimental workpieces and electrodes are cleaned using acetone to remove debris from the machining zone of workpiece. Before and after machining weights of tools and workpieces are



Fig. 2. Powder metallurgy-based electrodes

taken into the account for calculating the MRR and TWR, respectively [29]. The surface roughness of the machined area is measured using a surface roughness testing machine (Surf test SJ-210, Mitutoyo, Japan). Furthermore, SEM image analysis is carried out on the machined workpiece surfaces for a better understanding of the effect of tools on machining.

**Table 1.** Weight ratios of electrode

Electrodes type	Electrodes No	% of reinforcements		
		Cu	TiC	ZrSiO <sub>4</sub>
Cu	Cu	100	-	-
Cu <sub>90</sub>	Cu <sub>90</sub> (TiC) <sub>5</sub> (ZrSiO <sub>4</sub> ) <sub>5</sub>	90	5	5
Cu <sub>80</sub>	Cu <sub>80</sub> (TiC) <sub>10</sub> (ZrSiO <sub>4</sub> ) <sub>10</sub>	80	10	10

**Table 2.** Range of machining parameters

Symbol	Machining parameters	Unit	L-1	L-2	L-3
A	Electrode type	-	Cu	Cu <sub>90</sub>	Cu <sub>80</sub>
B	Peak current	[A]	8	16	24
C	Pulse on	[μs]	15	30	45
D	Gap voltage	[V]	50	75	100

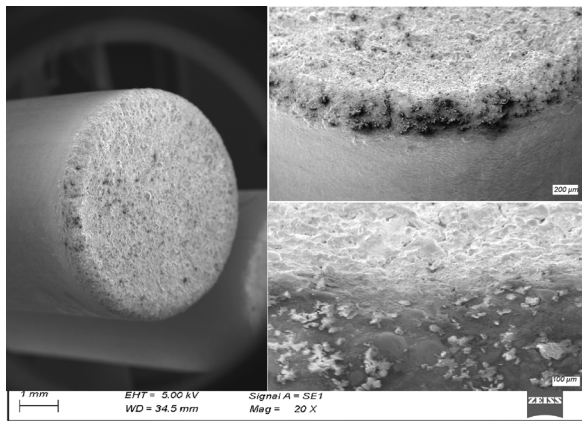


**Fig. 3.** Plain Cu electrode (Cu)

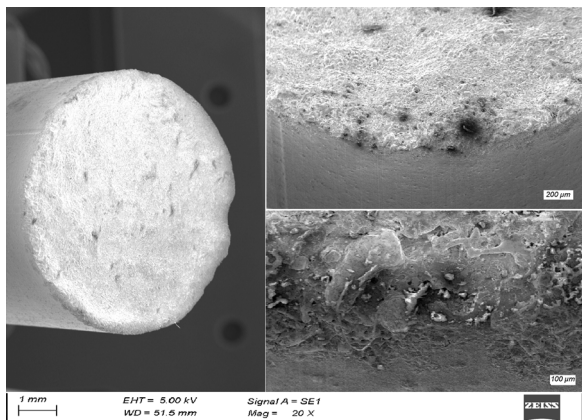


**Fig. 4.** Cu<sub>90</sub>(TiC)<sub>5</sub>(ZrSiO<sub>4</sub>)<sub>5</sub> electrode (Cu<sub>90</sub>)

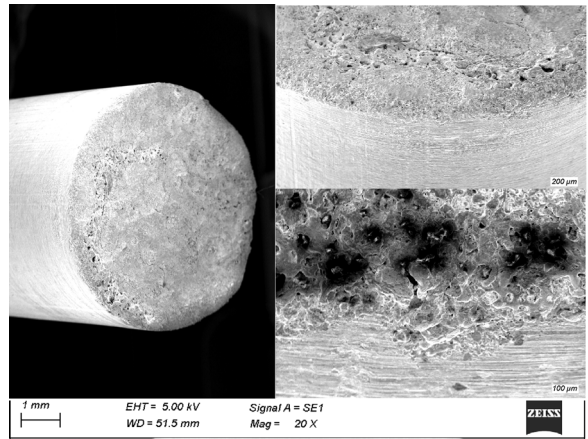


**Fig. 5.** Cu<sub>80</sub>(TiC)<sub>10</sub>(ZrSiO<sub>4</sub>)<sub>10</sub> electrode (Cu<sub>80</sub>)

**Table 3.** Experimental planning

Run	TE	PC	PT	GV	MRR [g/min]	TWR [g/min]	SR [μm]
1	1	8	15	50	0.0101	0.0533	4.12
2	1	16	30	75	0.0011	0.0253	4.39
3	1	24	45	100	0.0231	0.0538	5.27
4	2	8	15	75	0.0365	0.0451	5.89
5	2	16	30	100	0.0112	0.0423	6.92
6	2	24	45	50	0.0099	0.0266	5.87
7	3	8	30	50	0.0098	0.0451	5.94
8	3	16	45	75	0.0012	0.0296	6.12
9	3	24	15	100	0.0014	0.0091	7.14
10	1	8	45	100	0.0356	0.0478	7.82
11	1	16	15	50	0.0085	0.0225	7.18
12	1	24	30	75	0.0130	0.0489	8.23
13	2	8	30	100	0.0201	0.0589	7.87
14	2	16	45	50	0.0173	0.0149	8.12
15	2	24	15	75	0.0194	0.0412	8.94
16	3	8	45	75	0.0080	0.0072	8.15
17	3	16	15	100	0.0251	0.0188	7.25
18	3	24	30	50	0.0097	0.0419	8.92

### 1.1 Multi-objective Optimization

#### 1.1.1 Technique for Order of Preference by Similarity to Ideal Solution (TOPSIS)

TOPSIS is an appropriate technique to identify the suitable parametric solution from the set-off experimental combinations. The procedures followed in this method are provided below [30] and [31].

Step 1: Choices of variables, i.e., all the responses are employed in the matrix in *n* attributes and *m* alternatives, which is shown with Eq. (1).

$$E_m = \begin{bmatrix} R_{11} & R_{12} & R_{13} & \dots & R_{1n} \\ R_{21} & R_{22} & R_{23} & \dots & R_{2n} \\ R_{31} & R_{32} & R_{33} & \dots & R_{3n} \\ \vdots & \vdots & \vdots & \ddots & \vdots \\ R_{m1} & R_{m2} & R_{m3} & \dots & R_{mn} \end{bmatrix}, \quad (1)$$

where  $R_{ij}$  is the presentation of  $i^{th}$  alternative with respect to  $j^{th}$  attribute.

Step 2: Eq. (2) has been used for the normalization of matrix values, which can convert all values in a single form of units.

$$r_{ij} = \frac{R_{ij}}{\sqrt{\sum_{i=1}^m R_{ij}^2}}, \quad j = 1, 2, \dots, n. \quad (2)$$

Step 3: Weights for the output responses are assigned using Eq. (3) as  $W_j(j=1, 2, \dots, n)$ . The preferences for outcome responses are assigned based on the requirement.

$$Y = W_j r_{ij}, \quad (3)$$

where,  $\sum_{j=1}^n W_j = 1$ .

Step 4: Suitable (best) ideal result is estimated using Eq. (4) and the worst ideal result is attained through Eq. (5).

$$Y^+ = \left\{ \left( \sum_i^{\max} Y_{ij} \mid j \in J \mid i = 1, 2, \dots, m \right) \right\} \\ = \{y_1^+, y_2^+, y_3^+, \dots, y_n^+\}, \quad (4)$$

$$Y^- = \left\{ \left( \sum_i^{\min} Y_{ij} \mid j \in J \mid i = 1, 2, \dots, m \right) \right\} \\ = \{y_1^-, y_2^-, y_3^-, \dots, y_n^-\}. \quad (5)$$

Step 5: The value differences among the parameters are evaluated with the 'suitable ideal' solution is calculated using Eq. (6).

$$t_i^+ = \sqrt{\sum_{j=1}^n (Y_{ij} - y_j^+)^2}, \quad i = 1, 2, \dots, m. \quad (6)$$

The deviation of experimental results from the 'worst-ideal' solution is calculated using Eq. (7).

$$t_i^- = \sqrt{\sum_{j=1}^n (Y_{ij} - y_j^-)^2}, \quad i = 1, 2, \dots, m. \quad (7)$$

Step 6: Eq. (8) used to find the closeness of various parameters solution which is presented below.

$$P_i = \frac{t_i^-}{t_i^+ + t_i^-}, \quad i = 1, 2, \dots, m. \quad (8)$$

Step 7: Obtained preference values ( $P_i$ ) are ordered in a downward manner to identify the best parameter solution.

### 1.1.2 Grey Relational Analysis Technique (GRA)

With the GRA method, the output responses of different units should be converted into a homogeneous form (i.e., unit-less number). Therefore, the experimental results are converted from zero to one through the below-mentioned equations [30] and [31]. The output values (i.e., MRR, TWR and SR values) are estimated using Eqs. (9) and (10), respectively:

$$Y_i^*(P) = \frac{y_i(P) - \min y_i(P)}{\max y_i(P) - \min y_i(P)}, \quad (9)$$

where  $i = 1, 2, \dots, m, P = 1, 2, \dots, n$ ,

$$y_i^*(P) = \frac{\max y_i(P) - y(P)}{\max y_i(P) - \min y_i(P)}, \quad (10)$$

where  $i = 1, 2, \dots, m, P = 1, 2, \dots, n$ .

Here, the equation contains  $m$  means the total number of experiments and  $n$  means received data. Eq. (11) is employed to estimate the grey relational coefficient (GRC) with the normalized values:

$$k_i(N) = \frac{\Delta_{\min} + \zeta \Delta_{\max}}{\Delta_{oi}(Q) + \zeta \Delta_{\max}}. \quad (11)$$

Here,  $\Delta_{oi}(Q)$  divergence series is chosen from the reference sequence  $k(N)$  and comparability sequence  $k_i^*(N)$ . The range 0 to 1 has been used for the distinguished coefficient  $k_i$ .

$$T_i = \frac{1}{n} \sum_{p=1}^n j_i(N). \quad (12)$$

The weight values of each output response are in summation with GRC to find the grey relational grade (GRG)  $T_i$  is displayed in Eq. (12).

## 2 RESULT AND DISCUSSION

### 2.1 Influences of Input Parameters on MRR

The influences of the input parameters (i.e., electrode, peak current, pulse on time and gap voltage on MRR) are presented in Fig. 6. The experiments are conducted using three different tools, displayed in Table 3. The graphs are drawn according to the mean values of MRR against the input parameter values. It is clear from the figure that using composite tools exhibits higher MRR when compared to the plain copper tool, which produces 0.0319 g/min MRR. This value is 1.9 times higher than the existing composite tool used in the EDM process. The PM-based composite tools possess uneven surfaces at the end face tool with porosity. Hence, the passing of electric current has fast movement between the inter-electrode gap, which ensures higher MRR with the composite electrode [32]. Also, MRR is increased with the increasing percentage of titanium carbide and zirconium silicate in the composite tools. The softness of the composite tool is increased by the presence of zirconium silicate, which leads to high inter-metallic gaps among the particles. This phenomenon leads to better current conduction in the tool electrode and leads to the higher MRR.

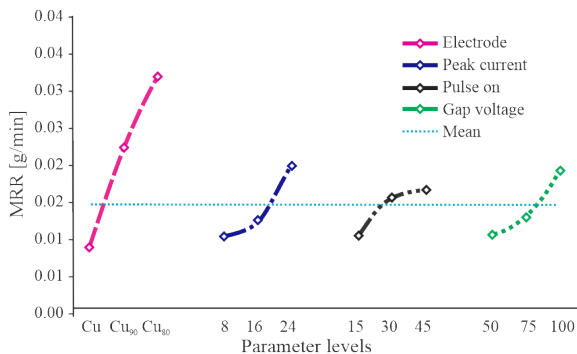


Fig. 6. Influences of input parameters on MRR

Moreover, from the figure, it is observed that increasing the peak current increases the MRR. It is a common fact that increasing the current with no flow disturbance in the electrode can produce the narrow power supply in the machining zone, which causes higher MRR [33]. The same trend of higher MRR has been obtained with the increasing of pulse on time and gap voltage. The timing of current passage and flow ability increases at higher level, which leads to the higher MRR for all tools.

### 2.2 Influences of Input Parameters on TWR

The effect of input parameters on TWR is displayed in Fig. 7. The figure shows that PM-based tools produce lower TWR (0.0234 g/min) when there is an increase in the percentage of titanium carbide and zirconium silicate. Increasing the percentage of compositions increases the wear resistance among particles and increases the porosity of the tools. Therefore, the connectivity of the current is disbursed when it is applied to the machining zone [34]. This character of tool electrodes leads to less TWR on PM tools at higher levels of parameter combinations. However, the percentage of titanium carbide and zirconium silicate at the middle stage electrode (i.e., 5 % TiC and 5 % ZrSiO<sub>4</sub>) shows the increased TWR with increasing of parametric range. It is because titanium carbide provides the additional energy to the electrode to pass the current by its conductivity nature. Therefore, the middle stage of composite electrodes produces the higher TWR. , due to the high spark energy of tool, higher TWR has been obtained with the higher peak current, pulse on time and gap voltages.

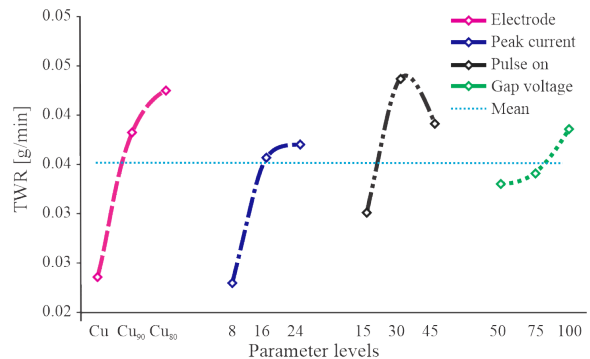


Fig. 7. Influences of input parameters on TWR

### 2.3 Influences of Input Parameters on SR

The effect of input parameters on the SR is displayed in Fig. 8. The SR shows the increasing trend with increases in parameters values. Better surface finish is observed with plain copper tool, producing the surface finish in the range of 6.16  $\mu\text{m}$  to 7.04  $\mu\text{m}$ , which is lower than other PM-based composite tools.

The PM composite tool produces crater surfaces, and it becomes the cause of higher MRR. The higher craters exhibit less surface finish and elements of the tool transferred over the machined surfaces. Hence, the surface finish of the machined area leads to the poor quality with PM composite tools than plain copper tool [35]. Also, the increasing of peak current, pulse on time, and gap voltage cause increasing spark

energy on the machining zone, which leads the excess material removal on the work material [36]. The SEM image of the machined area are shown in Figs. 9 and 10 for first and second optimal combinations. Furthermore, the machined products (debris) are deposited over the crater surface due to the improper flushing and form the recast layer on the machined surface.

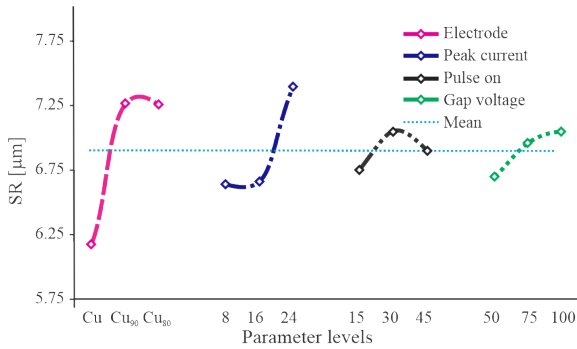


Fig. 8. Influences of input parameters on SR

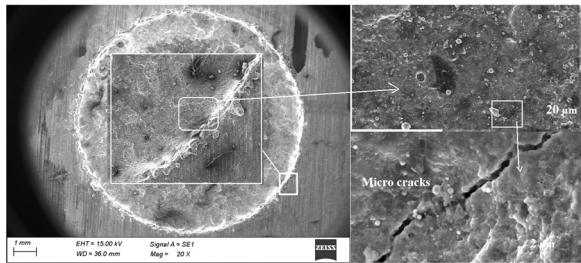


Fig. 9. SEM image of 1st optimal combination

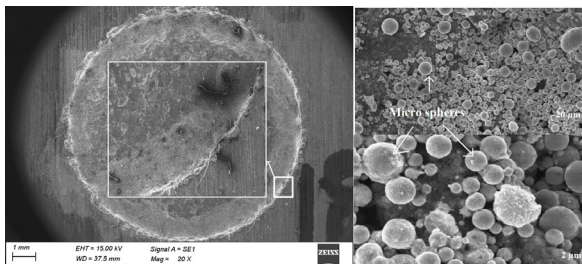


Fig. 10. SEM image of 2nd optimal combination

2.4 TOPSIS

The output values of EDM such as MRR, TWR and SR through PM based tools are optimized using the TOPSIS technique. Eqs. (1) to (8) have been used to obtain the preference value for the experimentations. Equal weights are assigned to all output responses under ideal conditions. The preferences values ( $P_i$ ) and their ranking orders are represented in Table 4. The outcomes of the research are converted from

multi-objective optimization to single attribute optimization through combined methods of Taguchi and TOPSIS. The furthest preference value is termed as optimal parameter solution and the maximum rank is considered as the first optimal solution. Therefore, it is observed that the 17<sup>th</sup> experimental run (0.6735) is chosen as the best optimal parameter solution for the best performance of EDM due to the highest  $P_i$  value. The experimental runs 4<sup>th</sup> (0.6714) and 10<sup>th</sup> (0.6259) show the second and third best optimal parameter combinations. Hence, the best optimal solution is found to be the Cu<sub>90</sub>(TiC)<sub>5</sub>(ZrSiO<sub>4</sub>)<sub>5</sub> PM-based tool, E8 Amp peak current, 15 µs pulse on time and 75 V gap voltage using TOPSIS.

Table 4. TOPSIS ranking

Experiment No.	$Y_i +$	$Y_i -$	$P_i$ (Preference value)	Rank
1	0.4504	0.2039	0.3116	13
2	0.4836	0.2561	0.3462	12
3	0.3388	0.3187	0.4847	5
4	0.2393	0.4890	0.6714	2
5	0.4100	0.1815	0.3068	14
6	0.3777	0.2520	0.4002	8
7	0.4281	0.1752	0.2904	16
8	0.4933	0.2032	0.2917	15
9	0.4773	0.3111	0.3946	9
10	0.2779	0.4649	0.6259	3
11	0.3970	0.2512	0.3876	10
12	0.4263	0.1713	0.2866	17
13	0.4042	0.2556	0.3874	11
14	0.2920	0.3462	0.5425	4
15	0.3479	0.2664	0.4337	7
16	0.4014	0.3309	0.4519	6
17	0.1972	0.4068	0.6735	1
18	0.4450	0.1545	0.2578	18

2.6 Table of ANOVA for TOPSIS

ANOVA is a prominent method to determine the important and insignificant factors. The  $P_i$  values of PM-based tools are statically analysed using ANOVA, and the influences of each parameter over the output responses are examined. In addition, the  $F$ -test outcomes are used to identify the most important factor to attain better performance. Table 5 shows that pulse on time plays a major role, which contributes around 46.8 % to the machining performance. The next important factor is the tool electrode, which controls the machining performances, contributing about 27.7 %.

**Table 5.** Table of ANOVA for TOPSIS

Machining parameter symbol	DOF	SS	MS	F-test	% Contri
TE	2	0.0835	0.0418	2.9863	27.76
PC	2	0.0417	0.0209	1.4913	13.86
PT	2	0.1410	0.0705	5.0434	46.89
GV	2	0.0123	0.0062	0.4406	4.09
E	9	0.1258	0.0140		7.38
Total	17	0.4044	0.0238		100

**2.7 GRA**

In GRA method, outcomes of EDM (i.e., MRR, TWR, and SR) for various tools are normalized using Eqs. 9 and 10. Eqs. 11 and 12 are used to determine the GRC and GRG, respectively, for all conducted experiments. Equal weights are assigned for all responses. GRG and its rankings are displayed in Table 6. The furthest GRG value has been considered the optimal parameter solution. Therefore, based on the table, the 4<sup>th</sup> experimental run (0.7887) is the best optimal parameter solution, and the 17<sup>th</sup> (0.7868) and 16<sup>th</sup> (0.7773) experimental runs are the next best optimal parameter solutions through GRA method. Hence, the optimal parameter solution found to be Cu<sub>90</sub>(TiC)<sub>5</sub> (ZrSiO<sub>4</sub>)<sub>5</sub> PM-based tool, 8 A peak current, 15 μs pulse on time and 75 V gap voltage using GRA.

**2.7 Table of ANOVA for GRG**

The GRG results of various tools are statically analysed using ANOVA, presented in Table 7. The outcomes of results for PM based tools are optimized using the GRA method.

Therefore, peak current shows the most significant contribution around 39.3 % on machining performance.

The next significant parameter is pulse on time, which contributes on performances around 36.8 %.

The ranking values of TOPSIS and GRA technique are presented as a graph in Figure 8, which is plotted for experimental run vs. TOPSIS and GRA values. The 4<sup>th</sup> and 17<sup>th</sup> experimental runs show the first two optimal combinations for the best performance of EDM using the TOPSIS and GRA methods. Moreover, in both techniques, they provide the same parametric combination for machining. Also, the 10<sup>th</sup> and 16<sup>th</sup> experimental runs show the third optimal combinations using the TOPSIS and GRA methods.

**Table 6.** GRG ranking

Experiment No.	GRC			GRG	Rank
	MRR	TWR	SR		
1	0.5729	0.5286	1.0000	0.5508	18
2	0.5000	0.7407	0.9470	0.6204	11
3	0.7254	0.5258	0.8074	0.6256	10
4	1.0000	0.5773	0.7314	0.7887	1
5	0.5832	0.5955	0.6325	0.5894	14
6	0.5708	0.7279	0.7336	0.6493	8
7	0.5703	0.5771	0.7259	0.5737	17
8	0.5007	0.6984	0.7067	0.5996	12
9	0.5023	0.9651	0.6148	0.7337	6
10	0.9745	0.5603	0.5657	0.7674	4
11	0.5585	0.7725	0.6117	0.6655	7
12	0.6010	0.5536	0.5398	0.5773	16
13	0.6839	0.5000	0.5624	0.5919	13
14	0.6484	0.8708	0.5465	0.7596	5
15	0.6742	0.6037	0.5000	0.6389	9
16	0.5545	1.0000	0.5446	0.7773	3
17	0.7568	0.8167	0.6063	0.7868	2
18	0.5691	0.5983	0.5010	0.5837	15

**Table 7.** Table of ANOVA for GRG

Machining parameter symbol	DOF	SS	MS	F test	% Contri
TE	2	0.0098	0.0049	0.284	8.03
PC	2	0.0479	0.024	17.20	39.30
PT	2	0.0449	0.0225	16.12	36.82
GV	2	0.0068	0.0034	2.43	5.56
E	9	0.0125	0.0014		10.27
Total	17	0.1219	0.0072		100

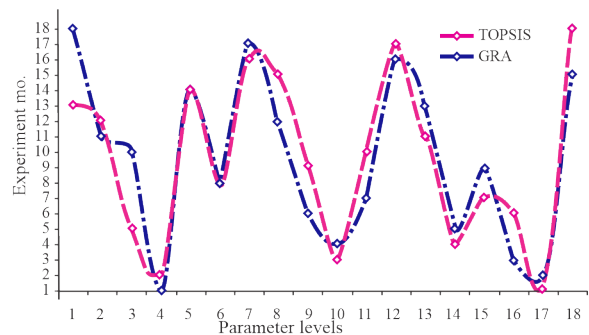


**Fig. 11.** Comparison of TOPSIS and GRA ranking

**3 CONCLUSIONS**

This research work aims to explore the benefits and performance measures of powder metallurgy-based copper electrodes in the EDM process. Two electrodes in different reinforcement combinations (i.e.,

$\text{Cu}_{90}(\text{TiC})_5(\text{ZrSiO}_4)_5$  and  $\text{Cu}_{80}(\text{TiC})_{10}(\text{ZrSiO}_4)_{10}$  are prepared using a PM technique, and their results are compared with a plain Cu electrode. The experiments are conducted based on the L-18 OA, and optimization techniques (e.g., TOPSIS and GRA) are used to find the optimal solution.

The results show that MRR and TWR increase with increasing of the percentage of reinforcements in the composite electrodes. The  $\text{Cu}_{90}$  (Copper composite) tool electrode exhibits 0.0319 g/min MRR and this value is 1.9 times higher when compared to the existing tool electrode. The TOPSIS and GRA optimization techniques produce the same optimal parametric solution for lesser TWR, SR and higher MRR. Hence, the 17<sup>th</sup> experimental run is proposed as optimal parameter combination:  $\text{Cu}_{90}(\text{TiC})_5(\text{ZrSiO}_4)_5$ , E8 Amp peak current, 15  $\mu\text{s}$  pulse on time and 75 V gap voltage. In addition, based on the ANOVA table of TOPSIS, pulse on time plays a major role, contributing around 46.8 % to the machining performance, and peak current shows the most significant contribution of around 39.3 % on machining performance using GRA values.

Therefore, the  $\text{Cu}_{90}$  composite tool is more appropriate for the higher MRR and less TWR. Furthermore, experiments can be conducted with various concentrations of reinforcements and different work materials to understand the behaviour of machining.

#### 4 REFERENCES

- [1] Sivakumar, K., Kumar, P.M., Amarkarthik, A., Jegadheeswaran, S., Shanmugaparakash, R. (2021). Empirical modeling of material removal rate and surface roughness of OHNS steel using Cu-TiB<sub>2</sub>Tool in EDM. *Materials Today: Proceedings*, vol. 45, part 2, p. 2725-2729, DOI:10.1016/j.matpr.2020.11.597.
- [2] Chakmakchi, M., Ntasi, A., Mueller, W. D., Zinelis, S. (2021). Effect of Cu and Ti electrodes on surface and electrochemical properties of Electro Discharge Machined (EDMed) structures made of Co-Cr and Ti dental alloys. *Dental Materials*, vol. 37, no. 4, p. 588-296, DOI:10.1016/j.dental.2021.01.012.
- [3] Yadav, V.K., Singh, R., Kumar, P., Dvivedi, A. (2021) Performance enhancement of rotary tool near-dry EDM process through tool modification. *Journal of Brazilian Society of Mechanical Sciences and Engineering*, vol. 43, art. ID 72, DOI:10.1007/s40430-021-02806-y.
- [4] Taherkhani, A., Ilani, M.A., Ebrahimi, F., Huu, P.N, Long, B.T., Dong, P.V., Tam, N.C., Minh, N.D., Duc, N.V. (2021). Investigation of surface quality in cost of goods manufactured (COGM) method of  $\mu\text{-Al}_2\text{O}_3$  powder-mixed-EDM process on machining of Ti-6Al-4V. *International Journal of Advanced Manufacturing Technology*, vol. 116, p. 1783-1799, DOI:10.1007/s00170-021-07573-7.
- [5] Phan, N.H., Pi, V.N., Shirguppikar, S., Patil, M.S., Ilani, M.A., Hung, L.X., Hung, T.Q. (2020). Material removal rate in electric discharge machining with aluminum tool electrode for Ti-6Al-4V titanium alloy. *International Conference on Engineering Research and Applications*, p. 527-533, DOI:10.1007/978-3-030-64719-3\_58.
- [6] Ilani, M.A., Khoshnevisan, M. (2021). Study of surfactant effects on intermolecular forces (IMF) in powder-mixed electrical discharge machining (EDM) of Ti-6Al-4V. *The International Journal of Advanced Manufacturing Technology*, vol. 116, p. 1763-1782, DOI:10.1007/s00170-021-07569-3.
- [7] Ilani, M.A., Khoshnevisan, M. (2020). Powder mixed-electrical discharge machining (EDM) with the electrode is made by fused deposition modeling (FDM) at Ti-6Al-4V machining procedure. *Multiscale and Multidisciplinary Modeling, Experiments and Design*, vol. 3, p. 173-186, DOI:10.1007/s41939-020-00070-6.
- [8] Phan N.H., Pi, V.N., Tuan, N.G., Shirguppikar, S., Patil, M.S., Ilani, M.A., Hung, L.X., Muthuramalingam, T., Hung, T.Q. (2021) Tool wear rate analysis of uncoated and AlCrNi coated aluminum electrode in EDM for Ti-6Al-4 V titanium alloy. *Advances in Engineering Research and Application. Lecture Notes in Networks and Systems*, vol. 178, DOI:10.1007/978-3-030-64719-3\_91.
- [9] Shaikh, M.S.N.M., Ahuja, B.B. (2020). Effects of primary and secondary metallization techniques on the performance of electric discharge machining (EDM) electrode produced by additive manufacturing and composite coating. *Materials Today: Proceedings*, vol. 41, part, 4, p. 874-885, DOI:10.1016/j.matpr.2020.09.441.
- [10] Walia, A.S., Srivastava, V., Jain, V., Bansal, S.A. (2020). Effect of Tic reinforcement in the copper tool on roundness during EDM process. *Advances in Materials Science and Engineering, Lecture Notes in Mechanical Engineering*, p. 125-135, DOI:10.1007/978-981-15-4059-2\_10.
- [11] Sahu, A.K., Mahapatra, S.S. (2020). Performance analysis of tool electrode prepared through laser sintering process during electrical discharge machining of titanium. *The International Journal of Advanced Manufacturing Technology*, vol. 106, p. 1017-1041, DOI:10.1007/s00170-019-04675-1.
- [12] Mahipal Reddy, L., Siva Rama Krishna, L., Sharath Kumar, S., Ravinder Reddy, P. (2020). A comparative study on performance of 3D-Printed EDM electrode with conventional EDM electrode. *Recent Trends in Mechanical Engineering. Lecture Notes in Mechanical Engineering*, p. 217-225, DOI:10.1007/978-981-15-1124-0\_19.
- [13] Yadav, V.K., Kumar, P., Dvivedi, A. (2019). Effect of tool rotation in near-dry EDM process on machining characteristics of HSS. *Materials and Manufacturing Processes*, vol. 34, no. 7, p. 779-790, DOI:10.1080/10426914.2019.1605171.
- [14] Padhi, S.K., Mahapatra, S.S., Padhi, R., Das, H.C. (2018). Performance analysis of a thick copper-electroplated FDM ABS plastic rapid tool EDM electrode. *Advances in Manufacturing*, vol. 6, p. 442-456, DOI:10.1007/s40436-018-0238-5.
- [15] Mathai, V.J., Dave, H.K., Desai, K.P. (2017). Experimental investigations on EDM of Ti6Al4V with planetary tool actuation. *Journal of Brazilian Society of Mechanical Sciences and*

- Engineering*, vol. 39, p. 3467-3490, DOI:10.1007/s40430-016-0657-9.
- [16] Wang, K., Zhang, Q., Zhu, G., Liu, Q., Huang, Y. (2017). Experimental study on micro electrical discharge machining with helical electrode. *International Journal of Advanced Manufacturing and Technology*, vol. 93, p. 2639-2645 DOI:10.1007/s00170-017-0747-6.
- [17] Vincent, N., Kumar, A.B. (2016). Experimental investigations into EDM behaviours of En41b using copper and brass rotary tubular electrode. *Procedia Technology*, vol. 25, p. 877-884. DOI:10.1016/j.protcy.2016.08.196.
- [18] Singh, N.K., Pandey, P.M., Singh, K.K. (2015). EDM with an air-assisted multi-hole rotating tool. *Materials and Manufacturing Processes*, vol. 31, no. 14, p. 1872-1878, DOI:10.1080/10426914.2015.1127954.
- [19] Banh, T.L., Nguyen, H.P., Ngo, C., Nguyen, D.T. (2018). Characteristics optimization of powder mixed electric discharge machining using titanium powder for die steel materials. *Proceedings of the Institution of Mechanical Engineers, Part E: Journal of Process Mechanical Engineering*, vol. 232, no. 3, p. 281-298, DOI:10.1177/0954408917693661.
- [20] Phan, N.H., Dong, P.V., Muthuramalingam, T., Thien, N.V., Dung, H.T., Hung, T.Q., Ly, N.T. (2021). Experimental investigation of uncoated electrode and PVD AlCrNi coating on surface roughness in electrical discharge machining of Ti-6Al-4V. *International Journal of Engineering*, vol. 34, no. 4, p. 928-934, DOI:10.5829/IJE.2021.34.04A.19.
- [21] Nguyen, H.P., Pham, V.D., Ngo, N.V. (2018). Application of TOPSIS to Taguchi method for multi-characteristic optimization of electrical discharge machining with titanium powder mixed into dielectric fluid. *The International Journal of Advanced Manufacturing Technology*, vol. 98, no. 5, p. 1179-1198, DOI:10.1007/s00170-018-2321-2.
- [22] Sundriyal, S., Vipin, V., Walia, R.S. (2020). Study on the influence of metallic powder in near-dry electric discharge machining. *Strojniški vestnik - Journal of Mechanical Engineering*, vol. 66, no. 4, p. 243-253, DOI:10.5545/sv-jme.2019.6475.
- [23] Sundriyal, S., Vipin, V., Walia, R. S. (2020). Experimental Investigation of the micro-hardness of EN-31 die steel in a powder-mixed near-dry electric discharge machining method. *Strojniški vestnik - Journal of Mechanical Engineering*, vol. 66, no. 3, p. 184-192, DOI:10.5545/sv-jme.2019.6474.
- [24] Yuvaraj, T., Suresh, P. (2019). Analysis of EDM process parameters on inconel718 using the Grey-Taguchi and Topsis methods. *Strojniški vestnik - Journal of Mechanical Engineering*, vol. 65, no. 10, p. 557-565, DOI:10.5545/sv-jme.2019.6194.
- [25] Sahu, A.K., Mahapatra, S.S. (2020). Performance analysis of Cu-W-B4C composite tool during electrical discharge machining of titanium alloy. *Proceedings of the Institution of Mechanical Engineers, Part C: Journal of Mechanical Engineering Science*, vol. 235, no. 11, p. 1992-2007, DOI:10.1177/0954406220951597.
- [26] Patowari, P.K., Saha, P., Mishra, P.K. (2011). Taguchi analysis of surface modification technique using W-Cu powder metallurgy sintered tools in EDM and characterization of the deposited layer. *The International Journal of Advanced Manufacturing Technology*, vol. 54, p. 593-604, DOI:10.1007/s00170-010-2966-y.
- [27] Tsai, H.C., Yan, B.H., Huang, F. Y. (2003). EDM performance of Cr/Cu-based composite electrodes. *International Journal of Machine Tools and Manufacture*, vol. 43, no.3, p. 245-252, DOI:10.1016/S0890-6955(02)00238-9.
- [28] Sahu, A.K., Mahapatra, S.S. (2020). Prediction and optimization of performance measures in electrical discharge machining using rapid prototyping tool electrodes. *Journal of Intelligent Manufacturing*, p. 1-21, DOI:10.1007/s10845-020-01624-8.
- [29] Ilani, M.A., Khoshnevisan, M. (2021). Mathematical and physical modeling of FE-SEM surface quality surrounded by the plasma channel within Al powder-mixed electrical discharge machining of Ti-6Al-4V. *The International Journal of Advanced Manufacturing Technology*, vol. 112, p. 3263-3277, DOI:10.1007/s00170-021-06626-1.
- [30] Soundarrajan, M., Thanigaivelan, R. (2018). Investigation on electrochemical micromachining (ECMM) of copper inorganic material using UV heated electrolyte. *Russian Journal of Applied Chemistry*, vol. 91, p. 1805-1813, DOI:10.1134/S1070427218110101.
- [31] Soundarrajan, M., Thanigaivelan, R. (2019). Investigation of electrochemical micromachining process using ultrasonic heated electrolyte. *Advances in Micro and Nano Manufacturing and Surface Engineering, Lecture Notes on Multidisciplinary Industrial Engineering*, p. 423-434, DOI:10.1007/978-981-32-9425-7\_38.
- [32] Khanra, A.K., Sarkar, B.R., Bhattacharya, B., Pathak, L.C., Godkhindi, M.M. (2007). Performance of ZrB<sub>2</sub>-Cu composite as an EDM electrode. *Journal of Materials Processing Technology*, vol. 183, no. 1, p. 122-126, DOI:10.1016/j.jmatprotec.2006.09.034.
- [33] Soundarrajan, M., Thanigaivelan, R. (2020). Effect of coated and geometrically modified tools on performance of electrochemical micromachining. *Materials and Manufacturing Processes*, vol. 35, no. 7, p. 775-782, DOI:10.1080/10426914.2020.1740252.
- [34] El-Taweel, T.A. (2009). Multi-response optimization of EDM with Al-Cu-Si-TiC P/M composite electrode. *The International Journal of Advanced Manufacturing Technology*, vol. 44, p. 100-113, DOI:10.1007/s00170-008-1825-6.
- [35] M.S. Shunmugam, P.K. Philip, Gangadhar, A. (1994). Improvement of wear resistance by EDM with tungsten carbide P/M electrode. *Wear*, vol. 171, no. 1-2, p. 1-5, DOI:10.1016/0043-1648(94)90340-9.
- [36] Singh, S., Maheshwari, S., Pandey, P.C. (2004). Some investigations into the electric discharge machining of hardened tool steel using different electrode materials, *Journal of Materials Processing Technology*, vol. 149, no. 1-3, p. 272-277, DOI:10.1016/j.jmatprotec.2003.11.046.

# A Method for Calculating Elliptic Gear Transmission Efficiency Based on Transmission Experiment

Changbin Dong<sup>1</sup> – Yongping Liu<sup>1</sup> – Gang Zhao<sup>2</sup>

<sup>1</sup>Lanzhou University of Technology, School of Mechanical and Electric Engineering, China

<sup>2</sup>Hubei Key Laboratory of Mechanical Transmission and Manufacturing Engineering, China

*Transmission efficiency is an important index to evaluate the transmission performance and energy consumption of gear transmission systems. To analyse the transmission efficiency of elliptic gears, the load torque fluctuation model of elliptic gear is established to analyse the influence of load torque of an elliptic gear transmission system on the torque of input and output. The torque data of input and output under different working conditions are obtained by conducting an elliptic gear transmission test. Finally, the transmission efficiency of the elliptic gear pair is obtained through the torque measurement data of the elliptic gear transmission test, and its variation law under different working conditions is analysed. The results show that the transmission efficiency of the elliptic gear transmission system changes constantly and presents an increasing trend with the increase of load torque and a decreasing trend with the increase of speed.*

**Keywords:** elliptic gear, transmission test, load fluctuation, torque, transmission efficiency

## Highlights

- The torque fluctuation calculation model of an elliptic gear is analysed and established.
- The elliptic gear transmission test rig is built, which can be used to obtain the corresponding dynamic data.
- The dynamic transmission efficiency of an elliptic gear pair is calculated and obtained, and the influence of various operating parameters on the instantaneous transmission efficiency of the system is analysed.

## 0 INTRODUCTION

With the development of mechanical products towards complexity and diversification, the demand for high-performance non-uniform transmission mechanisms increases day by day. The transmission mechanism represented by non-circular gear, which can achieve an accurate and stable speed ratio, shows unique advantages in improving equipment performance and realizing specific transmission requirements [1] and [2]. As a new type of gear transmission, the elliptic gear is mainly used to transmit the non-uniform motion between two shafts, and to realize the non-linear relationship between the rotation angles of driving and driven parts [3] and [4]. The non-circular gear transmission system represented by elliptic gear has a strong bearing capacity, a compact structure, and a variable ratio transmission. It is mainly used in low speed and high torque occasions, such as rotary vane engines, hydraulic pumps, hydraulic motors, printing presses, packaging machines, textile equipment, spacecraft frequency converters, tank fire control systems [5] and [6], continuously variable transmissions (CVT) [7], etc. Considering the expansion of its applications and the key role and special requirements in the transmission, it is meaningful to carry out in-depth research on the transmission efficiency of the elliptic gear transmission system.

Many research results have been accumulated for the transmission efficiency analysis method of gear transmission systems. Diez-Ibarbia et al. [8] combined the tooth surface friction coefficient and transmission efficiency, analysed the influence of the selection of friction coefficient on the transmission efficiency of modified spur gears. Wang et al. carried out a detailed study on the transmission efficiency of gear transmission systems. They combined tooth surface friction with power loss and tooth surface elastohydrodynamic lubrication [9] and proposed a calculation method of sliding friction loss of involute helical gear pair under load [10], considering assembly error, machining error, deformation, and other factors. On this basis, the friction power loss and transmission efficiency of the gear transmission system under different working conditions and design parameters are analysed [11] to [12], and the relevant data are obtained by building an experimental platform, which finally verifies the rationality of the proposed method [13] to [14]. Petry-Johnson et al. [15] obtained the transmission efficiency of the system under the condition of high speed and variable torque by building a gear transmission test and analysed the changing trend of the meshing efficiency of the gear transmission system and the total efficiency of the gearbox under the condition of different speed and load torque. Xu et al. [16] proposed and established the calculation model of friction-related mechanical

efficiency loss of parallel shaft gear pair on the basis of comprehensively considering gear load distribution model, friction model and mechanical efficiency formula. Through gear transmission testing, the effects of geometric parameters, tooth profile modification, working conditions, surface finish, and lubricant performance on mechanical efficiency loss were analysed. Based on the elastohydrodynamic lubrication model, Li and Kahraman [17] proposed a model to predict the load-related power loss of spur gear pair. The instantaneous rolling and sliding shear in lubricating oil are determined by transient pressure distribution and oil film thickness distribution, so as to determine the mechanical power loss of gear meshing. Li et al. [18] determined the calculation formula of the meshing efficiency of the conical involute gear based on the piecewise equivalent method and analysed the influence of different gear parameters on the contact line length, unit load and meshing efficiency in the meshing period. Liu et al. [1] and [2] constructed a non-uniform end face movable tooth transmission mechanism by combining the end face movable tooth mechanism and non-circular gear pairs and analysed the influence of tooth surface sliding friction on the transmission efficiency through simulation. Liu et al. [19] analysed the influence of time-varying meshing angle of non-circular gear pair on rolling rate loss caused by sliding friction and rolling friction by establishing a mathematical model of meshing efficiency of non-circular gear under elastohydrodynamic lubrication.

Although the above research results have irreplaceable guiding significance for the analysis of transmission efficiency of the elliptic gear transmission system, most of the analysis of transmission efficiency of non-circular gear is only theoretical calculation without systematic experimental analysis. In contrast, the experimental analysis can better reflect the authenticity and has more guiding significance. Therefore, this paper first analyses the load fluctuation of the elliptic gear transmission system and extracts the torque data of the input and output ends by building the elliptic gear transmission test-bed; it then calculates and obtains the instantaneous transmission efficiency of the elliptic gear transmission system.

### 1 CALCULATION MODEL OF TRANSMISSION EFFICIENCY OF ELLIPTIC GEAR

Because of the variable ratio transmission characteristics of elliptic gear pairs, their instantaneous transmission efficiency is always changing. The transmission efficiency of a gear pair can reflect its

load-carrying capacity and power loss, especially for elliptic gears, which are suitable for low-speed and high torque conditions. Therefore, it is of great significance to analyse its instantaneous transmission efficiency. In general, the transmission efficiency of elliptic gear system is defined as:

$$\eta = \frac{T_2}{T_1 i_{12}} \times 100, \quad [\%] \quad (1)$$

where  $T_1$  represents the arithmetic mean value of input torque,  $T_2$  represents the arithmetic mean value of the output torque, and  $i_{12}$  represents the transmission ratio of elliptic gear pair.

#### 1.1 Pitch Curve of Elliptic Gear

Fig. 1 shows the pitch curve of elliptic gear. The centre distance of the elliptic gear pair is  $a$ . The rotation angles of driving and driven gears are  $\theta_1$  and  $\theta_2$ , respectively. In the initial position,  $\theta_1 = \theta_2 = 0$ . The pitch curve equations of the driving and driven gears are as follows:

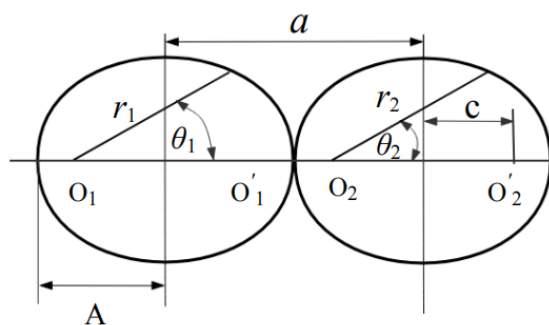


Fig. 1. Schematic diagram of elliptic gear pitch curve

$$r_1 = \frac{A(1 - e_1^2)}{1 - e_1 \cos(\theta_1)}, \quad (2)$$

$$r_2 = \frac{A(1 - e_2^2)}{1 + e_2 \cos(\theta_2)}, \quad (3)$$

where  $r_1$  and  $r_2$  represent the radius of pitch curve of driving gear and driven gear, respectively.  $A$  is the long half shaft of elliptic gear.  $e_1$  and  $e_2$  are the eccentricity of the driving and driven gears, respectively.  $c$  is the distance from the centre of elliptic symmetry to the focus, and  $c = eA$ .  $\theta_1$  and  $\theta_2$  are the rotation angles of driving and driven gears, respectively. The following are the relations between the rotation angles of driving and driven gears of elliptic gear pair:

$$\theta_2 = 2ac \tan \left[ \left( \frac{1 + e_1}{1 - e_1} \right) \tan \frac{\theta_1}{2} \right]. \quad (4)$$

### 1.2 Torque of Elliptic Gear Pair

The power transmission of the elliptic gear pair is similar to that of a cylindrical gear, and its transmission model is shown in Fig. 2a. Due to the time-varying curvature radius of the pitch curve of elliptic gears, there are certain differences among the teeth. Even if the load torque  $T_L$  on the driven shaft is constant, the torque fluctuation may occur on the driving side [20]. Therefore, in order to analyse the transmission torque of the elliptic gear pair, the load torque borne by the driven gear can be transformed into the driving gear, as shown in Fig. 2b.

The constant torque applied to the driven gear will lead to torque imbalance on the driving gear. Due to the time-varying transmission ratio function of the elliptic gear pair, the driven gear will produce a certain moment of inertia in the case of variable angular velocity. Therefore, under the condition that the drive shaft rotates at a constant speed, the total torque required to drive the load torque can be expressed as:

$$T_1 = \frac{T_2}{i_{12}} = \frac{T_L + I_2 \alpha_2}{i_{12}}, \quad (5)$$

where  $T_1$  and  $T_2$  are the loads on the driving and driven gears, respectively,  $T_L$  is the load torque,  $I_2$  is the moment of inertia of the driven gear, and  $\alpha_2$  is the angular acceleration of the driven gear.

It can be seen from Fig. 2 that when the angle of the elliptic gear is  $\theta_1 = \omega_1 t$ . The design parameters of the two elliptical gears are the same, so  $e_1 = e_2$ . The

transmission ratio of the elliptic gear pair can be expressed as:

$$i_{12} = \frac{a}{r_1} - 1 = \frac{1 + e_1^2 - 2e_1 \cos(\omega_1 t)}{1 - e_1^2}. \quad (6)$$

Then, the angular velocity and angular acceleration of the driven gear can be expressed as:

$$\omega_2 = \frac{(1 - e_1^2) \omega_1}{1 + e_1^2 - 2e_1 \cos(\omega_1 t)}, \quad (7)$$

$$\alpha_2 = \frac{d\omega_2}{dt} = -\frac{2\omega_1^2 e_1 (1 - e_1^2) \sin(\omega_1 t)}{[1 + e_1^2 - 2e_1 \cos(\omega_1 t)]^2}. \quad (8)$$

Because the profile of elliptic gear remains involute, its moment of inertia can be calculated according to the method of cylindrical gear. The elliptic gear is approximately equivalent to a cam, and the moment of inertia per unit tooth width of the elliptic gear can be expressed as:

$$I = \frac{\rho_0 [a(1 - e_1^2)]^4}{2} \int_0^\pi \frac{d\theta_1}{(1 + e_1 \cos \theta_1)^4}. \quad (9)$$

Let  $u = 1 + e \cos \theta_1$ , then Eq. (9) can be simplified as follows:

$$I = \frac{\rho_0 [a(1 - e_1^2)]^4}{2(e^2 - 1)^3} M \Big|_0^\pi = \frac{\pi \rho_0 [a(1 - e_1^2)]^4 (2 + 3e_1^2)}{4(1 - e_1^2)^3 \sqrt{1 - e_1^2}},$$

where  $\rho_0$  is the density of elliptic gear and  $M$  is as follows:

$$M = \left[ \frac{(e_1^2 - 1)^2}{3} - \frac{5(1 + e_1 \cos \theta_1)(e_1^2 - 1)}{6} + \frac{2(1 + e_1 \cos \theta_1)^2 (e_1^2 - 1)}{3} + \frac{5(1 + e_1 \cos \theta_1)^2}{2} \right] \cdot \frac{e_1 \cos \theta_1}{(1 + e_1 \cos \theta_1)^3} + \frac{2 + 3e_1^2}{2\sqrt{1 - e_1^2}} \arcsin \left( \frac{e_1 + \cos \theta_1}{1 + e_1 \cos \theta_1} \right).$$

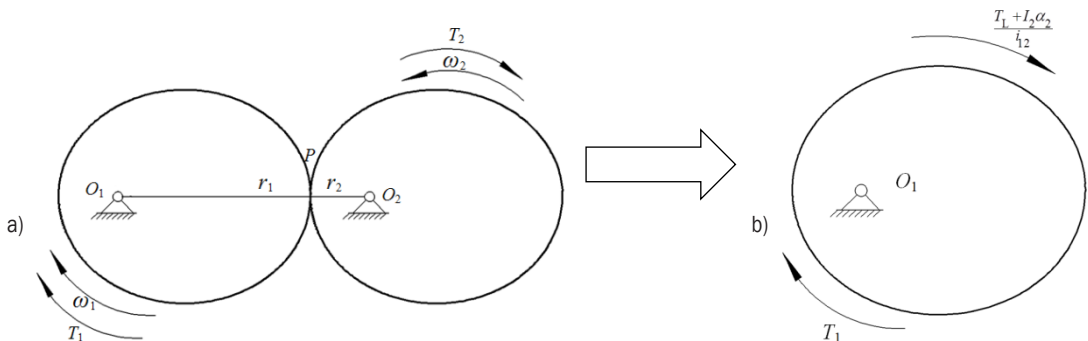


Fig. 2. Torque transmission model of elliptic gear pair;

a) the original elliptic gear meshing moment model, and b) the equivalent model after the load torque is applied to the driving gear

Substituting Eqs. (6) to (9) into Eq. (5), we obtain:

$$T_1 = \frac{(1 - e_1^2) \left[ T_L (1 + e_1^2 - 2e_1 \cos(\omega_1 t))^2 - I_2 2e_1 \omega_1 (1 - e_1^2) \sin(\omega_1 t) \right]}{(1 + e_1^2 - 2e_1 \cos(\omega_1 t))^3} \quad (10)$$

## 2 CONSTRUCTION OF ELLIPTIC GEAR TRANSMISSION TEST

The elliptic gear test adopts a horizontal mechanism composed of a precision mechanical system, measurement and control system, measurement software and other parts. The names and distribution positions of the main components of the test bench are shown in Fig. 3. The schematic diagram of its working principle is shown in Fig. 4. The elliptical gear reducer is installed in the gear test platform, the input and output ends of the reducer are connected through a coupling, and the signal is transmitted to the controller through computer control. The controller transmits the implementation command to the sensor and the driver, provides power and load by driving the motor, and then transmits the power and load to the reducer, so that the reducer can operate normally. The torque sensor and the vibration sensor sequentially collect the experimental data required to be measured and transmit them back to the computer through the controller to obtain the required experimental data. The elliptic gear transmission test is shown in Fig. 5.

The main machine of elliptic gear transmission test is mainly composed of a mechanical system, including input end components, output end components, reducer mounting bracket, and other parts. Each component is installed on the 2.6 m long cast iron platform base with a T-groove. The mounting bracket of the reducer is fixed in the middle

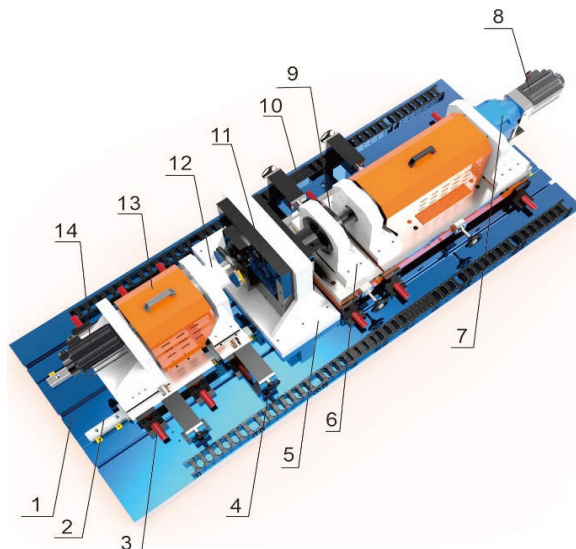


**Fig. 3.** The distribution of main engine components; 1 T-groove cast iron platform base; 2 linear guide rail; 3 Locking device; 4 hand wheel; 5 reducer base; 6 base; 7 Test planetary reducer; 8 Servo motor at output end; 9 Circular grating protective cover at output end; 10 drag chain; 11 reducer under test; 12 input end circular grating protective cover; 13 protective cover; 14 input servo motor

of the base. The left side is the input end assembly, and the right side is the output end assembly. The input end assembly includes input end motor slide

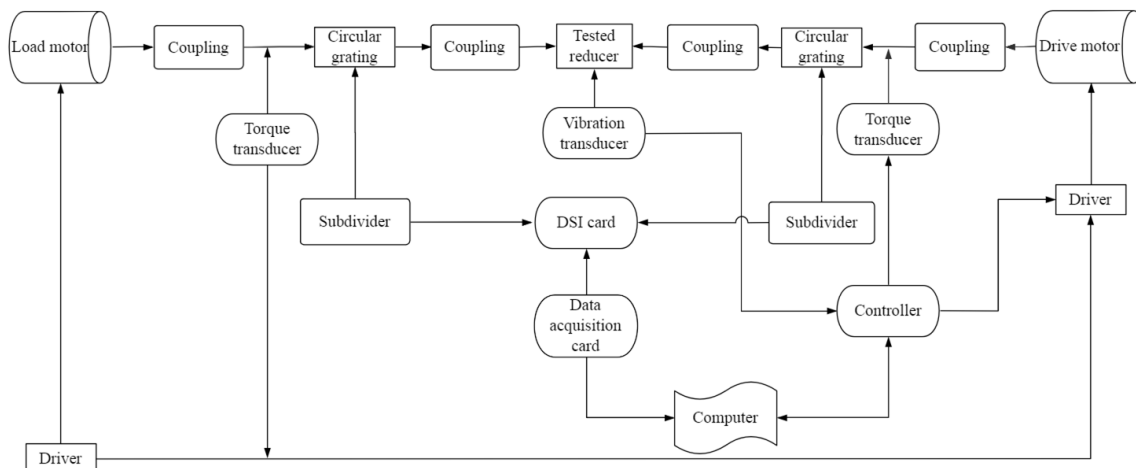


**Fig. 4.** Working principle of elliptic gear transmission test bench



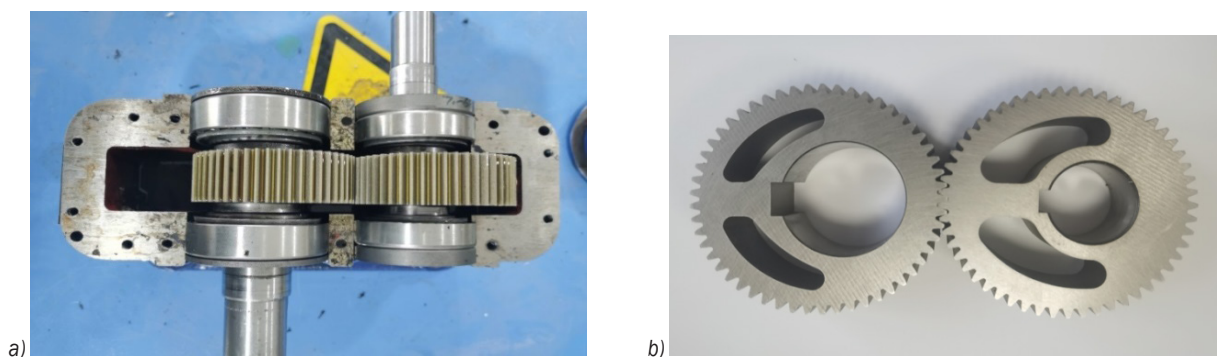
**Fig. 5.** The elliptic gear transmission test; a) overall view of the test bench, and b) partial view of the test bench

plate (installing input servo motor and input torque sensor) and input end grating encoder slide plate (installing input grating encoder). The output end assembly includes output end grating encoder slide plate (installing output grating encoder) and output end loading support slide plate (installing output servo motor and output torque sensor). Each slide plate is installed on the linear guide rail, which can be moved left and right through the hand gear to adjust the position. The input end is driven by an alternating current (AC) servo motor, which can work in speed mode and torque mode.

To realize the installation and test of different specifications and models of precision reducer, the test bench has a precision mounting bracket and supporting multi specification precision mounting accessories (connecting disc, input shaft and output shaft) so as to improve the universality of the test equipment. The whole system is controlled via an industrial computer, equipped with high-precision grating sensor system, high-precision torque sensor system and special measurement software, so as to realize the automatic measurement of the performance of precision reducer. The special feature of the test-bed is that it can be used for various types of reducers.

The mounting bracket of the reducer is fixed in the middle of the base, and the linear guide rail is installed on the cast iron platform base. The movement of the input and output components is realized through the gear rack mechanism.

The left-hand gear in Fig. 5b can ensure the implementation of lateral movement. There are similar mechanisms in the input end assembly and output end assembly, which can ensure the sliding of the input end motor and grating encoder slide plate and realize the connection or disconnection between the encoder and the output shaft of the tested reducer and the connection or disconnection between the output torque sensor and the output shaft of the tested reducer. In Fig. 5b, the right-hand gear can realize the vertical movement of the output component, which can make the slide plate of the input end grating encoder slide. To realize the connection or disconnection between the input shaft of the measured reducer and the reducer, the slide plate of the input end motor, and the connection or disconnection between the grating encoder and the input end torque sensor. Fig. 6 shows the processed elliptic gear pair, and its design parameters are shown in Table 1.



**Fig. 6.** The gear used in elliptic gear transmission experiment; a) elliptic gear reducer, and b) elliptic gear pair processed

**Table 1.** Elliptic gear design parameters

Parameter	Value
Module $m$ [mm]	1.5
Number of teeth $z$	53
Centre distance $a$ [mm]	80
Tooth width $B$ [mm]	28
Eccentricity $e$	0.2
Pressure angle $[\circ]$	20
Equation of pitch curves	$r = \frac{38.4}{1 + 0.2 \cos \theta}$
Material	Structural steel
Lubrication mode	Oil lubrication

### 3 TORQUE FLUCTUATION OF ELLIPTIC GEAR

According to Eq. (10), the change trend of the torque of the driving and driven gears of the elliptic gear pair under different eccentricity and load torque conditions can be obtained, as shown in Figs. 7 and 8.

In Fig. 7, with the increase of eccentricity, the torque of the driving and driven gears of the elliptic gear increases. The change trend of driving gear is more obvious. When the eccentricity is 0, the torque of the driving and driven gears of the elliptic gear pair is constant and will not fluctuate. When the eccentricity is not 0, the torque fluctuation of the driving and driven gears will occur. With the increase of eccentricity, the change of torque of driven gear is more regular.

In contrast, the change of driving gear shows the same trend, but there are some differences between different eccentricities. This is because the driven gear is connected to the output and the torque at the output is constant. The driven gears move along a specific transmission ratio function under the driving gear. The inconsistency of the tooth profile of the elliptic gear pair makes the torque difference between the driving gears and the driven gears.

Fig. 8, with the increase of load torque, also presents the same change trend. In contrast, the load

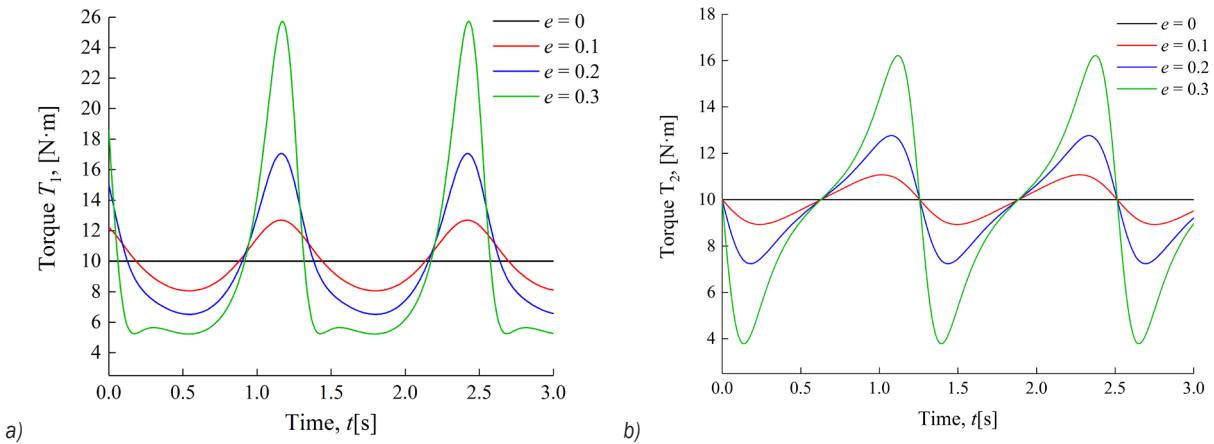


**Fig. 7.** Effect of eccentricity on torque of a) driving and b) driven gears

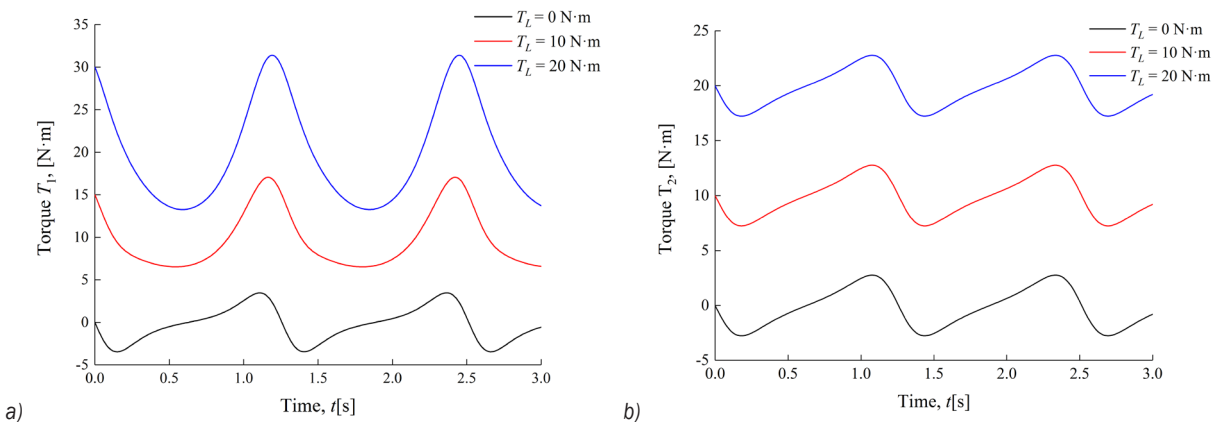


**Fig. 8.** Influence of load torque on a) driving and b) driven gear torque

change of driven gear is more uniform and smoother. The moment of inertia is produced by the non-uniform rotation of the elliptic gear. If the inertia moment is greater than the load moment, the torque of the driving shaft is opposite to the working driving direction, which will cause impact on the non-meshing tooth side of the gear. In Fig. 8, when the load torque is 0, that is, under no-load condition, the minimum torque of the driving and driven gears of the elliptic gear pair will be less than 0, which is negative and shows a periodic trend. This shows that there is tooth surface separation, which will lead to the vibration and noise of the gear transmission system, which is not conducive to the normal work of the system. With the increase of load torque, the phenomenon that the minimum torque of driving gear and driven gear is less than 0 will disappear, which indicates that the existence of load will always lead to the phenomenon of tooth separation.

#### 4 TRANSMISSION EFFICIENCY OF ELLIPTIC GEAR TRANSMISSION SYSTEM

In view of the inconsistency of elliptic gear tooth profile and the complexity of applicable working conditions, especially for reciprocating motion and forward-and-reverse motion (reversing device of pumping unit), it is necessary to analyse its transmission efficiency under the condition of forward and reverse motion so as to provide guidance for practical application. In the process of the experiment, the rated output torque is preset. When the reducer is loaded from 0 to rated torque by driving motor, the torque data of input and output are collected. Each group collects 99 data points. The transmission

efficiency of the elliptic gear pair is analysed by setting different operating parameters (torque and speed).

#### 4.1 Torque Analysis of Elliptic Gear Pair

Figs. 9 to 11 show the change trend of input shaft torque and output shaft torque under the condition of constant speed and increasing gradient of rated load torque.

With the increase of rated load torque, the torque of the input and output ends is increasing. In contrast, the input and output torque in the reverse case are larger than that in the case of positive rotation. The torque fluctuation of the output is small, and the input torque presents periodic change. With the increase of rated input torque, the difference between the two kinds of steering gradually increases. This is consistent with the torque fluctuation analysis results. The output torque is less than the input torque: the torque  $T_1$  of the driving gear is greater than the torque  $T_2$  of the driven gear. Therefore, the correctness of the torque calculation method of the ellipse gear proposed in this paper is proved.

Figs. 12 and 13 show the change trend of input shaft torque and output shaft torque under clockwise and counterclockwise conditions when the load torque remains constant and the speed changes. According to the analysis in Fig. 9, with the increase of speed, the torque at the input and output end also presents a periodic trend. With the increase of the speed, the fluctuation of the torque at the input end and the torque at the output end is also intensified. Similar to the distribution trend in Figs. 8 to 10, the input and output torques under clockwise rotation are

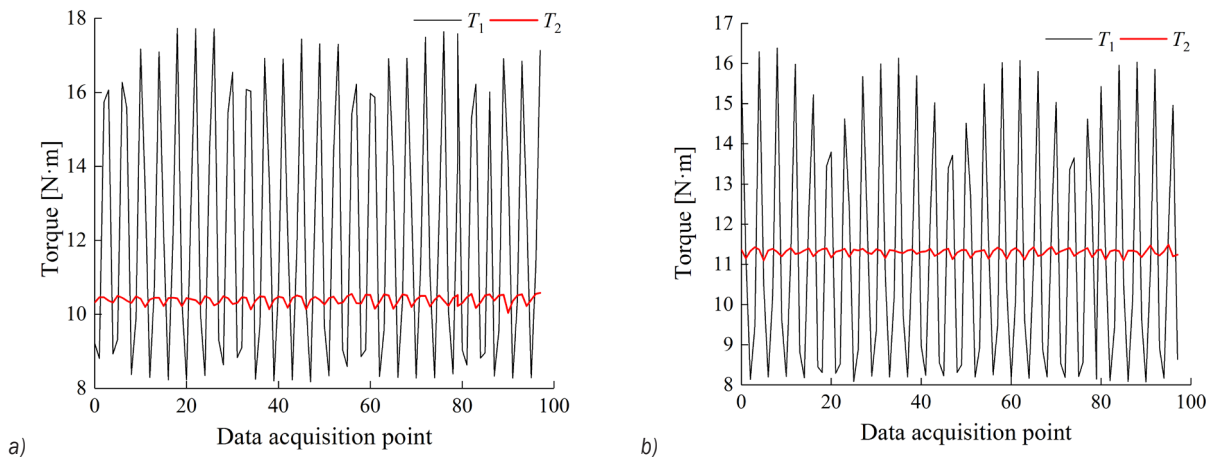
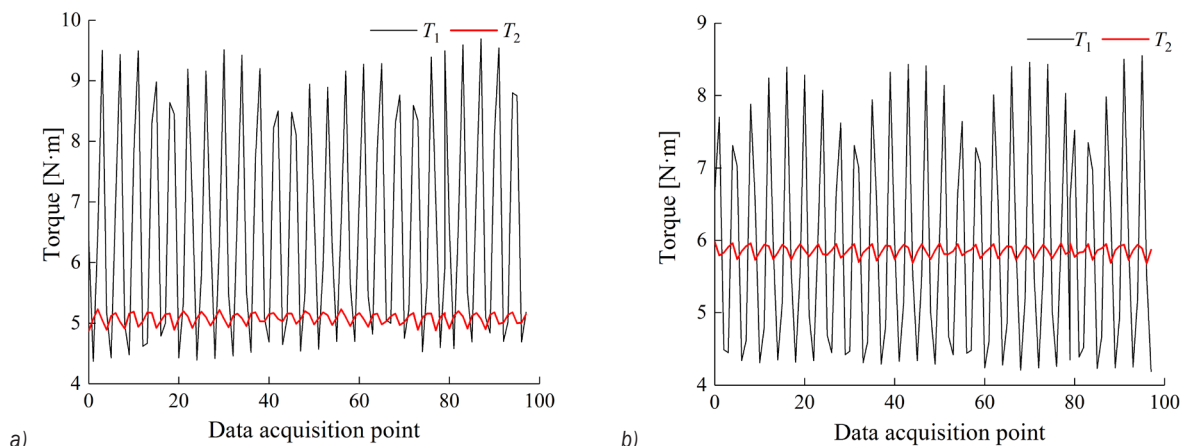
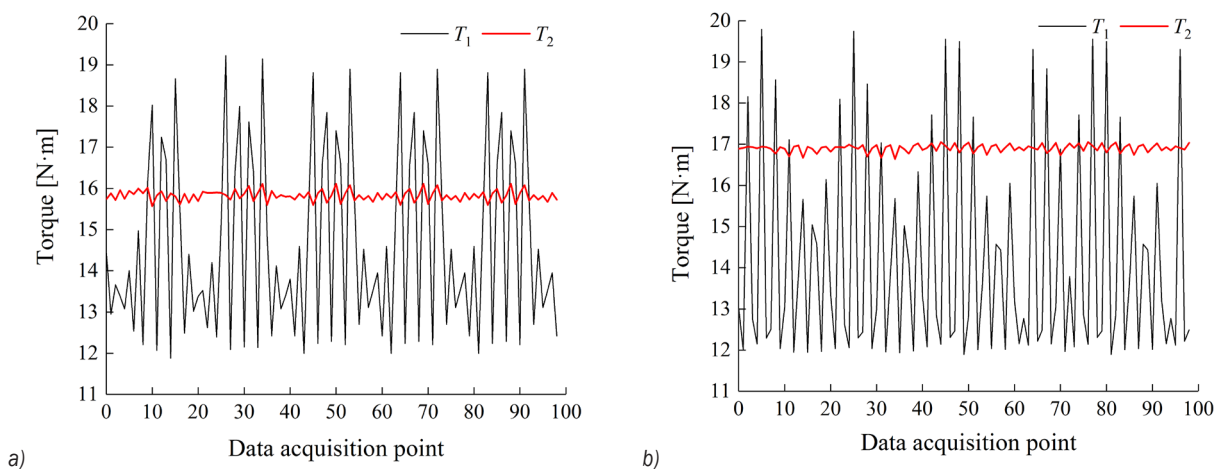


Fig. 9. The torque distribution law of elliptic gear pair when  $T_L = 5 \text{ N}\cdot\text{m}$ ; a)  $n = 5 \text{ r}/\text{min}$ , and b)  $n = -5 \text{ r}/\text{min}$



**Fig. 10.** The torque distribution law of elliptic gear pair when  $T_L = 10 \text{ N}\cdot\text{m}$ ; a)  $n = 5 \text{ r/min}$ , and b)  $n = -5 \text{ r/min}$



**Fig. 11.** The torque distribution law of elliptic gear pair when  $T_L = 15 \text{ N}\cdot\text{m}$ ; a)  $n = 5 \text{ r/min}$ , and b)  $n = -5 \text{ r/min}$

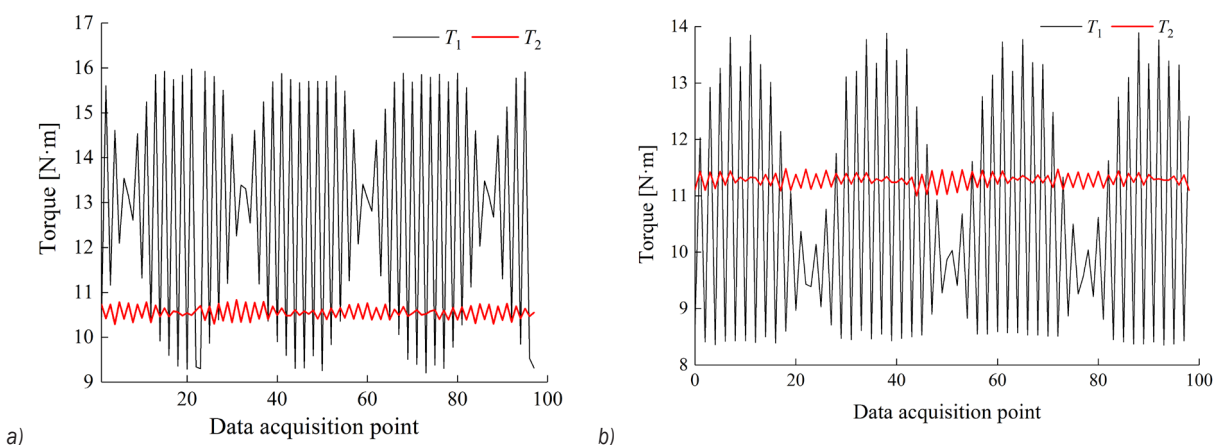


**Fig. 12.** The torque distribution law of elliptic gear pair when  $T_L = 10 \text{ N}\cdot\text{m}$ ; a)  $n = 10 \text{ r/min}$ , and b)  $n = -10 \text{ r/min}$

greater than those under counterclockwise rotation, which is related to the order of clockwise and counterclockwise rotation during the experiment. The first is the clockwise rotation experiment, and the

second is the counterclockwise rotation experiment. Due to the existence of friction torque, starting torque, and dynamic backlash between tooth profiles at the beginning of counterclockwise rotation after

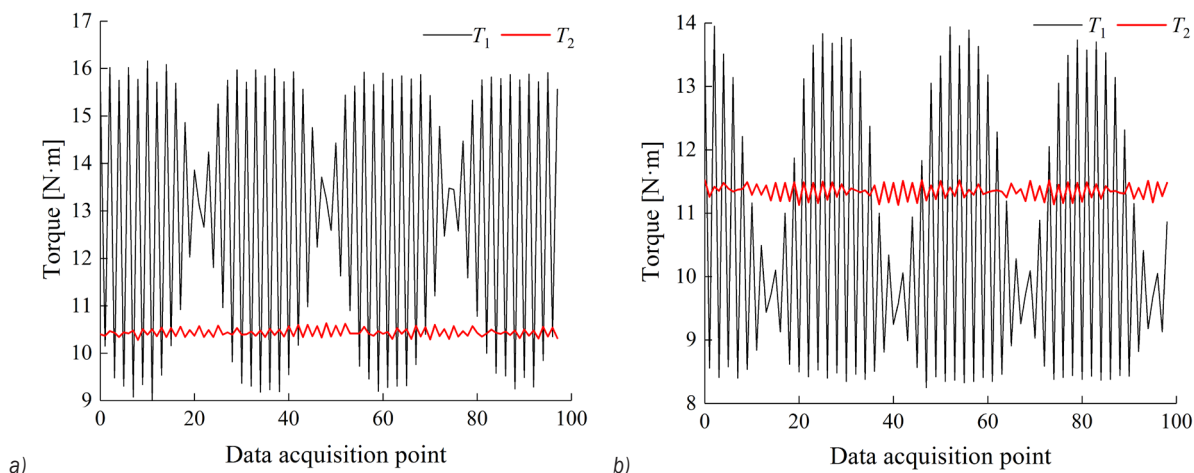


**Fig. 13.** The torque distribution law of elliptic gear pair when  $T_L = 10 \text{ N}\cdot\text{m}$ ; a)  $n = 20 \text{ r/min}$ , and b)  $n = -20 \text{ r/min}$

clockwise rotation, the torque under counterclockwise rotation is greater than that under clockwise rotation. Consistent with the previous analysis results, the torque  $T_1$  of the driving gear is greater than that of the driven gear  $T_2$ , which further verifies the correctness of the torque calculation method of the elliptic gear proposed in this paper. It also shows that the change trend of the output torque and input torque of the elliptic gear transmission system will not change significantly with the increase of the speed, but there is a slight difference in the value.

There is a certain error in the data collection process, which will cause a certain difference between the torque  $T_1$  at the input end and the torque  $T_2$  at the output end, which will affect the instantaneous transmission efficiency calculation of the gear transmission system. The way we reduce the error is to collect data multiple times, and the trend of

the collected data is basically consistent with the theoretical analysis, which also verifies the correctness of our experiment.

#### 4.2 Analysis of Transmission Efficiency of Elliptic Gear Pair

Figs. 14 to 16 show the distribution law of instantaneous transmission efficiency calculated by Eq. (1) while keeping the speed constant and the rated load torque  $T_2$  gradient changing. Under the two steering conditions, the instantaneous transmission efficiency of the elliptic gear pair changes all the time. In contrast, the transmission efficiency of the counterclockwise transient is greater than that of the clockwise transient. With the increase of rated load torque, the instantaneous transmission efficiency of the elliptic gear pair gradually presents a periodic trend, and the periodicity is more obvious.

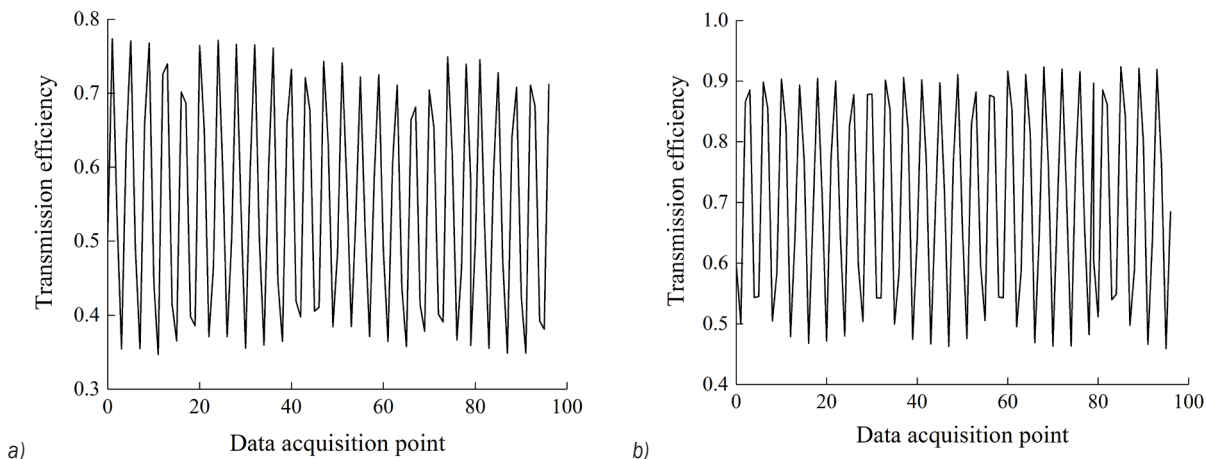


**Fig. 14 .** The transmission efficiency of elliptic gear when  $T_L = 5 \text{ N}\cdot\text{m}$ ; a)  $n = 5 \text{ r/min}$ , and b)  $n = -5 \text{ r/min}$

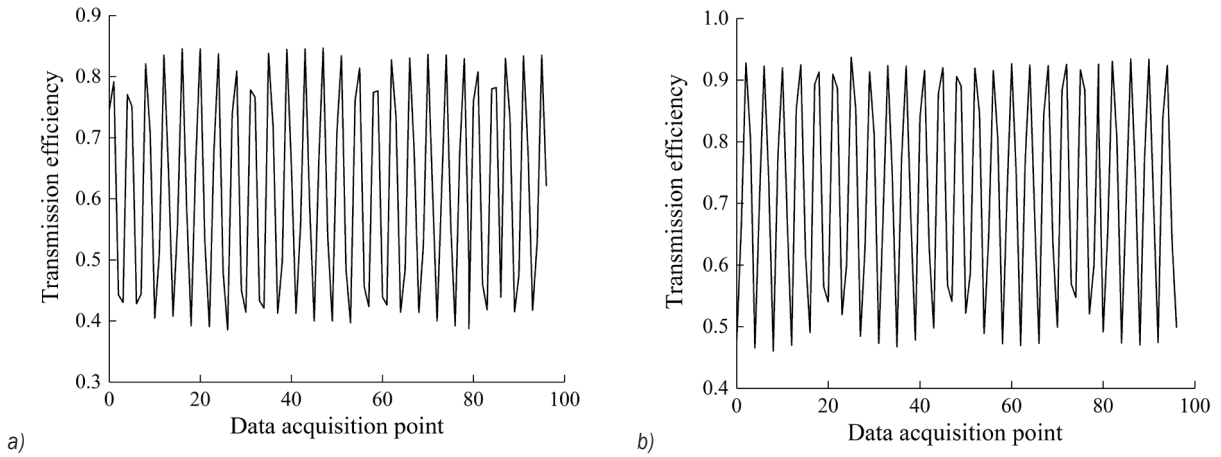


**Fig. 15.** The transmission efficiency of elliptic gear when  $T_L=10\text{ Nm}$ ; a)  $n = 5\text{ r/min}$ , and b)  $n = -5\text{ r/min}$

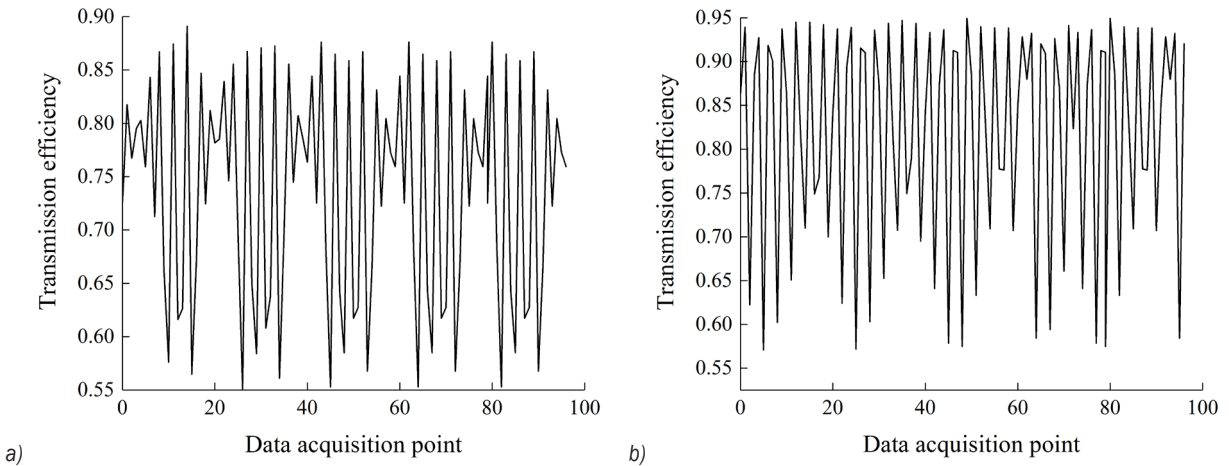


**Fig. 16.** The transmission efficiency of elliptic gear when  $T_L = 15\text{ Nm}$ ; a)  $n = 5\text{ r/min}$ , and b)  $n = -5\text{ r/min}$

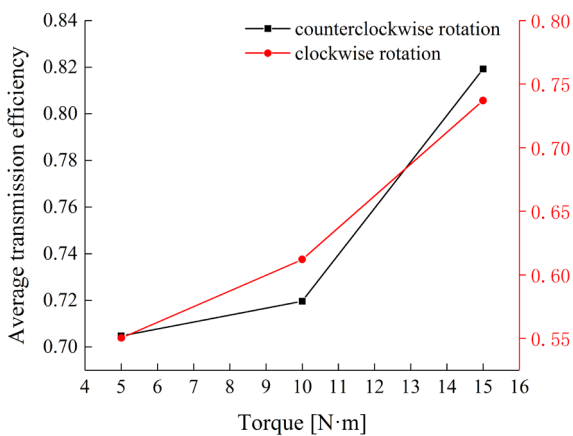


**Fig. 17.** The variation trend of transmission efficiency of elliptic gear with torque

Fig. 17 shows the change trend of average transmission efficiency of elliptic gear pair with the

change of load torque. With the increase of the load torque, the transmission efficiency of the elliptic gear pair shows an increasing trend. Therefore, on the premise of meeting the actual working conditions and the established motion law, increasing the load torque is conducive to improving the transmission efficiency of the elliptic gear pair.

Figs. 18 to 20 show the distribution law of instantaneous transmission efficiency of elliptic gear pair under clockwise and counterclockwise conditions when the load torque remains constant, and the speed gradient changes. It is consistent with the previous analysis when the speed is constant, the load gradient changes, and the transmission efficiency in counterclockwise transient is greater than that in clockwise transient. However, under the two steering conditions, there is a periodic trend, and with the increase of speed, the periodicity is gradually obvious.

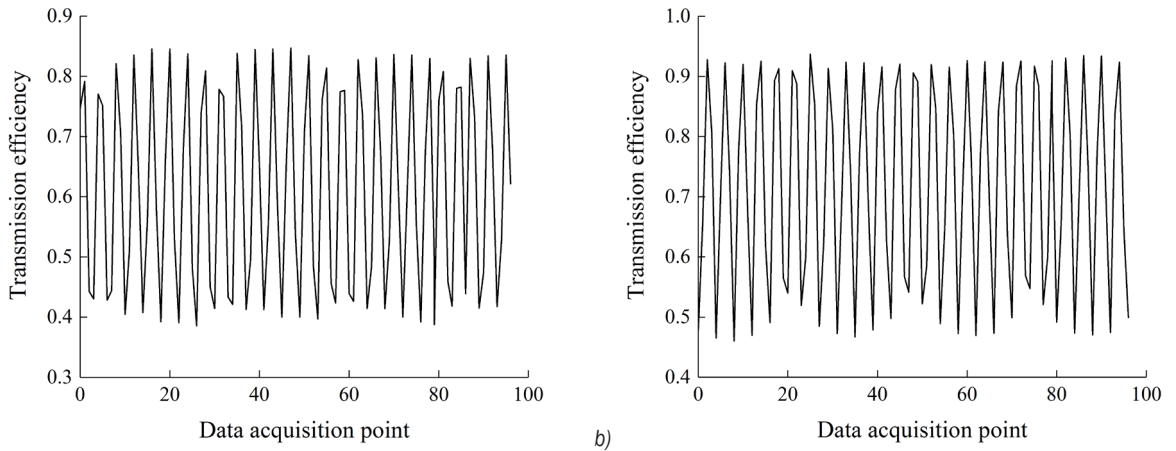


**Fig. 18.** Transmission efficiency of elliptic gear when  $T_L = 10 \text{ N}\cdot\text{m}$ ; a)  $n = 5 \text{ r/min}$ , and b)  $n = -5 \text{ r/min}$

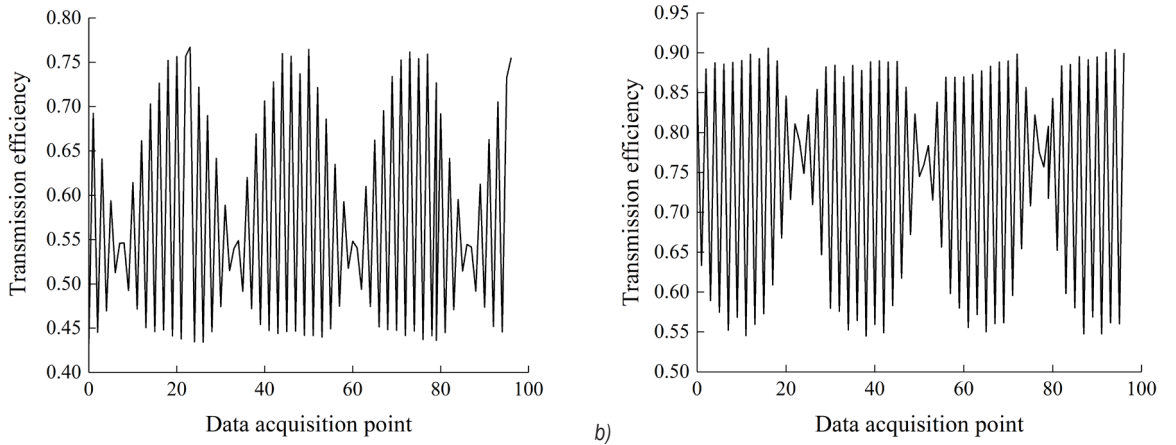


**Fig. 19.** Transmission efficiency of elliptic gear when  $T_L = 10 \text{ N}\cdot\text{m}$ ; a)  $n = 10 \text{ r/min}$ , and b)  $n = -10 \text{ r/min}$

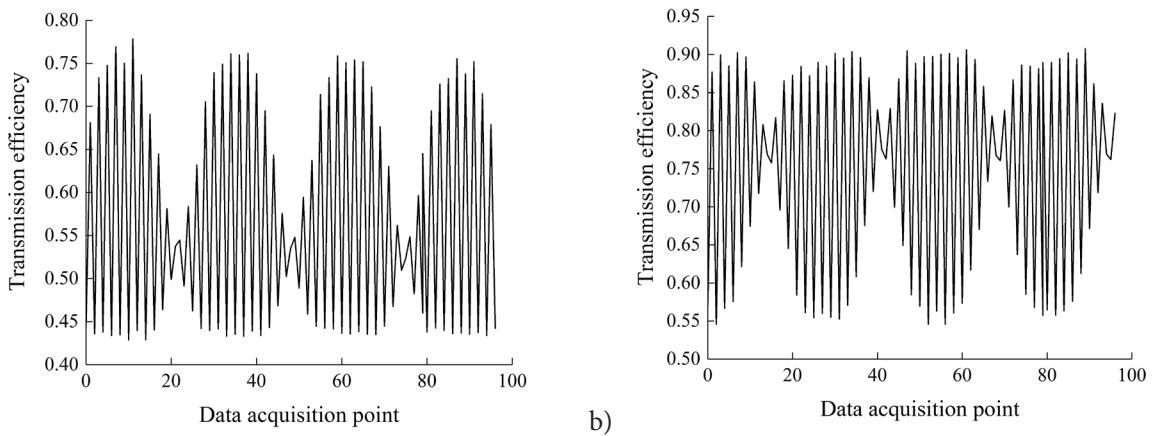


**Fig. 20.** Transmission efficiency of elliptic gear when  $T_L = 10 \text{ N}\cdot\text{m}$ ; a)  $n = 20 \text{ r/min}$ , and b)  $n = -20 \text{ r/min}$

In contrast, the counterclockwise transmission efficiency is greater than the forward transmission efficiency, and the transmission efficiency decreases with the increase of speed.

Fig. 21 shows the change trend of the average transmission efficiency of clockwise and counterclockwise rotation of elliptic gear pair with the change of speed. With the increase of rotation

speed, the average transmission efficiency clockwise and counterclockwise rotation of the elliptic gear pair presents a decreasing trend. This is closely related to the non-linear change of instantaneous coincidence degree and transmission ratio of elliptic gear. Therefore, the elliptic gear pair can present high instantaneous transmission efficiency at low speed. In the process of engineering application, the instantaneous transmission efficiency can be improved by appropriately reducing the speed on the premise of meeting the established working conditions and motion rules.

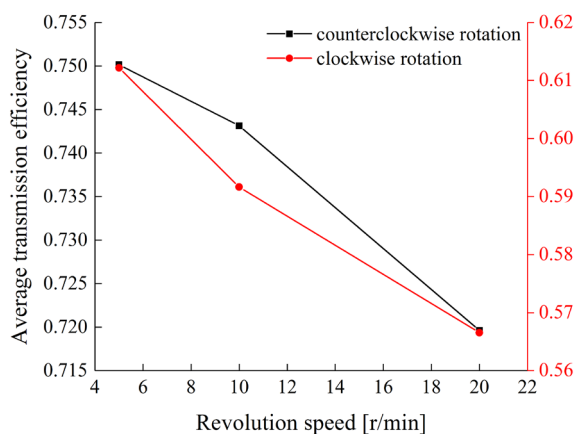


**Fig. 21.** The variation trend of elliptic gear transmission efficiency with torque

Due to the inconsistency of the tooth profile of the elliptic gear, the instantaneous transmission efficiency during the meshing process changes all the time, and its transmission efficiency will be lower than that of a general cylindrical gear. However, the elliptic pair is mainly suitable for low-speed, high-torque occasions and for some special variable-speed sports occasions. Therefore, under the conditions of low speed and high torque, its instantaneous transmission efficiency can reach more than 80 %, which can meet the requirements of working conditions.

## 5 CONCLUSIONS

Based on the load fluctuation model of elliptic gear, the test-bed of elliptic gear transmission is built, and the torque data values of input and output in forward and reverse rotation are obtained. On this basis, the transmission efficiency of the elliptic gear pair is calculated and obtained, and the influence of load torque and speed on the transmission efficiency of the system is analysed. The results show that:

1. Due to the time-varying pitch curve radius of the elliptic gear pair, the tooth profile is inconsistent, which makes the torque at the input end and output end have certain differences under the conditions of forward rotation and reverse rotation, so the transmission efficiency will have certain differences. Under the action of load torque, the torque on the driving and driven gears of elliptic gear will increase with the increase of the eccentricity and load torque of elliptic gear.
2. The load torque and speed have a certain influence on the transmission efficiency of the elliptic gear transmission system. The transmission efficiency will decrease with the increase of speed and increase with the increase of load torque, which also shows that the non-circular gear transmission system represented by elliptic gear is suitable for low speed and high torque conditions.
3. In view of the commonness of elliptic gear and non-circular gear and the subordinate relationship between them, the calculation method, and experimental means of transmission efficiency of elliptic gear proposed in this paper can be used for other types of non-circular gear transmission systems, and can provide some theoretical guidance for the calculation of transmission efficiency.

## 6 ACKNOWLEDGEMENTS

The research was support by the National Natural Science Founding of China (No. 51765032), and the Open Fund of Hubei Key Laboratory of Mechanical Transmission and Manufacturing Engineering at Wuhan University of Science and Technology (Grant No. MTMEOF2020B03)

## 7 REFERENCES

- [1] Liu, M., Liu, D., Zhang, K. (2020). Transmission theory and efficiency analysis of non-constant transmission of end face gear with movable teeth. *Journal of Mechanical Design*, vol. 34, no. 10, p. 20-25. (in Chinese)
- [2] Liu, M., Liu, D., Zhang, K., Yan, Y. (2016). Transmission theory and meshing efficiency of movable tooth transmission with speed integration. *Machine Design and Research*, vol. 32, no. 05, p. 64-67. (in Chinese)
- [3] Dong, C., Liu, Y., Wei, Y., Yun, B., Li, D., Dong, Z. (2020). Analysis on meshing characteristics and transmission error of elliptic gears. *Mathematical Problems in Engineering*, vol. 2020, art. ID 201728, DOI:10.1155/2020/2017218.
- [4] Dong, C., Liu, Y., Wei, Y. (2019). Dynamic contact characteristics analysis of elliptic cylinder gear under different load conditions. *Journal of Huazhong University of Science &*

- Technology (Natural Science Edition)*, vol. 48, no. 8, p. 103-107.
- [5] Dong, C., Liu, Y., Wei, Y. (2020). Dynamic meshing characteristics of elliptic cylinder gear based on tooth contact analysis. *International Journal of Engineering Transaction A: Basics*, vol. 33, no. 4, p. 676-685, DOI:10.5829/IJE.2020.33.04A.19.
- [6] Dong, C., Liu, Y., Wei, Y. (2020). Meshing error of elliptic cylinder gear based on tooth contact analysis. *International Journal of Engineering Transaction A: Basics*, vol. 33, no. 7, p. 1364-1374, DOI:10.5829/IJE.2020.33.07A.24.
- [7] Tucker, R.W., Wang, C., Librovich, B. (2003). Mathematical modelling of rotary vane engines. *Proceedings of the Institution of Mechanical Engineers, Part C: Journal of Mechanical Engineering Science*, vol. 217, no. 6, p. 687-704, DOI:10.1243/095440603321919608.
- [8] Diez-Ibarbia, A., Fernandez-Del-Rincon, A., Garcia, P., De-Juan, A., Iglesias, M., Viader, F. (2018). Assessment of load dependent friction coefficients and their influence on spur gears efficiency. *Meccanica*, vol. 53, p. 425-445, DOI:10.1007/s11012-017-0736-8.
- [9] Wang, C., Cui, H.Y., Zhang, Q.P., Wang, W.M. (2016) An approach of calculation on sliding friction power losses in involute helical gears with modification. *Proceedings of the Institution of Mechanical Engineers, Part C: Journal of Mechanical Engineering Science*, vol. 203-210, no. 9, p. 1521-1531, DOI:10.1177/0954406215573977.
- [10] Wang, C., Shi, Z. (2017). A dynamic calculation method of sliding friction losses for a helical gear pair. *Journal of the Brazilian Society of Mechanical Sciences and Engineering*, vol. 39, p. 1521-1528, DOI:10.1007/s40430-016-0585-8.
- [11] Wang, C. (2020). Dynamic model of a helical gear pair considering tooth surface friction. *Journal of Vibration and Control*, vol. 26, no. 15-16, p. 1356-1366, DOI:10.1177/1077546319896124.
- [12] Wang, C., Ken, M. (2020). A calculation method of sliding friction coefficient on tooth surface for helical gear pair based on loaded tooth contact analysis and elastohydrodynamic lubrication theory. *Proceedings of the Institution of Mechanical Engineers, Part J: Journal of Engineering Tribology*, vol. 235, no. 8, p. 1551-1560, DOI:10.1177/1350650120966894.
- [13] Wang, C., Wang, S., Wang, G. (2018). A method for calculating gear meshing efficiency by measured data from gear test machine. *Measurement*, vol. 119, p. 97-101, DOI:10.1016/j.measurement.2018.01.031.
- [14] Wang, C. (2020). The effect of planetary gear/star gear on the transmission efficiency of closed differential double helical gear train. *Proceedings of the Institution of Mechanical Engineers, Part C: Journal of Mechanical Engineering Science*, vol. 234, no. 21, p. 4215-4223, DOI:10.1177/0954406220921205.
- [15] Petry-Johnson, T.T., Kahraman, A., Anderson, N.E., Chase, D.R. (2008). An experimental investigation of spur gear efficiency. *Journal of Mechanical Design*, vol. 130, no. 6, art. ID 062601, DOI:10.1115/1.2898876.
- [16] Xu, H., Kahraman, A., Anderson, N.E., Maddock, D.G. (2007). Prediction of mechanical efficiency of parallel-axis gear pairs. *Journal of Mechanical Design*, vol. 129, no. 1, p. 58-68, DOI:10.1115/1.2359478.
- [17] Li, S., Kahraman, A. (2010). Prediction of spur gear mechanical power losses using a transient elastohydrodynamic lubrication model. *Tribology Transactions*, vol. 53, no. 4, p. 554-563, DOI:10.1080/10402000903502279.
- [18] Li, Y., Wang, G., Zou, S. (2017). The calculation of meshing efficiency of a new type of conical involute gear. *Strojniški vestnik - Journal of Mechanical Engineering*, vol. 63, no. 5, p. 320-330, DOI:10.5545/sv-jme.2016.3843.
- [19] Liu, W., Peng, H., Cai, Z., Ma, X. (2021). Study on meshing efficiency of non-circular gear based on elastohydrodynamic lubrication. *Journal of Mechanical Transmission*, vol. 45, no. 2, p. 1-5, DOI:10.16578/j.issn.1004.2539.2021.02.001. (in Chinese)
- [20] Gao, N., Meesap, C., Wang, S., Zhang, D. (2020). Parametric vibrations and instabilities of an elliptic gear pair. *Journal of Vibration and Control*, vol. 26, no. 19-20, p. 1721-1734, DOI:10.1177/1077546320902543.

# Investigation of Hydrodynamic Flow Characteristics in Helical Coils with Ovality and Wrinkles

Govindaraj Periasamy<sup>1,\*</sup> – Senthilkumar Mouleeswaran<sup>2</sup> – Prabhu Raja Venugopal<sup>1</sup> – Chellapandi Perumal<sup>3</sup>

<sup>1</sup> PSG College of Technology, Department of Mechanical Engineering, India

<sup>2</sup> PSG College of Technology, Department of Production Engineering, India

<sup>3</sup> Indian Institute of Technology Madras, Department of Applied Mechanics, India

*The forming of helical coils using a rolling process results in geometrical irregularities (wrinkles and ovality) that are likely to influence the hydrodynamic behaviour of the flow field inside the coil in applications such as air generators. In this study, the above behaviour was investigated by experimental and numerical analyses considering the heat exchanger used in dry air generators. In experimental analysis, a three-turn copper helical coil with wrinkles and ovality was investigated to estimate the global hydrodynamic characteristics inside the helical coil. The results were compared with that of the ideal geometry of a coil without wrinkles and ovality. The effect of wrinkles was assessed through friction factor, and the corresponding equivalent surface roughness was found to increase by 5.7 times, owing to the presence of wrinkles in the helical coil. Numerical simulation was conducted to determine the pressure distribution, velocity distribution, and secondary flow inside the helical coil; the results were validated with experimental data. A critical portion of the helical coil with multiple wrinkles was considered for numerical simulation to investigate the localized effects of wrinkles on the flow field behaviour. The analysis in the vicinity of wrinkles revealed negative pressure development during flow, which in turn would cause re-circulation and cavitation that are undesirable.*

**Keywords:** helical coil, flow characteristics, ovality, wrinkles, computational fluid dynamics

## Highlights

- The effect of wrinkles and ovality on the flow field in a copper helical coil was investigated by experimental and numerical analysis.
- The maximum ovality in a helical coil was found to be 3.2 %, and it does not significantly affect the hydrodynamic characteristics of the flow field.
- The wrinkles contribute significantly to the pressure drop in the helical coil; the maximum pressure drop was doubled due to the presence of wrinkles when the Reynolds number ( $Re$ ) attains 100,000.
- The effect of wrinkles was assessed through the friction factor, and the corresponding equivalent surface roughness was found to increase by 5.7 times owing to the presence of wrinkles in helical coils.
- The numerical analysis of the critical portion of the helical coil exhibited local damage mechanisms, such as cavitation due to negative pressure developed in the vicinity of wrinkles.

## 0 INTRODUCTION

Helical coils are extensively used in several industries in various applications due to their compact size and ability to accommodate thermal expansion at elevated temperatures. The fluid flowing through the helical coil experiences a centrifugal force due to the curvature effect and leads to secondary flow perpendicular to the axial flow of the fluid. Due to secondary flow, the fluid particles move towards the outer wall and retract back to the inner wall [1]. The torsion effect in the helical coil along with secondary flow leads to increased pressure drop and makes the flow more complex. Dean [2] presented the correlations for flow in curved tubes and defined the Dean effect associated with curvature. The geometric parameters of the helical coil (i.e., helical pitch, pitch circle diameter (PCD), number of helical turns, and secondary flow) highly influence the flow behaviour of fluid inside the helical coil [3]. The effect of geometry and inlet

conditions is vital in predicting the mass flow rate for the given Reynolds number [4]. The secondary flow characteristics and their influence on the pressure drop in a helical coil depend on geometrical parameters [5]. The different flow configurations of the coil will significantly affect the performance of coils [6]. Fluid flow and heat transfer characteristics in spiral coils are interrelated [7]. The above parameters also influence the heat transfer rate of tube-in-tube helical coils [8]. The heat transfer behaviour in the laminar and turbulent conditions of tube-in-tube helical coils can be characterized by the local Nusselt number [9]. The heat transfer rates in helical coils are more dependent on the geometrical parameters when compared with straight tubes [10]. The heat transfer in heat exchangers with dimple patterns will depend on the geometry of the dimple pattern; therefore, it is important to analyse the influence of wrinkles in coils [11]. The helical double pipe heat exchanger will have both geometrical and flow complexities owing to

its flow behaviour. It is important to understand the hydrodynamics of the fluid inside the coil to enhance heat transfer rate [12] and [13].

Tube-in-tube co-axial helical coils are widely used as heat exchangers in refrigeration air dryer systems as pre-coolers and evaporators to remove moisture content from compressed air. To maximize the heat transfer rate, copper is selected as the tube material. Copper tubes of lengths of 5 to 7 metres are manufactured and rolled into tube-in-tube helical coils of required pitch circle diameter using a three-roller tube bending machine. During the transportation of straight tubes, minor dimples form in the copper tubes. While rolling the lengthy tubes into compact helical coils, wrinkles form at the intrados of the tubes. Thinning and thickening take place at extrados and intrados of the helical tube, respectively, and result in flattening of helical coil. The resulting geometrical irregularities, namely, ovality and wrinkles, obstruct the flow of fluid and create turbulence during fluid flow, which results in pressure drop during operation. The pressure drop affects the effectiveness of heat transfer and results in insufficient dry air generation [14]. Based on an exhaustive literature review, it was found that limited work has been done on the influence of geometrical irregularities on the flow behaviour in helical coils. Hence, the present work aims to investigate the implications of wrinkles and ovality on the flow fields in helical coils, taking into consideration the flow velocity variations.

## 1 MEASUREMENT OF OVALITY AND SYNTHESIS OF WRINKLES IN HELICAL COILS

The helical coils formed during bending have two major geometrical irregularities: ovality and wrinkles. The ovality or flattening of a bend is defined as the difference between the maximum and minimum outside diameters at any cross-section, expressed as a percentage of the nominal outside diameter. The heat exchanger used in a dry air generator is considered for the present study. It consists of tube-in-tube copper helical coils, formed using a three-roller pipe bending machine, as shown in Fig. 1.

A three-turn helical coil used in the tube-in-tube co-axial heat exchanger for the selected industrial application is taken up for investigation. Further, only the outer coil ( $D = 50.08$  mm) without the inner coil ( $d = 15$  mm) is considered for study since the outer coil, with the larger coil diameter, is susceptible to higher wrinkle formation during pipe bending. To fabricate the outer helical coil, a long tube of outer diameter 50.08 mm, thickness 1 mm, and the

developed length of 5 m was passed between the upper and lower rollers. The three-turn coil was formed in three stages, by passing the copper coil between rollers and gradually increasing the feed to achieve the intended pitch circle diameter of 650 mm and pitch of 52 mm.

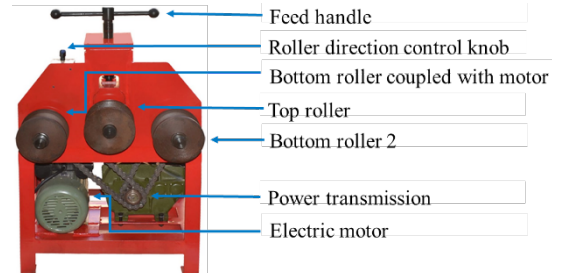


Fig. 1. Three roller tube bending machine

As per ASME B31.1 (N-129.1.1) standard [15], ovality shall not exceed 8 % for tubes exposed to internal pressure. For tubes subjected to external pressure, ovality shall not exceed 3 %.

$$\text{Percentage ovality} = \frac{D_{max} - D_{min}}{D} \times 100. \quad (1)$$

The relation for calculating percentage ovality is given in Eq. (1), where  $D_{max}$  and  $D_{min}$  represent the major and minor diameters of the geometrical irregularity in the form of the ovality, as shown in Fig. 2.

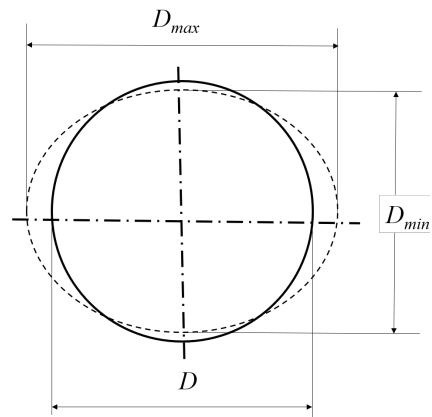


Fig. 2. Geometric representation of ovality

Considering several helical coils for measuring ovality, the maximum ovality was 3.2 % which is well within the allowable limits as per ASME B31.3 code. Hence, ovality is not likely to influence the flow behaviour.

The other geometrical irregularity, wrinkles, occurs only at the intrados due to compression while

forming helical coils. Considering a critical portion of a sample coil for a length of 300 mm, there were 24 wrinkles of different sizes, as represented in Fig. 3.

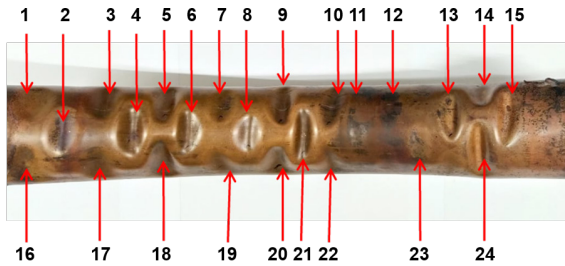


Fig. 3. Wrinkles in critical portion of helical coil

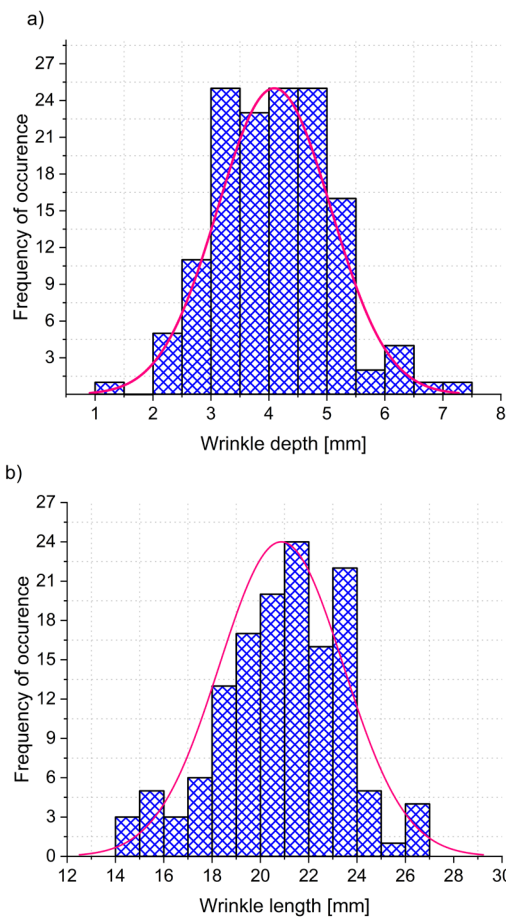


Fig. 4. Probability distribution of wrinkles; a)  $\mu = 4.07$ ,  $\sigma = 1.39$ , and b)  $\mu = 20.89$ ,  $\sigma = 3.75$

Considering the total length of 5 m of another full coil, 139 wrinkles of varying size were measured, and their distribution is obtained by employing Gaussian fit using MATLAB®. Fig. 4 shows the frequency of occurrence of wrinkles in terms of depth and length, and the histogram reveals a normal distribution.

Among the wrinkles, the maximum depth and length were 6.8 mm and 32 mm, respectively. Subsequently, the effect of wrinkles on the hydrodynamic flow characteristics in the helical coil is investigated.

The measured pressure drop will be used to analytically determine the friction factor and subsequently the equivalent surface roughness of the coil.

## 2 ASSESSMENT OF THE EFFECT OF WRINKLES ON EQUIVALENT SURFACE ROUGHNESS OF HELICAL COIL

### 2.1 Measurement of Pressure Drop

A schematic representation of the experimental set up is shown in Fig. 5. The set-up contains the following components: a copper helical tube, centrifugal pump, flow meter, pressure gauges, valves, and tube lines. Compressed air at room temperature was pumped to a storage tank and allowed to flow through the pneumatic circuit. As the coil was mounted vertically, it resulted in a downstream flow of air. Since the coil being investigated is meant for use in a dry air generator, a wider range of operating flow conditions needs to be considered. Hence, a valve was used to regulate the flow. The mass flow rate was measured using the differential pressure flow measurement principle. Pressure gauges were provided to measure the operating pressure at salient points in the circuit.

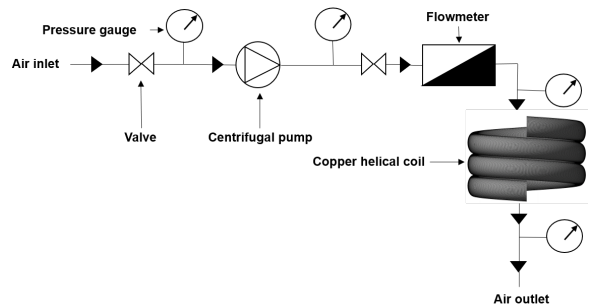


Fig. 5. Schematic diagram of experimental set-up

The flow rate was varied from 34 m<sup>3</sup>/h to 850 m<sup>3</sup>/h in steps with corresponding pressures varying from 7 bar to 16 bar. The pressure drop in the coil was obtained by measuring the air pressures at the inlet and outlet of the coil. The global  $R_e$  was calculated experimentally based on the velocity of compressed air inside the coil using Eq. (2).

$$R_e = \frac{\rho V D}{\mu}, \quad (2)$$

where  $\rho$ ,  $V$ ,  $D$  and  $\mu$  are density of air [ $\text{kg/m}^3$ ], average flow velocity of air [ $\text{m/s}$ ], coil diameter [ $\text{m}$ ] and dynamic viscosity of air [ $\text{kg/(ms)}$ ] respectively. Three trials of experiments were carried out for every operating condition. The variations in pressure drop with increase in  $R_e$  were investigated by considering coils, with and without wrinkles, and a comparison is shown in Fig. 6.

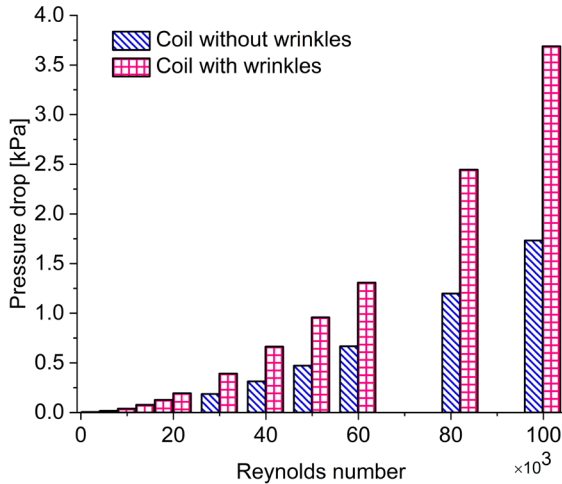


Fig. 6. Pressure drop based on experimental results

It is observed that wrinkles contribute significantly to pressure drop in the helical coil. A peak pressure difference of 2 kPa was observed when  $R_e$  of 100,000 was attained. A smooth pipe with wrinkles and ovality behaves as a rough pipe [16]. Hence, the friction factor is calculated from the experimental value of pressure drop for a specific  $R_e$  in order to arrive at an equivalent surface roughness of the coil.

### 2.1 Determination of Friction Factor and Equivalent Surface Roughness of Helical Coil

The equivalent surface roughness is the roughness of a non-wrinkled coil whose friction factor is equal to that of a wrinkled coil. In order to assess the effect of wrinkles, the fanning friction factor [17], which contributes to the pressure drop, is calculated from,

$$\Delta P = \frac{2f_c \rho u^2 L}{D}, \quad (3)$$

where  $u$ ,  $f_c$ ,  $\Delta P$ ,  $\rho$ ,  $D$  and  $L$  are average flow velocity of air [ $\text{m/s}$ ], fanning friction factor, pressure drop [ $\text{Pa}$ ], density of air [ $\text{kg/m}^3$ ], coil diameter [ $\text{m}$ ], coil length [ $\text{m}$ ] respectively. The effect of wrinkles and  $R_e$  on friction factor is shown in Fig. 7.

The friction factor increases by 78 % at the lowest  $R_e$  owing to the presence of wrinkles, which will have higher implications on the flow field. The friction factor is independent of  $R_e$  beyond 60,000 and it is found to be 0.010 and 0.018 for coil without wrinkles and coil with wrinkles, respectively.

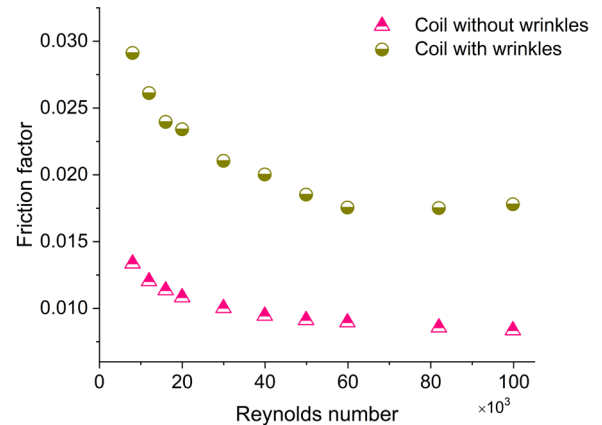


Fig. 7. Friction factor of coils

The widely accepted Colebrook [18] formula (Eq. (4)) gives a relation between the friction factor,  $R_e$  and equivalent surface roughness ( $\epsilon$ ), for  $R_e$  above 4000. It is used to arrive at  $\epsilon$ , given the friction factor for a specific Reynolds number [19].

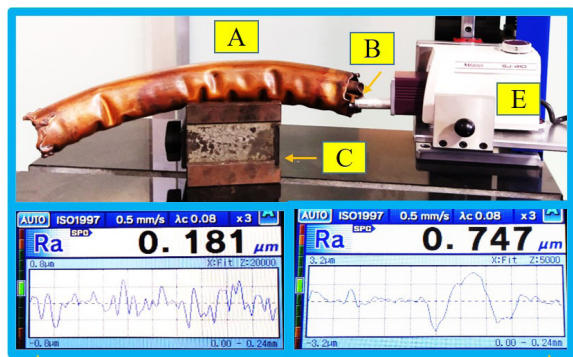
$$\frac{1}{\sqrt{f}} = -4 \log \left[ \frac{\epsilon}{3.7D} + \frac{1.256}{R_e \sqrt{f}} \right]. \quad (4)$$

Initially, the surface roughness of the coil at the inner wall, in no flow condition, was measured using a portable surface roughness tester (SURFTEST SJ - 410® series), as shown in Fig. 8. Five trials were taken at each section with a cut-off range of 0.25 mm and 0.08 mm, and the roughness values were found to be 0.747, 0.181, 2.075, 1.100 and 1.470. The average surface roughness of 1.11  $\mu\text{m}$  is taken as the reference as shown as a horizontal line in Fig. 9.

It is found from the figure that the maximum  $\epsilon$  of 6.17  $\mu\text{m}$  is 5.7 times more than that of the commercially available tubes, which is attributed to the combined influence of wrinkles and flow at lowest  $R_e$ . It is also found that the roughness of coil with wrinkles and that without wrinkles is 2.3  $\mu\text{m}$  and 0.3  $\mu\text{m}$  beyond  $R_e$  of 60,000. At the lowest  $R_e$ , the equivalent surface roughness of the coil will cause a significant pressure drop (Fig. 6) and will affect the overall heat transfer performance of the coil.

When  $R_e$  is 10,000, the copper coil is found to behave like a rough pipe without wrinkles. To visualize and better understand the effect of wrinkles

on the performance of helical coil, a numerical investigation is carried out.



- A – Helical coil
- B – Inner wall surface to be tested
- C – V block to hold helical coil
- D – Sample trial measurements
- E – Portable surface roughness tester

Fig. 8. Surface roughness measurement

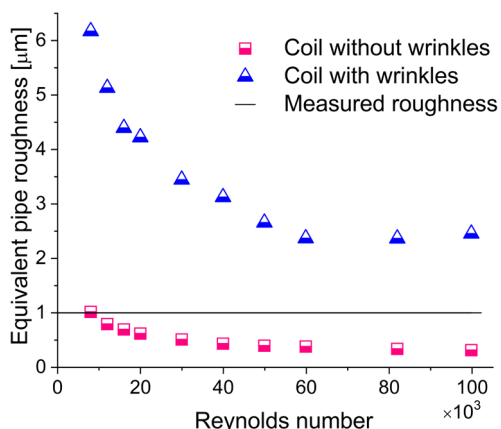


Fig. 9. Equivalent surface roughness of coil

### 3 NUMERICAL INVESTIGATIONS ON THE IMPLICATIONS OF WRINKLES AND OVALITY ON THE FLOW FIELD IN HELICAL COIL

The numerical investigation is conducted in two stages: (i) global analysis of three-turn coil with and without geometrical irregularities and (ii) local analysis of flow field in a critical portion of coil with wrinkles. Prior to investigating the effect of wrinkles and ovality on flow behaviour, an idealized coil without any geometrical irregularities was considered for analysis. The results will be used as a benchmark while investigating the fluid flow behaviour in the coil with wrinkles and ovality. Owing to the vertical

orientation of coils, downstream flow is considered for analysis.

### 3.1 Global Analysis of Hydrodynamic Behaviour of Fluid Field in Helical Coil

For global analysis, the helical coil without wrinkles was modelled using Creo® and the model was imported into computational fluid dynamics (CFD) module of ANSYS® software. The boundary conditions that are applied on the model of an ideal coil are shown in Fig. 10.

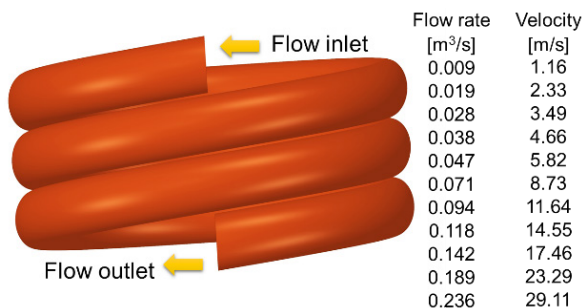


Fig. 10. Geometry and operating velocity range

A steady-state simulation was carried out by solving governing equations in a stationary framework. Air at 25 °C was used as the working fluid, and copper was assigned as the solid medium for the simulation of both models (i.e., ideal coil and wrinkled coil). The coil selected for analysis is designed to handle flow of air in the range of 0.009  $\text{m}^3/\text{s}$  to 850  $\text{m}^3/\text{s}$  and the corresponding flow velocity is ranging from 1.16 m/s to 29.11 m/s. The “velocity inlet” condition is defined, and it is varied using the inlet “parameter set” option for simulation. The present investigation is mainly focused on the hydrodynamic behaviour of coils with geometrical deviation; hence, the outlet of coil is specified as the “open” condition. The scale and quality of the mesh were verified, and the solver type was selected as a velocity-based formulation considering downstream flow. Four turbulence models were used to perform simulation prior to arriving at a suitable model. The selected SST  $k-\epsilon$  model was found to be better at predicting flow characteristics in a helical coil than other models were; Piazza and Ciofalo [20] had similar findings. The solution method was specified as pressure-velocity coupling by adopting the SIMPLE scheme for solving the governing equation with a second-order upwind scheme.

### 3.1.1 Mesh Convergence Study

A fine mesh was generated with a inflation layer for solid-fluid interfaces, and a grid independence study (Fig. 11) was performed by adequate edge sizing and inflation growth rates. Since mesh convergence was attained at point D, the mesh corresponding to point D was used for further investigation. The same procedure was repeated for a coil with wrinkles, whose model was obtained by reverse engineering.

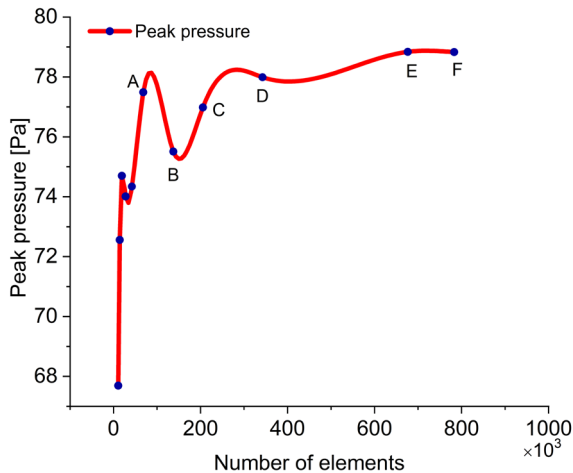


Fig. 11. Mesh sensitivity

The meshed model with inflation contains a combination of tetra and hexahedral elements to represent wrinkles of different sizes that have a combination of very steep to smooth surfaces. The adaptive meshing option aided in obtaining very fine meshing at the locations where wrinkles were present.

### 3.1.2 Pressure Distributions at Different Angular Positions

The pipe curvature causes centrifugal forces to act on the flowing fluid, resulting in a secondary flow pattern perpendicular to the main axial flow. Fig. 12 shows the pressure distribution ( $Re = 49,000$ ) along the outer wall, where secondary flow can be visualized at the extrados.

Up to an angle of  $180^\circ$ , secondary flow influences the pressure distribution and hence the pressure plots are maximum at the outer periphery of the coil; gradually, the pressure becomes uniform as the fluid approaches further turns of the helical coil. The helical coil was initially scanned using a blue light scanner (ATOS Compact Scan 2M) by placing stickers on the geometry, and the point cloud data was obtained to form a surface model. The above model

was converted into a solid model using Geomagic Design X<sup>®</sup> software (Fig. 13).

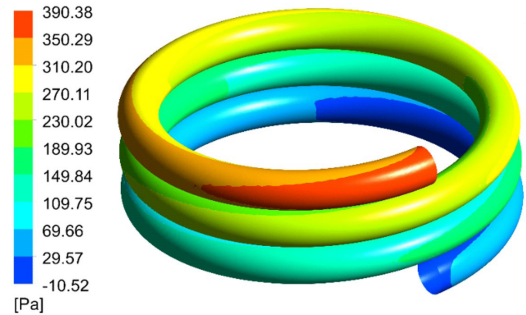


Fig. 12. Pressure distribution along the length in coil

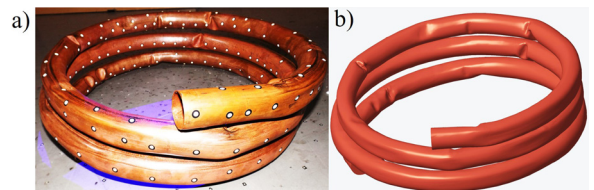


Fig. 13. Reverse engineering of wrinkled helical coil; a) reverse engineering, and b) extracted wrinkled coil

The model was used to perform finite element simulation after incorporating the same boundary conditions that were used for experimentation. The pressure distribution inside the wrinkled helical coil is shown in Fig. 14.

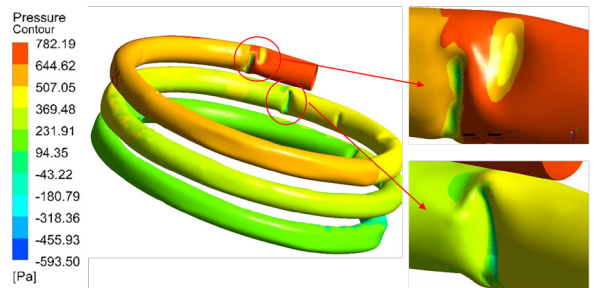


Fig. 14. Pressure distribution in wrinkled coil

It is found that there is a significant pressure drop in the wrinkled coil compared to the ideal coil, and there was considerable negative pressure developed in the wrinkled portions. This would lead to an increased velocity gradient in the vicinity of wrinkles and contribute to unsteady flow along the length of coil.

### 3.1.3 Comparison of Streamline Patterns for Different Flow Parameters

The surface velocity streamline at the vertical mid-plane of the helical coil is represented in Fig. 15. In

a wrinkled coil, it can be observed that there is an unsteady surface streamline at the sections where wrinkles are present, and the shape imperfection has also influenced the formation of streamline in the corresponding sections of the plot. The maximum pressure in the wrinkled coil is found to be twice as that of the ideal coil without wrinkles.

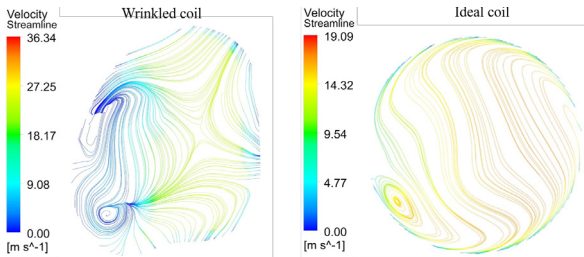


Fig. 15. Velocity streamline in wrinkled and ideal coils

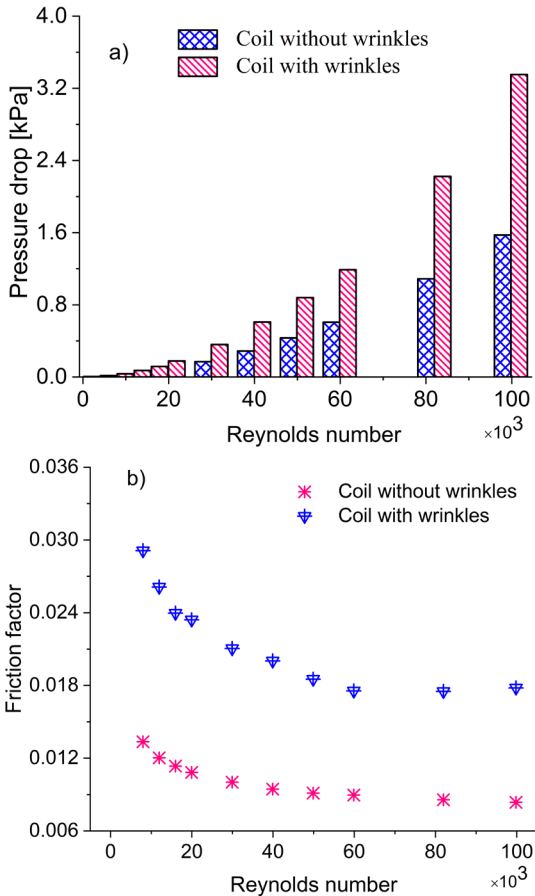


Fig. 16. Comparison of a) pressure drop, and b) friction factor based on numerical results

The parameters considered for numerical investigation are the same as those used for experimentation; a comparison of pressure drop and

friction factor for various Reynolds numbers is shown in Fig. 16a and b, respectively.

It was found that the wrinkled coil experiences a two-fold higher pressure drop and friction factor when compared to a coil without wrinkles. It would significantly affect the overall pumping power and global heat transfer rate for tube-in-tube helical coil heat exchangers.

### 3.1.4 Global Analysis of Velocity Variations along the Length of the Coil

The behaviour of the flow field inside the helical coil was visualized using CFD software. The developed length of the coil of 5 m was considered for globally investigating the velocity along the length of the helical coil for a range of  $Re$  from 3976 to 99,801 (Fig. 17).

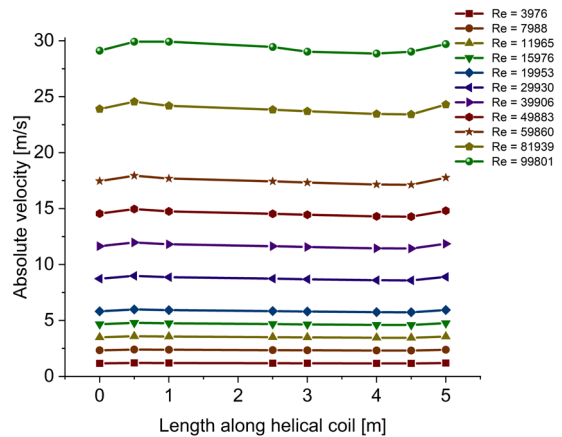


Fig. 17. Velocity fluctuation along the length of coil without wrinkles and ovality

The observed velocity profile remains almost constant for a specific Reynolds number. The velocity fluctuations are observed to be increasing to a considerable range beyond  $Re$  of 40,000. The secondary flow due to helix angle and turbulence in the flow field are the primary reasons for velocity fluctuations in helical coils without wrinkles.

The flow velocities were measured at nine sections of the coil, as shown in Fig. 18. The absolute velocity of air along the length of the coil is found to be oscillating owing to the presence of wrinkles, which tend to reduce the cross-sectional area locally. By extracting the data on fluid velocity and cross-sectional area from the simulation software, the discharge is found to be a constant with a magnitude of  $0.057 \text{ m}^3/\text{s}$  and thus satisfying the continuity equation.

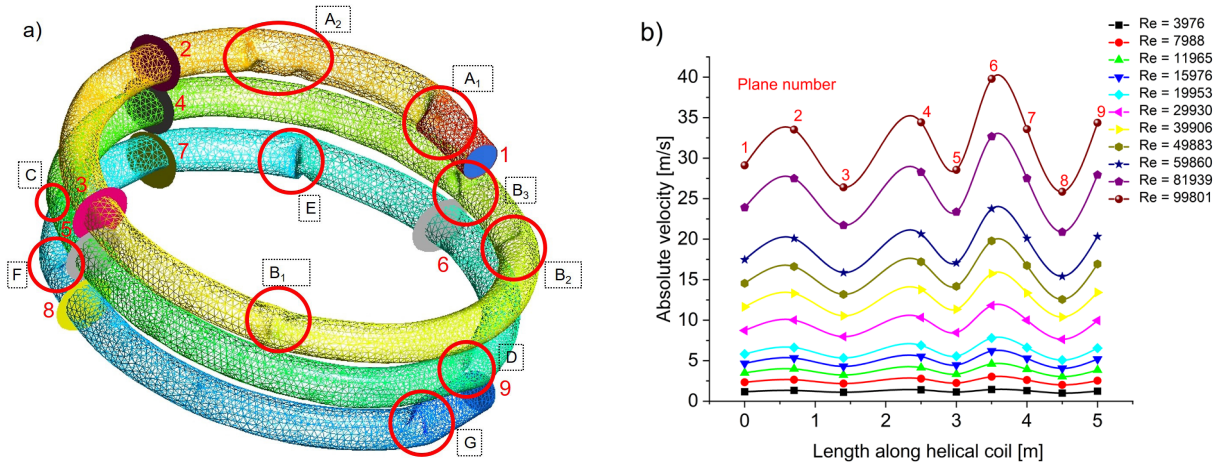


Fig. 18. a) Representation of critical wrinkles; and b) absolute velocity at selected sections

This implies that the sectional area owing to the presence of wrinkles could cause noticeable velocity variations cyclically along the length of the coil.

**3.1.5 Assessment of Influence of Ovality and Wrinkles on Flow Field through FRICTION FACTOR**

The maximum ovality of the helical coil was found to be 3.2 % by measurement. The difference in friction factor between ideal coil and coil with ovality is 8.5 %, whereas the difference in friction factor between ideal and wrinkled coils is 80.5 %. Hence, it is evident that ovality does not significantly influence the global behaviour of the flow field (Table 1).

Table 1. Comparison of friction factor

Geometry (three turn helical coil)	Method	Pressure drop [Pa]	Friction factor
Without ovality and wrinkles	Numerical	1293	0.0111
	Experimental	1303	0.0113
With ovality	Numerical	1342	0.0121
With ovality and wrinkles	Numerical	2036	0.0262
	Experimental	2132	0.0281

The isolated wrinkles in the helical coil contribute to a significant global pressure drop and have a dominant effect on local behaviour, such as negative pressure. The above behaviour will affect the heat transfer aspects of a helical coil, leading to crack initiation. In the event of the fluid being a refrigerant, it will have a considerable environmental impact. Hence, it is necessary to investigate the local behaviour by considering a critical portion of the coil.

A much finer mesh is used for the critical portion to better capture the flow behaviour.

**3.2 Local Analysis of Flow Field in a Critical Portion of Helical Coil with Wrinkles**

A critically wrinkled portion of the coil is considered for numerical investigation, as already shown in Fig. 3. The geometric model for the critical portion of the coil was obtained using a reverse engineering approach. A finer mesh scheme was used to capture turbulence near the vicinity of wrinkles while developing the numerical model. The circumferential pressure distribution at a selected critical plane of the helical coil is shown in Fig. 19.

It can be observed that the pressure increases in all the cases near the extrados of the coil. The wrinkles increase the turbulence in the flow field and thereby causes higher secondary flow. This will result in flow loss due to increased wall shear stress. It can also be observed that the isolated wrinkles are not identical in shape and size; hence, the plots of circumferential pressure vary from each other.

**3.2.1 Effect of Negative Pressure in Wrinkled Coils**

To visualize the negative pressure zones, the positive pressure distribution along the coil was made to be 0 MPa, and negative pressure zones (Fig. 20) alone were concentrated.

The negative pressure formation is attributed to the coil's wrinkles and would create a vortex. The pressure and velocity distribution of air has been analysed. It is found that the local dents were

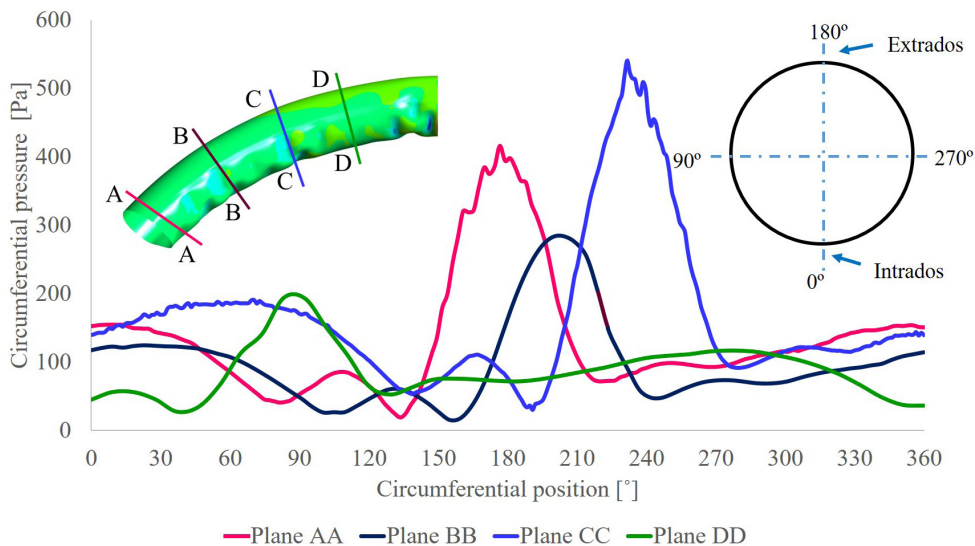


Fig. 19. Circumferential pressure distribution at critical sectional planes

isolated, which causes local re-circulation. At isolated locations, the occurrence of negative pressure may cause cavitation resulting in pitting.

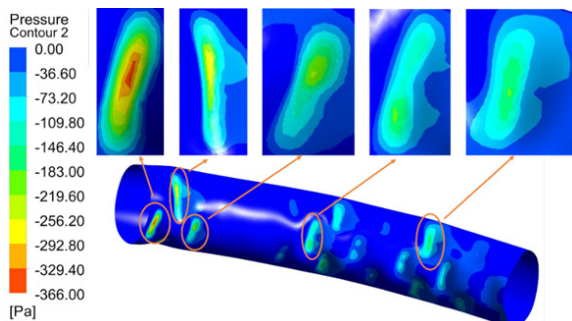


Fig. 20. Negative pressure formation

#### 4 CONCLUSIONS

The major conclusions of the present work are as follows:

1. The numerical investigation revealed that the maximum ovality of 3.2 % does not significantly influence the flow field in a helical coil.
2. The wrinkles are found to have significant effects on both the global and local flow behaviour. The global analysis of pressure drop and velocity field revealed the effect of wrinkles on the flow field in the form of a rise in equivalent roughness of the helical coil and oscillation of velocity distributions due to sectional area variations along the length of the helical coil.

3. The analysis of a critical portion of the helical coil revealed increased turbulence in the flow field. The resulting secondary flow has resulted in considerable negative pressure in the flow field, which would initiate localized damage mechanisms, such as cavitation and pitting. The above mechanisms would lead to more severe consequences when helical coils with wrinkles are used in heat exchangers for critical applications like nuclear, medical, etc.
4. Further investigation on material and structural damage is required to quantify heat transfer and other process effects in addition to the local negative pressure fields by considering the other geometrical irregularities, namely, thinning at extrados and thickening at the intrados.
5. The results of the present work are based on the investigation carried out for a particular size of coil; hence, it is valid only for the above configuration and for similar coils that have distributions of wrinkles as considered in the present work. Therefore, a parametric study that accounts for variations in coil geometry and associated wrinkle distribution and size is required.

#### 5 ACKNOWLEDGEMENTS

We acknowledge PSG College of Technology for providing the necessary support required to carry out the work successfully. We also acknowledge M/s GEM Equipments Private Limited, Coimbatore, India

for supporting us to conduct experiments in their facility.

## 6 REFERENCES

- [1] Eustice, J. (1911). Experiments on stream-line motion in curved pipes. *Proceedings of the Royal Society A: Mathematical, Physical and Engineering Sciences*, vol. 85, no. 576, p. 119-131, DOI:10.1098/rspa.1911.0026.
- [2] Dean, W.R. (1927). XVI. Note on the motion of fluid in a curved pipe. *The London, Edinburgh, and Dublin Philosophical Magazine and Journal of Science*, vol. 4, no. 20, p. 208-223, DOI:10.1080/14786440708564324.
- [3] Jayakumar, J., Mahajani, S., Mandal, J., Vijayan, P., Bhoi, R. (2008). Experimental and CFD estimation of heat transfer in helically coiled heat exchangers. *Chemical Engineering Research and Design*, vol. 86, no. 3, p. 221-232, DOI:10.1016/j.cherd.2007.10.021.
- [4] Dubba, S.K., Kumar, R. (2018). Experimental investigation on flow of r-600a inside a diabatic helically coiled capillary tube: Concentric configuration. *International Journal of Refrigeration*, vol. 86, p. 186-195, DOI:10.1016/j.ijrefrig.2017.10.035.
- [5] Tang, L., Yuan, S., Malin, M., Parameswaran, S. (2017). Secondary vortex-based analysis of flow characteristics and pressure drop in helically coiled pipe. *Advances in Mechanical Engineering*, vol. 9, no. 4, p. 1-11, DOI:10.1177/1687814017700059.
- [6] Sharqawy, M.H., Saad, S.M., Ahmed, K.K. (2019). Effect of flow configuration on the performance of spiral-wound heat exchanger. *Applied Thermal Engineering*, vol. 161, art. ID 114157, DOI:10.1016/j.applthermaleng.2019.114157.
- [7] Patil, R.H. (2019). Fluid flow and heat transfer analogy for laminar and turbulent flow inside spiral tubes. *International Journal of Thermal Sciences*, vol. 139, p. 362-375, DOI:10.1016/j.ijthermalsci.2019.01.036.
- [8] Neshat, E., Hossainpour, S. (2017). Numerical investigation of unsteady natural convection heat transfer from the outer surface of helical coils. *Proceedings of the Institution of Mechanical Engineers, Part E: Journal of Process Mechanical Engineering*, vol. 231, no. 3, p. 383-391, DOI:10.1177/0954408915598130.
- [9] Elattar, H.F., Fouda, A., Nada, S.A., Refaey, H.A., Al-Zahrani, A. (2018). Thermal and hydraulic numerical study for a novel multi tubes in tube helically coiled heat exchangers: Effects of operating/geometric parameters. *International Journal of Thermal Sciences*, vol. 128, p. 70-83, DOI:10.1016/j.ijthermalsci.2018.02.020.
- [10] Prabhanjan, D.G., Raghavan, G.S.V., Rennie, T.J. (2002). Comparison of heat transfer rates between a straight tube heat exchanger and a helically coiled heat exchanger. *International Communications in Heat and Mass Transfer*, vol. 29, no. 2, p. 185-191, DOI:10.1016/S0735-1933(02)00309-3.
- [11] Močnik, U., Blagojevič, B., Muhič, S. (2020). Numerical analysis with experimental validation of single-phase fluid flow in a dimple pattern heat exchanger channel. *Strojniški vestnik - Journal of Mechanical Engineering*, vol. 66, no. 9, p. 10, DOI:10.5545/sv-jme.2020.6776.
- [12] Hashemi Karouei, S.H., Mousavi Ajarostaghi, S.S. (2021). Influence of a curved conical turbulator on heat transfer augmentation in a helical double-pipe heat exchanger. *Heat Transfer*, vol. 50, no. 2, p. 1872-1894, DOI:10.1002/htj.21960.
- [13] Sheeba, A., Abhijith, C.M., Prakash, M.J. (2019). Experimental and numerical investigations on the heat transfer and flow characteristics of a helical coil heat exchanger. *International Journal of Refrigeration*, vol. 99, p. 490-497, DOI:10.1016/j.ijrefrig.2018.12.002.
- [14] Jamshidi, N., Farhadi, M., Ganji, D.D., Sedighi, K. (2013). Experimental analysis of heat transfer enhancement in shell and helical tube heat exchangers. *Applied Thermal Engineering*, vol. 51, no. 1-2, p. 644-652, DOI:10.1016/j.applthermaleng.2012.10.008.
- [15] Ravigururajan, T.S., Bergles, A.E. (1996). Development and verification of general correlations for pressure drop and heat transfer in single-phase turbulent flow in enhanced tubes. *Experimental Thermal and Fluid Science*, vol. 13, no. 1, p. 55-70, DOI:10.1016/0894-1777(96)00014-3.
- [16] Woods, G.E., Baguley, R.B., Bringas, J.E. (2000). *Casti Guidebook to ASME B31.3*. McGraw-Hill, New York.
- [17] Colebrook, C.F., Blench, T., Chatley, H., Essex, E.H., Finnicome, J.R., Lacey, G., Williamson, J., Macdonald, G.G. (1939). Correspondence. Turbulent flow in pipes, with particular reference to the transition region between the smooth and rough pipe laws.(includes plates). *Journal of the Institution of Civil Engineers*, vol. 12, no. 8, p. 393-422, DOI:10.1680/ijoti.1939.14509.
- [18] Tang, L., Tang, Y., Parameswaran, S. (2016). A numerical study of flow characteristics in a helical pipe. *Advances in Mechanical Engineering*, vol. 8, no. 7, p. 1-8, DOI:10.1177/1687814016660242.
- [19] Churchill, S.W., SW, C. (1977). Friction-factor equation spans all fluid-flow regimes. *Chemical Engineering*, vol 84, p. 91-92.
- [20] Green, D.W., Perry, R.H. (2008). *Perry's Chemical Engineers' Handbook*. McGraw-Hill, New York.
- [21] Di Piazza, I., Ciofalo, M. (2010). Numerical prediction of turbulent flow and heat transfer in helically coiled pipes. *International Journal of Thermal Sciences*, vol. 49, no. 4, p. 653-663, DOI:10.1016/j.ijthermalsci.2009.10.001.

# Synchronization and Stability of a Three Co-Rotating Rotor System Coupled with Springs in a Non-Resonance System

Mingjun Du<sup>1,\*</sup> – Yongjun Hou<sup>1</sup> – Tong Tang<sup>2</sup> – Lian Tang<sup>3</sup> – Jialong Wang<sup>1</sup> – Hongbo Gao<sup>1</sup>

<sup>1</sup>Southwest Petroleum University, School of Mechatronics Engineering, China

<sup>2</sup>AECC Chengdu Engine Company Limited, China

<sup>3</sup>Sichuan Aviation Industry Chuanxi Machinery Company Limited, China

*With the rapid development of horizontal drilling technology, the drilling fluid shale shaker (DFSS) features high capacity and high efficiency. Hence, a vibrating mechanism of a three co-rotating rotor system coupled with springs is proposed for designing large-sized and heavy-duty vibrating screens in petroleum drilling engineering. To master synchronization of the vibrating system, the dynamic equations of three co-rotating rotors coupled with springs are first developed based on Lagrange's equations. Second, synchronous conditions of the system are derived based on the average method, and its stability criterion is obtained by adopting Hamilton's principle. Furthermore, the influences of various factors, including positional parameters of three motors, stiffness coefficient of the springs and frequency ratio on synchronization behaviour, are numerically analysed in the steady state. Additionally, the Runge-Kutta algorithm with adaptive control is employed to build an electromagnetic coupling model, and the relationships between the synchronization state of the system and its mechanical-electrical coupling characteristics are investigated. Finally, an experimental prototype is designed to validate the theory and numerical analysis. The research result shows that the in-phase synchronization of three co-rotating rotors coupled with springs is easy to implement with the selection of a sufficiently large stiffness.*

**Keywords:** synchronization, dynamic characteristic, synchronous conditions, stability criterion, springs

## Highlights

- A vibrating mechanism of a three co-rotating rotor system coupled with springs is proposed.
- The synchronization characteristics of the system are investigated using theory and numerical analysis.
- The stable phase difference of three motors are stabilized at zero by the selection of a sufficiently large stiffness.
- An experimental prototype is designed to prove the correctness of theory and numerical analysis.
- The presented model can be applied to high capacities and efficiencies in the DFSS.

## 0 INTRODUCTION

Vibration utilization has always played an important role in a variety of manufacturing industries, such as the vibration conveyer, vibration-impact pile driver, vibratory centrifuge, vibratory crusher, vibratory feeder, etc. The vibrating screen is the most common vibration utilization equipment, especially in petroleum drilling engineering. The vibrating screen is a kind of solid control equipment to separate drilling cuttings from circulating drilling fluid in the process of drilling, which not only undertakes the task of removing a large number of cuttings but can also create a necessary condition for the normal operation of the next solid control equipment. Studies on the drilling fluid shale shaker (DFSS) focus on structural design, screening performance, synchronization theory, etc. In the structural design and screening performance of the vibrating screen, Baragetti suggested increasing the structural and functional performance of the screen by means of a modification of the two side-walls of the mechanical system and studied the dynamic and structural behaviour of the original and modified

vibrating screen by using theoretical and numerical models [1]. Dong et al. adopted a three-dimensional discrete element method to study the effect of aperture shape on particle flow and separation in a vibrating screen process [2] and [3]. For the synchronization theory of rotors, Blekhman first proposed a method of the direct separation of motions to solve many engineering problems [4] to [6]. Balthazar et al. investigated the synchronization of two unbalanced rotating motors mounted on the horizontal beam by means of numerical simulations [7] and [8]. Subsequently, Wen et al. [9] and [10] investigated the synchronization problem of two motors in a non-resonance system by using small parameter averaging method, and various synchronous vibrating machines were invented to improve productivity [9] and [10]. Based on Wen's method, Zhang et al. investigated the synchronization of two or three exciters in a far-resonant vibrating system of plane motion [11] and [12]. Fang and Hou [13] and Fang et al. [14] discussed the dynamic characteristics of a rotor-pendula system via theoretical analysis and numerical simulations; they determined that the synchronous behaviour

is determined by mass ratio coefficients, structure parameters, rotating directions, and frequency ratios. Chen et al. used the average method of small parameters to explore the synchronization of two eccentric rotors with a common rotational axis in the far-resonant spatial system. It can be found that the phase difference of two eccentric rotors with a common rotational axis is easily approaching  $\pi$  during the running process of the steady-state [15] and [16]. Furthermore, Huang et al. [17] and [18] and Kong et al. [19] and [20] studied the composite synchronization of the vibrating system driven by a multi-motor by applying a cross-coupling control strategy and modified master-slave control structure.

Nowadays, on the one hand, with the rapid development of horizontal drilling technology, the DFSS takes a higher demand for its processing capacity and separating efficiency. On the other hand, as the space of on-site drilling is limited, many companies have proposed improving the processing capacity by increasing the screen layers, which caused the total mass of the vibrating body to increase, and the vibrating system driven by multiple motors are required to achieve a greater exciting force. Hence, many scholars developed a vibrating system with multiple non-identical exciters in a far-resonant vibrating system to apply in DFSS [21] to [25]. However, for the synchronization of three non-identical coupled exciters, those results prove that the phase difference of co-rotating motors stabilized in the neighbourhood of  $\pi$  and the exciting force of two exciters are counteracted each other [11]. To improve the amplitude and screening efficiency of the system, a vibrating mechanism of a three co-rotating rotor system coupled with springs in a non-resonance

system is proposed for designing large-sized and heavy-duty vibrating screens in petroleum drilling engineering.

In this paper, to further explore the synchronous mechanism of the proposed system and master its synchronous characteristics, the main contents are as follows: In Section 1, a mechanical model of three co-rotating rotors coupled with springs is introduced. Then, the synchronous conditions and the stability criterion of the system are obtained. Next, the influence of positional parameters of three motors, stiffness coefficient of the coupling springs, frequency ratio, the total mass of the system etc., on the steady phase difference are discussed in Section 2. In Section 3, we studied the relationships between synchronization state of the system and its mechanical-electrical coupling characteristics by utilizing the Runge–Kutta algorithm with adaptive control. In addition, an experimental prototype of three co-rotating rotors system coupled with springs is designed and manufactured. Synchronous tests and dynamic tests of the vibrating system are implemented in Section 4. Finally, several important conclusions are summarized in Section 5.

## 1 SYNCHRONIZATION MECHANISM

### 1.1 Mechanical Model and Dynamical Equations

Fig. 1 shows a vibrating system driven by three co-rotating rotors coupled with springs, which consists of three motors, a rigid frame, an elastic foundation, two coupling springs and four supporting springs. Unbalanced rotors actuated by three identical asynchronous motors are modelled with an eccentric

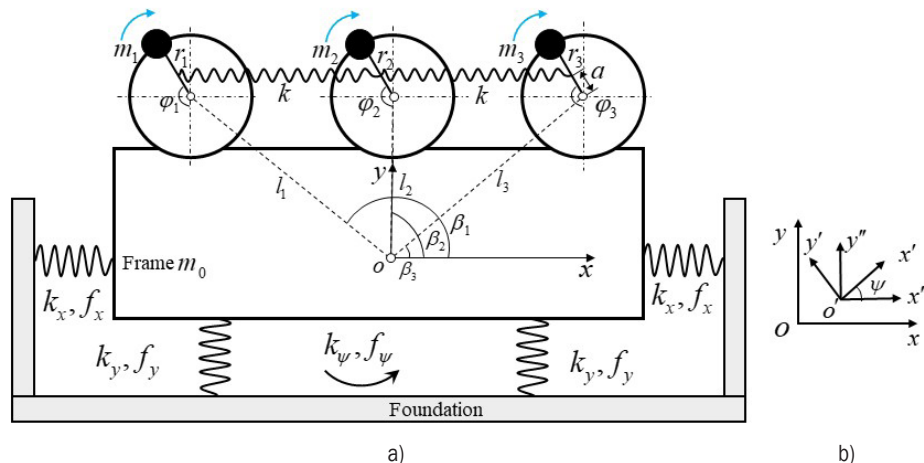


Fig. 1. A vibrating system driven by three co-rotating rotors coupled with springs: a) simplified mechanical model; and b) coordinate system

lump  $m_i$  and attached eccentric length  $r_i$  ( $i=1,2,3$ ). Three motors are parallelly installed on a rigid frame, and the adjacent two motors are connected with a spring with a stiffness coefficient  $k$ . The distance from the rotating centre of each motor to the connection of the end of coupling spring is  $a$ . The vibrating body is connected with a fixed foundation by four supporting springs with stiffness  $k_j$  and damping  $f_j$  in  $j$ -direction. When three motors are simultaneously provided an electromagnetic force, the impact energy produced by its asynchronous motion is absorbed by the coupling springs during the start-up stage of the system. Then the impact energy is absorbed by the coupling springs is increasingly released as the operation of the vibrating system. The steady-state motion of the system is finally implemented under the action of the coupling springs. In the vibrating system, choosing  $q=[x,y,\psi,\varphi_1,\varphi_2,\varphi_3]$  as a generalized coordinate. Then, the generalized active forces of the system are  $Q_j=[0,0,0,T_{e1},T_{e2},T_{e3}]$  in the  $-q_j$  direction. Due to the mass of three motors being far less than the rigid frame ( $m_i \ll m_0$ ) and the swaying displacement being extremely small ( $\psi \ll 1$ ), the coupling inertial moment caused by an asymmetric installation of three motors can be ignored. Consider that the three motors are symmetrically arranged on the rigid frame, and its structure parameters satisfy:  $l_1=l_3=l$ ,  $l_2=l \sin \beta$ ,  $\beta_1=\pi-\beta$ ,  $\beta_2=\pi/2$ ,  $\beta_3=\beta$ . According to the general form of Lagrange's equation, the dynamics equations of the vibrating system are derived:

$$M\ddot{x} + f_x \dot{x} + k_x x = \sum_{i=1}^3 m_i r_i [\ddot{\varphi}_i \cos \varphi_i - \dot{\varphi}_i^2 \sin \varphi_i],$$

$$M\ddot{y} + f_y \dot{y} + k_y y = \sum_{i=1}^3 m_i r_i [-\ddot{\varphi}_i \sin \varphi_i - \dot{\varphi}_i^2 \cos \varphi_i],$$

$$J\ddot{\psi} + f_\psi \dot{\psi} + k_\psi \psi = \sum_{i=1}^3 m_i l_i r_i [\ddot{\varphi}_i \sin(\varphi_i + \beta_i) + \dot{\varphi}_i^2 \cos(\varphi_i + \beta_i)],$$

$$J_1 \ddot{\varphi}_1 + f_1 \dot{\varphi}_1 = T_{e1} + m_1 r_1 \ddot{x} \cos \varphi_1 - m_1 r_1 \dot{y} \sin \varphi_1 + m_1 r_1 l_1 \ddot{\psi} \sin(\varphi_1 + \beta_1) - m_1 r_1 l_1 \dot{\psi}^2 \cos(\varphi_1 + \beta_1) + ka^2 \sin(\varphi_2 - \varphi_1) - kla \cos(\varphi_1 - \beta) + kal \sin \beta \sin \varphi_1 + kl \cos \beta f_1(k, \varphi_1, \varphi_2, \beta, l, a),$$

$$J_2 \ddot{\varphi}_2 + f_2 \dot{\varphi}_2 = T_{e2} + m_2 r_2 \ddot{x} \cos \varphi_2 - m_2 r_2 \dot{y} \sin \varphi_2 + m_2 r_2 l_2 \ddot{\psi} \sin(\varphi_2 + \beta_2) - m_2 r_2 l_2 \dot{\psi}^2 \cos(\varphi_2 + \beta_2) - ka^2 \sin(\varphi_2 - \varphi_1) + ka^2 \sin(\varphi_3 - \varphi_2) + kl \cos \beta f_2(k, \varphi_1, \varphi_2, \beta, l, a),$$

$$J_3 \ddot{\varphi}_3 + f_3 \dot{\varphi}_3 = T_{e3} + m_3 r_3 \ddot{x} \cos \varphi_3 - m_3 r_3 \dot{y} \sin \varphi_3 + m_3 r_3 l_3 \ddot{\psi} \sin(\varphi_3 + \beta_3) + kal \sin \beta \sin \varphi_3 - m_3 r_3 l_3 \dot{\psi}^2 \cos(\varphi_3 + \beta_3) - ka^2 \sin(\varphi_3 - \varphi_2) + kla \cos(\varphi_3 + \beta) + kl \cos \beta f_3(k, \varphi_1, \varphi_2, \beta, l, a), \quad (1)$$

where  $M = m_0 + \sum_1^3 m_i$ ,  $J = J_0 + \sum_1^3 m_i l_i^2 + \sum_1^3 m_i r_i^2$ ,  $J_1 = J_{o1} + m_1 r_1^2$ ,  $J_2 = J_{o2} + m_2 r_2^2$ ,  $J_3 = J_{o3} + m_3 r_3^2$ .

Here  $M$  is the total mass of the system;  $J$  is the rotational inertia of the system;  $f_i(k, \varphi_1, \varphi_2, \beta, l, a)$  is a coupling term of the springs, and its expressions are given in the Appendix.

### 1.2 Steady-State Response

Due to the motion of the system changing periodically during the running process of the steady-state, the average velocity of three motors is also periodic, and their average values with the least common multiple period  $T$  are approximately equal to a constant  $\omega_m$ :

$$\omega_m = \frac{1}{T} \int_{t_0}^{t_0+T} \dot{\varphi} dt = \text{constant}. \quad (2)$$

Assuming the average phase  $\varphi$  of the three motors in steady state, and their phase differences are expressed by  $\alpha_{12}$  and  $\alpha_{23}$ , respectively, i.e.  $\varphi_1 - \varphi_2 = \alpha_{12}$ ,  $\varphi_2 - \varphi_3 = \alpha_{23}$ . Hence, we have

$$\varphi_1 = \varphi + \frac{1}{2} \alpha_{12}, \quad \varphi_2 = \varphi - \frac{1}{2} \alpha_{12}, \quad \varphi_3 = \varphi - \frac{1}{2} \alpha_{12} - \alpha_{23}. \quad (3)$$

Considering the coefficients of the instantaneous change with the average speed of three motors and their phase difference are expressed as  $\varsigma_0, \varsigma_{12}, \varsigma_{23}$ , respectively. i.e.,

$$\dot{\varphi} = \omega_m (1 + \varsigma_0), \quad \Delta \dot{\alpha}_{12} = \omega_m \varsigma_{12}, \quad \Delta \dot{\alpha}_{23} = \omega_m \varsigma_{23}. \quad (4)$$

Introducing small parameters  $\varepsilon_i$  ( $i=1,2,3$ ) to Eq. (3), we know that the vibrating system operates at a steady state when the average values  $\varepsilon_i$  ( $i=1,2,3$ ) with one period are equal to zero. Hence, the acceleration of three motors can be written as follows:

$$\begin{aligned} \dot{\varphi}_1 &= \omega_m \left( 1 + \varsigma_0 + \frac{1}{2} \varsigma_{12} \right) = (1 + \varepsilon_1) \omega_m, \\ \dot{\varphi}_2 &= \omega_m \left( 1 + \varsigma_0 + \frac{1}{2} \varsigma_{12} \right) = (1 + \varepsilon_2) \omega_m, \\ \dot{\varphi}_3 &= \omega_m \left( 1 + \varsigma_0 + \frac{1}{2} \varsigma_{12} - \varsigma_{23} \right) = (1 + \varepsilon_3) \omega_m. \end{aligned} \quad (5)$$

Furthermore, introducing following dimensionless parameters:

$$\begin{aligned} \zeta_x &= \frac{f_x}{2\omega_{nx}M}, \zeta_y = \frac{f_y}{2\omega_{ny}M}, \zeta_\psi = \frac{f_\psi}{2\omega_{n\psi}J}, \\ n_j &= \frac{\omega_m}{\omega_{nj}}, \eta_1 = \frac{m_1}{m_0}, \eta_2 = \frac{m_2}{m_0}, \eta_3 = \frac{m_3}{m_0}, j = x, y, \psi, \\ r_m &= \frac{m_0}{M}, l_e = \sqrt{\frac{J}{M}}, r_{li} = \frac{l_i}{l_e}, r_{ri} = \frac{r_i}{r_0}, i = 1, 2, \end{aligned} \quad (6)$$

where,  $\omega_{nx} = \sqrt{k_x/M}$ ,  $\omega_{ny} = \sqrt{k_y/M}$ ,  $\omega_{n\psi} = \sqrt{k_\psi/J}$ . Here,  $m_0$  is the standard mass of the system and  $r_0$  is the standard radius of three rotors. Inserting the dimensionless parameters Eq. (6) into Eq. (1) yields the dimensionless formulas of the dynamic equations of the system in  $j$ - ( $j=x, y, \psi$ ) direction as:

$$\begin{aligned} \ddot{x} + 2\zeta_x\omega_{nx}\dot{x} + \omega_{nx}^2x &= -\omega_m^2r_m r_0 \left[ \begin{aligned} &\eta_1 r_{r1} \sin \varphi_1 + \eta_2 r_{r2} \sin \varphi_2 \\ &+ \eta_3 r_{r3} \sin \varphi_3 \end{aligned} \right], \\ \ddot{y} + 2\zeta_y\omega_{ny}\dot{y} + \omega_{ny}^2y &= -\omega_m^2r_m r_0 \left[ \begin{aligned} &\eta_1 r_{r1} \cos \varphi_1 + \eta_2 r_{r2} \cos \varphi_2 \\ &+ \eta_3 r_{r3} \cos \varphi_3 \end{aligned} \right], \\ \ddot{\psi} + 2\zeta_\psi\omega_{n\psi}\dot{\psi} + \omega_{n\psi}^2\psi &= \frac{\omega_m^2r_m r_0}{l_e} \left[ \begin{aligned} &\eta_1 r_{l1} r_{r1} \cos(\varphi_1 + \beta_1) \\ &+ \eta_2 r_{l2} r_{r2} \cos(\varphi_2 + \beta_2) \\ &+ \eta_3 r_{l3} r_{r3} \cos(\varphi_3 + \beta_3) \end{aligned} \right]. \end{aligned} \quad (7)$$

When the vibrating system operates at the steady state, the periodic solutions of the system in  $j$ - ( $j=x, y, \psi$ ) direction can be expressed as:

$$\begin{aligned} x &= -r_m r_0 \mu_x [\eta_1 r_{r1} \sin(\varphi_1 - \gamma_x) \\ &+ \eta_2 r_{r2} \sin(\varphi_2 - \gamma_x) + \eta_3 r_{r3} \sin(\varphi_3 - \gamma_x)], \\ y &= -r_m r_0 \mu_y [\eta_1 r_{r1} \cos(\varphi_1 - \gamma_y) \\ &+ \eta_2 r_{r2} \cos(\varphi_2 - \gamma_y) + \eta_3 r_{r3} \cos(\varphi_3 - \gamma_y)], \\ \psi &= \frac{r_m r_0 \mu_\psi}{l_e} [\eta_1 r_{l1} r_{r1} \cos(\varphi_1 + \beta_1 - \gamma_\psi) \\ &+ \eta_2 r_{l2} r_{r2} \cos(\varphi_2 + \beta_2 - \gamma_\psi) \\ &+ \eta_3 r_{l3} r_{r3} \cos(\varphi_3 + \beta_3 - \gamma_\psi)], \end{aligned} \quad (8)$$

here,

$$\begin{aligned} \mu_j &= \frac{n_j^2}{\sqrt{(1-n_j^2)^2 + (2\zeta_j n_j)^2}}, \\ \gamma_j &= \begin{cases} \arctan\left(\frac{2\zeta_j n_j}{1-n_j^2}\right) & 1-n_j^2 \geq 0 \\ \pi + \arctan\left(\frac{2\zeta_j n_j}{1-n_j^2}\right) & \text{other} \end{cases} \end{aligned}$$

### 1.3 Synchronous Conditions

Since the far-resonant vibrating system is commonly used in engineering applications, the exciting frequency of the system is 3 to 10 times greater than its natural frequency, i.e.  $n_j \geq 3$ , and the vibrating system with small damping ( $\zeta_j \leq 0.07$ ) [10]. Hence,  $\mu_j \cong n_j^2 / (n_j^2 - 1)$ ,  $\gamma_j = \pi + \arctan(2\zeta_j n_j / (1 - n_j^2))$ . In light of literature [11] and [12], the rated slip of the motors ranges from 0.02 to 0.08 during the running process of the steady-state. When the three rotors are rotated with an equal velocity ( $\dot{\varphi}_i = \omega_m$ ), their electromagnetic torque can be written in the form:

$$T_{ei} = T_{e0i} - \bar{k}_{e0i} \bar{\varepsilon}_i, \quad (9)$$

where  $T_{e0i}$  and  $\bar{k}_{e0i}$  are given in the literature [14]. Differentiating Eq. (8) to obtain  $\dot{x}, \ddot{x}, \dot{y}, \ddot{y}, \dot{\psi}$  and  $\ddot{\psi}$ . Then, inserting them into the dynamical equations of the rotors in Eq. (1), and integrating them with one period, we obtain the matrix form of  $\bar{\varepsilon}_i$  in the form:

$$\mathbf{P} \bar{\varepsilon} = \mathbf{Q} \bar{\varepsilon} + \boldsymbol{\mu}, \quad (10)$$

where  $\bar{\varepsilon} = [\bar{\varepsilon}_1 \quad \bar{\varepsilon}_2 \quad \bar{\varepsilon}_3]^T$ ,  $\boldsymbol{\mu} = [\mu_1 \quad \mu_2 \quad \mu_3]^T$ ,

$$\mathbf{P} = \begin{bmatrix} \rho_{11} & \chi'_{12} & \chi'_{13} \\ \chi'_{21} & \rho_{12} & \chi'_{23} \\ \chi'_{31} & \chi'_{32} & \rho_{13} \end{bmatrix}, \quad \mathbf{Q} = -\omega_m \begin{bmatrix} k_{11} & \chi_{12} & \chi_{13} \\ \chi_{21} & k_{22} & \chi_{23} \\ \chi_{31} & \chi_{32} & k_{33} \end{bmatrix}.$$

Parameters  $\rho_{11}$ ,  $\chi'_{12}$ , etc. are shown in the Appendix.

The symbol  $\mathbf{P}$  represents the coupling matrix of three rotors; the symbol  $\mathbf{Q}$  is defined as the stiffness matrix of the vibrating system; the symbol  $\boldsymbol{\mu}$  is the torque coupling matrix of three rotors. When the vibrating system operates at the steady state, the coefficients of the instantaneous change are approximate to zero, i.e.,  $\zeta_0 = 0$ ,  $\zeta_{12} = 0$ ,  $\zeta_{23} = 0$ . Hence, the values of  $\bar{\varepsilon}$  also tend to zero. Inserting them into Eq. (10), we obtain  $\boldsymbol{\mu} = 0$ , and adding them together to obtain the following expression:

$$\begin{aligned} &\sum_{i=1}^3 T_{e0i} - \omega_m \sum_{i=1}^3 f_i \\ &- \frac{1}{2} m_0 r_0^2 \omega_m^2 \sum_{i=1}^3 (\eta_i^2 r_{ri}^2 W_{si}) + kl \cos \beta F(\alpha_{12}, \alpha_{23}) / 2\pi \\ &+ \frac{1}{2} m_0 r_0^2 \omega_m^2 \eta_1 \eta_3 r_{r1} r_{r3} \\ &\cdot [-W_{s13} \sin(\alpha_{12} + \alpha_{23} + \theta_{s13}) - W_{s13} \cos(\alpha_{12} + \alpha_{23} + \theta_{s13})] \\ &- m_0 r_0^2 \omega_m^2 \eta_2 \eta_3 r_{r2} r_{r3} W_{s23} \cos(\alpha_{23} + \theta_{s23}) \\ &- m_0 r_0^2 \omega_m^2 \eta_1 \eta_2 r_{r1} r_{r2} W_{s12} \cos(\alpha_{12} + \theta_{s12}) = 0, \end{aligned} \quad (11)$$

where

$$F(\alpha_{12}, \alpha_{23}) = \int_0^{2\pi} \frac{-2la \cos \beta \sin \frac{\alpha_{12}}{2} \sin \varphi}{\left[ l^2 \cos^2 \beta + 2a^2 - 2a^2 \cos \alpha_{12} + 4la \cos \beta \sin \frac{\alpha_{12}}{2} \cos \varphi \right]^{0.5}} d\varphi$$

$$+ \int_0^{2\pi} \frac{-2la \cos \beta \sin \frac{\alpha_{23}}{2} \sin \left( \varphi - \frac{\alpha_{12} + \alpha_{23}}{2} \right)}{\left[ l^2 \cos^2 \beta + 2a^2 - 2a^2 \cos \alpha_{23} + 4la \cos \beta \sin \frac{\alpha_{23}}{2} \cos \left( \varphi - \frac{\alpha_{12} + \alpha_{23}}{2} \right) \right]^{0.5}} d\varphi$$

Eq. (11) is the equilibrium equation of the dynamic moment of the whole system. The first term  $\left(\sum_{i=1}^3 T_{e0i}\right)$  represents the sum of the output torque of three motors; the second term  $\left(\omega_m \sum_{i=1}^3 f_i\right)$  is the sum of resistance torque of three motors during operation; the remaining terms denote the mechanical load of three motors operating in the steady state and the coupling torque of those connecting springs among three rotors. Moreover, it can be seen that there is no coupling term with connecting spring in Eq. (11). An optimal zero phase synchronization of three motors is achieved, i.e.,  $\alpha_{12}=0, \alpha_{23}=0$ . That is to say, the deformation rate of these connecting springs is always equal to zero during the running process of the steady-state. Due to  $\mathbf{m}=0$ , the difference equations of two of motors can be obtained:

$$\begin{aligned} & [T_{e01} - \omega_m f_1] - [T_{e02} - \omega_m f_2] + ka^2 [\sin \alpha_{23} - 2 \sin \alpha_{12}] \\ & + \frac{kl \cos \beta}{2\pi} [F_1(\varphi) - F_2(\varphi)] \\ & + \frac{1}{2} m_0 r_0^2 \omega_m^2 \left[ \begin{aligned} & -\eta_1^2 r_{r1}^2 W_{s1} + \eta_2^2 r_{r2}^2 W_{s2} \\ & -2\eta_1 \eta_2 r_{r1} r_{r2} W_{c12} \sin(\alpha_{12} + \theta_{c12}) \end{aligned} \right] \\ & - \frac{1}{2} m_0 r_0^2 \omega_m^2 \eta_1 \eta_3 r_{r1} r_{r3} \left[ \begin{aligned} & W_{c13} \sin(\alpha_{12} + \alpha_{23} + \theta_{c13}) \\ & + W_{s13} \sin(\alpha_{12} + \alpha_{23} + \theta_{s13}) \end{aligned} \right] \\ & + \frac{1}{2} m_0 r_0^2 \omega_m^2 \eta_2 \eta_3 r_{r2} r_{r3} \left[ \begin{aligned} & W_{c23} \sin(\alpha_{23} + \theta_{c23}) \\ & + W_{s23} \cos(\alpha_{23} + \theta_{s23}) \end{aligned} \right] = 0, \quad (12) \end{aligned}$$

$$\begin{aligned} & [T_{e02} - \omega_m f_2] - [T_{e03} - \omega_m f_3] \\ & + ka^2 [\sin \alpha_{12} - 2 \sin \alpha_{23}] + \frac{kl \cos \beta}{2\pi} [F_2(\varphi) - F_3(\varphi)] \\ & + \frac{1}{2} m_0 r_0^2 \omega_m^2 \eta_1 \eta_2 r_{r1} r_{r2} \left[ \begin{aligned} & W_{c12} \sin(\alpha_{12} + \theta_{c12}) \\ & - W_{s12} \cos(\alpha_{12} + \theta_{s12}) \end{aligned} \right] \\ & + \frac{1}{2} m_0 r_0^2 \omega_m^2 \left[ \begin{aligned} & -\eta_2^2 r_{r2}^2 W_{s2} + \eta_3^2 r_{r3}^2 W_{s3} \\ & -2\eta_2 \eta_3 r_{r2} r_{r3} W_{c23} \sin(\alpha_{23} + \theta_{c23}) \end{aligned} \right] \\ & - \frac{1}{2} m_0 r_0^2 \omega_m^2 \eta_1 \eta_3 r_{r1} r_{r3} \left[ \begin{aligned} & W_{c13} \sin(\alpha_{12} + \alpha_{23} + \theta_{c13}) \\ & - W_{s13} \cos(\alpha_{12} + \alpha_{23} + \theta_{s13}) \end{aligned} \right] = 0 \quad (13) \end{aligned}$$

Eqs. (12) and (13) are dimensionless difference equations with respect to  $\alpha_{12}$  and  $\alpha_{23}$ , which reveals the coupling property of the system when the vibrating system operates at the steady state.

### 1.4 Stability Criterion

In this study, neglecting the effect of system damping, the vibrating system is encountering not only gravitational forces but also the output torque of motors during the running process of the steady-state. Thereby, three co-rotating rotors system coupled with springs is a nonholonomic conservation system. According to Hamilton's principle, we obtain the following expression:

$$\int_0^{2\pi} \left[ \delta(T - V) + \sum_{i=1}^3 Q_i \delta q_i \right] d\varphi = 0, \quad (14)$$

where  $T, V, Q_i$  and  $q_i$  represent the total kinetic energy, the total potential energy, the generalized force, and the generalized coordinate of the system, respectively. From the model proposed in Fig. 1, we obtain the total kinetic energy of the system:

$$T = \frac{1}{2} m_0 (\dot{x}^2 + \dot{y}^2) + \frac{1}{2} J_0 \dot{\psi}^2 + T_z. \quad (15)$$

Here  $T_z$  is the sum of kinetic energy with three motors. Since their rotation speeds are identical to each other during the running process of the steady-state,  $T_z$  can be regarded as a constant. The total potential energy of the vibrating system can be written as:

$$V = \frac{1}{2} k_x x^2 + \frac{1}{2} k_y y^2 + \frac{1}{2} k_\psi \psi^2 + \frac{1}{2} k \Delta\alpha_1^2 + \frac{1}{2} k \Delta\alpha_2^2. \quad (16)$$

The Hamiltonian interaction of the system over one period can be written the following:

$$H = \int_0^T (T - V) dt = \int_0^{2\pi} (T - V) d\varphi. \quad (17)$$

As the model of three co-rotating rotors system has two degrees of freedoms (DOFs), we choose  $\Delta\alpha_{12}, \Delta\alpha_{23}$  to be a generalized coordinate. Three rotors are rotating with an equal velocity ( $\omega_m$ ) when the vibrating system operates at the steady state. Simultaneously, the values of  $\Delta\alpha_{12}$  and  $\Delta\alpha_{23}$  are approximately equal to a constant ( $\Delta\alpha_{12}^*$  and  $\Delta\alpha_{23}^*$ ). According to a mechanical system with integrity constraint, the system can be changed from one position to another under the action of conservative forces, and the movement of the system tends to be stable when its Hamiltonian interaction has a minimum. Therefore, a stability criterion of the system can be obtained in the form:

$$\frac{\partial^2 H}{\partial \Delta \alpha_{12}^2} > 0, \quad \frac{\partial^2 H}{\partial \Delta \alpha_{12}^2} \cdot \frac{\partial^2 H}{\partial \Delta \alpha_{23}^2} - \left( \frac{\partial^2 H}{\partial \Delta \alpha_{12} \partial \Delta \alpha_{23}} \right)^2 > 0. \quad (18)$$

## 2 NUMERICAL DISCUSSION

Some theoretical results with regard to synchronous conditions and stability criteria for the three co-rotating rotors system coupled with springs are described in the preceding section. From Eqs. (12), (13) and (18), it can be seen that the synchronous state of the system is mainly determined by the positional parameters of three motors, the stiffness coefficient of the coupling springs, the frequency ratio, the total mass of the system, etc. To deeply grasp the influence of various factors on the synchronous state

of the system, some numerical analyses for solving Eqs. (12) and (13) under the conditions of Eq. (18) are performed to analyse the influence of positional parameters of the three motors and the frequency ratio on the synchronous characteristic of the vibrating system.

When the vibrating system operates at the steady state, the synchronization state of the system is defined as follows: the phase difference of rotors is always close to  $(-\pi/2, \pi/2)$  or  $(-90^\circ, 90^\circ)$ , the vibrating system is called the in-phase synchronization. Also, the phase difference of rotors is always close to  $(\pi/2, 3\pi/2)$  or  $(90^\circ, 270^\circ)$ ; the system is called the anti-phase synchronization. Considering installation angle  $\beta$  of motors are set as  $15^\circ, 30^\circ, 42^\circ, 60^\circ$ , respectively, and the influence of stiffness coefficient

**Table 1.** The structural parameters of the vibrating system in engineering

unbalanced rotors ( $i=1, 2, 3$ )	a rigid frame	motor	coupling springs
	$M = 90 \text{ kg}$		
	$J = 6.8 \text{ kg}\cdot\text{m}^2$		
$m_i = 2 \text{ kg}$	$k_x = 8 \times 10^4 \text{ N/m}, 6.6 \times 10^6 \text{ N/m}$	$l_1 = 0.35 \text{ m}, 0.52 \text{ m}, 0.64 \text{ m}, 0.85 \text{ m}$	
$r = 0.04 \text{ m}$	$k_y = 8 \times 10^4 \text{ N/m}, 6.6 \times 10^6 \text{ N/m}$	$l_2 = 0.12 \text{ m}, 0.18 \text{ m}, 0.22 \text{ m}, 0.30 \text{ m}$	$k = 1 \sim 4.2 \times 10^4 \text{ N/m}$
$\omega_m = 157 \text{ rad/s}$	$k_\psi = 6 \times 10^3 \text{ N/m}, 4.96 \times 10^5 \text{ N/m}$	$l_3 = 0.35 \text{ m}, 0.52 \text{ m}, 0.64 \text{ m}, 0.85 \text{ m}$	$a = 0.02 \text{ m}$
$f_i = 0.02 \text{ N}\cdot\text{s/m}$	$f_x = 1000 \text{ N}\cdot\text{s/m}$	$\beta_1 = 160^\circ, 78^\circ, 20^\circ$	
	$f_y = 1000 \text{ N}\cdot\text{s/m}$		
	$f_\psi = 1000 \text{ N}\cdot\text{s/m}$		

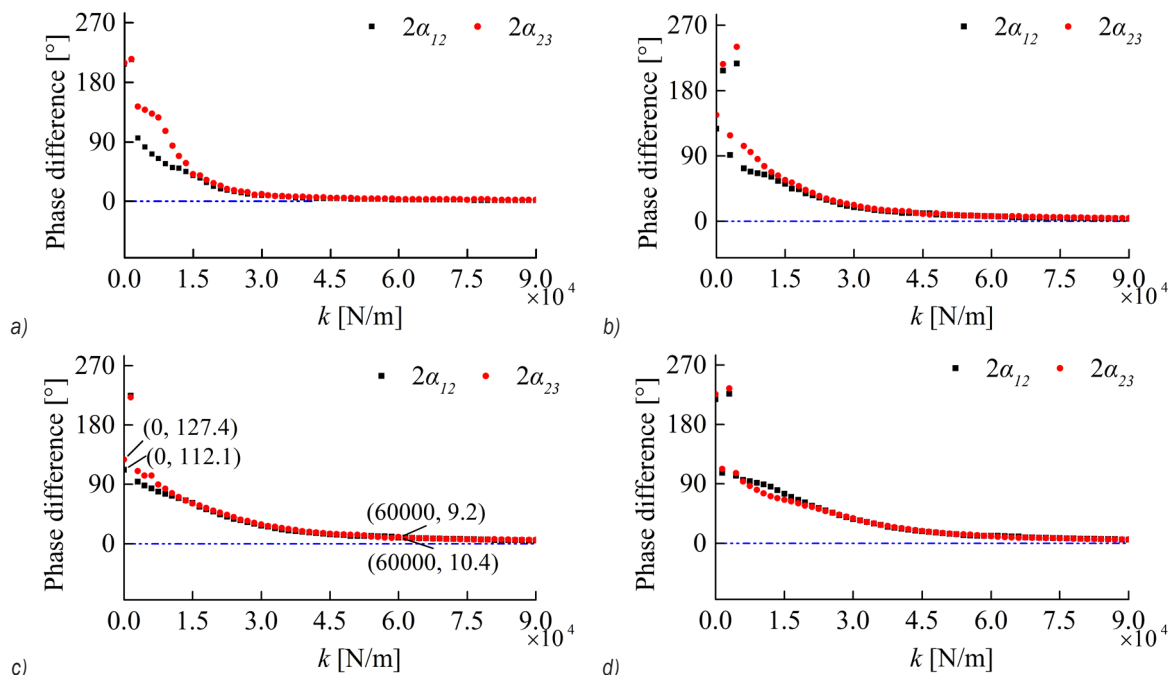


**Fig. 2.** Installation angle of motors and stiffness coefficient of the coupling springs are major influences on the dynamic characteristics; a)  $\beta = 15^\circ$ , b)  $\beta = 30^\circ$ , c)  $\beta = 42^\circ$ , and d)  $\beta = 60^\circ$

of the coupling springs on the synchronization state is presented in Fig. 2. When  $k=0$ , meaning that there is no coupling springs among these rotors, the phase differences between  $2\alpha_{12}$  and  $2\alpha_{23}$  consistently tend

towards anti-phase synchronization. From Fig. 2c, it can be found that the values of  $2\alpha_{12}$  and  $2\alpha_{23}$  are equal to  $127.4^\circ$  and  $112.1^\circ$ , respectively, when  $\beta=42^\circ$ . For the coupling springs with a small coefficient,

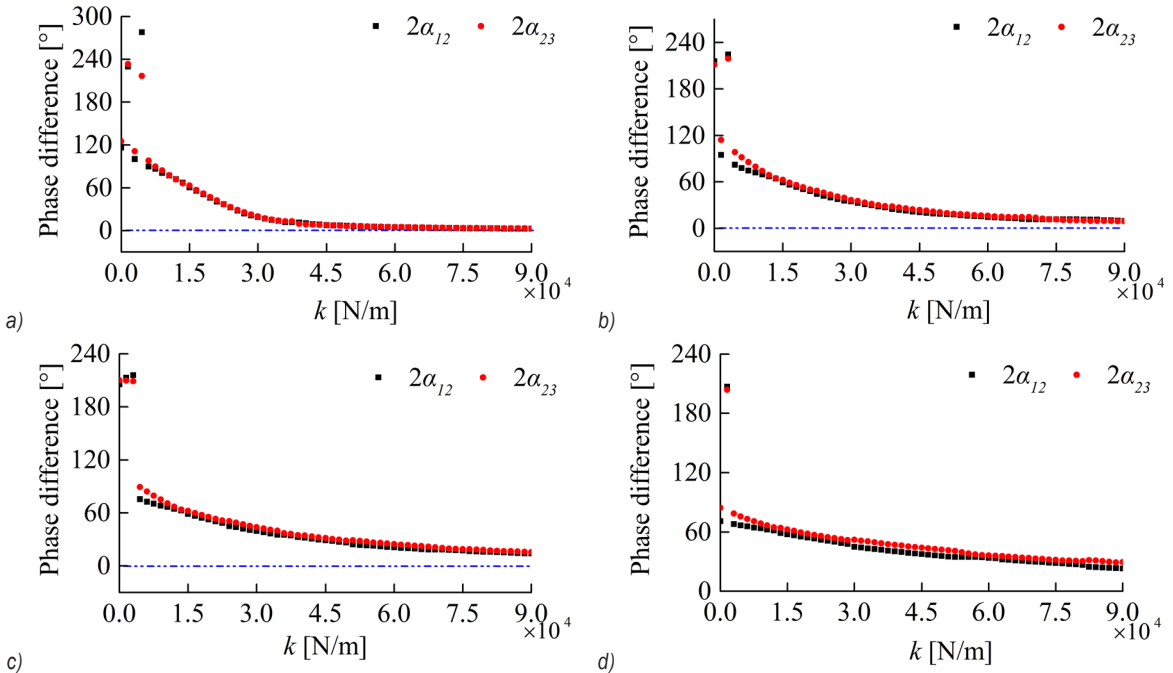


**Fig. 3.** Installation distance of motors and stiffness coefficient of the coupling springs are major influences on the dynamic characteristics; a)  $l = 0.32$  m, b)  $l = 0.64$  m, c)  $l = 0.85$  m, and d)  $l = 1.28$  m

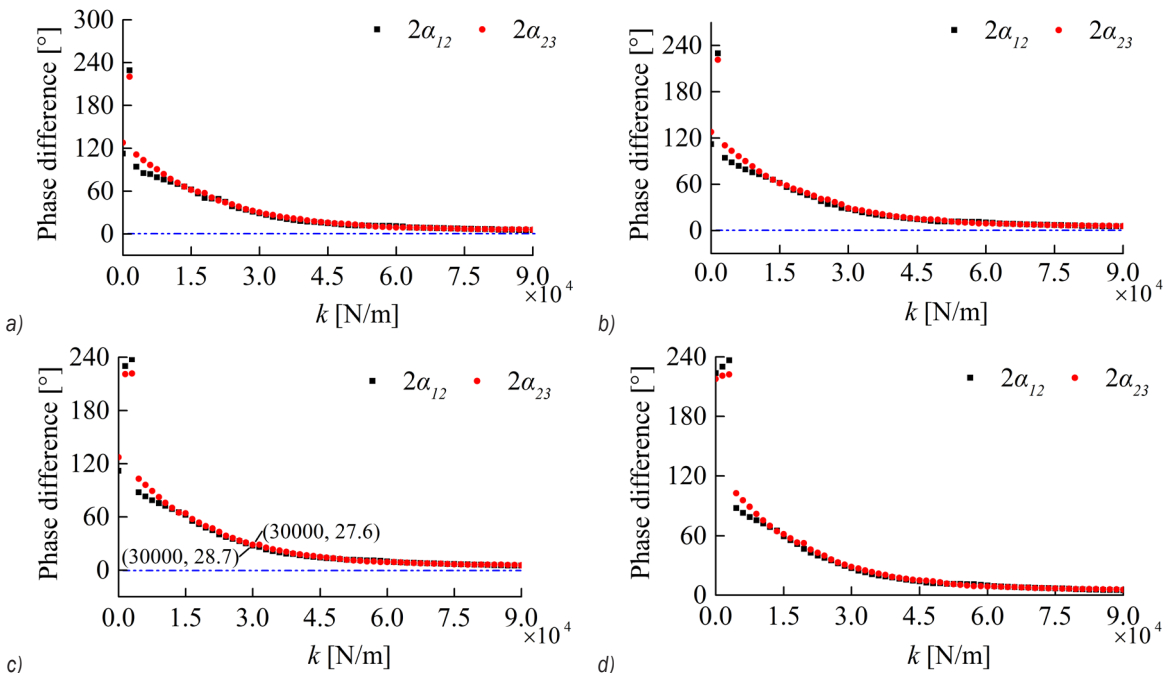


**Fig. 4.** Frequency ratio and stiffness coefficient of the coupling springs are major influences on the dynamic characteristics; a)  $n_j = 4.47$ , b)  $n_j = 5$ , c)  $n_j = 6.8$ , and d)  $n_j = 8.95$

their elastic force has no influence on synchronous characteristic of the vibrating system. However, with the increasing of  $k$  over a critical value, the phase differences between each pair of the rotors gradually stabilize at zero. Accordingly, the synchronous state of the system is suddenly changed from anti-phase synchronization to the in-phase synchronization. Moreover, from the contrasting results shown in Fig. 2, it is also demonstrated that the installation angles of the three motors have significantly impacted the synchronous behaviour of the vibrating system.

We assume that  $\beta = 42^\circ$  and the value of  $l$  is equal to 0.32 m, 0.64 m, 0.85 m, 1.28 m, respectively. The influences of the stiffness coefficient of the coupling springs on synchronization state are illustrated in Fig. 3. Compared with numerical results with different installation distances, the parameter  $l$  has an appreciable effect on the synchronous behaviour of the vibrating system when  $k = 0$ . In addition, anti-phase synchronization occurs for the coupling springs with a small coefficient. However, with the increasing  $k$  over a critical value, the phase differences between each pair of the rotors gradually stabilize at zero. Accordingly, it can be concluded that the changing trends closing to zero are different when three motors are installed in different locations.

Fig. 4 shows that the stiffness coefficient of the coupling springs is a major influence on the dynamic characteristics of the vibrating system under the conditions of different frequency ratios. It can be concluded that the frequency ratio of the system has no influence on synchronous behaviour. However, for different frequency ratios, the changing rule of phase difference with changing of stiffness coefficient of the coupling springs in the steady state are consistent with those preceding conclusions in Figs. 2 and 3.

### 3 SIMULATION VERIFICATION

Based on the dynamics Eq. (1), a simulation model with three co-rotating rotors system coupled with springs is established by means of the Runge–Kutta algorithm with adaptive control. The relationships between the synchronization state of the system and their mechanical-electrical coupling characteristics are investigated, and further analysis results are employed to verify the correctness of theoretical derivation and numerical analysis. Simulation parameters are identical with numerical results in Table 1.

#### 3.1 Dynamic Characteristics for $k = 0$ N/m, $l = 0.48$ m, and $n_j = 5.48$

Simulation results for  $n_j$  ( $j=x, y, \psi$ ) = 5.48,  $l = 0.48$  m,  $k = 0$  N/m are shown in Fig. 5. Here,  $k_x = 8 \times 10^4$  N/m,  $k_y = 8 \times 10^4$  N/m,  $k_\psi = 1.28 \times 10^4$  rad/m. The vibrating system is gradually changed from a desynchronyous state to synchronization for about 3 seconds, and the driving torques of three motors are changed near 3.9 N·m, 3.71 N·m, 3.71 N·m, respectively, as shown in Fig. 5(a). Moreover, three rotors are rotated with the same velocity 152.7 rad/s when the vibrating system operates at the steady state, the phase difference  $2\alpha_{12}$  between rotor 1 and rotor 2 is stabilized at  $-4.49$  rad ( $102.7^\circ \triangleq -4.49$  rad  $-2\pi$ ), and the phase difference  $2\alpha_{23}$  between rotor 2 and rotor 3 is stabilized at  $8.42$  rad ( $122.4^\circ \triangleq 8.42$  rad  $-2\pi$ ), as shown in Fig. 5f. Compared with numerical result of the corresponding parameter in Fig. 2c, the results show that simulation results are proven to be in good agreement with the numerical results. Figs. 5c, d and e show phase diagrams of the vibrating system in the DOFs. As seen from those diagrams, the rigid frame was not rapidly excited owing to its large mass during the initial process of the vibrating system, which caused the phase diagram of the mass centre of the system to be chaotic in the DOFs. The synchronous behaviour of the vibrating system is gradually implemented as the system kept running, the phase diagram of the mass centre of the system in the  $x$ - $y$  plane is a closed ellipse, and its amplitude in the DOFs is  $2.82 \times 10^{-3}$  m,  $2.8 \times 10^{-4}$  m,  $3.34 \times 10^{-4}$  rad, respectively, as schematically illustrated in Fig. 5g.

#### 3.2 Dynamic characteristics for $k = 60000$ N/m, $l = 0.48$ m, and $n_j = 5.48$

For the system parameters in Section 4.1, changing the value  $k = 60000$  N/m, and simulation results are shown in Fig. 6. When three motors are simultaneously provided with electromagnetic force, the synchronization phenomenon occurs after 4 seconds, and the rotational velocities of three motors are stabilized at 151.8 rad/s, as shown in Fig. 6b. As illustrated in Fig. 6a, the driving torque of three motors in synchronous state are 4.72 N·m, 4.4 N·m, 4.4 N·m, respectively. Figs. 6c, d and 6e show phase diagrams of the vibrating system in  $x$ -,  $y$ -, and  $\psi$ -directions, respectively. The results show that the phase diagram of the mass centre of the system is chaotic during the initial process of the vibrating system. Moreover, its phase diagram in the  $x$ - $y$  plane is a closed ellipse when the vibrating system operates

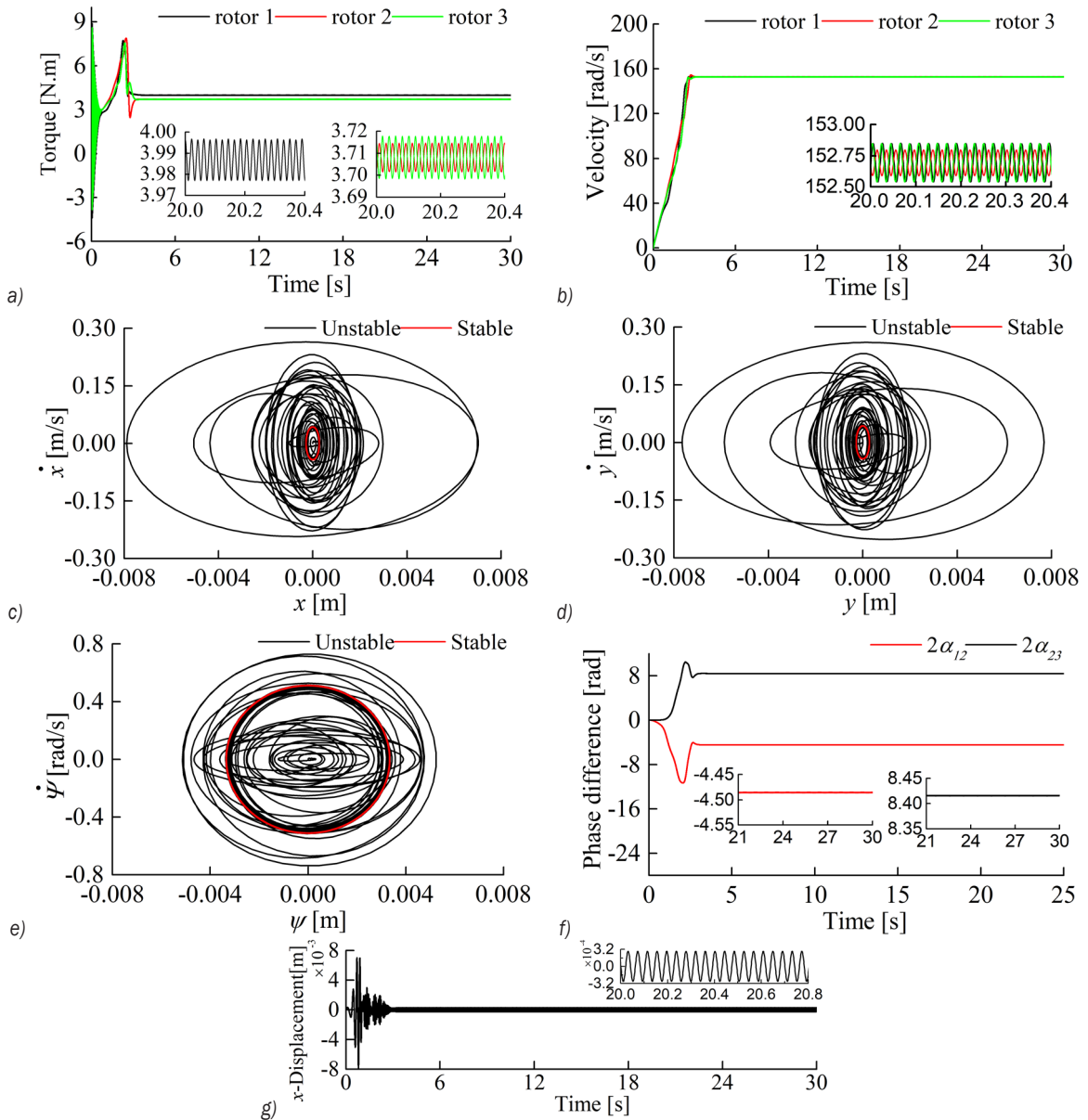


**Fig. 5.** Simulation results for  $k = 0 \text{ N/m}$ ,  $l = 0.48 \text{ m}$ ,  $n_j = 5.48$ ; a) driving torque of three motors, b) rotational velocity of three motors, c) phase diagram of the system in  $x$ -direction, d) phase diagram of the system in  $y$ -direction, e) phase diagram of the system in  $\psi$ -direction, f) phase difference of three motors, and g) displacement response of the rigid frame in  $x$ -,  $y$ -,  $\psi$ -directions, respectively

at the steady state. The value of  $2\alpha_{12}$  is approximately equal to  $0.194 \text{ rad}$  ( $11.1^\circ \triangleq 0.194 \text{ rad}$ ), and the value of  $2\alpha_{23}$  is approximately equal to  $0.181 \text{ rad}$  ( $10.4^\circ \triangleq 0.181 \text{ rad}$ ). By comparison, the simulation results are in good agreement with numerical results. Fig. 6g shows the amplitude of the mass centre of the system in a synchronous state, and its magnitudes are  $3.1 \times 10^{-3} \text{ m}$ ,  $3.1 \times 10^{-3} \text{ m}$ ,  $4.64 \times 10^{-3} \text{ rad}$ , respectively, as shown in Table 2. In addition, comparing simulation results in Figs. 5 and 6, it is demonstrated that

synchronous state of the system is significantly changed by those coupling springs among the rotors, which makes the system transit from anti-phase synchronization to the in-phase synchronization. Moreover, it can be seen that adjusting the value of the coupling spring stiffness can make the phase difference close to zero to meet the requirements of the strongly exciting designing large-sized and heavy-duty vibrating screens in engineering.

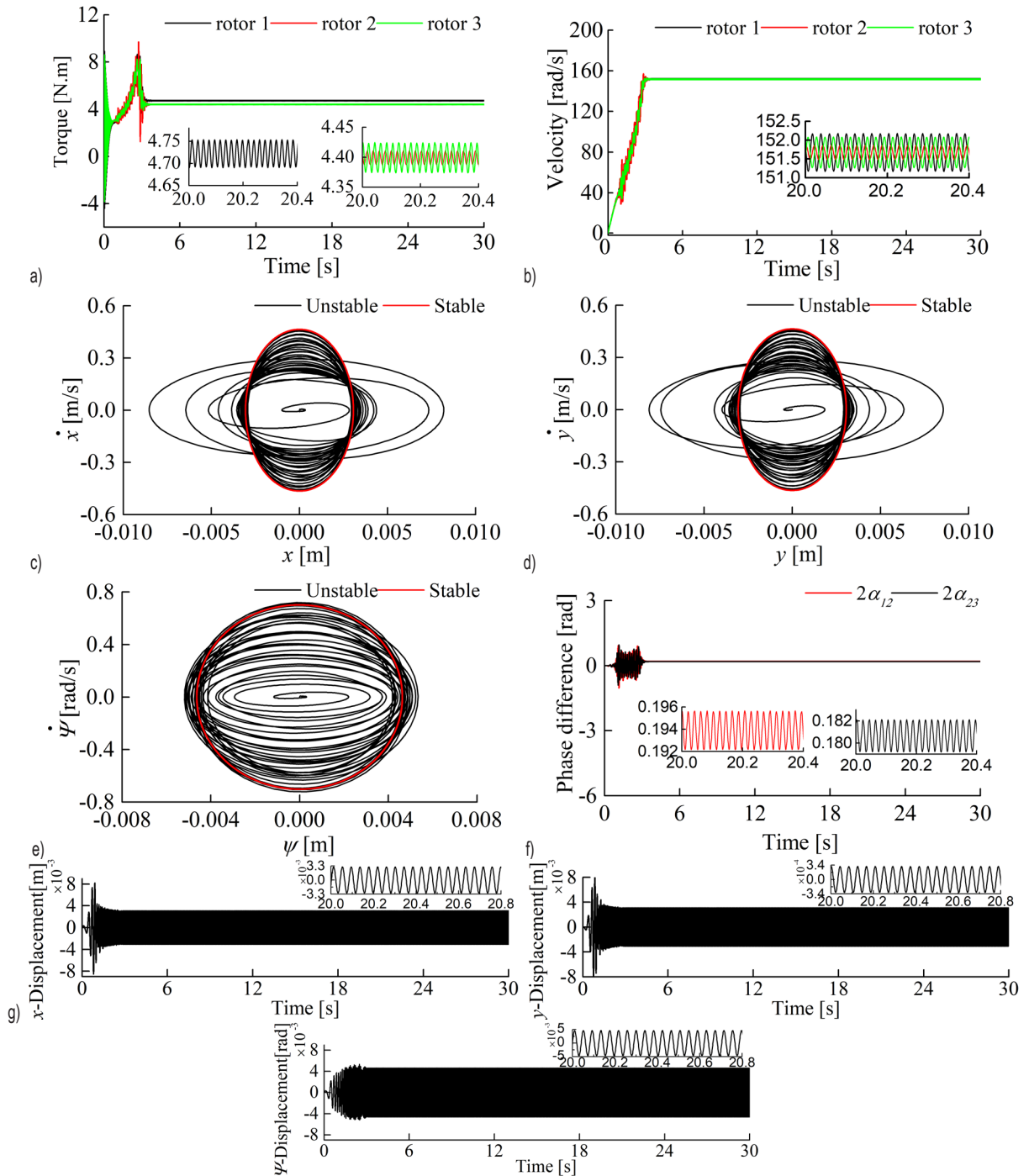


**Fig. 6.** Simulation results for  $k = 60000 \text{ N/m}$ ,  $l = 0.48 \text{ m}$ ,  $n_f = 5.48$ ; a) driving torque of three motors, b) rotational velocity of three motors, c) phase diagram of the system in  $x$ -direction, d) phase diagram of the system in  $y$ -direction, e) phase diagram of the system in  $\psi$ -direction, f) phase difference of three motors, and g) displacement response of the rigid frame in  $x$ -,  $y$ -,  $\psi$ -directions, respectively

**Table 2.** Displacement amplitude of the vibrating system with the changing of the stiffness of the coupling springs

	$x$ -direction [mm]	$y$ -direction [mm]	$\psi$ -direction [mm]
$k = 0$	2.82	0.28	3.34
$k = 60000$	3.1	3.1	4.64

**3.3 Dynamic Characteristics for  $k = 30000$  N/m,  $l = 0.48$  m, and  $n_j = 6.8$**

Fig. 7 presents results of a computer simulation in which  $k = 30000$  N/m,  $l = 0.48$  m,  $n_j = 6.8$ . Here,  $k_x =$

$k_y = 5.2 \times 10^4$  N/m,  $k_\psi = 8.32 \times 10^3$  rad/m. The synchronous velocity of three rotors is rotating at a speed of 152.5 rad/s while the vibrating system operates at the steady state, and their output torques are stabilized at 4.28 N·m, 3.99 N·m, 3.99 N·m,

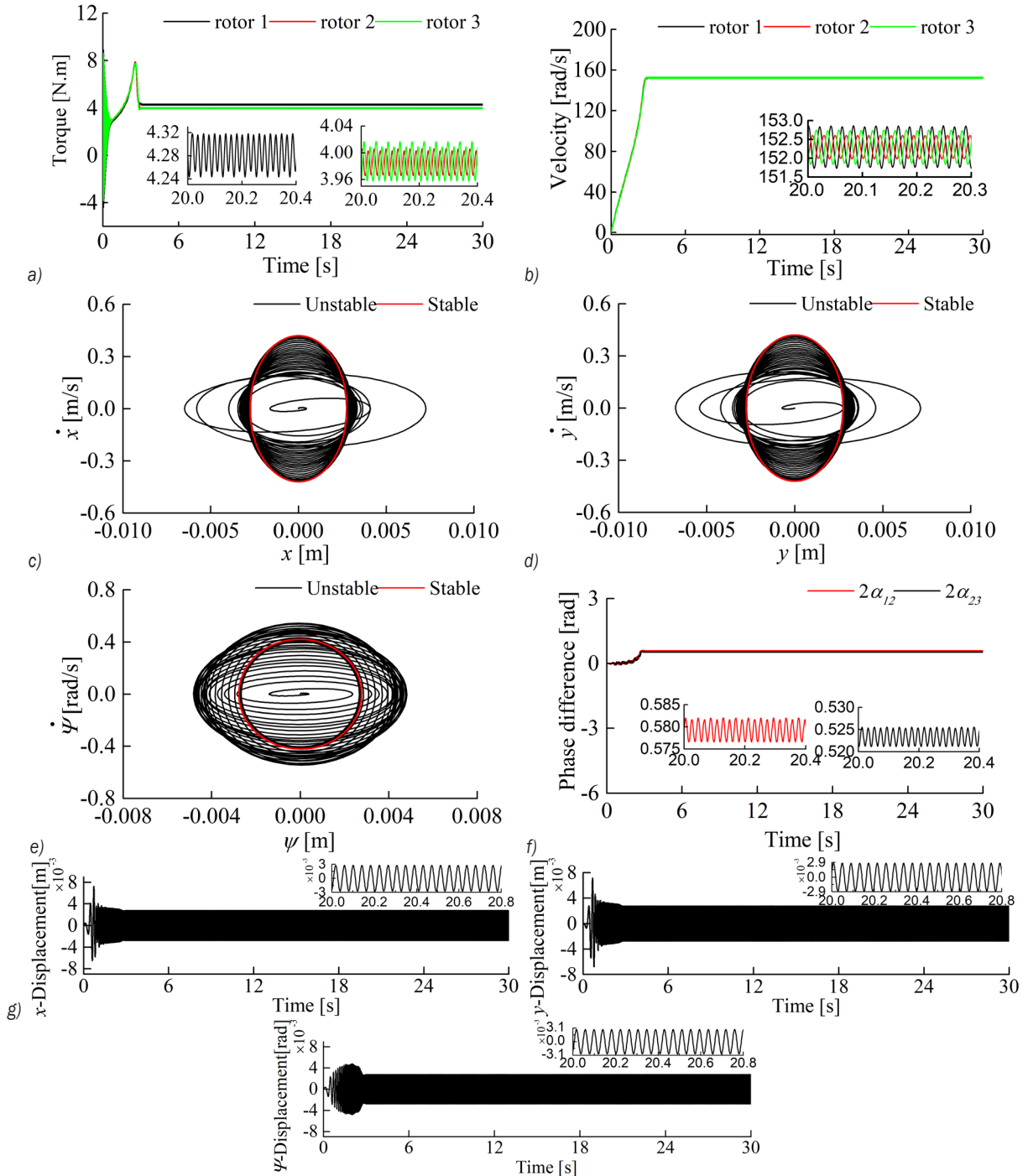


**Fig. 7.** Simulation results for  $k = 30000$  N/m,  $l = 6.8$  m,  $n_j = 5.48$ ; a) driving torque of three motors, b) rotational velocity of three motors, c) phase diagram of the system in  $x$ -direction, d) phase diagram of the system in  $y$ -direction, e) phase diagram of the system in  $\psi$ -direction, f) phase difference of three motors, and g) displacement response of the rigid frame in  $x$ -,  $y$ -,  $\psi$ -directions, respectively

respectively. The value of  $2\alpha_{12}$  is  $0.58 \text{ rad}$  ( $33.2^\circ \triangleq 0.58 \text{ rad}$ ), and the value of  $2\alpha_{23}$  is  $0.523 \text{ rad}$  ( $29.97^\circ \triangleq 0.523 \text{ rad}$ ). Thus, the simulation results are in good agreement with the numerical results discussed in Figs. 5 and 7. Fig. 7g shows the amplitude of the mass centre of the system in a synchronous state, and its magnitudes are  $3 \times 10^{-3} \text{ m}$ ,  $2.9 \times 10^{-3} \text{ m}$ ,  $3 \times 10^{-3} \text{ rad}$ , respectively.

#### 4 EXPERIMENTAL VERIFICATION

To validate the correctness of above-mentioned theory and numerical analysis, it is necessary to conduct some further corresponding experimental analyses. An experimental strategy with synchronous tests and dynamic tests of the vibrating system is introduced, which consists of high-speed imaging system and dynamic testing system. The experimental prototype, including induction motors (YZS-1.5-4), coupling springs, a rigid frame, an elastic foundation, four supporting springs, etc., are shown in Fig. 8. The motor performance parameters of YZS-1.5-4 are shown in Table 3. Two in-series springs in the coupling springs are always subjected to a changing force alternately in compression when the vibrating system operates at the steady state, which ensures that the three rotors rotating in the same directions are easy to achieve in-phase synchronization. The main parameters of the experimental prototypes are  $l_1 = 0.41 \text{ m}$ ,  $l_2 = 0.15 \text{ m}$ ,  $l_3 = 0.4 \text{ m}$ ,  $\beta_1 = 159^\circ$ ,  $\beta_2 = 83^\circ$ , and the other parameters are identical with Table 1. The location parameters of the four measuring points on the prototype are  $P_1(-0.45, -0.23)$ ,  $P_2(-0.22, -0.23)$ ,  $P_3(0.23, -0.23)$ ,  $P_4(0.46, -0.23)$ , respectively.

The dynamic testing results of three co-rotating rotors in a vibrating system are shown in Fig. 9. From the spectral analyses shown in Fig. 9a, it can be seen that the peak spectra of point  $P_2$  and point  $P_3$  in horizontal and vertical directions reaches a maximum when the system frequency is approximately equal to  $24.125 \text{ Hz}$ . Figs. 9b and c show acceleration of four measuring points in the horizontal and vertical directions. It can be concluded that their magnitudes are almost the same with a value  $24.4 \text{ m/s}^2$ . However, the phase constants of the acceleration with points 1 and 4 are different than points 2 and 3 in the horizontal direction, and both the magnitudes and phase constants of their acceleration are different in the vertical direction. Figs. 9d and e show the velocity of four measuring points in horizontal and vertical directions, and Figs. 9f, g, h, and i show the displacement of four measuring points in the horizontal and vertical directions, respectively. The motion trajectories of four measuring point in  $x$ - $o$ - $y$  plan are elliptical, as illustrated in Fig. 9j. However, its ovality and vibrating direction on the rigid frame are different, because both the magnitudes and phase constants of their displacements are different in the horizontal and vertical directions. In addition, some simulation results of corresponding experimental prototype are employed to verify the correctness of theoretical analysis based on Eq. (1). The comparison between the dynamic test results and the simulation results with the three co-rotating rotor system are given in Table 4. Those results show that the dynamic test results are proven to be in good agreement with simulation results, and all ranges of error for the

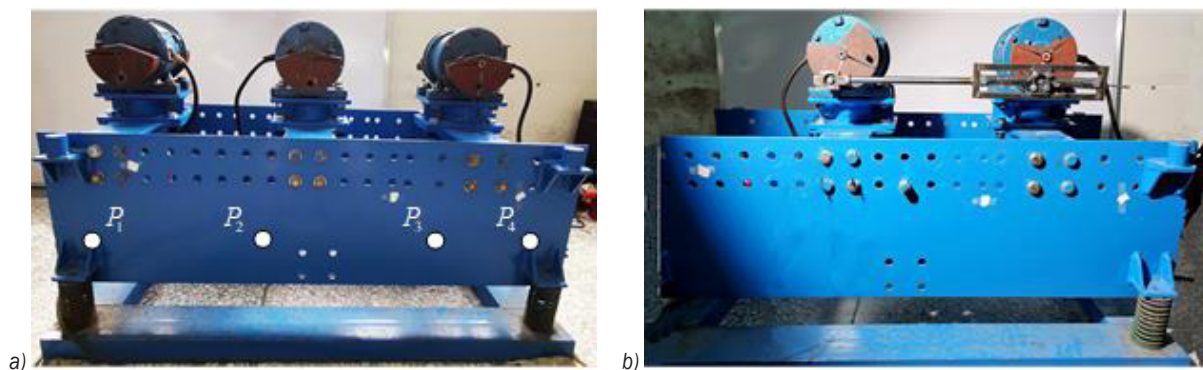
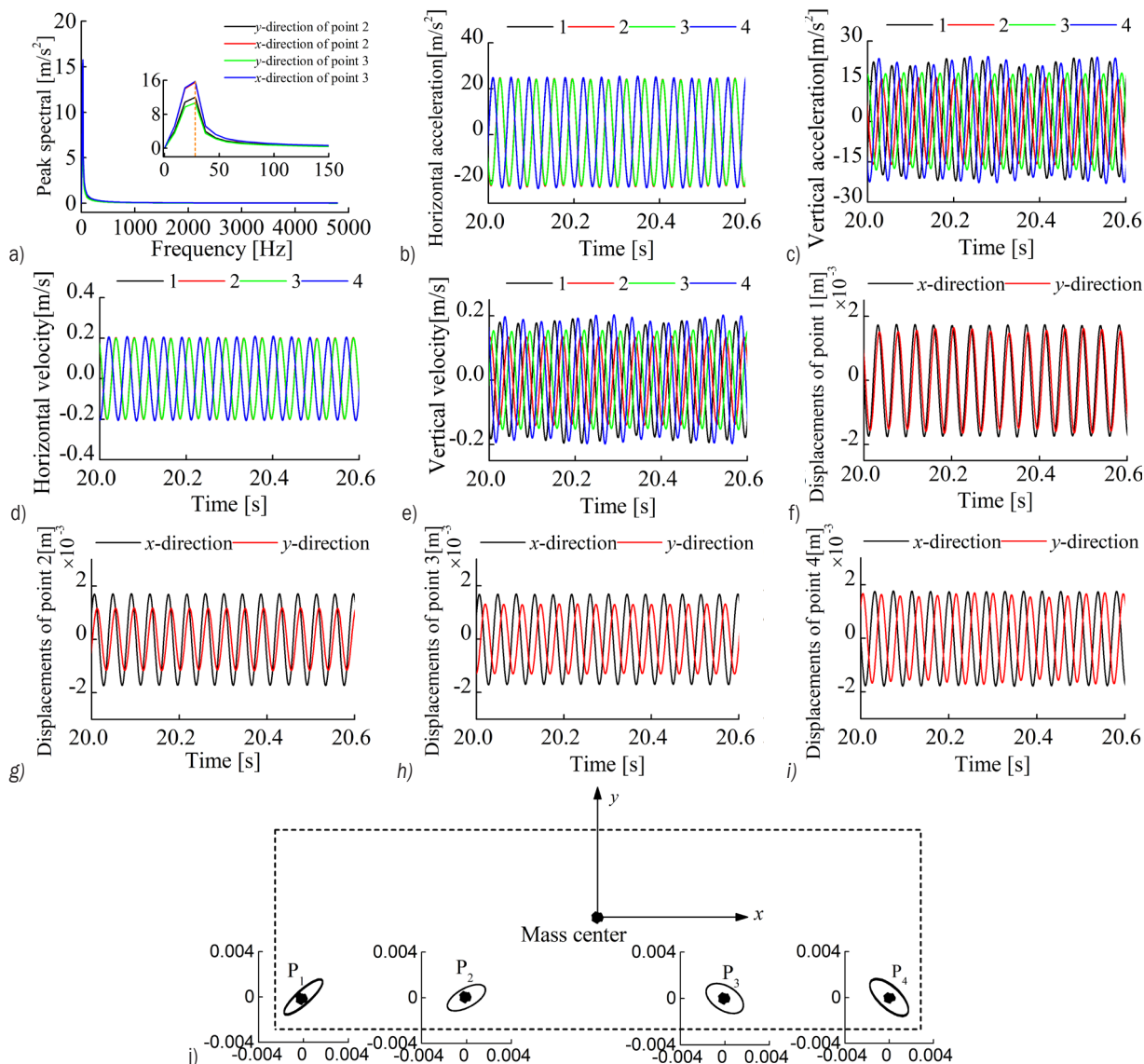


Fig. 8. Experimental prototypes; a) three co-rotating rotors in a vibrating system, b) two co-rotating rotors coupled with two in-series springs

Table 3. Parameters for vibration three-phase asynchronous motor (YZS-1.5-4)

Parameter	Voltage [V]	Power rating [Hz]	Output power [kW]	Current [A]	Frequency [r/min]	Exciting force [kN]	Weight [kg]
Value	380	50	0.12	0.36	1500	1.5	16



**Fig. 9.** Dynamic characteristics of three co-rotating rotors system; a) spectral analysis, b) horizontal accelerations of the measuring point, c) vertical accelerations of the measuring point, d) horizontal velocity of the measuring point, e) vertical velocity of the measuring point, f) displacements of the point 1, g) displacements of the point 2, h) displacements of the point 3, i) displacements of the point 4 and j) motion trail of the measuring point in x-o-y plane

**Table 4.** The amplitude comparison between the dynamic testing results and the simulation results with three co-rotating rotors system

	Results of dynamical testing		Results of dynamical simulation		Error value [%]	
	x-direction	y-direction	x-direction	y-direction	x-direction	y-direction
Measuring point $P_1$	0.0017	0.0016	0.0015	0.0018	11.8	11.1
Measuring point $P_2$	0.0017	0.0011	0.0014	0.0015	17.6	26.7
Measuring point $P_3$	0.0017	0.0013	0.0014	0.0013	17.6	0
Measuring point $P_4$	0.0018	0.0018	0.0015	0.0016	16.7	11.1

measuring-point in the vibrating body are within 30 %.

Fig. 10 shows the transient state of three co-rotating rotors at different moments. As can be seen

those diagrams, the value of  $\Delta\alpha_{12}$  is 3.56 rad, and the value of  $\Delta\alpha_{23}$  is 4.04 rad. It is concluded that the synchronous state of any two motors is in anti-phase synchronization when the vibrating system operates

at the steady state. Compared with the simulation results of corresponding experimental prototype, the simulation values of  $\Delta\alpha_{12}$  and  $\Delta\alpha_{23}$  are 3.46 rad, 3.47 rad, respectively, and their error of magnitudes are within 30 %, as shown in Table 5.

For the experimental prototype with two co-rotating rotors coupled with springs in a vibrating system, the testing results of dynamic characteristics are shown in Fig. 11. From Figs. 11a and b, it can be seen that the connecting springs with a stress state occurring periodically can be ensured the synchronous operation of the system, the magnitudes of acceleration of point  $P_2$  and point  $P_3$  in the horizontal direction are almost the same with a value 20 m/s<sup>2</sup>. However, the magnitudes of their acceleration in the

vertical direction are more different with values 44.1 m/s<sup>2</sup> and 19.3 m/s<sup>2</sup>, respectively. Integrating once and twice for the acceleration during the running process of the steady-state, respectively, we can obtain the velocity and displacement of point  $P_2$  and point  $P_3$  in horizontal and vertical directions, as shown in Figs. 11c to f.

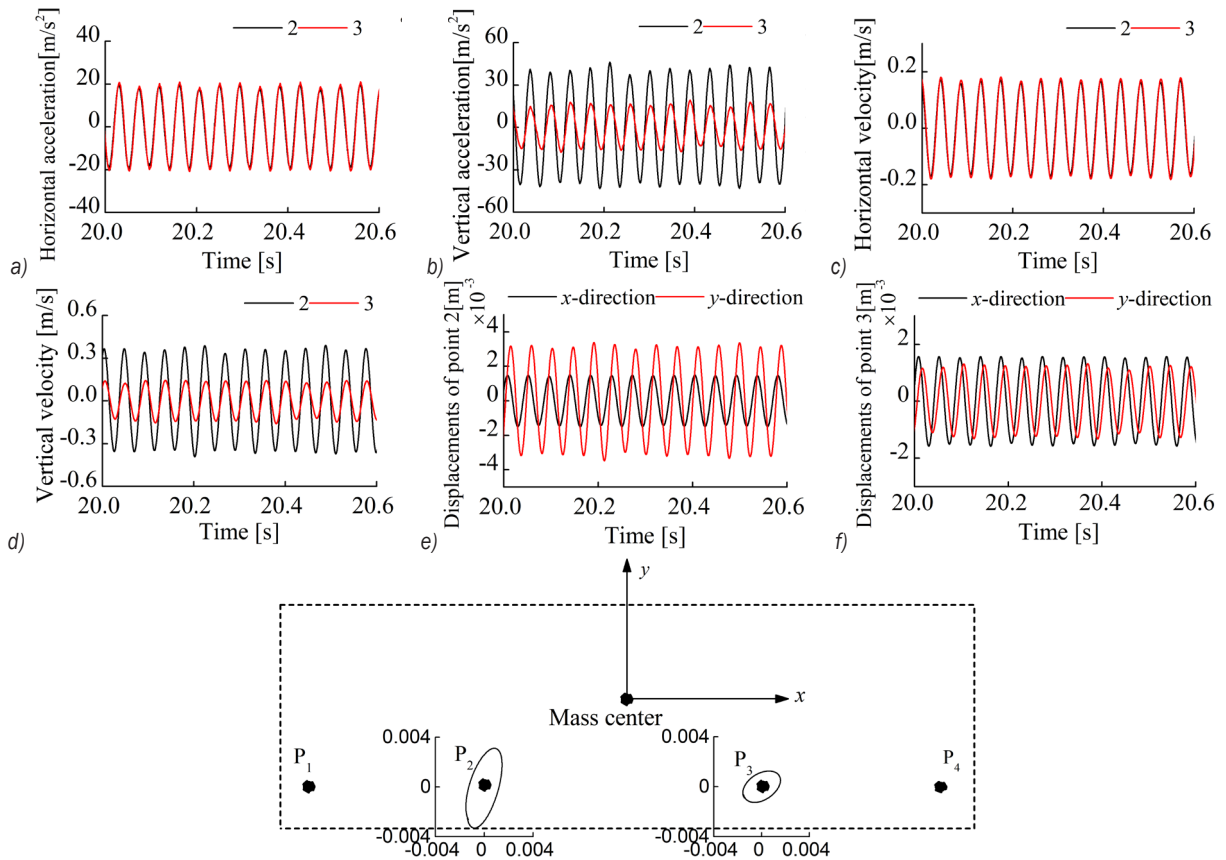
Moreover, comparing simulation results of corresponding parameters, it can be seen that the results of dynamic testing and simulation with two co-rotating rotors coupled with springs are in good agreement, as shown in Table 6. Fig. 11g shows the motion trajectories of point  $P_2$  and point  $P_3$  during the running process of the system; it is easily found that its motions are elliptically when the vibrating system



Fig. 10. Phase difference with three co-rotating rotors system

Table 5. The comparison between the testing value and the simulation value of phase difference with three co-rotating rotors system

	Experimental test results [rad]		The result of computer simulation [rad]		Error value [%]	
	$2\alpha_{12}$	$2\alpha_{23}$	$2\alpha_{12}$	$2\alpha_{23}$	$\Delta\alpha_{12}$	$\Delta\alpha_{23}$
Phase difference	$204^\circ \triangleq 3.56$	$-128.8^\circ \triangleq 4.04$	3.46	3.47	2.8	14.1



**Fig. 11.** Dynamic characteristics of two co-rotating rotors coupled with springs in a vibrating system; a) horizontal accelerations of the measuring point, b) vertical accelerations of the measuring point, c) horizontal velocity of the measuring point, d) vertical velocity of the measuring point, e) displacements of the point 2, f) displacements of the point 3, and g) motion trail of the measuring point in x-o-y plane

**Table 6.** The amplitude comparison between the dynamic testing results and the simulation results with two co-rotating rotors coupled with springs in a vibrating system

	Results of dynamical testing		Results of dynamical simulation		Error value [%]	
	x-direction	y-direction	x-direction	y-direction	x-direction	y-direction
Measuring point $P_2$	0.0017	0.0016	0.0021	0.0015	19	23.8
Measuring point $P_3$	0.0032	0.0014	0.0027	0.0018	15.6	22.2

operates at the steady state. However their ovality and vibrating direction on the rigid frame are different.

As can be seen from Fig. 12, the transient state of two co-rotating rotors coupled with springs are presented with an experimental test. Moreover, its comparison between the testing value and the simulation value of phase difference are listed in Table 7. It can be seen that the in-phase synchronization of two co-rotating rotors coupled with springs is easy to implement by the springs suffering from the stress state and unstressed state periodically and alternately. That is to say, the coupling springs can make the phase difference between the three rotors close to zero during the running process of the steady-state. The

experimental results are in good agreement with the simulation results in the vibrating system.

## 5 CONCLUSION

In this work, a vibrating mechanism of three co-rotating rotors system coupled with springs in a non-resonance system is proposed to design large-sized and heavy-duty vibrating screens. The paper is focused on the research of theoretical derivation, numerical analysis, computer simulations, and experimental verification. The conclusions are as follows:

1. For the coupling springs with a small stiffness  $k$ , the springs have little influence on the

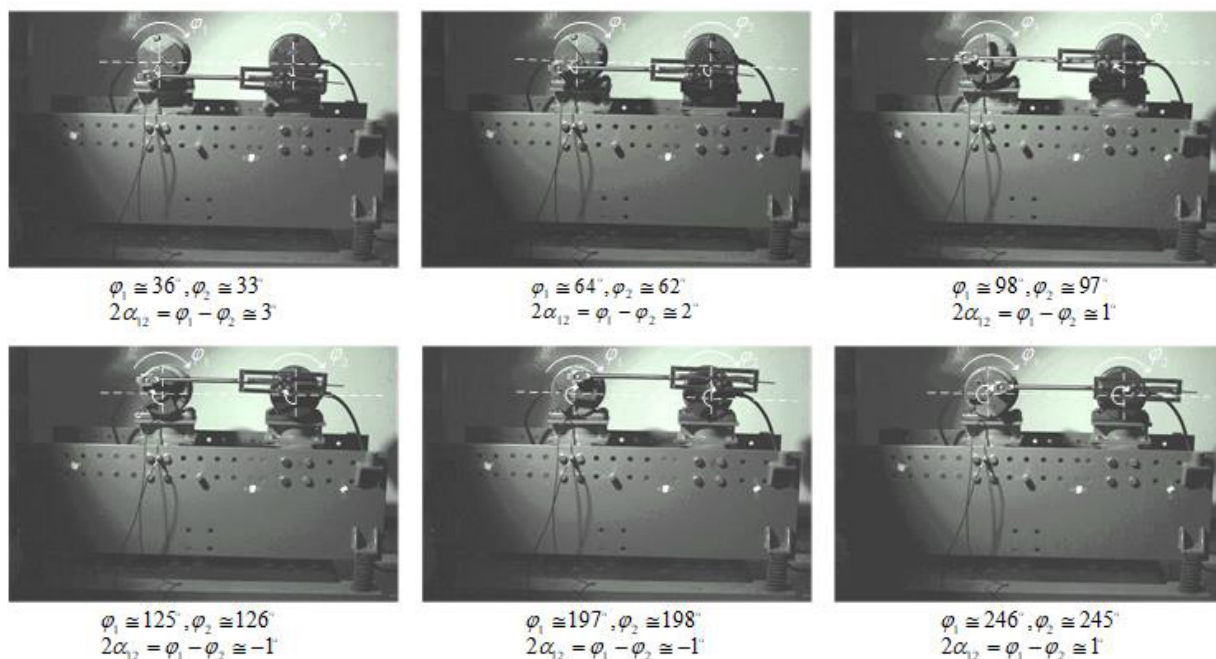


Fig. 12. Phase difference with two co-rotating rotors coupled with springs in a vibrating system

Table 7. The comparison between the testing value and the simulation value of phase difference with two co-rotating rotors coupled with springs in a vibrating system

	The results of the indirect experimental tests	The result of computer simulation	Error value
Phase difference $2\alpha_{12}$	$0.67^\circ \triangleq 0.012 \text{ rad}$	$0.75^\circ \triangleq 0.013 \text{ rad}$	7.7 %

synchronization characteristics of the vibrating system. Moreover, the synchronous state of motors is always maintained in anti-phase synchronization. However, with the increasing  $k$  over a critical value, the phase difference among each two rotors gradually stabilizes at zero. Accordingly, the synchronous state of the system is changed from anti-phase synchronization to in-phase synchronization. Additionally, it can be concluded that the frequency ratio of the system has little influence on synchronous behaviour, but the synchronous state of the system is influenced by positional parameters of three motors, stiffness coefficient of the coupling springs.

- An electromechanical coupled dynamic model of three co-rotating rotors system coupled with springs is established based on the Runge–Kutta algorithm with adaptive control. The relationships between the synchronization state of the system and their mechanical-electrical coupling characteristics are investigated. It can be found that the coupling springs with a large enough stiffness can make the phase difference among the three rotors close to zero during the

running process of the steady-state. Finally, an experimental prototype including synchronous tests and dynamic tests of the vibrating system is designed to prove to be in good agreement with theory and numerical analysis results.

- The presented model in this paper can be applied to large-sized and heavy-duty vibrating screens, which can promote the rapid development of new drilling technology and the DFSS towards high capacity, high efficiency, low noise, intelligent, energy-saving, environmental protection, etc.

## 6 ACKNOWLEDGEMENTS

This research was supported by Chengdu International Science and Technology Cooperation Project [No. 2019-GH02-00035-HZ].

## 7 NOMENCLATURES

- $m_i$  mass of the rotor  $i, i=1,2,3$ , [kg]
- $m_0$  mass of the rigid frame, [kg]
- $r_i$  eccentric radius of the rotor  $i, i=1,2,3$ , [m]
- $r_0$  a standard radius, [m]

- $\varphi_i$  angular displacement of the rotor  $i$ ,  $i=1,2,3$ , [rad]
- $\beta_i$  installation angle of the rotor  $i$ ,  $i=1,2,3$ , [°]
- $l_i$  distance from centre of mass to the rotor  $i$ ,  $i=1,2,3$ , [m]
- $J_i$  rotational inertia of the motor  $i$ ,  $i=1,2,3$ , [kg·m<sup>2</sup>]
- $f_i$  damping coefficient of motor  $i$ ,  $i=1,2,3$ , [N·s/m]
- $M$  the total mass of the vibrating system,  $M = m_0 + \sum_1^3 m_i$ , [kg]
- $J$  rotational inertia of the vibrating system,  $J = J_0 + \sum_1^3 m_i l_i^2 + \sum_1^3 m_i r_i^2$ , [kg·m<sup>2</sup>]
- $f_j$  damping constant of the vibrating system in  $j$ -direction,  $j=x,y,\psi$ , [N·s/m]
- $k_j$  stiffness of four supporting spring in  $j$ -direction,  $j=x,y,\psi$ , [N/m]
- $k$  stiffness coefficient of the connecting spring, [N/m]
- $a$  distance between the rotating centre of motor  $i$  and the end of coupling springs, [m]
- $\alpha_{12}$  phase differences between motor 1 and motor 2, [°]
- $\alpha_{23}$  phase differences between motor 2 and motor 3, [°]
- $\varepsilon_i$  instantaneous change coefficients,  $i=1,2,3$
- $\zeta_0, \zeta_{12}, \zeta_{23}$  coefficients of the instantaneous change with  $\omega_m$ ,  $\alpha_{12}$  and  $\alpha_{23}$ ,
- $\zeta_x, \zeta_y, \zeta_\psi$  damping coefficient of the vibrating system in  $j$ -direction,  $j=x,y,\psi$ ,  $\zeta_x = f_x / (2\omega_{nx} M)$ ,  $\zeta_y = f_y / (2\omega_{ny} M)$ ,  $\zeta_\psi = f_\psi / (2\omega_{n\psi} M)$ ,
- $\omega_{nj}$  natural frequency of the vibrating system in  $j$ -direction,  $j=x,y,\psi$ ,  $\omega_{nx} = \sqrt{k_x / M}$ ,  $\omega_{ny} = \sqrt{k_y / M}$ ,  $\omega_{n\psi} = \sqrt{k_\psi / M}$ , [rad/s]
- $r_m$  dimensionless parameters,  $r_m = m_0 / M$ ,  $i=1,2,3$ ,
- $l_e$  dimensionless parameters,  $l_e = \sqrt{J / M}$ ,  $i=1,2,3$ ,
- $r_{li}$  dimensionless parameters,  $r_{li} = l_i / l_e$ ,  $i=1,2,3$ ,
- $r_{ri}$  dimensionless parameters,  $r_{ri} = r_i / r_0$ ,  $i=1,2,3$ ,
- $\eta_i$  dimensionless parameters,  $\eta_i = m_i / m_0$ ,  $i=1,2,3$ ,
- $n_j$  frequency ratio in in  $j$ -direction,  $j=x,y,\psi$ ,
- $T_{ei}$  driving torque of the rotor  $i$ ,  $i=1,2,3$ , [N·m]
- $T_{e0i}$  output torque of the rotor  $i$ ,  $i=1,2,3$ , [N·m]
- $\bar{k}_{e0i}$  scaling factor of electrical and mechanical damping,  $i=1,2,3$ ,
- $T$  total kinetic energy of the system, [J]
- $V$  total potential energy of the system, [J]
- $Q_i$  generalized force of the system
- $q_i$  generalized coordinate of the system
- $T_z$  the sum of kinetic energy with three motors, [J]
- $\langle \bar{\bullet} \rangle$  integrating over one period  $T$  of time,  $\langle \bar{\bullet} \rangle = \int_T^{t_0+T} (\bullet) dt$
- $(\dot{\bullet})$  The first derivative of time,  $d(\bullet)/dt$
- $(\ddot{\bullet})$  The second derivative of time,  $d^2(\bullet)/dt^2$

## 8 REFERENCES

- [1] Baragetti, S. (2015). Innovative structural solution for heavy loaded vibrating screens. *Minerals Engineering*, vol. 84, p. 15-26, DOI:10.1016/j.mineng.2015.09.011.
- [2] Dong, K., Esfandiary, A.H., Yu, A.B. (2017). Discrete particle simulation of particle flow and separation on a vibrating screen: Effect of aperture shape. *Powder Technology*, vol. 314, p. 195-202, DOI:10.1016/j.powtec.2016.11.004.
- [3] Dong, K.J., Yu, A.B. (2012). Numerical simulation of the particle flow and sieving behaviour on sieve bend/low head screen combination. *Minerals Engineering*, vol. 31, no. 4, p. 2-9, DOI:10.1016/j.mineng.2011.10.020.
- [4] Blekhman, I.I. (1988). *Synchronization in Science and Technology*. ASME Press, New York.
- [5] Blekhman, I.I., Sorokin, V.S. (2018). On a "deterministic" explanation of the stochastic resonance phenomenon. *Nonlinear Dynamics*, vol. 93, p. 767-778, DOI:10.1007/s11071-018-4225-y.
- [6] Blekhman, I.I., Sorokin, V.S. (2010). On the separation of fast and slow motions in mechanical systems with high-frequency modulation of the dissipation coefficient. *Journal of Sound and Vibration*, vol. 329, no. 23, p. 4936-4949, DOI:10.1016/j.jsv.2010.06.008.
- [7] Balthazar, J.M., Felix, J.L.P., Brasil, R.M.L.R.F. (2005). Some comments on the numerical simulation of self-synchronization of four non-ideal exciters. *Applied Mathematics & Computation*, vol. 164, no. 2, p. 615-625, DOI:10.1016/j.amc.2004.06.010.
- [8] Balthazar, J.M., Felix, J.L.P., Brasil, R.M.L.R.F. (2016). Short comments on self-synchronization of two non-ideal sources supported by a flexible portal frame structure. *Journal of Vibration and Control*, vol. 10, no. 12, p. 1739-1748, DOI:10.1177/1077546304041754.
- [9] Wen, B., Fan, J., Zhao, C., Xiong, W. (2012). *Vibratory and Controlled Synchronization Engineering*. Alpha Science, Paris.
- [10] Wen, B., Zhang, H., Liu, S., He, Q., Zhao, C. (2010). *Theory and Techniques of Vibrating Machinery and Their Applications*. Science Press, Beijing.
- [11] Zhang, X.L., Wen, B.C., Zhao, C.Y. (2013). Synchronization of three non-identical coupled exciters with the same rotating directions in a far-resonant vibrating system. *Journal of Sound and Vibration*, vol. 332, no. 9, p. 2300-2317, DOI:10.1016/j.jsv.2012.12.003.
- [12] Zhang, X., Wen, B., Zhao, C. (2014). Vibratory synchronization transmission of two exciters in a super-resonant vibrating system. *Journal of Mechanical Science and Technology*, vol. 28, p. 2049-2058, DOI:10.1007/s12206-014-0108-4.
- [13] Fang, P., Hou, Y.J. (2018). Synchronization characteristics of a rotor-pendula system in multiple coupling resonant systems. *Proceedings of the Institution of Mechanical Engineers, Part C: Journal of Mechanical Engineering Science*, vol. 232, no. 10, p. 1802-1822, DOI:10.1177/0954406217711468.
- [14] Fang, P., Hou, Y.J., Du, M.J. (2019). Synchronization behavior of triple-rotor-pendula system in a dual-superfar resonance system. *Proceedings of the Institution of Mechanical Engineers, Part C: Journal of Mechanical*

Engineering Science, vol. 233, no. 5, p. 1620-1640, DOI:10.1177/0954406218774585.

- [15] Chen, X., Kong, X., Liu, Y., Wen, B. (2016). Synchronization and coupling dynamic characteristics of a dual-rotors exciter. *Journal of Vibroengineering*, vol. 18, no. 5, p. 3318-3328, DOI:10.21595/jve.2016.16918.
- [16] Chen, X.Z., Kong, X.X., Zhang, X.L., Li, L.X., Wen, B.C. (2016). On the synchronization of two eccentric rotors with common rotational axis: Theory and experiment. *Shock and Vibration*, vol. 2016, art. ID 6973597, DOI:10.1155/2016/6973597.
- [17] Huang, Z.L., Song, G.Q., Li, Y.M., Sun, M.N. (2019). Synchronous control of two counter-rotating eccentric rotors in nonlinear coupling vibration system. *Mechanical Systems and Signal Processing*, vol. 114, p. 68-83, DOI:10.1016/j.ymssp.2018.05.006.
- [18] Huang, Z., Song, G., Zhang, Z., Zhang, X. (2019). Control synchronization of two nonidentical homodromy exciters in nonlinear coupled vibration system. *IEEE Access*, vol. 7, p. 109934-109944, DOI:10.1109/access.2019.2933033.
- [19] Kong, X.X., Chen, C.Z., Wen, B.C. (2018). Composite synchronization of three eccentric rotors driven by induction motors in a vibrating system. *Mechanical Systems and Signal Processing*, vol. 102, p. 158-179, DOI:10.1016/j.ymssp.2017.09.025.
- [20] Kong, X.X., Zhang, X.L., Chen, X.Z., Wen, B.C., Wang, B. (2016). Phase and speed synchronization control of four eccentric rotors driven by induction motors in a linear vibratory feeder with unknown time-varying load torques using adaptive sliding mode control algorithm. *Journal of Sound and Vibration*, vol. 370, p. 23-42, DOI:10.1016/j.jsv.2016.02.013.
- [21] Huang, Z.L., Li, Y.M., Song, G.Q., Zhang, X.L., Zhang, Z.C. (2019). Speed and phase adjacent cross-coupling synchronous control of multi-exciter in vibration system considering material influence. *IEEE Access*, vol. 7, p. 63204-63216, DOI:10.1109/Access.2019.2916983.
- [22] Zhang, X., Wen, B., Zhao, C. (2014). Vibratory synchronization and coupling dynamic characteristics of multiple unbalanced rotors on a mass-spring rigid base. *International Journal of Non-Linear Mechanics*, vol. 60, p. 1-8, DOI:10.1016/j.ijnonlinmec.2013.12.002.
- [23] Hou, Y. (2007). The synchronism theory of three motor self-synchronism exciting elliptical motion shaker. *Journal of Southwest Petroleum University*, vol. 29, p. 168-172.
- [24] Wang, C., Liu, J., Luo, Z. (2019). Suppression of self-excited vibrations in rotating machinery utilizing leaf springs. *Strojniški vestnik - Journal of Mechanical Engineering*, vol. 65, P. 599-608, DOI:10.5545/sv-jme.2019.6112.
- [25] Si, H., Cao, L., Li, P. (2020). Dynamic characteristics and stability prediction of steam turbine rotor based on mesh deformation. *Strojniški vestnik - Journal of Mechanical Engineering*, vol. 66, p. 164-174, DOI:10.5545/sv-jme.2019.6283.

### 9 APPENDIX

$$\rho_{11} = \frac{J_1}{m_0 r_0^2} + \frac{1}{2} \eta_1^2 r_1^2 W_{c1}, \quad \rho_{12} = \frac{J_2}{m_0 r_0^2} + \frac{1}{2} \eta_2 r_{r2} \eta_2 r_2 W_{c2}, \quad \rho_{13} = \frac{J_3}{m_0 r_0^2} + \frac{1}{2} \eta_3 r_{r3} \eta_3 r_3 W_{c3},$$

$$\chi'_{12} = \frac{1}{2} \eta_1 \eta_2 r_1 r_2 [W_{c12} \cos(\alpha_{12} + \theta_{c12}) - W_{s12} \sin(\alpha_{12} + \theta_{s12})], \quad \chi'_{13} = \frac{1}{2} \eta_1 \eta_3 r_1 r_3 [W_{c13} \cos(\alpha_{12} + \alpha_{23} + \theta_{c13}) - W_{s13} \sin(\alpha_{12} + \alpha_{23} + \theta_{s13})],$$

$$k_{11} = \frac{\bar{k}_{e01}}{m_0 r_0^2 \omega_m^2} + \frac{f_1}{m_0 r_0^2 \omega_m} + \eta_1^2 r_1^2 W_{s1}, \quad k_{22} = \frac{\bar{k}_{e02}}{m_0 r_0^2 \omega_m^2} + \frac{f_2}{m_0 r_0^2 \omega_m} + \eta_2^2 r_2^2 W_{s2}, \quad k_{33} = \frac{\bar{k}_{e03}}{m_0 r_0^2 \omega_m^2} + \frac{f_3}{m_0 r_0^2 \omega_m} + \eta_3 r_{r3} \eta_3 r_3 W_{s3},$$

$$\chi_{12} = \eta_1 r_1 \eta_2 r_2 [W_{c12} \sin(\alpha_{12} + \theta_{c12}) + W_{s12} \cos(\alpha_{12} + \theta_{s12})], \quad \chi_{13} = \eta_1 r_1 \eta_3 r_3 [W_{c13} \sin(\alpha_{12} + \alpha_{23} + \theta_{c13}) + W_{s13} \sin(\alpha_{12} + \alpha_{23} + \theta_{s13})],$$

$$\mu_1 = \frac{T_{e01}}{m_0 r_0^2 \omega_m} - \frac{f_1}{m_0 r_0^2} - \frac{1}{2} \eta_1 r_1 \eta_1 r_1 \omega_m W_{s1} - \frac{1}{2} \eta_1 r_1 \eta_2 r_2 \omega_m [W_{c12} \sin(\alpha_{12} + \theta_{c12}) + W_{s12} \cos(\alpha_{12} + \theta_{s12})]$$

$$- \frac{1}{2} \eta_1 r_1 \eta_3 r_3 \omega_m [W_{c13} \sin(\alpha_{12} + \alpha_{23} + \theta_{c13}) + W_{s13} \sin(\alpha_{12} + \alpha_{23} + \theta_{s13})] - \frac{ka^2}{m_0 r_0^2 \omega_m} \sin \alpha_{12} + \frac{F_1}{m_0 r_0^2},$$

$$\chi'_{21} = \frac{1}{2} \eta_2 r_2 \eta_1 r_1 [W_{c12} \cos(\alpha_{12} + \theta_{c12}) + W_{s12} \sin(\alpha_{12} + \theta_{s12})], \quad \chi'_{23} = \frac{1}{2} \eta_2 r_2 \eta_3 r_3 [W_{c23} \cos(\alpha_{23} + \theta_{c23}) - W_{s23} \sin(\alpha_{23} + \theta_{s23})],$$

$$\chi_{21} = -\eta_2 r_2 \eta_1 r_1 [W_{c12} \sin(\alpha_{12} + \theta_{c12}) - W_{s12} \cos(\alpha_{12} + \theta_{s12})], \quad \chi_{23} = \eta_2 \eta_3 r_2 r_3 [W_{c23} \sin(\alpha_{23} + \theta_{c23}) + W_{s23} \cos(\alpha_{23} + \theta_{s23})],$$

$$\mu_2 = \frac{T_{e02}}{m_0 r_0^2 \omega_m} - \frac{f_2}{m_0 r_0^2} + \frac{1}{2} \eta_1 \eta_2 r_1 r_2 \omega_m [W_{c12} \sin(\alpha_{12} + \theta_{c12}) - W_{s12} \cos(\alpha_{12} + \theta_{s12})] - \frac{1}{2} \eta_2^2 r_2^2 \omega_m W_{s2}$$

$$- \frac{1}{2} \eta_2 \eta_3 r_2 r_3 \omega_m [W_{c23} \sin(\alpha_{23} + \theta_{c23}) + W_{s23} \cos(\alpha_{23} + \theta_{s23})] + \frac{ka^2}{m_0 r_0^2 \omega_m} (\sin \alpha_{12} - \sin \alpha_{23}) + \frac{F_2}{m_0 r_0^2},$$

$$\chi'_{31} = \frac{1}{2} \eta_3 r_3 \eta_1 r_1 [W_{c13} \cos(\alpha_{12} + \alpha_{23} + \theta_{c13}) + W_{s13} \sin(\alpha_{12} + \alpha_{23} + \theta_{s13})], \quad \chi'_{32} = \frac{1}{2} \eta_3 r_3 \eta_2 r_2 [W_{c23} \cos(\alpha_{23} + \theta_{c23}) + W_{s23} \sin(\alpha_{23} + \theta_{s23})],$$

$$\chi_{31} = -\eta_3 r_3 \eta_1 r_1 [W_{c13} \sin(\alpha_{12} + \alpha_{23} + \theta_{c13}) - W_{s13} \cos(\alpha_{12} + \alpha_{23} + \theta_{s13})], \quad \chi_{32} = -\eta_3 r_3 \eta_2 r_2 [W_{c23} \sin(\alpha_{23} + \theta_{c23}) - W_{s23} \cos(\alpha_{23} + \theta_{s23})],$$

$$\mu_3 = \frac{T_{e03}}{m_0 r_0^2 \omega_m} - \frac{f_3}{m_0 r_0^2} + \frac{1}{2} \eta_3 r_3 \eta_1 r_1 \omega_m [W_{c13} \sin(\alpha_{12} + \alpha_{23} + \theta_{c13}) - W_{s13} \cos(\alpha_{12} + \alpha_{23} + \theta_{s13})]$$

$$+ \frac{1}{2} \eta_3 r_3 \eta_2 r_2 \omega_m [W_{c23} \sin(\alpha_{23} + \theta_{c23}) - W_{s23} \cos(\alpha_{23} + \theta_{s23})] - \frac{1}{2} \eta_3 r_3 \eta_3 r_3 \omega_m W_{s3} + \frac{ka^2}{m_0 r_0^2 \omega_m} \sin \alpha_{23} + \frac{F_3}{m_0 r_0^2},$$

$$W_{c1} = r_m \left[ \mu_x \cos \gamma_x + \mu_y \cos \gamma_y + \mu_\psi r_{11}^2 \cos \gamma_\psi \right], \quad W_{c2} = r_m \left[ \mu_x \cos \gamma_x + \mu_y \cos \gamma_y + \mu_\psi r_{12}^2 \cos \gamma_\psi \right],$$

$$W_{c3} = r_m \left[ \mu_x \cos \gamma_x + \mu_y \cos \gamma_y + \mu_\psi r_{13}^2 \cos \gamma_\psi \right],$$

$$W_{s1} = r_m \left[ \mu_x \sin \gamma_x + \mu_y \sin \gamma_y + \mu_\psi r_{11}^2 \sin \gamma_\psi \right], \quad W_{s2} = r_m \left[ \mu_x \sin \gamma_x + \mu_y \sin \gamma_y + \mu_\psi r_{12}^2 \sin \gamma_\psi \right],$$

$$W_{s3} = r_m \left[ \mu_x \sin \gamma_x + \mu_y \sin \gamma_y + \mu_\psi r_{13}^2 \sin \gamma_\psi \right],$$

$$a_{s12} = \mu_x \sin \gamma_x + \mu_y \sin \gamma_y + \mu_\psi r_{11} r_{12} \sin \gamma_\psi \cos(\beta_1 - \beta_2), \quad b_{s12} = \mu_\psi r_{11} r_{12} \sin \gamma_\psi \sin(\beta_1 - \beta_2),$$

$$W_{s12} = r_m \sqrt{a_{s12}^2 + b_{s12}^2}, \quad \theta_{s12} = \begin{cases} \arctan(b_{s12}/a_{s12}) & a_{s12} \geq 0 \\ \pi + \arctan(b_{s12}/a_{s12}) & a_{s12} < 0 \end{cases}$$

$$a_{s13} = \mu_x \sin \gamma_x + \mu_y \sin \gamma_y + \mu_\psi r_{11} r_{13} \sin \gamma_\psi \cos(\beta_1 - \beta_3), \quad b_{s13} = \mu_\psi r_{11} r_{13} \sin \gamma_\psi \sin(\beta_1 - \beta_3),$$

$$W_{s13} = r_m \sqrt{a_{s13}^2 + b_{s13}^2}, \quad \theta_{s13} = \begin{cases} \arctan(b_{s13}/a_{s13}) & a_{s13} \geq 0 \\ \pi + \arctan(b_{s13}/a_{s13}) & a_{s13} < 0 \end{cases}$$

$$a_{s23} = \mu_x \sin \gamma_x + \mu_y \sin \gamma_y + \mu_\psi r_{12} r_{13} \sin \gamma_\psi \cos(\beta_2 - \beta_3), \quad b_{s23} = \mu_\psi r_{12} r_{13} \sin \gamma_\psi \sin(\beta_2 - \beta_3),$$

$$W_{s23} = r_m \sqrt{a_{s23}^2 + b_{s23}^2}, \quad \theta_{s23} = \begin{cases} \arctan(b_{s23}/a_{s23}) & a_{s23} \geq 0 \\ \pi + \arctan(b_{s23}/a_{s23}) & a_{s23} < 0 \end{cases}$$

$$a_{c12} = \mu_x \cos \gamma_x + \mu_y \cos \gamma_y + \mu_\psi r_{11} r_{12} \cos \gamma_\psi \cos(\beta_1 - \beta_2), \quad b_{c12} = \mu_\psi r_{11} r_{12} \cos \gamma_\psi \sin(\beta_1 - \beta_2)$$

$$W_{c12} = r_m \sqrt{a_{c12}^2 + b_{c12}^2}, \quad \theta_{c12} = \begin{cases} \arctan(b_{c12}/a_{c12}) & a_{c12} \geq 0 \\ \pi + \arctan(b_{c12}/a_{c12}) & a_{c12} < 0 \end{cases}$$

$$a_{c13} = \mu_x \cos \gamma_x + \mu_y \cos \gamma_y + \mu_\psi r_{11} r_{13} \cos \gamma_\psi \cos(\beta_1 - \beta_3), \quad b_{c13} = \mu_\psi r_{11} r_{13} \cos \gamma_\psi \sin(\beta_1 - \beta_3),$$

$$W_{c13} = r_m \sqrt{a_{c13}^2 + b_{c13}^2}, \quad \theta_{c13} = \begin{cases} \arctan(b_{c13}/a_{c13}) & a_{c13} \geq 0 \\ \pi + \arctan(b_{c13}/a_{c13}) & a_{c13} < 0 \end{cases}$$

$$a_{c23} = \mu_x \cos \gamma_x + \mu_y \cos \gamma_y + \mu_\psi r_{12} r_{13} \cos \gamma_\psi \cos(\beta_2 - \beta_3), \quad b_{c23} = \mu_\psi r_{12} r_{13} \cos \gamma_\psi \sin(\beta_2 - \beta_3),$$

$$W_{c23} = r_m \sqrt{a_{c23}^2 + b_{c23}^2}, \quad \theta_{c23} = \begin{cases} \arctan(b_{c23}/a_{c23}) & a_{c23} \geq 0 \\ \pi + \arctan(b_{c23}/a_{c23}) & a_{c23} < 0 \end{cases}$$

$$f_1(k, \varphi_1, \varphi_2, \varphi_3, \beta, l, a) = \frac{-a^2 \sin(\varphi_2 - \varphi_1) + la \cos \varphi_1 \cos \beta}{\sqrt{l^2 \cos^2 \beta + 2a^2 - 2a^2 \cos(\varphi_2 - \varphi_1) + 2la \sin \varphi_1 \cos \beta - 2la \sin \varphi_2 \cos \beta}},$$

$$f_2(k, \varphi_1, \varphi_2, \varphi_3, \beta, l, a) = \frac{a^2 \sin(\varphi_2 - \varphi_1) - la \cos \varphi_2 \cos \beta}{\sqrt{l^2 \cos^2 \beta + 2a^2 - 2a^2 \cos(\varphi_2 - \varphi_1) + 2la \sin \varphi_1 \cos \beta - 2la \sin \varphi_2 \cos \beta}}$$

$$+ \frac{-a^2 \sin(\varphi_3 - \varphi_2) + la \cos \varphi_2 \cos \beta}{\sqrt{l^2 \cos^2 \beta + 2a^2 - 2a^2 \cos(\varphi_3 - \varphi_2) + 2la \sin \varphi_2 \cos \beta - 2la \sin \varphi_3 \cos \beta}},$$

$$f_3(k, \varphi_1, \varphi_2, \varphi_3, \beta, l, a) = \frac{a^2 \sin(\varphi_3 - \varphi_2) - la \cos \varphi_3 \cos \beta}{\sqrt{l^2 \cos^2 \beta + 2a^2 - 2a^2 \cos(\varphi_3 - \varphi_2) + 2la \sin \varphi_2 \cos \beta - 2la \sin \varphi_3 \cos \beta}},$$

$$F_1 = \frac{1}{2\pi} \int_0^{2\pi} f_1(k, \varphi_1, \varphi_2, \varphi_3, \beta, l, a) d\varphi, \quad F_2 = \frac{1}{2\pi} \int_0^{2\pi} f_2(k, \varphi_1, \varphi_2, \varphi_3, \beta, l, a) d\varphi, \quad F_3 = \frac{1}{2\pi} \int_0^{2\pi} f_3(k, \varphi_1, \varphi_2, \varphi_3, \beta, l, a) d\varphi,$$

$$f_1(k, \varphi_1, \varphi_2, \varphi_3, \beta, l, a) = \frac{-a^2 \sin(\varphi_2 - \varphi_1) + la \cos \varphi_1 \cos \beta}{\sqrt{l^2 \cos^2 \beta + 2a^2 - 2a^2 \cos(\varphi_2 - \varphi_1) + 2la \sin \varphi_1 \cos \beta - 2la \sin \varphi_2 \cos \beta}},$$

$$f_2(k, \varphi_1, \varphi_2, \varphi_3, \beta, l, a) = \frac{a^2 \sin(\varphi_2 - \varphi_1) - la \cos \varphi_2 \cos \beta}{\sqrt{l^2 \cos^2 \beta + 2a^2 - 2a^2 \cos(\varphi_2 - \varphi_1) + 2la \sin \varphi_1 \cos \beta - 2la \sin \varphi_2 \cos \beta}}$$

$$+ \frac{-a^2 \sin(\varphi_3 - \varphi_2) + la \cos \varphi_2 \cos \beta}{\sqrt{l^2 \cos^2 \beta + 2a^2 - 2a^2 \cos(\varphi_3 - \varphi_2) + 2la \sin \varphi_2 \cos \beta - 2la \sin \varphi_3 \cos \beta}},$$

$$f_3(k, \varphi_1, \varphi_2, \varphi_3, \beta, l, a) = \frac{a^2 \sin(\varphi_3 - \varphi_2) - la \cos \varphi_3 \cos \beta}{\sqrt{l^2 \cos^2 \beta + 2a^2 - 2a^2 \cos(\varphi_3 - \varphi_2) + 2la \sin \varphi_2 \cos \beta - 2la \sin \varphi_3 \cos \beta}},$$

$$F_1 = \frac{1}{2\pi} \int_0^{2\pi} f_1(k, \varphi_1, \varphi_2, \varphi_3, \beta, l, a) d\varphi, \quad F_2 = \frac{1}{2\pi} \int_0^{2\pi} f_2(k, \varphi_1, \varphi_2, \varphi_3, \beta, l, a) d\varphi, \quad F_3 = \frac{1}{2\pi} \int_0^{2\pi} f_3(k, \varphi_1, \varphi_2, \varphi_3, \beta, l, a) d\varphi,$$

# Electro-Hydraulic Drive of the Variable Ratio Lifting Device under Active Load

Kosucki, A. – Stawiński, Ł. – Morawiec, A. – Goszczak, J.

Andrzej Kosucki<sup>1</sup> – Łukasz Stawiński<sup>1</sup> – Adrian Morawiec<sup>1</sup> – Jarosław Goszczak<sup>2</sup>

<sup>1</sup>Lodz University of Technology, Institute of Machine Tools and Production Engineering, Poland

<sup>2</sup>Lodz University of Technology, Department of Vehicles and Fundamentals of Machine Design, Poland

Hydraulic systems fed by fixed displacement pumps driven by frequency-controlled electric motors can replace conventional throttling systems due to their ability to control the speed of hydraulic cylinders regardless of the value and direction of the load. These systems can improve the energy efficiency of the drive or even provide the possibility of energy recuperation during lowering. This paper presents experimental studies of the new drive system with volumetric control of the speed of the lifted/lowered payload using the example of a scissor lift. The system uses a reversible gear pump driven by an asynchronous motor fed by a frequency inverter operating in field-oriented control mode. Comparative studies of the mapping of the assumed speed of the hydraulic cylinder and platform are presented, as well as studies of the influence of the load change on the speed and positioning of the mechanism driven by the open-loop controlled system.

**Keywords:** hydraulic drives, speed controlled pump, variable-ratio device, lifting system

## Highlights

- High-speed accuracy is achieved regardless of the load direction.
- The structure of the drive system is simplified compared to classic solutions.
- The system makes it possible to use volumetric control even for low-power and low-efficiency systems.
- Improving the energy efficiency of the drive is possible.

## 0 INTRODUCTION

Hydraulic excavators, elevators, wheel loaders, various forklifts, scissor lifts, and other mobile and stationary machinery use hydraulic lifting systems with hydraulic cylinders to drive the payload with throttling control during payload lowering. The lowering phase is usually caused by gravity. Generally, this requires the use of appropriate valves or complex control systems to protect the load against uncontrolled falling. The most common solution is to use a throttle valve. The typical hydrostatic lifting system, presented in Fig. 1, consists of a hydraulic power supply unit equipped with an oil tank assembly (3), the motor (1), the oil pump (2), and a set of valves, such as the pressure relief valve (4), the directional valve (5), the one-way throttling valve (6) and the rupture valves (7) screwed into the inlets of hydraulic cylinders (8).

The one-way throttling valve during the lowering payload operates as an adjustable choke in which the oil flow rate depends on a pressure drop between the inlet and outlet  $Dp_s$ , according to Eq. (1):

$$Q_D = A_D \cdot c_D \cdot \sqrt{\frac{2\Delta p_s}{\rho}}, \quad (1)$$

where  $A_D$  is the cross-sectional area of the valve orifice,  $c_D$  the coefficient of flow losses, and  $\rho$  the density of the hydraulic liquid.

Usually, the throttle valve is set to the defined value of the cross-sectional area of the orifice. When the hydraulic cylinder is loaded with a constant force, this results in a constant pressure under the piston and a constant lowering speed, according to Eq. (2):

$$v_s = \frac{dx_s}{dt} = \frac{Q_D}{\frac{\pi \cdot d_s^2}{4}}, \quad (2)$$

where  $x_s$  is the length of the hydraulic cylinder, and  $d_s$  the diameter of the hydraulic cylinder.

However, many mechanisms act on hydraulic cylinders with a variable force during their movement, which could be caused by a load change or a variable ratio of driven mechanisms. The changing force acting on the hydraulic cylinder causes the variable pressure under the piston. The higher the pressure, the greater the flow rate through the throttle valve, and thus the increase of the payload lowering speed. It happens when the mechanism ratio changes during the duty cycle (together with the extension/retraction of the hydraulic cylinder). Then the speed of the piston rod changes with the change of mechanism ratio, as shown in Fig. 2.

This type of drive has many disadvantages, such as heating the oil on the throttle valve during the lowering phase, resulting in the need to dissipate the potential energy. It could be then necessary to use oil coolers, which increases the cost of the system. The

dynamic overloads of the cylinder and mechanism appear caused by a directional valve that is rapidly opened (or closed) by a solenoid, which can lead to premature wear of the machine. The speed of payload lowering using the throttle valve is less controllable.

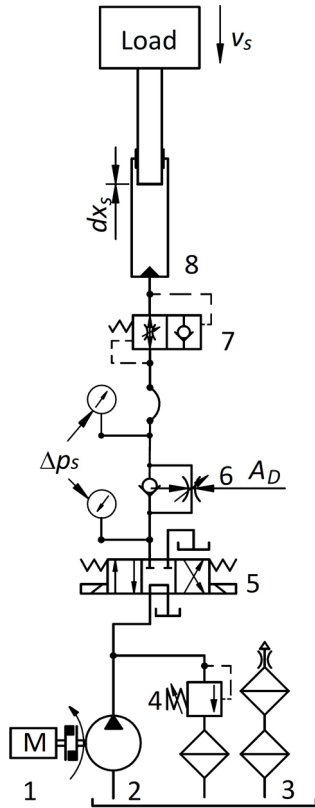


Fig. 1. Schematic of the conventional hydraulic lifting system

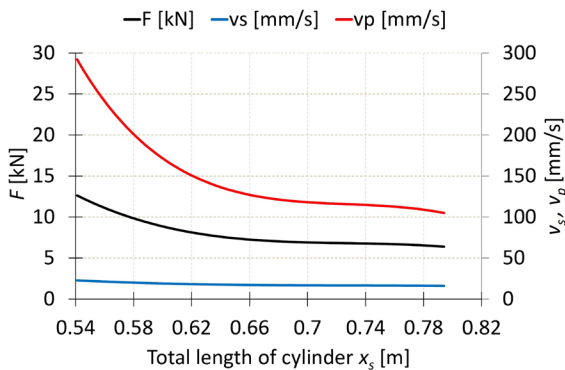


Fig. 2. The exemplary relationship between the speed of the piston rod  $v_s$ , the speed of the platform  $v_p$ , and its load  $F$  during lowering

In addition to systems with a throttle valve, other solutions are used in hydraulic systems to control hydraulic cylinders loaded with the active force. The review of the controllability of such systems

is described in [1]. These systems use variable displacement pumps, throttle valves, or proportional and servo valves. There are also special braking valves used in hydrostatic systems driving hydraulic cylinders with an active load, called counterbalance valves, described in [2]. In [3], variable hydraulic cylinder load (from passive to active) during one full cycle of motion was discussed. The author dealt with the subject of piston rod braking with the use of, among others, controlled check valves and various types of counterbalance valves. The principle of operation and the benefits of counterbalance valves, which are load holding, load control, and load safety, described in [4]. Incorrect application can lead to negative pressure or stoppage of operation of the device due to insufficient pressure difference. Problems that may occur in systems with counterbalance valves are described in [5]. The use of the right valve depends on the needs, which is why it is so important to know about the capabilities of a given element. A detailed division of counterbalance valves and their advantages and disadvantages are described in [6] and [7].

Counterbalance valves are used to control the movement of the actuator, usually with an active or variable load. Authors in [8] describe an approach that shifts the task of throttling the return flow from the counterbalance valve to the directional valve. The counterbalance valve can also be used to start and stop rotating parts smoothly. The controlled motion of hydraulically actuated transmissions characterized by large inertias, backlash, and several parallel-coupled gearmotors is described in [9]. The analysis of the operation of the counterbalance valves was also tested on the basis of simulation models. The principle of operation of a pressure valve with two control signals is described in [10]. Based on the counterbalance valve model, the author [11] attempted to analyse the influence of the brake valve setting on the valve response. The counterbalance valve operation model with its various settings was verified in the crane's drive system [12]. The use of counterbalance valves can also reduce the energy consumption of the systems. In [13], a closed-circuit system with hydraulic motors and counterbalance valves for supplying an electro-hydraulic actuator is described. The use of such systems yields a 50 % lower energy consumption. The possibilities of reducing pressure peaks and drops, described in [14], lead to a reduction of energy consumption by up to 80 %. The use of a counterbalance valve in a variable load system in a truck crane [15] reduces the oscillation by up to 40 %, which increases the efficiency and extends the service life of the machine. During the operation of such

systems, the problem may be the need to generate additional pressure for pump operation and oil heating because of the friction caused by flowing through these valves. In addition, the settings of such valves must be adapted to the acting forces.

The solution that eliminates the problem of load change is the load-sensing system. A comparative study of scissor lift drives carried out based on digital simulation technology of the quantitative pump hydraulic system and the load-sensing hydraulic system is presented in [16]. The author found that the load-sensing hydraulic system is more energy-saving, stable, and prevents interference than the conventional one. However, the system is sensitive to setting the pressure difference on the valve, which was set after the batch analysis. Moreover, it is still an expensive solution.

A volumetric control can be used to control the speed of the hydraulic cylinder. A variable displacement pump can be used, but preferably in systems with higher power (8 cm<sup>3</sup>/rev). Another method is to use a device that changes the speed of the motor driving the fixed displacement pump, called a variable speed pump drive (VSPD). The problem of maintaining the assumed speed of the motor is solved in electric drives by using a frequency inverter (FI), which are increasingly used in hydraulic systems instead of complex and expensive systems with variable volume pumps.

The implementation of electronics to hydraulic systems gives a much greater possibility of controlling the movement of actuators and increases energy benefits in relation to typical valve solutions. Positioning control methods can be based on digital pump-motor technology with multiple independent outlets connected directly to the cylinder chambers, which eliminates the need for valves and the generation of energy losses. Described in [17], the digital hydraulic power management system (DHPMS) is a solution that significantly improves the energy efficiency of hydraulic systems [17]. Another example to achieve the double goals of high precise tracking performance and high energy efficiency, a completely new hardware configuration that connects a direct driven pump and independent metering valves is proposed in [18]. The combination of a pump efficiency control system in the form of a variable speed drive motor and a proportional valve set offers energy advantages over conventional valve systems. Both systems operate only in an open-loop controlled based on the position tracking of the hydraulic cylinder.

In [19], an experimental forklift drive with the possibility of energy recovery is presented. However, this is not a very popular method of controlling the speed of a hydraulic cylinder. Three different ways of control, the pressure of the hydrostatic drive using variable displacement pump and FI were presented in [20]. The authors in [21] presented the possibility of controlling the output flow of a hydraulic pump driven by a motor with FI. In [22], the authors described the use of FI in several hydrostatic systems, including the drive of hydraulic cylinders. These systems operate based on direction pumps in the following configurations: variable displacement pumps co-operating with a motor supplied by the power network or a fixed displacement pump with a motor fed by FI. Performances for the same three systems in [23] have been discussed, more specifically including efficient displacement.

An interesting combination of methods of controlling the speed of an actuator loaded with variable force is the research on a self-contained electro-hydraulic cylinder (SCC) presented in [24]. The system, in the author's opinion, has the potential to replace both conventional hydraulic systems and electro-mechanical counterparts, enhancing energy efficiency and reducing maintenance. The system combines an electric servomotor and a fixed displacement pump, the single rod double-acting cylinder, and a low-pressure accumulator arranged in a closed-circuit configuration. The issue of energy recovery in hydrostatic systems with double-acting cylinders also appears in [25]. The double-pump system, with its displacement balanced with the piston area ratio, is used.

Most of the available literature deals with a double-acting cylinder, where the control possibilities are wider than in the case of a plunger cylinder (single-acting), which is presented in this article.

The use of the FI in typical drive systems with directional flow valves is the simplest and relatively inexpensive solution. In [26], the research of the use of FI together with a simple flow directional valve to control the scissor lift operation was presented. The authors described the possibility of lifting the system with a variable ratio, with different loads, maintaining a constant speed of the working platform. Based on the platform position sensor and known machine geometry, the FI control function was calculated. The generated input functions proportional to the assumed speed with proper acceleration and deceleration times allowed reducing the vibration of the hydraulic cylinder, the entire machine structure,

and the transported payload. However, lowering the payload using a scissor lift is a more complex matter and requires additional assumptions, which have not yet been presented in the publications. Additionally, the usage of the proposed system can also improve the energy efficiency, as presented in [27].

The proposed new simple electro-hydraulic system with a fixed displacement pump driven by an electric motor fed by FI in field-oriented mode and a simple controller fulfill the main goals of this control system, which are:

- ability to shape the speed of the hydraulic cylinder (or any actuator) freely, both during lifting and lowering;
- maintaining the assumed speed of the hydraulic cylinder (or any actuator) independently from the value and direction of the load.

The authors developed a simple hydraulic system, which, using the FI properties, allows full control of the speed of the cylinder or the lift platform when lowering (or lifting) the payload. It is a complete change of the control method compared to the most commonly used solutions, specifically, throttling control with volumetric control. A new control method can also reduce the oil temperature raising effect existing in drives with throttle control. The drive was installed on a real scissor lift.

This paper aims to introduce the experimentally confirmed system that achieves the assumed speed mapping of the plunger cylinder regardless of the load during the lowering cycle (active load) of the variable-ratio mechanism. The proposed drive can be used either with high or low nominal power installed. The case of active load (e.g., during the lowering phase) in hydraulic systems is difficult to control using the throttle control method (speed depends on the load), and the systems with variable displacement pumps or proportional valves used are expensive.

The paper is organized as follows: Chapter 1 presents the problem statement. Chapter 2 describes the presented solution. The test stand and its main parameters are presented in Chapter 3. The results of the experimental tests are shown in Chapter 4. Conclusions are drawn in Chapter 5.

## 1 PROBLEM STATEMENT

There are many examples of drives when the force on the hydraulic cylinder changes during machine operation due to the kinematic connections of subsequent structural members of the machine. As an example of such a stationary machine, a scissor lift was considered (Fig. 3). It is a mechanical handling

device designed for lifting people or payloads to a defined height. Different designs of the driving system of scissor lifts are presented in [28]. A complex geometry results in a variable ratio  $i$ , which causes a change in a platform speed at a constant speed of the hydraulic cylinder. The variable ratio also entails a variable force on the drive unit as a function of the lifting height (or cylinder stroke), resulting from the weight of the structure and the payload being carried. The problem of the optimal design of the construction and reducing the force acting on the hydraulic cylinders is presented in [29] and [30]. The design of a scissor lift aims at obtaining the smallest mechanism ratio changes, meaning small changes of the working platform speed concerning the speed of the hydraulic cylinder.

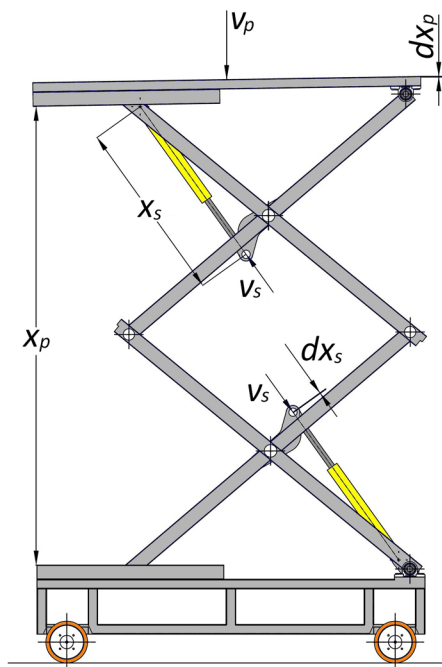


Fig. 3. Scissor lift

Fig. 3 presents a schematic drawing of the discussed scissor lift. The height of the platform  $x_p$  is determined from the length of the hydraulic cylinder  $x_s$ . The nonlinear dependence between the displacement of the hydraulic cylinder and the platform indicates the variable mechanism ratio  $i$ , calculated according to Eq. (3), where  $v_p$  and  $v_s$  are the platform and hydraulic cylinder speeds, respectively.

$$i = \frac{v_p}{v_s} = \frac{dx_p}{dx_s}. \quad (3)$$

Furthermore, the lower the platform position, the higher pressure in the system. In commonly used

systems, the platform speed increases inversely with the height of the platform. It is related to the use of throttle valves to control the lowering payload. It should be emphasized that during lowering the payload, the electric motor may be off or if it operates, the pump may force oil to the tank, for example, according to the right position of the directional valve 5 shown in Fig. 1. However, the dependence of the speed on the load in the classical system has an impact on the energy consumption. The lowering phase time increases with the decreasing load, and thus the supply time of the directional valve coil increases.

The pump flow rate  $Q_p$ , according to the Eq. (4), depends on parameters of the pump, such as volumetric efficiency  $\eta_{vp}$  and displacement  $q_p$  and angular speed of the pump shaft  $\omega_m$ .

$$Q_p = \frac{q_p \cdot \omega_m}{\eta_{vp}}. \quad (4)$$

The consequence is maintaining the hydraulic cylinder speed  $v_s$  proportional to the oil flow rate  $Q_p$ , and inversely proportional to the cross-sectional area of the piston  $A_s$ , according to Eq. (5).

$$v_s = \frac{Q_p}{A_s}. \quad (5)$$

The use of a drive with a motor fed by FI enables the full control of the speed of lowering the platform, regardless of the load. To obtain the assumed speed of the electric motor, FI is used. Nowadays, most FIs are equipped with a vector control mode (VFD), also called field-oriented control (FOC), which keeps a stable motor speed regardless of its load. FOC mode ensures work safety and the ability to work at low speeds, for example, during precise load positioning. Moreover, this mode allows stopping a hanging load at any height without using an electro-mechanical motor brake and resuming the movement at any time. The correctness of speed mapping is very high (up to 0.01 %). Therefore, the presented studies are carried out using an electric motor fed by the FI operating in FOC mode.

## 2 SOLUTION CONCEPT

The main features of the new control system, in addition to changing the control method from throttling to volumetric, are the simplicity and the possibility of using it in a typical hydraulic system, equipped with a fixed displacement pump, an asynchronous electric motor, and hydraulic valves. The elements of the new system (Fig. 4) are as follows:

- electric motor fed by FI operating in FOC mode;

- reversible gear pump;
- solenoid operated check valve 2/2 (SOCV);
- open-loop controller (OLC);
- the hydraulic cylinder position sensor (in the case of variable-ratio mechanism).

The use of the SOCV allows both lifting and lowering of the hydraulic cylinder. During a power failure, the valve is closed and prevents the cylinder from falling. Lowering is carried out by sending a piloted signal to the coil of this valve simultaneously with the FI input signal, proportional to the assumed speed. The oil flows from the hydraulic cylinder through the valve to the hydraulic reversible pump, which operates as a hydraulic motor. The electric motor is driven by the pump and acts as a generator. The assumed speed of the electric motor (and pump) is maintained using the FI. The appropriate torque on the pump shaft is the result of the FI control system operation.

The controller allows declaring any voltage function that will be sent to the FI. This can be useful during automation, as well as to reduce overloads and ensures the safety of people or goods, which can increase the lifetime of the system.

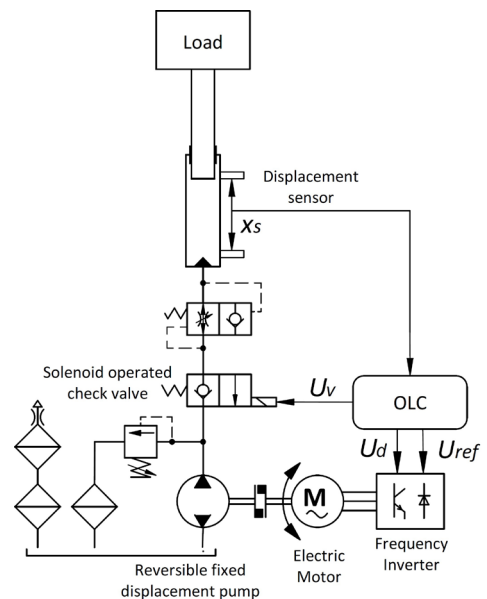


Fig. 4. The hydraulic and control system

The use of a position sensor located on the hydraulic cylinder is necessary only when the system drives the mechanism with a variable ratio, and the working element is controlled (in the presented case: the platform). Based on the position sensor mounted on the hydraulic cylinder and the known, determined because of geometric data, variable ratio, it is possible

to control the speed of any selected element of the structure (e.g. scissor lift platform). The principle of operation of the control system is presented in Fig. 5. In the OLC algorithm, the current position of the hydraulic cylinder  $x_s$  allows determining momentary mechanism ratio  $i$ , which is calculated as a polynomial function, presented in Eq. (6).

$$i = \sum_{i=0}^n a_i \cdot x_s^i. \quad (6)$$

The displacement of the working element with assumed speed  $v_{Aset}$  is realized by forcing the appropriate speed  $\omega_{mset}$  of the electric motor according to Eq. (7).

$$\omega_{mset} = v_{Aset} \cdot \frac{A_s}{q_p}. \quad (7)$$

The reference signal from the OLC to the FI  $U_{ref}$  is proportional to the motor speed and is defined by Eq. (8), where  $k_\omega$  is the conversion coefficient, and  $i_{min}$  is the minimum value of the mechanism ratio:

$$U_{ref} = \frac{\omega_{mset}}{i} \cdot i_{min} \cdot k_\omega. \quad (8)$$

In the case of lowering the payload, the controller simultaneously sends binary signals to the solenoid-operated check valve 2/2 (opening the flow from the cylinder to pump) and FI (reverse direction of the motor rotation). The oil begins to flow from the hydraulic cylinder to a pump that works like a hydraulic motor.

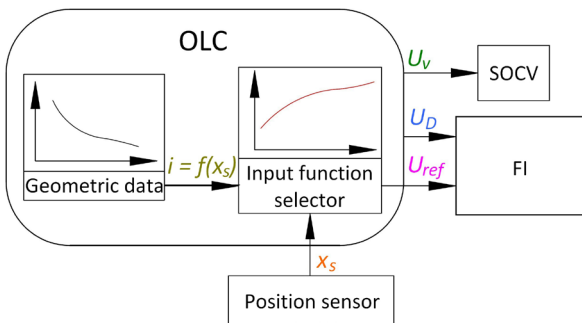


Fig. 5. Open-loop controller (OLC)

3 TEST STAND

Experimental tests were carried out on a custom-designed scissor lift prototype (Fig. 6).

The stand was equipped with the drive components and the proposed speed control system shown in Table 1. For the determination of the mechanism ratio, a position sensor of the hydraulic cylinder piston rod is installed. Additionally, a platform position sensor is

used to verify the movement of the actuator element and the power network analyser is used to measure the power consumption of the drive system. The OLC has been designed using the LabVIEW software installed on a PC co-operating with a multifunction input/output (I/O) device.

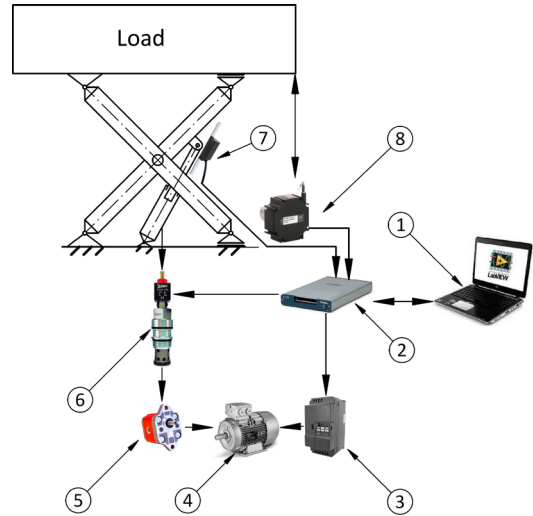


Fig. 6. Scissor lift test stand

The principle of operation of the controller is based on the equations described above. The mechanism ratio  $i$  as a function of the hydraulic cylinder displacement  $x_s$ , shown in Fig. 7, was described by a 6<sup>th</sup>-degree polynomial. The mechanism ratio changes from 13 in the lower platform position to 6.6 in its upper position.

Table 1. Test stand setup

No.	Component	Parameters
1	PC + LabVIEW	Dell Inspiron 17 G3 3779
2	Software NI USB 6434	16 AI, 2 AO, 24 DIO USB
3	Frequency Inverter SX2400-OR7G-2	0.75 kW / 0 V to 10 V
4	Motor Simotics GP 1AV1082B	0.55 kW / 1385 rpm
5	Pump XV-OR/0.98	0.92 cm <sup>3</sup> /rev
6	Solenoid-operated check valve 2/2 EP-08W-05-M-04	350 bar / 30 l/min
7	Hydraulic cylinder position sensor EMAX-000-01.5-2-CAO	1.5 m / 125 kBit/s
8	Platform position sensor WDS-3000-P96-CR-TTL	3000 mm / 11.53 pulses/mm

The presented mechanism is the only case that requires an additional sensor. This is due to the variable ratio of the mechanism and the necessity of determining the ratio to maintain the assumed speed of the platform. This entails the need to know the

geometry of the mechanism and its ratio. Constant ratio mechanisms do not require a sensor of cylinder displacement.

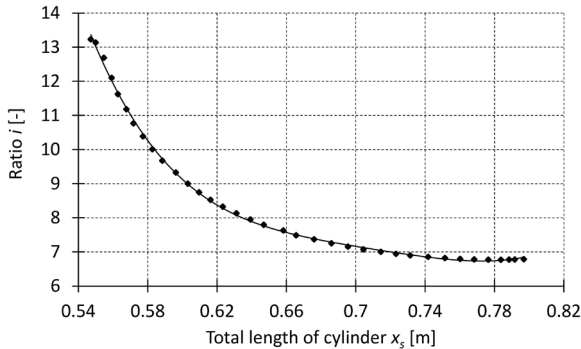


Fig. 7. Mechanism ratio  $i$  as a function of the hydraulic cylinder displacement  $x_s$

4 EXPERIMENTAL INVESTIGATION AND RESULTS

The experimental tests were divided into two sections:

1. Comparison of the assumed speeds with measured on the stand.
2. Testing the influence of the load on maintaining the assumed speeds.

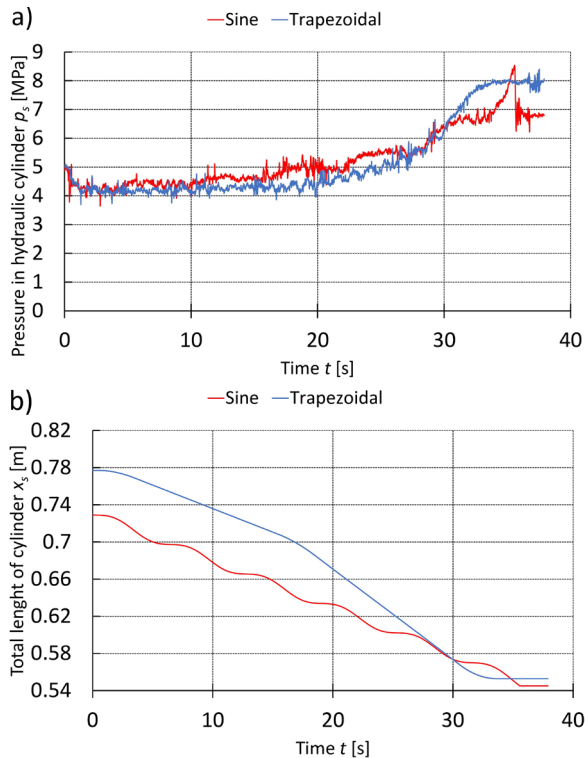


Fig. 8. Comparison of a) sine and trapezoidal functions for pressure in the hydraulic cylinder, and b) total hydraulic cylinder length during the lowering cycle

Each section was tested separately for the assumed speed of the hydraulic cylinder and the actuator - a scissor lift platform.

4.1 Verification of the OLC

The scissor lift loaded with a nominal load of 96 kg (100 % load) was used for the tests. The platform was lowered using two control functions: sine and trapezoidal. These functions are the base for further studies related to the minimization of dynamic loads, in which both types of inputs will be used. Fig. 8a presents the pressure change  $p_s$  in hydraulic cylinders during the lowering. It is a visible change of the pressure from 4.5 MPa at the start (upper) position to almost 7 MPa (sine) and 8 MPa (trapezoidal) at the end cycle when the platform is at the bottom position. Fig. 8b presents the actual length of the hydraulic cylinder  $x_s$ .

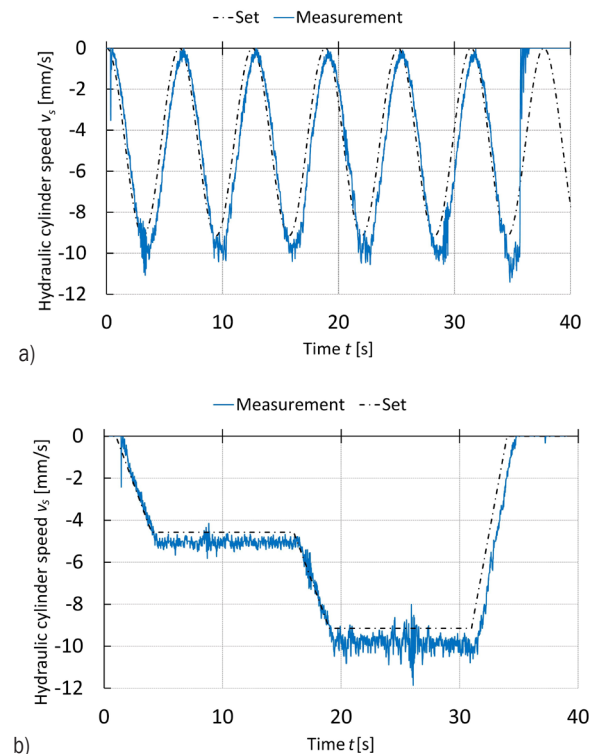


Fig. 9. Comparison of the set and measured speeds of the hydraulic cylinder ( $v_s$ ); a) sine, and b) trapezoidal

The waveforms presented in Fig. 9 show the speed of the hydraulic cylinder with a) sine, and b) trapezoidal control functions. In both cases, the difference between the speeds increases with time. This is due to the diminishing volumetric efficiency of the pump due to the increasing leaks under pressure

growth in the hydraulic system during lowering. The maximum difference between the set speed and the actual speed is 2.4 mm/s.

The OLC allows continuous adjustment of the speed of the hydraulic cylinder and thus the scissor lift platform. The assumed and measured waveforms of the platform speed are presented, respectively, in Fig. 10. As with the hydraulic cylinder, the platform speed increases when the platform is lowered. The proposed control system does not consider the change of efficiency of the pump. This is a field for further research and development of the possibilities of the presented method of speed regulation. However, in this case, the maximum difference between the set speed and the actual speed is 5.9 mm/s.

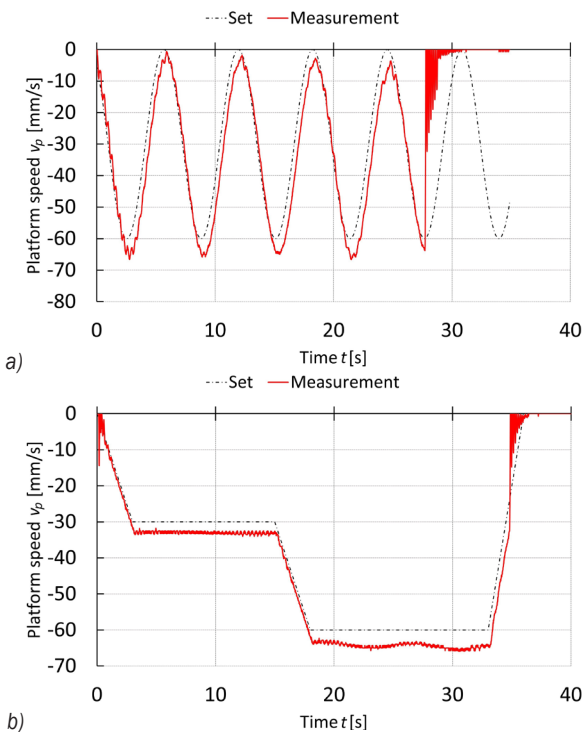


Fig. 10. Comparison of the set and measured speeds of the scissor lift platform ( $v_p$ ); a) sine, and b) trapezoidal

#### 4.2 Load Impact on the OLC

The objective of the second section of the experiments is to validate the proposed control structure for different test cases covering the operating range of the drive. Operation of the system is evaluated with an external load at the level of (0, 50, 100) % of the nominal load (respectively, 0 kg, 48 kg and 92 kg) for lowering the platform from a height of 2150 mm. The voltage reference functions are carried out in the following cases:

- $U_{ref}$  as a function proportional to the assumed speed of the hydraulic cylinder  $v_s = -9.15$  mm/s with smooth acceleration and deceleration 1-second ramp (Fig. 11).
- $U_{ref}$  as a function proportional to the assumed speed of the platform  $v_p = 60$  mm/s with smooth acceleration and deceleration 1-second ramp (Fig. 12).

To facilitate the reading of Figs. 11 to 13, the magnifications of the selected areas of the charts are placed.

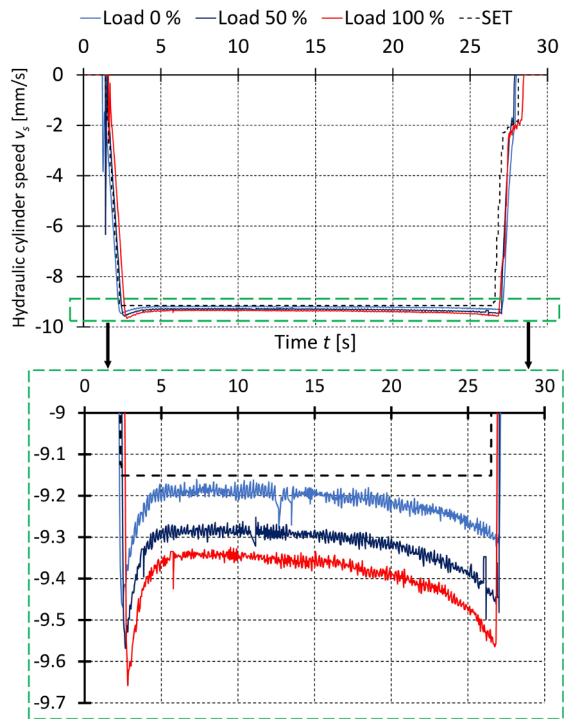


Fig. 11. Comparison of the set and measured speeds  $v_s$  of the hydraulic cylinder with different loads

The applied ramps reduced the overloads and vibrations emerging in the system. This increases the service life of the entire machine and affects the safety of the transported cargo or the comfort of people.

Both the speed of the hydraulic cylinder and the platform maintain the assumed speeds regardless of the load. The maximum difference between the set platform speed is 10 % and the average is 6 %. Detailed differences are presented in Table 2, where set is reference value of the platform speed, maximal actual value of the platform speed, and mean arithmetical mean of the actual platform speed during steady motion.

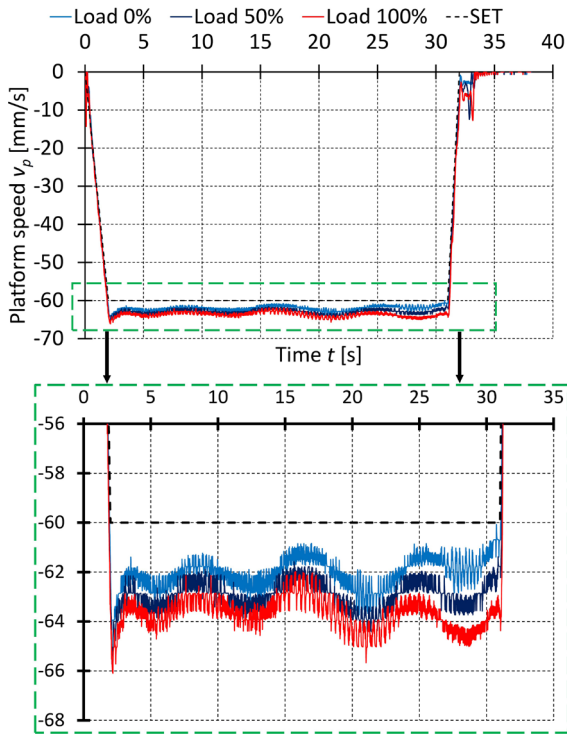


Fig. 12. Comparison of the set and measured speeds  $v_p$  of the scissor lift platform with different loads

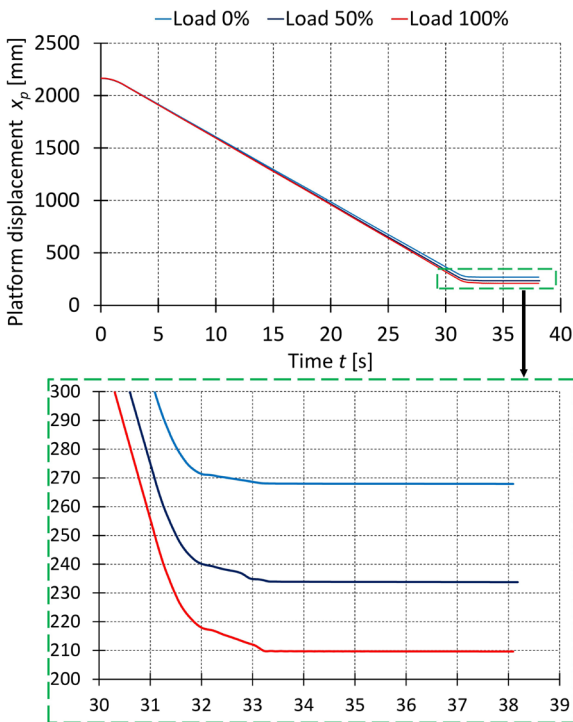


Fig. 13. Platform displacement  $x_p$  with different loads

The difference in the position of the platform after lowering it over the same period is 58 mm between a fully loaded and empty lift. The displacements of lowering the platform for different loads are shown in Fig. 13.

These values result from a decline in the volumetric efficiency of the pump with increasing pressure. To eliminate these differences, a pump leakage compensation system or close loop control system should be used. During the tests, the electrical parameters in the line supplying of the stand were also recorded. Measurement of instantaneous power allowed to determine the energy consumed in each cycle. A conventional drive system and a new one were used for comparison.

Table 2. Comparison of platform speed  $v_p$  for different loads

Load [%]	Platform speed		
	set $v_p$ [mm/s]	max $v_p$ [mm/s]	mean $v_p$ [mm/s]
0	-60	-64.33	-62.05
50	-60	-65.73	-62.93
100	-60	-66.10	-63.70

Fig. 14 presents the comparison of power consumption during the lowering cycle. To illustrate the cycle, the platform displacement is presented as well. The actual power consumption of the conventional drive is at the constant level during the whole cycle, what is visible in Fig. 14a. It results from the constant power demand of the device control system and the supply of the throttle valve coil. One of the disadvantages of this system is the dependence of the load on the lowering time, which can reach over 120 s for an empty platform. The new setup of the valve can change these cycle times. Fig. 14b shows that the power consumption depends on the platform displacement, but all cycles are about 35 s. The duration of the cycle depends only on the settings of its parameters, such as the assumed speed or the times of the individual cycle phases. The FI installed on the stand cannot return energy into the power network. To estimate the energy balance of a drive capable of returning energy to the power network, based on the measured hydraulic quantities associated with the pump, the power recoverable  $P_m$  during lowering was determined according to dependency:

$$P_m = q_p \cdot \omega_m \cdot p_p \cdot \eta_m \cdot \eta_p, \quad (9)$$

where  $q_p$  is pump displacement,  $\omega_m$  actual angular speed of the pump shaft,  $p_p$  actual pressure on the pump outlet,  $\eta_p$  pump efficiency, and  $\eta_m$  electric motor efficiency.

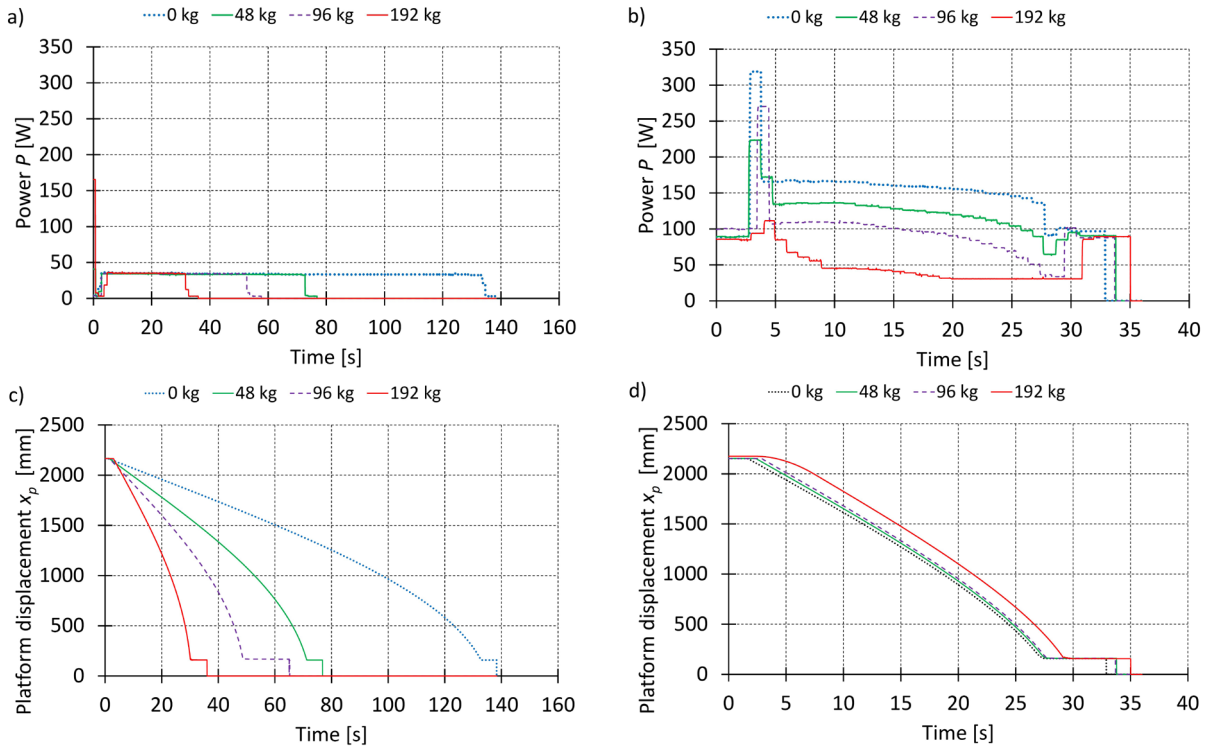


Fig. 14. Power consumption  $P$  and platform displacement  $x_p$  during lowering cycle: a), c) conventional, b), d) new

To estimate the energy consumption  $E$ , the power function was integrated according to the Eq. (10):

$$E = \int_0^t (P - P_m) dt. \quad (10)$$

Fig. 15 presents the comparison of the lowering energy of the three systems:

- conventional with directional and throttle valves,
- new with FI,
- new with FI and energy recuperation estimation.

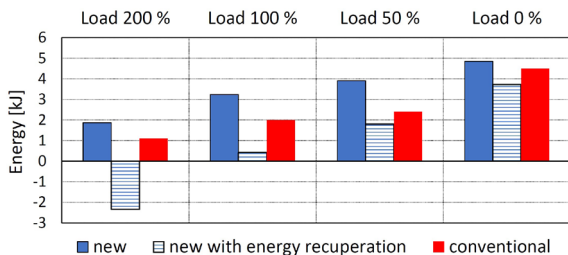


Fig. 15. Lowering energy comparison with different platform loads and drive systems

It is visible that the ability to free mapping of the speed using the new system costs a certain amount of energy. Differences reached even about 60 % for the

system without energy recuperation. It should be noted that this is a low-capacity drive and the difference in energy demand decreases with increasing load.

When this feature is included, the system gives lower energy consumption for the empty platform and small loads (from 20 % to 87 %) and energy recuperation in case of maximum load. The reduction in power consumption results from the fact that the motor working during lowering as a generator, transfers electric power to the DC link of FI, which in common FI's is lost to the resistor. The FI's equipped with the regenerative unit allows energy to return to the grid when the DC link voltage level is too high. It causes a real decrease in energy demand, e.g., in lowering cycles.

## 5 CONCLUSIONS

The proposed system of controlling the lowering of the hydraulic cylinder maintains the set speed with high accuracy. The used method of control simplifies the structure of the hydraulic system, among others the throttle valve and directional valve are removed. New drive allows freely shaping of the speed of the piston rod or working element (e.g. platform) depending on the needs. However, it causes the increased energy

consumption in relation to the classical system. The presented system can be, although energy efficient by using FI equipped with a regenerative unit, despite that the scissor lift is a relatively low-capacity machine.

This system has significant advantages over other methods of speed control and positioning for lowering payload. These are, among others: simple structure, low price, the possibility of using any size, and type of pump. This means that the presented solution of the volumetric control of hydrostatic drives can be used without any limitation of a pump size in contrary to variable displacement pumps, which are produced in sizes above 8 cm<sup>3</sup>/rev. This extends the possibility of volumetric control also to low power driving systems.

Additionally, the possibility of continuous adjustment of the pump motor speed allows minimizing adverse phenomena occurring during acceleration, such as vibrations or overloads.

The presented solution significantly extends the possibilities of controlling hydraulic systems in both passive and active loads.

## 7 NOMENCLATURES

$A_D$	cross-sectional area of valve orifice, [m <sup>2</sup> ]
$A_s$	cross-sectional area of piston, [m <sup>2</sup> ]
$c_D$	coefficient of flow losses, [-]
$d_s$	diameter of hydraulic cylinder, [m]
$E$	energy consumption, [J]
$i$	mechanism ratio, [-]
$k_\omega$	conversion coefficient, [V·s/rad]
$P_m$	recoverable power, [W]
$p_p$	actual pressure on pump outlet, [MPa]
$\Delta p_s$	pressure drop between valve inlet and outlet, [MPa]
$q_p$	pump displacement, [m <sup>3</sup> /rev]
$Q_D$	throttling valve flow rate, [m <sup>3</sup> /s],
$Q_p$	pump flow rate, [m <sup>3</sup> /s],
$U_{ref}$	reference signal from OLC, [V]
$v_{Aset}$	assumed speed of working element, [m/s]
$v_p$	and $v_s$ are the platform speed, [m/s]
$v_s$	hydraulic cylinder speed, [m/s]
$x_p$	height of platform, [m]
$x_s$	length of hydraulic cylinder, [m]
$\eta_m$	electric motor efficiency, [-]
$\eta_p$	pump efficiency, [-]
$\eta_{vp}$	pump volumetric efficiency, [-]
$\rho$	density of hydraulic liquid, [kg/m <sup>3</sup> ]
$\omega_m$	actual angular speed of pump shaft, [rad/s]
$\omega_{mset}$	assumed speed of electric motor, [rad/s].

## 6 REFERENCES

- [1] Liu, Y.; Li, W., Li, D. (2018). Review on inlet/outlet oil coordinated control for electro-hydraulic power mechanism under sustained negative load. *Applied Sciences*, vol. 8, no. 6: art. ID 886, DOI:10.3390/app8060886.
- [2] Bednarski, S. (2012). Controlled movement of the hydraulic cylinder with active load. *Hydraulika I Pneumatyka*, no. 2, p. 10-14. (in Polish)
- [3] Stawiński, Ł. (2011) Hydrostatic systems for driving cylinders with variable direction loading of the piston rod. *Hydraulika i Pneumatyka*, no. 1, 17-20. (in Polish)
- [4] Dabholkar, R., Indulkar, S. (2012). Overcenter valves are key to hydraulic control. *Design World*, from <https://www.designworldonline.com/overcenter-valves-are-key-to-hydraulic-control/>, accessed on 2020-11-23.
- [5] Hitchcox, A. (2009). *The Truth about Problem Valves*, Hydraulics & Pneumatics, The Penton Media Buildings, Cleveland.
- [6] Johnson, J.L., (2009). *Counterbalance Valve Circuits*, Hydraulics & Pneumatics, The Penton Media Building, Cleveland.
- [7] Zähle, B. (2010). Für einen besseren Wirkungsgrad. *Auswahl und Verschaltung von Senkbremssventilen*. SUN Hydraulik GmbH in Erkelenz, Mainz.
- [8] Nordhammer, P.A., Bak, M.K., Hansen, M.R. (2012). A method for reliable motion control of pressure compensated hydraulic actuation with counterbalance valve. *Proceedings of the 12<sup>th</sup> International Conference on Control. Automation and Systems*, p. 759-763.
- [9] Nordhammer, P.A., Bak, M.K., Hansen, M.R. (2012). Controlling the slewing motion of hydraulically actuated crane using sequential activation of counterbalance valve. *Proceedings of the 12<sup>th</sup> International Conference on Control. Automation and Systems*, p. 773-778.
- [10] Dasgupta, K., Watton, J. (2018). Modeling and dynamics of a two-stage pressure rate controllable relief valve: A bondgraph approach. *International Journal of Modelling and Simulation*, vol. 28, no. 1, p. 11-19, DOI:10.1080/02286203.2008.11442444.
- [11] Stawiński, Ł. (2016). Experimental and modeling studies of hydrostatic systems with the counterbalance valves which are used in hydraulic lifting systems with passive and active load. *Eksplotacja i Niezawodność - Maintenance and Reliability*, vol. 18, no. 3, p. 406-412, DOI:10.17531/ein.2016.3.12.
- [12] Zhao, L., Xinhui, L., Tongjian, W. (2010). Influence of counterbalance valve parameters on stability of the crane lifting system. *Proceedings of the International Conference on Mechatronics and Automation*, p. 1010-1014, DOI:10.1109/icma.2010.5589356.
- [13] Agostini, T., De Negri, V., Minav, T., Pietola, M. (2020). Effect of energy recovery on efficiency in electro-hydrostatic closed system for differential actuator. *Actuators*, vol. 12, Iss. 9, art. ID 12, DOI:10.3390/act9010012.
- [14] Cochran, K. (2012). Cartridge valve and manifold technologies - a component approach to improved energy efficiency. *Proceedings of the Energy Efficient Hydraulics and Pneumatics Conference*, Rosemont.

- [15] Andersen, B.R. (2009). Energy efficient load holding valve. *Proceedings of the 11<sup>th</sup> Scandinavian International Conference on Fluid Power*, Linköping.
- [16] Bao, Z. (2019). Study on simulation of system dynamic characteristics of hydraulic scissor lift based on load-sensing control technology. *IOP Conference Series: Materials Science and Engineering*, vol. 612, no. 4, art. ID 042036, DOI:10.1088/1757-899X/612/4/042036.
- [17] Heikkilä, M., Linjama, M. (2013). Displacement control of a mobile crane using a digital hydraulic power management system. *Mechatronics*, vol. 23, no. 4, p. 452-461, DOI:10.1016/j.mechatronics.2013.03.009.
- [18] Lyu, L., Chen, Z., Yao, B. (2018). High precision and high efficiency control of pump and valves combined hydraulic system. *Proceedings of the 15<sup>th</sup> International Workshop on Advanced Motion Control (AMC)*, p. 391-396, DOI:10.1109/AMC.2019.8371124.
- [19] Minav, T., Immonen, P., Laurila, L., Vtorov, V., Pyrhonen, J., Niemela, M. (2011). Electric energy recovery system for a hydraulic forklift - theoretical and experimental evaluation. *IET Electric Power Application*, vol. 5, no. 4, p. 377-385, DOI:10.1049/iet-epa.2009.0302.
- [20] Lovrec, D., Tic, V., Tasner, T. (2017). Dynamic behaviour of different hydraulic drive concepts - comparison and limits. *International Journal of Simulation Modelling*, vol. 16, no. 3, p. 448-457, DOI:10.2507/ijssimm16(3)7.389.
- [21] Avram, M., Spânu, A., Sârbu, V. (2018). Method for controlling the hydraulic pump flow following an imposed frequency law for AC motors. *IOP Conference Series: Materials Science and Engineering*, vol. 444, no. 4, art. ID 042009, DOI:10.1088/1757-899X/444/4/042009.
- [22] Kosucki, A., Stawiński, Ł. (2016). Studies on hydrostatic systems powered by frequency inverters. *Proceedings of the International Scientific and Technical Conference: Hydraulic and Pneumatic Drives and Control*, vol. 1, p. 5-16. (in Polish)
- [23] Yang, X., Gong, G., Yang, H., Jia, L., Zhou, J. (2017). An investigation in performance of a variable-speed-displacement pump-controlled motor system. *IEEE/ASME Transactions on Mechatronics*, vol. 22, no. 2, p. 647-656, DOI:10.1109/tmech.2016.2544440.
- [24] Padovani, D., Ketelsen, S., Hagen, D., Schmidt, L. (2019). A self-contained electro-hydraulic cylinder with passive load-holding capability. *Energies*, vol. 292, no. 12, art. ID 292, DOI:10.3390/en12020292.
- [25] Ritelli, G.F., Vacca, A. (2013). Energetic and dynamic impact of counterbalance valve in fluid power machines. *Energy Conversion and Management*, vol. 76, p. 701-711, DOI:10.1016/j.enconman.2013.08.021.
- [26] Stawiński, Ł., Kosucki, A., Morawiec, A., Sikora, M. (2019). A new approach for control the velocity of the hydrostatic system for scissor lift with fixed displacement pump. *Archives of Civil and Mechanical Engineering*, vol. 19, no. 4, p. 1104-1115, DOI:10.1016/j.acme.2019.06.001.
- [27] Stawinski, Ł., Zaczynski, J., Morawiec, A., Skowronska, J., Kosucki, A. (2021). Energy consumption structure and its improvement of low-lifting capacity scissor lift. *Energies*, vol. 14, no. 5, art. ID 1366, DOI:10.3390/en14051366.
- [28] Stancek, J., Bulej, V. (2015). Design of driving system for scissor lifting mechanism. *Academic Journal of Manufacturing Engineering*, vol. 13, no. 4, p. 38-43.
- [29] Hongyu, T., Ziyi, Z. (2011). Design and simulation based on Pro/E for a hydraulic lift platform in scissors type. *Procedia Engineering*, vol. 16, p. 772-781, DOI:10.1016/j.proeng.2011.08.1153.
- [30] Liu, T., Jian, S. (2009). Simulative calculation and optimal design of scissor lifting mechanism. *Proceedings of the Chinese Control and Decision Conference*, p. 2079-2082.

# Applicability of MCDM Algorithms for the Selection of Phase Change Materials for Thermal Energy Storage Heat Exchangers

Paul Gregory Felix\* - Velavan Rajagopal - Kannan Kumaresan  
PSG College of Technology, Department of Mechanical Engineering, India

*Latent heat thermal energy storage heat exchangers store heat energy by virtue of the phase transition that occurs in the thermal storage media. Since phase change materials (PCMs) are utilized as the media, there is a critical necessity for the appropriate selection of the PCM utilized. Since multiple thermo-physical properties and multiple PCMs are required to be evaluated for the selection, there arises a need for multiple criteria decision making (MCDM) algorithms to be adopted for the selection. But owing to the different weight estimation techniques employed and the voluminous quantity of selection algorithms available, there arises a need for a comparative methodology to be adopted. This study was intended to select an optimal PCM for a sustainable steam cooking application coupled with a thermal energy storage system. In this research study, six PCMs were chosen as the alternatives and five thermo-physical properties were chosen as the criteria for the evaluation. 11 different algorithms were augmented with 3 different weight estimation techniques and therefore a total of 33 algorithms were employed in this study. All of the algorithms have chosen Erythritol as the optimal PCM for the application. The outcomes of the MCDM algorithms have been validated through an intricate Pearson's correlation coefficient study.*

**Keywords:** latent heat, multiple criteria decision making, phase change material, thermal energy storage

## Highlights

- A comparative methodology has been proposed to select the optimal PCM for thermal energy storage heat exchangers.
- An optimal PCM for a sustainable steam cooking application has been selected by adopting multiple MCDM algorithms.
- A clear demarcation has been presented between the functionality of all of the algorithm combinations adopted.
- A three case Pearson's correlation coefficient study has validated the reliability of the ranking outcomes.

## 0 INTRODUCTION

Phase change materials (PCMs) play an important role in latent heat thermal energy storage (TES) systems. PCMs act as heat sinks to absorb and store excess heat energy from then heat source and then release the stored heat energy as and when required. To facilitate this process of heat energy storage and release, TES heat exchangers are employed at the application site. Several types of heat exchangers can be adopted for such latent heat systems [1]. On the other hand, the research outcomes based on renewable sources of energy, more specifically, based on solar thermal energy has improved over the recent years, that even steam cooking can be done directly using steam generated from solar parabolic trough collectors (PTCs) [2]. But the non-availability of solar energy throughout the day and night demands the necessity for a TES system that would store the excess thermal energy during sunshine hours, and the stored thermal energy could be retrieved during the off-sunshine hours. At the application site, steam generated from the TES heat exchanger can be utilized for cooking during the off-sunshine hours, whereas the steam generated directly from the solar source (PTCs) can be utilized for cooking during the sunshine hours.

Taking into consideration the fact that latent heat TES systems based on PCMs store much more higher heat than sensible heat systems, it can be asserted that such TES systems are suitable for this sustainable steam cooking application. For designing TES heat exchangers for this application, the first important step has to be the appropriate selection of the PCM [3]. This is because, each PCM has different thermo-physical properties and the choice of the PCM explicitly affects the design. For instance, PCMs having lower latent heat will increase the size of the heat exchanger. Hence, the selection of the appropriate PCM suitable for the application is required to be performed on scientific evaluation grounds with multiple criteria and alternatives (PCMs) considered.

Multiple criteria decision making (MCDM) has evolved as a mathematical tool to aid designers to perform subjective evaluations in operation research [4]. The applications of MCDM algorithms in the domain of mechanical engineering are multiple. Few examples include determination of the threshold for extreme load extrapolation [5], choosing systems for drying paltry-seeds [6], assessment of energy crops for producing bio-gas [7], ranking renewable energy resources [8] and optimal material selection [9]. Concerning PCMs, it has also been observed that

\*Corr. Author's Address: PSG College of Technology, Department of Mechanical Engineering, Avinashi road, Coimbatore, India, 1807rm01@psgtech.ac.in

researchers have applied MCDM algorithms to select the appropriate PCM for low-temperature applications [10], ground source heat pump application [11] and even for domestic water heating [12]. While selecting a suitable material, it is necessary to estimate strategic weights for each evaluative criterion such that the decision becomes subjective. But the choice of the algorithms applied for a particular case depends on the decision of the heat exchanger designer. It has been observed from peer literature that many research studies have limited their study designs to a very few algorithms with a limited choice of weight estimation techniques. Concerning the weight estimation techniques, it has been learned that using either only subjective or only objective weighting scheme in the study can be considered as a deficiency [11]. Hence, heat exchanger designers are required to refer to multiple literature sources to understand the functional mechanism of several algorithms and will need to perform an intricate study on various weight estimation and MCDM techniques to arrive at a conclusion to select which MCDM algorithm would be appropriate. But, in this study, a methodology incorporating a comparative study design has been proposed.

This current study presents a novel comparative approach than several previous works such that an intricate comparative selection can be made. This research study, through its proposed methodology, asserts that, for a PCM selection involving multiple alternatives, a comparative study involving multiple MCDM algorithms can provide a reliable solution to the selection process. This is asserted because, the methodology does not rely only on one algorithm, but instead has adopted multiple combination of algorithms for the selection. Hence, the PCM selected through this methodology will be a reliable choice for the heat exchanger.

## 1 METHODS

### 1.1 Study Design

This current study was performed in three parts. The first part of this study was to select the alternative PCMs and criteria through a pre-screening and then estimating the desired weights through entropy weight method (EWM), criteria importance through inter-criteria correlation (CRITIC) method and analytic hierarchy process (AHP) method. The second part was to apply the derived weights to select the suitable PCM through 11 selected algorithms. The third part of the research was to perform a Pearson's

correlation coefficient study to correlate the outcomes of various algorithms and validate the concurrence of the outcomes. The study design adopted is presented in Fig. 1.

Since steam is required to be generated (from the heat exchanger) at the application site at a minimum temperature of 100 °C, PCMs were desired to have a melting temperature around 120 °C. Hence from an initial screening, six PCMs were selected. The selected PCMs along with their thermo-physical properties (criteria) are presented in Table 1. In Table 1, it can be observed that a mix of both laboratory grade PCMs and commercial PCMs have been considered. But however, all of the PCMs were selected such that they share a close melting temperature to 120 °C. But, out of the alternatives, one PCM is required to be selected based on the other thermo-physical properties. There has been no specific preference among the mix of laboratory grade and commercial grade PCMs in this analysis. The research methodology has been oriented such that there exists no bias between selecting laboratory and commercial grade materials and hence this methodology can be envisaged to select any kind of PCM that would be technically appropriate for the particular application in study. Among the listed criteria, specific heat alone was categorized as a non-beneficial criterion. This is because, for the steam cooking application, higher magnitudes of melting temperature, heat of fusion, density, thermal conductivity was preferred. Hence, the aforementioned four parameters were considered as beneficial criteria. Whereas, for the application, lower specific heat magnitude is preferred, as a higher specific heat will increase the melting time of the PCM. Since this steam cooking application is intended to be integrated with solar energy, faster melting and charging of the PCM was preferred as the entire charging process will have to be completed within the sunshine hours. Hence specific heat alone was considered as a non-benefit criterion.

### 1.2 Estimation of the criteria weights

#### 1.2.1 EWM

In this method, the decision matrix  $X$  was normalized using the sum method (Eq. (1)), and the weights  $w_j$  were estimated through calculating the entropy value  $E_j$  [12], as presented in Eq. (2). The decision matrix  $X$  is an array of the considered  $m$  alternatives and  $n$  criteria. In the equation,  $p_{ij}$  indicates the normalized value of the decision matrix  $X$ .

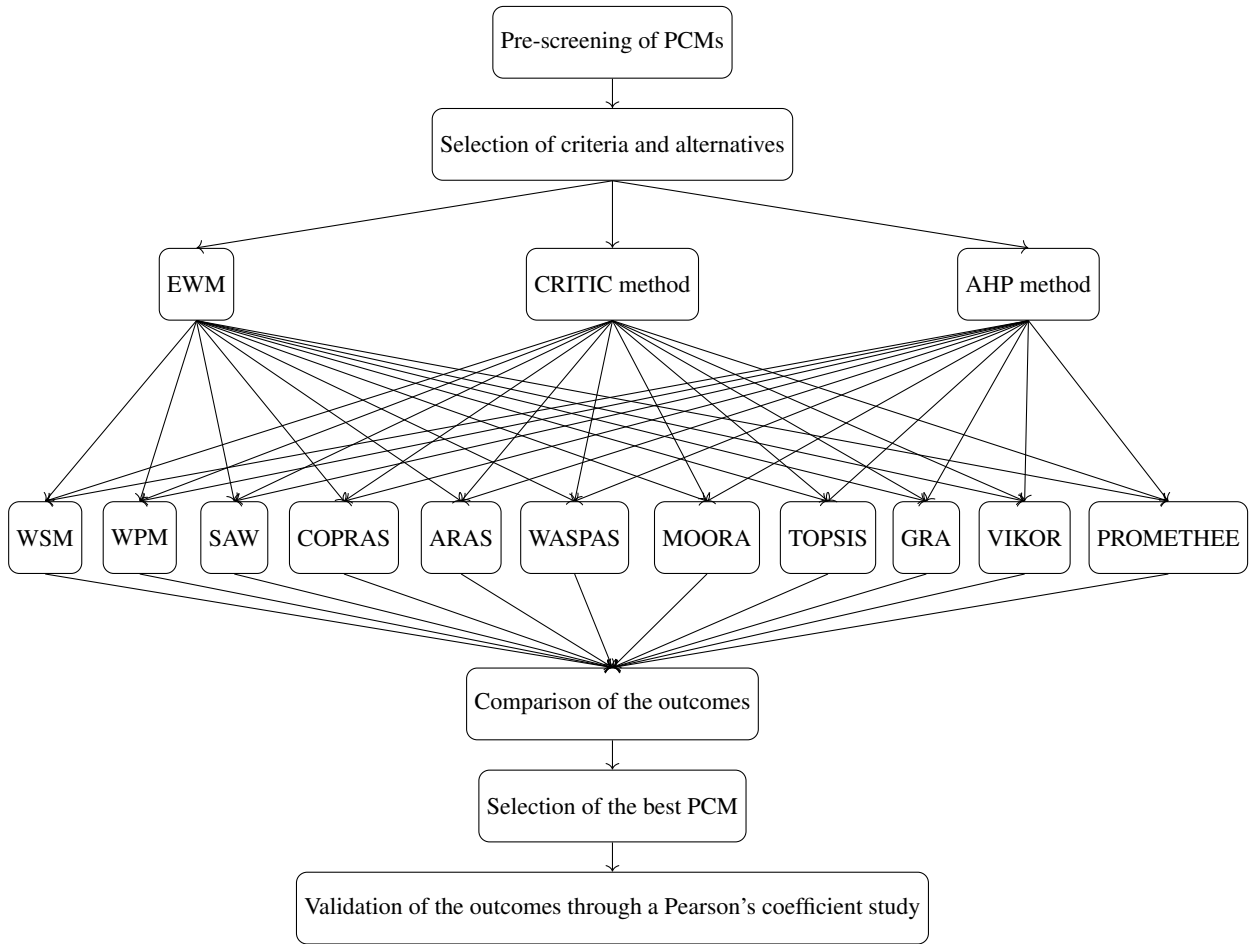


Fig. 1. Study design adopted

Table 1. Considered alternatives and criteria

PCM no.	Name	Melting temperature [°C]	Heat of fusion [kJ kg <sup>-1</sup> ]	Density [kg m <sup>-3</sup> ]	Thermal conductivity [W m <sup>-1</sup> K <sup>-1</sup> ]	Specific heat [kJ kg <sup>-1</sup> K <sup>-1</sup> ]	Reference
1	Erythritol	120	331	1480	0.733	1.35	[14]
2	MgCl <sub>2</sub> ·6H <sub>2</sub> O	117.5	200	1569	0.704	2.25	[15]
3	PlusICE A118	118	195	900	0.22	2.2	[16]
4	PlusICE H120	120	120	2220	0.506	1.51	[17]
5	PlusICE S117	117	125	1450	0.7	2.61	[16]
6	PlusICE X120	120	180	1245	0.36	1.5	[17]

$$p_{ij} = \frac{x_{ij}}{\sum_{j=1}^n x_{ij}}, \quad (1)$$

$$E_j = -\frac{\sum_{i=1}^m p_{ij} \cdot \ln p_{ij}}{\ln n} \quad \text{and} \quad w_j = \frac{1 - E_j}{\sum_{i=1}^m (1 - E_j)}. \quad (2)$$

### 1.2.2 CRITIC Method

In this method, the decision matrix elements  $x_{ij}$  were normalized using Eq. (3) and the weights were estimated using  $C_j$  as presented in Eq. (4) [13]. In the equation,  $r_{jj^n}$  represents the relative correlation coefficient between the  $j^{\text{th}}$  and  $j^n$  criteria and  $\sigma_j$  represents the standard deviation of the normalized matrix.

$$p_{ij} = \frac{x_{ij} - \min_j(x_{ij})}{\max_j(x_{ij}) - \min_j(x_{ij})}, \quad (3)$$

$$w_j = \frac{C_j}{\sum_{j^n=1}^n C_j} = \frac{\left[ \sigma_j \sum_{j^n=1}^n (1 - r_{jj^n}) \right]}{\sum_{j^n=1}^n \left[ \sigma_j \sum_{j^n=1}^n (1 - r_{jj^n}) \right]}. \quad (4)$$

**1.2.3 AHP method**

In this method, a relative importance decision matrix with elements  $a_{jj^n}$  was constructed using the Saaty’s scale [10] and the weights were estimated by using Eq. (5). The relative matrix is a matrix representing the importance of one criterion over another.

$$w_j = \frac{a_{jj^n}}{\left[ \sum_{j^n=1}^n a_{jj^n} \right] n}. \quad (5)$$

**1.3 Estimation of the Optimal PCM**

**1.3.1 Weighted Sum Method (WSM)**

In this method, the decision matrix was normalized using the square root method. The alternatives were ranked based on the weighted sums  $S_i^{WSM}$  estimated using Eq. (6).

$$S_i^{WSM} = \sum_{j=1}^n w_j \times \frac{x_{ij}}{p_{ij}} = \sum_{j=1}^n w_j \times \frac{x_{ij}}{\sqrt{\sum_{j=1}^n x_{ij}^2}}. \quad (6)$$

**1.3.2 Weighted Product Method (WPM)**

In this method, the weighted product for each alternative was estimated by raising the normalized decision matrix elements to the power of the weights, as presented in Eq. (7) and the alternatives were ranked based on  $P_i^{WPM}$ .

$$P_i^{WPM} = \prod_{j=1}^n \left[ \frac{x_{ij}}{p_{ij}} \right]^{w_j} = \prod_{j=1}^n \left[ \frac{x_{ij}}{\sqrt{\sum_{j=1}^n x_{ij}^2}} \right]^{w_j}. \quad (7)$$

**1.3.3 Simple Additive Weighting (SAW) method**

This method is similar to WSM, except to the fact that the normalization of the decisive matrix with elements  $x_{ij}$  was performed separately for both the benefit criteria elements and the non-benefit criterion

elements. The normalization was performed using Eq. (8). The preference index  $V_i$  was then estimated using Eq. (6) and the alternatives were ranked.

$$p_{ij} = \begin{cases} \frac{x_{ij}}{\max_j x_{ij}}, & \text{for benefit criteria.} \\ \frac{\min_j x_{ij}}{x_{ij}}, & \text{for non-benefit criterion.} \end{cases} \quad (8)$$

**1.3.4 Complex Proportional Assessment (COPRAS) Method**

In this method, the decision matrix was normalized using the sum method. Then, the maximizing index  $S_{+i}$  for the benefit criteria was estimated as a row-wise sum of the weighted normalized matrix for the benefit criteria values, and the minimizing index  $S_{-i}$  was estimated in the same way for the non-benefit criterion [18]. Utilizing the estimated values, the relative weight  $Q_{c,i}$  was computed using Eq. (9). Then the performance index  $U_i$  was estimated using Eq. (10) and the alternatives were then ranked based on  $U_i$ .

$$Q_{c,i} = S_{+i} + \frac{\min_i S_{-i} \sum_{i=1}^m S_{-i}}{S_{-i} \sum_{i=1}^m \frac{\min_i S_{-i}}{S_{-i}}}, \quad (9)$$

$$U_i = \frac{Q_{c,i}}{Q_{c,max}} \times 100. \quad (10)$$

**1.3.5 Additive Ratio Assessment (ARAS) Method**

In this method, for each criterion, the optimal value was determined based on whether the criterion was a benefit or a non-benefit attribute and the decision matrix augmenting the optimal value was then weight normalized using the sum method. Then, the optimality function  $S_i$  and the utility degree  $K_i$  was estimated using Eq. (11) [19]. The alternatives were then ranked based on  $K_i$ .

$$K_i = \frac{S_i}{S_{opt}} = \frac{\sum_{j=1}^n p_{ij}^{aug} w_j}{S_{opt}}. \quad (11)$$

**1.3.6 Weighted Aggregated Sum Product Assessment (WASPAS) Method**

This method is a combination of WSM and WPM. In this method, the normalized decision matrix was estimated by segregating the beneficial criteria and non-beneficial criterion using the maximum-minimum method as presented in Eq. (8). Then the total relative importance  $Q_i$  was estimated through Eq. (12) [20]. The alternatives were ranked based on the total

relative importance. In the equation,  $\lambda$  represents a transformation constant. In this case, a  $\lambda$  of 0.5 was adopted.

$$Q_i = \lambda \sum_{j=1}^n p_{ij} w_j + (1 - \lambda) \prod_{j=1}^n p_{ij}^{w_j}. \quad (12)$$

**1.3.7 Multi-Objective Optimization on the Basis of Ratio Analysis (MOORA) Method**

In this method, the decision matrix was normalized using the square root method as in WSM and WPM [21]. Then the normalized assessment sum  $S_i$  for each alternative was estimated by subtracting the weighted sum of the non-benefit attributes from the weighted sum of the benefit attributes, as presented in Eq. (13). Then the alternatives were ranked based on the assessment sum.

$$S_i = \underbrace{\sum_{j=1}^n p_{ij} \times w_j}_{\text{Weighted sum of non-benefit attributes}} - \underbrace{\sum_{j=1}^n p_{ij} \times w_j}_{\text{Weighted sum of benefit attributes}}. \quad (13)$$

**1.3.8 Technique for Order Preference by Similarity to Ideal Solution (TOPSIS)**

In this method, the decision matrix was normalized using the square root method as in Eq. (6). Then the relative closeness to the ideal solution  $P_i$  was estimated by Eq. (14) [12]. In the equation,  $A_j^*$  represents the best criterion value of the weighted normalized matrix (positive ideal) and  $A_j^-$  represents the worst criterion value (negative ideal). The alternatives were then ranked based on the relative closeness.

$$P_i = \frac{\sqrt{\sum_{j=1}^n (p_{ij} \cdot w_j - A_j^-)^2}}{\sqrt{\sum_{j=1}^n (p_{ij} \cdot w_j - A_j^*)^2} + \sqrt{\sum_{j=1}^n (p_{ij} \cdot w_j - A_j^-)^2}}. \quad (14)$$

**1.3.9 Grey Relational Analysis (GRA) method**

In this method, the alternatives were ranked based on the grey relational degree  $b_i$  [22]. The deviation  $\Delta_{0i}$  was estimated as a difference between the reference series (largest value series) and the individual alternative series [22]. By estimating  $\Delta_{0i}$ , the values of  $b_i$  were calculated as presented in Eq. (15).

$$b_i = \sum_{j=1}^n w_j \frac{\min_i \min_j \Delta_{0i}(j) + \delta \min_i \min_j \Delta_{0i}(j)}{\Delta_{0j}(j) + \delta \min_i \min_j \Delta_{0i}(j)}. \quad (15)$$

**1.3.10 VIKOR method**

VIKOR is an abbreviation for its Serbian expansion ‘Vise kriterijumska optimizacija i kompromisno resenje’ which means Multi-criteria compromise ranking. In this method, the normalized decision matrix was obtained using the square root method as in Eq. (6). From the normalized matrix, the maximum criterion value  $p_j^*$  and the minimum criterion value  $p_j^-$  were estimated and were applied to Eqs. (16) to (18) to estimate the aggregate function  $U_i^V$  (also referred as VIKOR index) for each alternative. In the equations, the superscripts ‘\*’ and ‘-’ represents the maximum and minimum value respectively. The alternatives were then ranked in the **increasing** order of  $U_i^V$  [23].

$$U_i^V = v \underbrace{\left[ \frac{S_i - S^*}{S^- - S^*} \right]}_I + (1 - v) \underbrace{\left[ \frac{R_i - R^*}{R^- - R^*} \right]}_{II}, \quad (16)$$

$$I = \frac{\left[ \sum_{j=1}^n w_j \left( \frac{p_j^* - p_{ij}}{p_j^* - p_j^-} \right) \right] - \left[ \sum_{j=1}^n w_j \left( \frac{p_j^* - p_{ij}}{p_j^* - p_j^-} \right) \right]^*}{\left[ \sum_{j=1}^n w_j \left( \frac{p_j^* - p_{ij}}{p_j^* - p_j^-} \right) \right]^- - \left[ \sum_{j=1}^n w_j \left( \frac{p_j^* - p_{ij}}{p_j^* - p_j^-} \right) \right]^*}, \quad (17)$$

$$II = \frac{\left[ \max_i w_j \left( \frac{p_j^* - p_{ij}}{p_j^* - p_j^-} \right) \right] - \left[ \max_i w_j \left( \frac{p_j^* - p_{ij}}{p_j^* - p_j^-} \right) \right]^*}{\left[ \max_i w_j \left( \frac{p_j^* - p_{ij}}{p_j^* - p_j^-} \right) \right]^- - \left[ \max_i w_j \left( \frac{p_j^* - p_{ij}}{p_j^* - p_j^-} \right) \right]^*}. \quad (18)$$

**1.3.11 Preference Ranking Organization Method for Enrichment Valuation (PROMETHEE)**

In this method, the decision matrix was normalized and the overall global preference index  $P_j$  was estimated by estimating the difference in the values of one alternative criterion with another (preference matrix). Using the preference matrix, the positive preference flow  $\phi^+(i)$  and negative preference flow  $\phi^-(i)$  (for non-benefit criterion) was estimated. Then the net flow  $\phi(i)$  was ultimately estimated using Eq. (19) [24]. Then the alternatives were ranked based on the net flow (PROMETHEE II).

$$\phi(i) = \underbrace{\frac{1}{m-1} \sum_{x \in X} \sum_{j=1}^n w_j P_j(i, x)}_{\phi^+(i)} - \underbrace{\frac{1}{m-1} \sum_{x \in X} \sum_{j=1}^n w_j P_j(x, i)}_{\phi^-(i)}. \quad (19)$$

**Table 2.** Estimated evaluating parameters through the employed algorithms

Algorithm index	Algorithm name	Evaluating parameter		Phase change material					
		Parameter	Symbol	1	2	3	4	5	6
1	WSM-EWM	Weighted sum	$S_i^{WSM}$	0.5064	0.4511	0.2896	0.3581	0.4097	0.3107
2	WSM-CRITIC	Weighted sum	$S_i^{WSM}$	0.4662	0.4413	0.3189	0.3811	0.4166	0.3320
3	WSM-AHP	Weighted sum	$S_i^{WSM}$	0.5350	0.4385	0.3282	0.3284	0.3780	0.3277
4	WPM-EWM	Weighted product	$S_i^{WPM}$	0.4868	0.4489	0.2641	0.3407	0.3910	0.3076
5	WPM-CRITIC	Weighted product	$S_i^{WPM}$	0.4491	0.4394	0.2944	0.3651	0.4027	0.3275
6	WPM-AHP	Weighted product	$S_i^{WPM}$	0.5140	0.4363	0.3037	0.3082	0.3574	0.3240
7	SAW-EWM	Preference index	$V_i$	0.9407	0.5017	0.8331	0.8166	0.1956	0.3776
8	SAW-CRITIC	Preference index	$V_i$	0.9402	0.6142	0.8684	0.8425	0.1014	0.1942
9	SAW-AHP	Preference index	$V_i$	0.9752	0.5584	0.7802	0.8887	0.1086	0.2075
10	COPRAS-EWM	Performance index	$U_i, \%$	100	78.6542	49.3705	69.8570	67.6893	61.4469
11	COPRAS-CRITIC	Performance index	$U_i, \%$	100	82.0728	58.1734	79.7784	73.2509	70.3310
12	COPRAS-AHP	Performance index	$U_i, \%$	100	73.1212	54.0881	59.7485	59.4716	61.2537
13	ARAS-EWM	Utility degree	$K_i$	0.9403	0.7420	0.4625	0.6609	0.6408	0.5787
14	ARAS-CRITIC	Utility degree	$K_i$	0.9358	0.7710	0.5473	0.7517	0.6908	0.6621
15	ARAS-AHP	Utility degree	$K_i$	0.9752	0.7164	0.5273	0.5888	0.5858	0.6
16	WASPAS-EWM	Relative importance	$Q_i$	0.9356	0.7423	0.4453	0.6525	0.6339	0.5758
17	WASPAS-CRITIC	Relative importance	$Q_i$	0.9350	0.7785	0.5435	0.7523	0.6940	0.6699
18	WASPAS-AHP	Relative importance	$Q_i$	0.9728	0.7217	0.5144	0.5891	0.5852	0.6031
19	MOORA-EWM	Assessment sum	$S_i$	0.4205	0.3080	0.1497	0.2620	0.2437	0.2153
20	MOORA-CRITIC	Assessment sum	$S_i$	0.3750	0.2877	0.1687	0.2779	0.2383	0.2296
21	MOORA-AHP	Assessment sum	$S_i$	0.4555	0.3061	0.1986	0.2315	0.2243	0.2393
22	TOPSIS-EWM	Relative closeness	$P_i$	0.8452	0.6029	0.2191	0.4195	0.4786	0.3134
23	TOPSIS-CRITIC	Relative closeness	$P_i$	0.7929	0.5895	0.2070	0.4866	0.4722	0.3467
24	TOPSIS-AHP	Relative closeness	$P_i$	0.9369	0.4902	0.3004	0.2579	0.3232	0.3080
25	GRA-EWM	Grey Relational degree	$b_j$	0.1510	0.1024	0.0632	0.099	0.0929	0.0782
26	GRA-CRITIC	Grey Relational degree	$b_j$	0.1509	0.0917	0.0648	0.1190	0.0827	0.0989
27	GRA-AHP	Grey Relational degree	$b_j$	0.1601	0.0933	0.0666	0.0909	0.0818	0.0843
28	VIKOR-EWM	VIKOR index	$U_i^V$	0	0.1744	0.5	0.3973	0.3833	0.3116
29	VIKOR-CRITIC	VIKOR index	$U_i^V$	0	0.2273	0.5	0.3362	0.3394	0.2726
30	VIKOR-AHP	VIKOR index	$U_i^V$	0	0.2912	0.3043	0.5	0.4870	0.3434
31	PROMETHEE-EWM	Net flow	$\phi(i)$	0.4902	0.0918	-0.3992	0.0254	-0.0867	-0.1214
32	PROMETHEE-CRITIC	Net flow	$\phi(i)$	0.4635	-0.0482	-0.3844	0.1832	-0.2380	0.0238
33	PROMETHEE-AHP	Net flow	$\phi(i)$	0.5879	0.0347	-0.2866	-0.0674	-0.2162	-0.0524

**1.4 Validation of the Outcomes**

To validate the reliability of the outcomes, a correlation of outcomes method adopted by Villacreses et al. [25] was adopted in this current study. The ranking outcomes achieved through all of the 33 algorithms were correlated with each other. Three cases of correlations were performed and Pearson’s correlation coefficient was estimated for all of the cases. In the first case, the outcomes were correlated by considering all of the PCMs. In the second case, a rank-wise frequency estimation was performed and the alternatives witnessing highest first, second and third rank frequencies alone were considered for the correlation. In the third case, adopting the similar procedure, the alternatives witnessing highest first and second rank frequencies alone were considered. Based on the results of the three cases, the concurrence of the outcomes were validated. The Pearson’s coefficients  $r_{kl}$  were estimated using Eq. (20). In the validation

process, all 33 algorithms were correlated with each other and hence a total of 1089 Pearson’s coefficients were estimated for a single case.

$$r_{kl} = \frac{\sum_{i=1}^m (k_i - \bar{k})(l_i - \bar{l})}{\sqrt{\sum_{i=1}^m (k_i - \bar{k})^2} \sqrt{\sum_{i=1}^m (l_i - \bar{l})^2}} \tag{20}$$

**2 RESULTS AND DISCUSSION**

**2.1 Selection of the Optimal PCM through MCDM Algorithms**

In this study, a total of 33 solution combinations were tested. The weights were obtained, and further the obtained weights were employed to estimate the evaluating parameters. The evaluating parameter for each algorithm was estimated and the alternative PCMs were ranked based on the magnitude of the

**Table 3.** Estimated weights through the employed methods

Criteria	EWM	CRITIC	AHP
Melting temperature	0.0003	0.2030	0.0676
Heat of fusion	0.3077	0.2021	0.4531
Density	0.1778	0.1794	0.0743
Thermal conductivity	0.3615	0.2515	0.2636
Specific heat	0.1528	0.1640	0.1414

evaluating parameters. The estimated evaluating parameters are presented in Table 2 and the graphical form of the ranking outcomes is presented in Fig. 2. The weights obtained for each case is presented in Table 3. From the table, it can be observed that the weights obtained through the objective and subjective methods differ from each other. Since the weights differ, the functional priority for each criterion is changed. This will have implications on the outcomes as well. The objective method EWM has prioritized thermal conductivity over the others, and has estimated melting temperature to be the least prioritized criteria. But in the case of the CRITIC method, though thermal conductivity has been prioritized over the others, all other criteria have been estimated to have similar weights. Further, observing the weights obtained through the subjective AHP method, heat of fusion has been estimated to have the highest priority and melting temperature has been estimated to have the least priority. This was expected because EWM and CRITIC are objective methods, wherein the outcomes were purely based on mathematical outcomes and AHP is a subjective approach wherein the outcomes were based on the preferences from the designer. Since in the EWM and CRITIC methods, thermal conductivity has been estimated to have the highest priority, the outcomes employing those weight will prefer materials with higher thermal conductivity. On the contrary, AHP has estimated the highest priority for latent heat of fusion. Hence the method will prefer corresponding outcomes. The results are reliable as there is a clear demarcation between the subjective and objective weighting scheme outcomes. But since this current study is intended to select a PCM through a comparative approach, this variation will be helpful to select the optimal PCM from a holistic approach. The necessity for such a holistic approach arises as this research study addresses the research gap due to the deficiency of utilizing limited weight estimation schemes.

From the figure, it can be observed that the first alternative PCM Erythritol has been ranked as the best alternative in all of the algorithms. Also, it

can be observed that the PCM  $\text{MgCl}_2 \cdot 6\text{H}_2\text{O}$  (MCHH) has been ranked as the second best PCM in most algorithms. On a comparative note, it can be further observed that the solutions derived through applying EWM weights and CRITIC weights are similar in most cases. But comparing the efforts required for each method, it was observed that COPRAS, GRA, PROMETHEE methods required more level of mathematical computations than the other methods.

## 2.2 Pearson's Coefficient Study

To validate the reliability of the outcomes, a three case Pearson's coefficient study was performed. The results of the study are presented in Fig. 3. In the first case of the Pearson's study, it was observed that most of the correlation coefficients were above 0.5, but yet there was a significant quantity of coefficients below 0.5. This indicates that all six ranks of the 33 algorithms did not concur each other. But, the objective of this study was to select the optimal PCM for the TES heat exchanger. If one would accentuate the objective, it is necessary that the first ranked PCM and the second ranked PCM is similar in most cases. This approach to study the concurrence of the first ranked and the second ranked PCM was employed to validate the reliability of this comparative study and as it could be noted from Table 3, PCMs were ranked purely based on their evaluating parameters. Even when there is a very small difference between the evaluating parameters, the PCMs will still be ranked based on the differences. Further, the approach does not rely upon a single combinational algorithm, but depends on the comparative conclusion derived through employing 33 combinational algorithms. In this study, all of the algorithms had ranked Erythritol as the suitable PCM, irrespective of the type of algorithm and the weight estimation scheme employed. Further, most of the algorithms have ranked MCHH as the second best suited PCM. Hence, the ranking scheme is reliable. To verify the reliability of the outcomes, two more cases were performed. A frequency study was performed to proceed further. A rank wise frequency was recorded. The rank wise data is presented in Fig. 3. It has been observed that Erythritol was the best ranked PCM (Rank 1) in all of the algorithms. Further, MCHH has been estimated as the second best PCM in 28 of 33 algorithms. Similarly for all other ranks, the frequencies were recorded. From the frequency study, it was observed that Erythritol, MCHH, and PlusICE H120 were the first three prioritized PCMs from majority of the algorithms. Hence, for the second case of Pearson's study, only the three were considered

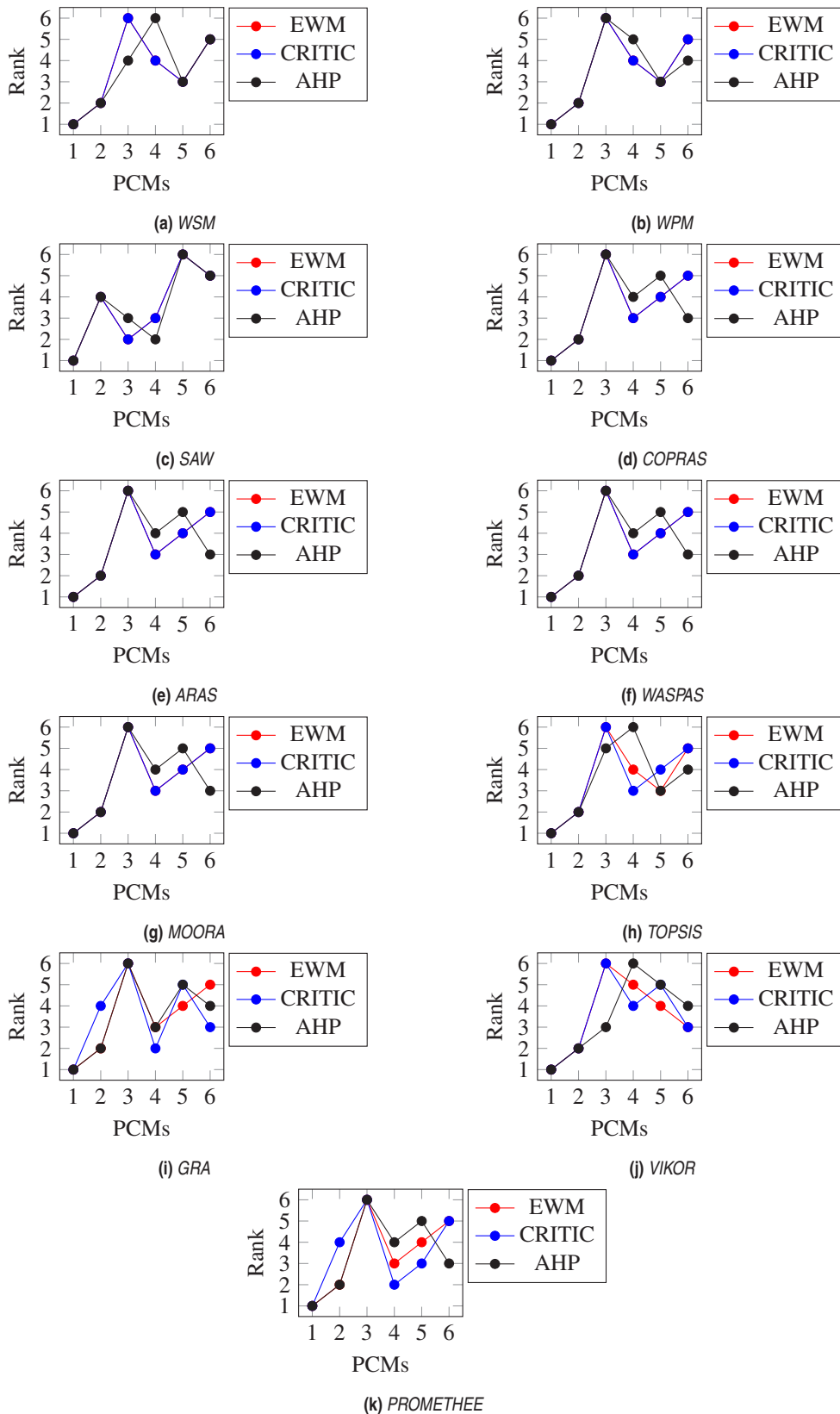


Fig. 2. Comparison of the various ranking outcomes

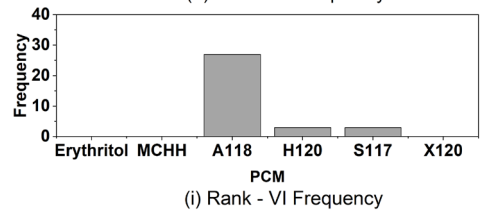
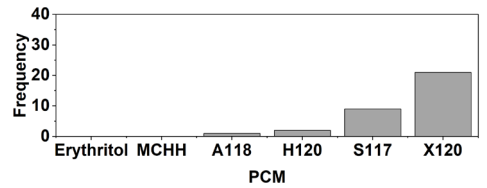
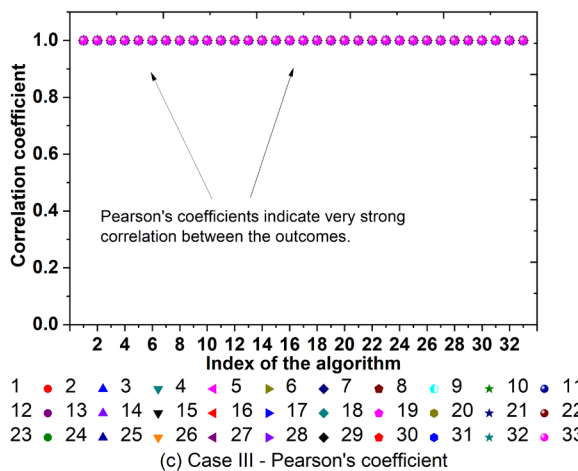
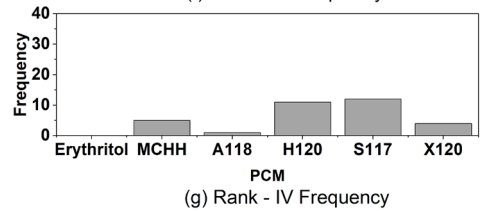
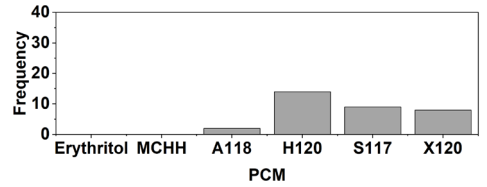
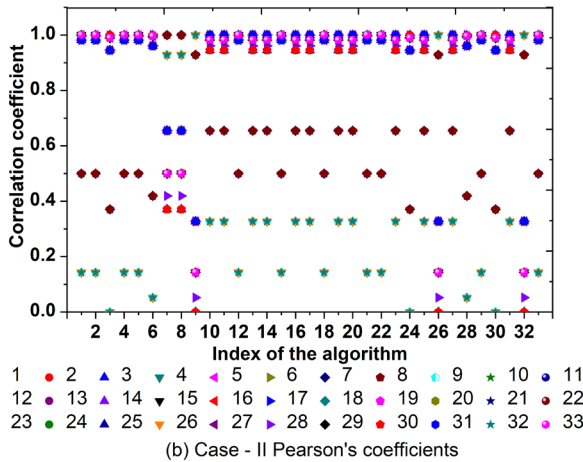
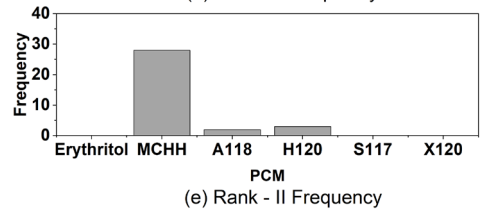
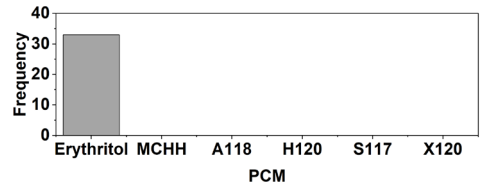
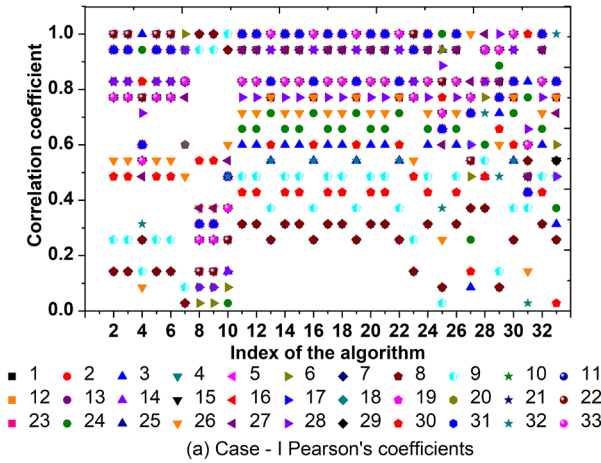


Fig. 3. Panels (a)-(c) present the variation of the Pearson's correlation coefficients for different cases and panels (d)-(i) presents the ranking outcome frequencies of the PCM alternatives

for correlation and for the third case of the Pearson's study, only Erythritol and MCHH were considered. The second case correlations indicates that there is comparatively stronger correlation than the first case. Further, the third case indicates that there is very strong correlation compared to other cases. All of the third case correlations have rendered a coefficient of 1. Hence from this three case analysis, the reliability of the results have been validated.

### 2.3 Discussion from Heat Exchanger Perspective

By applying the aforementioned algorithms, Erythritol has been selected as the optimal PCM for the steam cooking application. If one would intricately observe the functionality of the various weight estimation techniques, it can be observed that the objective techniques EWM and CRITIC have prioritized thermal conductivity whereas subjective AHP has prioritized latent heat of fusion. This can be ascribed to the Saaty's scale weights provided by the the authors. But despite this observation, all algorithms have selected Erythritol. Erythritol has the highest latent heat of fusion ( $331 \text{ kJkg}^{-1}$ ) among the alternatives, and hence less quantity of the PCM is required. Since, less quantity of PCM is required, the heat exchanger size will be comparatively smaller than when other PCMs are used. Further, Erythritol chosen has the highest thermal conductivity and hence the melting time of the PCM will also be comparatively lower. The lower specific heat of Erythritol also is an added benefit. Further, if one would consider the highest density, PlusICE H120 has the highest density, but since latent heat and thermal conductivity were prioritized over density, the algorithms have preferred Erythritol over PlusICE H120 PCM. Hence, from a heat exchanger design perspective, it can be inferred that the chosen PCM can be strongly envisaged to be suitable for the sustainable steam cooking application.

From this study, a clear demarcation has been asserted between the functionality of all of the considered algorithms. From the study, by combining the weights and the main algorithms, it was observed that TOPSIS, GRA, VIKOR and PROMETHEE algorithms have significantly distinguished the outcomes based on each weight estimation scheme. Further instead of relying on one single algorithm, this method has made a reliable selection out of the various combinational algorithms proposed. Hence, this novel method integrating MCDM and Pearson's coefficient study is highly recommended for industrial practice.

### 3 CONCLUSIONS

Renewable energy based steam cooking paves the way for a sustainable steam cooking process when integrated with PCM based TES heat exchangers. However the optimal selection of the PCM plays a crucial role in the heat exchanger design. Hence, this research work has performed a comparative study for the selection of the appropriate PCM for the application. This study has tested 11 MCDM algorithms with 3 weight estimation techniques and through all of the algorithms, Erythritol has been chosen as the appropriate PCM. Erythritol has satisfactory thermo-physical properties to be used in the TES heat exchanger for the application. The ranking outcomes from various algorithms were validated through a three case Pearson's correlation coefficient study. The Pearson's correlation coefficient study has validated that all of the algorithms have very strong correlation in selecting the first and the second best PCMs.

### 4 ACKNOWLEDGEMENTS

The authors would like to thank the Department of Science and Technology (DST), Government of India and PSG College of Technology, Coimbatore, India for their financial support.

### 5 REFERENCES

- [1] Sharma, S.D., Sagara, K. (2005). Latent heat storage materials and systems - A Review. *International Journal of Green Energy*, vol. 2, p. 1-56, DOI:10.1081/GE-200051299.
- [2] Motwani, K., Patel, J. (2019). Cost analysis of solar parabolic trough collector for cooking in Indian hostel – a case study. *International Journal of Ambient Energy*, DOI:10.1080/01430750.2019.1653968.
- [3] Xu, H., Sze, J.Y., Romagnoli, A., Py, X. (2017). Selection of Phase Change Material for Thermal Energy Storage in Solar Air Conditioning Systems. *Energy Procedia*, vol. 105, p. 4281-4288, DOI:10.1016/j.egypro.2017.03.898.
- [4] Mardani, A., Jusoh, A., Nor, K.M.D., Khalifah, Z., Zakwan, N., Valipour, A. (2015). Multiple criteria decision-making techniques and their applications – a review of the literature from 2000 to 2014. *Economic Research-Ekonomska Istraživanja*, vol. 28, no. 1, p. 516-571, DOI:10.1080/1331677X.2015.1075139.
- [5] Wang, J., Zhai, X., Liu, C., Zhang, Y. (2017). Determination of the Threshold for Extreme Load Extrapolation Based on Multi-Criteria Decision-Making Technology. *Strojniški vestnik-Journal of Mechanical Engineering*, vol. 63, no. 3, p. 201-211, DOI:10.5545/sv-jme.2016.3557.

- [6] Prvulovic, S., Tolmac, D., Radovanovic, L. (2011). Application of Promethee-Gaia Methodology in the Choice of Systems for Drying Paltry-Seeds and Powder Materials. *Strojniški vestnik-Journal of Mechanical Engineering*, vol. 57, no. 10, p. 778-784, DOI:10.5545/sv-jme.2008.068.
- [7] Vindiš, P., Muršec, B., Rozman, Č., Čus, F. (2010). A Multi-Criteria Assessment of Energy Crops for Biogas Production. *Strojniški vestnik-Journal of Mechanical Engineering*, vol. 56, no. 1, p. 63-70.
- [8] Lee, H.C., Chang, C.T. (2018). Comparative analysis of MCDM methods for ranking renewable energy sources in Taiwan. *Renewable and Sustainable Energy Reviews*, vol. 2, p. 883-896, DOI:10.1016/j.rser.2018.05.007.
- [9] Emovon, I., Ogheneyorvwho, S. (2020). Application of MCDM method in material selection for optimal design: A review. *Results in Materials*, vol. 7, p. 100115, DOI:10.1016/j.rinma.2020.100115.
- [10] Wang, Y., Zhang, Y., Yang, W., Ji, H. (2015). Selection of Low-Temperature Phase-Change Materials for Thermal Energy Storage Based on the VIKOR Method. *Energy Technology*, vol. 3, p. 84-89, DOI:10.1002/ente.201402098.
- [11] Yang, K., Zhu, N., Chang, C., Wang, D., Yang, S., Ma, S. (2018). A methodological concept for phase change material selection based on multi-criteria decision making (MCDM): A case study. *Energy*, vol. 165, p. 1085-1096, DOI:10.1016/j.energy.2018.10.022.
- [12] Gadhave, P., Prabhune, C., Pathan, F. (2020). Selection of phase change material for domestic water heating using multi criteria approach. *Australian Journal of Mechanical Engineering*, DOI:10.1080/14484846.2020.1842297.
- [13] Adali, E.A., Işık, A.T. (2017). Critic and Maut Methods for the Contract Manufacturer Selection Problem. *European Journal of Multidisciplinary Studies*, vol. 2, no. 5, p. 93-101, DOI:10.26417/ejms.v5i1.p93-101.
- [14] Mayilvelnathan, V., Arasu, A.V. (2019). Characterisation and thermophysical properties of graphene nanoparticles dispersed erythritol PCM for medium temperature thermal energy storage applications. *Thermochimica Acta*, vol. 676, p. 94-103, DOI:10.1016/j.tca.2019.03.037.
- [15] Hühlein, S.H., König-Haagen, A., Brüggemann, D. (2017). Thermophysical Characterization of  $MgCl_2 \cdot 6H_2O$ , Xylitol and Erythritol as Phase Change Materials (PCM) for Latent Heat Thermal Energy Storage(LHTES). *Materials*, vol. 10, p. 444, DOI:10.3390/ma10040444.
- [16] PlusICE Product Catalogue. Arena, from <https://www.pcmproducts.net/files/PlusICE%20Range%202021-1.pdf>, accessed on 2021-06-10.
- [17] Xu, H., Sze, J.Y., Romagnoli, A., Py, X. (2017). Selection of Phase Change Material for Thermal Energy Storage in Solar Air Conditioning Systems. *Energy Procedia*, vol. 105, p. 4281-4288, DOI:10.1016/j.egypro.2017.03.898.
- [18] Organ, A., Yalçın, E. (2016). Performance Evaluation Of Research Assistants By Copras Method. *European Scientific Journal*, p. 102-109.
- [19] Zavadskas, E.K., Turskis, Z. (2010). A new additive ratio assessment (ARAS) method in multicriteria decision making. *Ukio Technologinis ir Ekonominis Vystymas*, vol. 16, no. 2, p. 159-172, DOI:10.3846/tede.2010.10.
- [20] Chakraborty, S., Zavadskas, E.K. (2014). Applications of WASPAS Method in Manufacturing Decision Making. *Informatica*, vol. 25, no. 1, p. 1-20, DOI:10.15388/Informatica.2014.01.
- [21] Brauers, W.K.M., Zavadskas, E.K. (2006). The MOORA method and its application to privatization in a transition economy. *Control and Cybernetics*, vol. 35, no. 2, p. 445-469.
- [22] Wu, W. (2017). Grey Relational Analysis Method for Group Decision Making in Credit Risk Analysis. *Eurasia Journal of Mathematics, Science and Technology Education*, vol. 13, no. 12, p. 7913-7920, DOI:10.12973/ejmste/77913.
- [23] San Cristóbal, J.R. (2011). Multi-criteria decision-making in the selection of a renewable energy project in Spain: The VIKOR method. *Renewable Energy*, vol. 36, p. 498-502, DOI:10.1016/j.renene.2010.07.031.
- [24] Bogdanovic, D., Nikolic, D., Ilić, I. (2012). Mining method selection by integrated AHP and PROMETHEE method. *Anais da Academia Brasileira de Ciências*, vol. 84, no. 1, p. 219-233, DOI:10.1590/S0001-37652012000100023.
- [25] Villacreses, G., Gaona, G., Martínez-Gómez, J., Jijón, D.J. (2017). Wind farms suitability location using geographical information system (GIS), based on multi-criteria decision making (MCDM) methods: The case of continental Ecuador. *Renewable Energy*, vol. 109, p. 275-286, DOI:10.1016/j.renene.2017.03.041.



# Vsebina

**Strojniški vestnik - Journal of Mechanical Engineering**  
**letnik 67, (2021), številka 11**  
**Ljubljana, november 2021**  
**ISSN 0039-2480**

**Izhaja mesečno**

## **Razširjeni povzetki (extended abstracts)**

Duraisivam Saminatharaja, Suresh Periyakgounder, Mahalingam Selvaraj, Jamuna Elangandhi: Študija zmogljivosti procesa EDM z elektrodo iz kompozita bakra in ojačitvenih delcev TiC/ZrSiO <sub>4</sub>	SI 69
Changbin Dong, Yongping Liu, Gang Zhao: Metoda za izračun izkoristka eliptične zobniške dvojice na osnovi eksperimentalnih podatkov	SI 70
Govindaraj Periasamy, Senthilkumar Mouleeswaran, Prabhu Raja Venugopal, Chellapandi Perumal: Raziskava hidrodinamičnih lastnosti toka v cevni kači z ovalnostjo in gubami	SI 71
Mingjun Du, Yongjun Hou, Tong Tang, Lian Tang, Jialong Wang, Hongbo Gao: Sinhronizacija in stabilnost treh sovrtečih se rotorjev, povezanih z vzmetmi v neresonančni sistem	SI 72
Andrzej Kosucki, Łukasz Stawiński, Adrian Morawiec, Jarosław Goszczak: Elektrohيدرavlčni pogon aktivno obremenjene dvigalne naprave z variabilnim razmerjem	SI 73
Paul Gregory Felix, Velavan Rajagopal, Kannan Kumaresan: Uporaba algoritmov MCDM pri izbiri fazno spremenljivih snovi v prenosnikih toplote sistemov za shranjevanje toplotne energije	SI 74



# Študija zmogljivosti procesa EDM z elektrodo iz kompozita bakra in ojačitvenih delcev TiC/ZrSiO<sub>4</sub>

Duraisivam Saminatharaja<sup>1,\*</sup> – Suresh Periyakgounder<sup>2</sup> – Mahalingam Selvaraj<sup>3</sup> – Jamuna Elangandhi<sup>1</sup>

<sup>1</sup>Tehniški kolidž Kavery, Oddelek za strojništvo, Indija

<sup>2</sup>Tehniški kolidž Sona (avtonomni), Oddelek za mehatroniko, Indija

<sup>3</sup>Tehniški kolidž Sona (avtonomni), Oddelek za strojništvo, Indija

Proces elektroerozijske obdelave (EDM) se pogosto uporablja za izdelavo delov kompleksnih oblik iz materialov, ki jih je težko obdelovati z odrezavanjem. Izdelava orodij za proces EDM po tradicionalnih postopkih je časovno potratna. Nerjavno jeklo (SS)-304 je razširjeno v različnih panogah proizvodne industrije zaradi visoke žilavosti ter obstojnosti proti obrabi in koroziji.

Pri izboljševanju zmogljivosti elektroerozijske obdelave imajo poleg električnih parametrov ključno vlogo parametri kot so modifikacije orodja, spremembe dielektrika, vrtenje in vibracije orodja.

Pregled literature je pokazal, da se raziskovalci lotevajo izboljšav procesa EDM na različne načine. Izdelava orodij za elektroerozijsko obdelavo po postopkih prašne metalurgije je manj raziskana. Nekaj člankov sicer opisuje uporabo sintranih orodij, pri vseh metodah pa sta se kakovost površine in hitrost obdelave izkazali za neustrezni zaradi neprimerne ojačitve bakrene elektrode. Delci titanovega karbida in cirkonijevega silikata imajo zaradi svoje kristalne strukture visoko afiniteto do bakra.

Za to raziskavo sta bili s tehniko prašne metalurgije pripravljene dve elektrodi z različnim deležem ojačitve: 90 % Cu, 5 % TiC, 5 % ZrSiO<sub>4</sub> (Cu<sub>90</sub>) in 80 % Cu, 5% TiC, 5 % ZrSiO<sub>4</sub> (Cu<sub>80</sub>). Velikost ojačitvenih delcev je bila pri vseh elektrodah manjša od 75 μm. Pripravljene so bile kompozitne elektrode premera 10 mm in dolžine 5 cm. Za material obdelovanca je bilo izbrano nerjavno jeklo SS 304 debeline 5 mm. Zasnovano je bilo ortogonalno polje (OA) L 18 s temi vhodnimi parametri: trije tipi orodij (Cu, Cu<sub>90</sub>, Cu<sub>80</sub>), maksimalni tok razelektritve (PC) v A, čas impulza (PT) v μs in napetost v reži (GV) v V. Zmogljivost EDM je bila ocenjena s stopnjo odvzema materiala (MRR), stopnjo obrabe orodja (TWR) in površinsko hrapavostjo (SR). Parametri procesa so bili optimizirani s tehniko razvrstitve po podobnosti z idealno rešitvijo (TOPSIS) in sivo relacijsko analizo (GRA). Optimizacijski tehniki TOPSIS in GRA sta dali enako kombinacijo optimalnih parametrov za nižjo vrednost TWR in SR ter višjo vrednost MRR: orodje Cu<sub>90</sub>, tok 8 A, čas impulza 15 μs in napetost v reži 75 V.

Tabela ANOVA po analizi TOPSIS kaže, da daje čas impulza poglobliten prispevek k zmogljivosti obdelave v višini pribl. 46,8 %, maksimalni tok razelektritve pa daje prispevek k zmogljivosti obdelave v višini pribl. 39,3 % po analizi GRA.

Opravljen je bila tudi analiza obdelane površine z vrstično elektronsko mikroskopijo (SEM) za razumevanje vpliva orodja na kakovost obdelave.

**Ključne besede: prašna metalurgija, kompozitno orodje, baker, EDM, TOPSIS, GRA**

# Metoda za izračun izkoristka eliptične zobniške dvojice na osnovi eksperimentalnih podatkov

Changbin Dong<sup>1</sup> – Yongping Liu<sup>1</sup> – Gang Zhao<sup>2</sup>

<sup>1</sup> Tehniška univerza v Landžovu, Šola za strojništvo in elektrotehniko, Kitajska

<sup>2</sup> Državni laboratorij province Hubej za mehanske prenosnike in proizvodni inženiring, Kitajska

Članek podaja predlog metode za analizo izkoristka eliptičnega zobniškega prenosnika.

Zgrajeno je bilo preizkuševališče za eliptične zobniške prenosnike in iz zbranih podatkov je bil izračunan izkoristek zobniške dvojice.

Po modelu nihanja obremenitev pri eliptičnih zobnikih je bilo zgrajeno preizkuševališče za te prenosnike. Pridobljene so bile vrednosti navora na vhodu in na izhodu za vrtenje v obeh smereh. Na podlagi teh podatkov je bil izračunan izkoristek prenosa eliptične zobniške dvojice ter analiziran vpliv obremenitve in hitrosti nanj. Navor na pogonskem in gnanem zobniku pod obremenitvijo se povečuje z ekscentričnostjo in z obremenitvijo eliptične zobniške dvojice. Izkoristek prenosnika se zmanjšuje s povečevanjem hitrosti in navora na vhodu. To dokazuje, da je prenosnik z zobniki neokrogle (eliptične) oblike primeren za nizke hitrosti in velike napore.

V literaturi ni člankov, ki bi obravnavali izkoristek eliptičnih zobniških prenosnikov. Pričujoči članek prvič podaja predlog za izračun izkoristka eliptičnih zobnikov. Rezultati raziskave dajejo teoretične smernice za določanje izkoristka prenosa in za nadaljnje eksperimentalne raziskave neokroglih zobniških dvojic oz. prenosnikov.

**Ključne besede:** eliptični zobnik, preskus prenosnika, nihanje obremenitve, navor, izkoristek prenosa

# Raziskava hidrodinamičnih lastnosti toka v cevni kači z ovalnostjo in gubami

Govindaraj Periasamy<sup>1,\*</sup> – Senthilkumar Mouleeswaran<sup>2</sup> – Prabhu Raja Venugopal<sup>1</sup> – Chellapandi Perumal<sup>3</sup>

<sup>1</sup> Tehniški kolidž PSG, Oddelek za strojništvo, Indija

<sup>2</sup> Tehniški kolidž PSG, Oddelek za proizvodni inženiring, Indija

<sup>3</sup> Indijski inštitut za tehnologijo Madras, Oddelek za uporabno mehaniko, Indija

Preoblikovanje cevnih kač z valjanjem povzroča pojav geometrijskih napak v obliki nagubanosti in ovalnosti, ki lahko vplivajo na hidrodinamične lastnosti toka fluida v cevni kači pri aplikacijah, kot so razvlaževalniki zraka. Ovalnost cevi povzroči tanjšanje sten na zunanji strani zaradi nateznih napetosti ter odebelitev sten na notranji strani zaradi tlačnih sil med procesom preoblikovanja. Na notranji strani kače se pojavi tudi nagubanje zaradi čezmernih tlačnih sil. Najtanjša zunanja stena se lahko v primeru visokega porasta tlaka v kači celo poruši. Odvečen material v gubah na notranji steni vpliva na integriteto cevne kače ter povzroči povečanje teže prenosnikov toplote za aplikacije, kot so razvlaževalniki zraka. Geometrijske nepravilnosti vplivajo na hidrodinamične lastnosti toka v cevni kači ter povzročajo nezaželene turbulence in s tem večje pretočne izgube.

V tej študiji je bila opravljena eksperimentalna in numerična analiza hidrodinamičnega vedenja toka v cevni kači za primer prenosnika toplote v razvlaževalniku zraka. Meritev ovalnosti več cevnih kač je pokazala, da je največja vrednost ovalnosti 3,2 %, kar je še znotraj dopustnih mej po standardu ASME B31.3. Zato ni mogoče pričakovati, da bi ovalnost lahko vplivala na pretok.

Nagubanost kot druga vrsta geometrijske nepravilnosti se pojavlja na notranji strani kač zaradi stiskanja med postopkom preoblikovanja cevi. Za eksperimentalno analizo je bila izbrana bakrena cevna kača s tremi zavoji, gubami in ovalnostjo za ocenitev globalnih hidrodinamičnih lastnosti toka skozi cevno kačo, rezultati pa so bili primerjani s cevno kačo z idealno geometrijo, torej brez nagubanosti in ovalnosti. Ugotovljeno je bilo, da nagubanost pomembno prispeva k tlačnemu padcu v cevni kači. Pri vrednosti  $R_e$  v višini 100.000 je bila ugotovljena največja tlačna razlika v višini 2 kPa. Sicer gladka cev z gubami in ovalnostjo se tedaj obnaša kot groba cev. Vpliv nagubanosti je bil ocenjen s količnikom trenja, ustreza ekvivalentna površinska hrapavost pa se je zaradi prisotnosti gub na cevni kači povečala za 5,7-krat. Ekvivalentna hrapavost cevne kače z gubami in brez nje pri vrednostih  $R_e$  nad 60.000 znaša 2,3  $\mu\text{m}$  oz. 0,3  $\mu\text{m}$ .

Opravljene so bile numerične simulacije za določitev porazdelitve tlaka, porazdelitve hitrosti in sekundarnega toka v cevni kači. Rezultati so bili nato še eksperimentalno potrjeni. Numerična analiza globalnega tlačnega padca in hitrostnega polja je razkrila vpliv gub na pretočno polje v obliki porasta ekvivalentne hrapavosti cevne kače in nihanj v hitrostni porazdelitvi zaradi spremenljivega preseka po dolžini cevne kače. V numeričnih simulacijah je bil zajet kritični del cevne kače z več gubami za preučitev lokaliziranega vpliva gub na pretočno polje. Lokalna analiza je pokazala povečanje turbulentnosti toka. Sekundarni tok povzroči znaten podtlak v pretočnem polju, ta pa je povezan z mehanizmi lokalnih poškodb, kot sta kavitacija in nastanek jamic. Omenjeni mehanizmi bi lahko povzročili resnejše posledice pri uporabi nagubanih cevnih kač v prenosnikih toplote za kritične aplikacije, kot sta npr. jedrska tehnika in medicina.

Rezultati pričujočega dela se nanašajo le na cevno kačo določene velikosti in zato veljajo le za to konfiguracijo oz. za podobne cevne kače s tako porazdelitvijo gub. Zato bo treba opraviti še parametrično študijo, ki bo upoštevala variabilnost geometrije cevnih kač ter s tem povezani porazdelitev in velikost gub. Potrebne bodo še dodatne analize poškodb v materialu in konstrukciji za kvantifikacijo vpliva ostalih dejavnikov poleg lokalnega podtlaka v pretočnem polju na prenos toplote in na druge procese, t.j. vpliva tanjšanja sten na zunanji strani ter odebelitve sten na notranji strani kače. Rezultati dajejo nov vpogled v vpliv geometrijskih nepravilnosti na zmogljivost cevnih kač med življenjsko dobo.

**Ključne besede:** cevna kača, pretočne lastnosti, ovalnost, nagubanost, računalniška dinamika fluidov, sekundarni tok

# Sinhronizacija in stabilnost treh sovrtečih se rotorjev, povezanih z vzmetmi v neresonančni sistem

Mingjun Du<sup>1,\*</sup> – Yongjun Hou<sup>1</sup> – Tong Tang<sup>2</sup> – Lian Tang<sup>3</sup> – Jialong Wang<sup>1</sup> – Hongbo Gao<sup>1</sup>

<sup>1</sup> Jugozahodna univerza za nafto, Šola za mehatroniko, Kitajska

<sup>2</sup> AECC Chengdu Engine Co., Kitajska

<sup>3</sup> Sichuan Aviation Industry Chuanxi Machinery Co., Kitajska

S hitrim razvojem tehnologije usmerjenega vrtnja se povečujeta kapaciteta in učinkovitost vibracijskih miz za vrtno tekočino (angl. drilling fluid shale shaker – DFSS). V članku je podan predlog mehanizma za ustvarjanje vibracij s tremi sovrtečimi se rotorji, povezanimi z vzmetmi, ki je namenjen velikim in težkim vibracijskim mizam v naftni industriji.

Predlagani vibrator učinkovito varčuje z električno energijo in izboljšuje zmogljivost opreme. Rezultati pričujoče raziskave bodo uporabni kot teoretično izhodišče za projektiranje velikih in težkih vibracijskih miz.

Za analizo sinhronizacije sistema za ustvarjanje vibracij je bila najprej na osnovi Lagrangeovih enačb popisana dinamika treh sovrtečih se rotorjev, povezanih z vzmetmi. Nato so bili po metodi povprečenja izpeljani pogoji za sinhrono delovanje sistema, kriterij stabilnosti pa je bil določen po Hamiltonovem načelu. Analiziran je bil tudi vpliv raznih faktorjev na sinhronizacijo v stacionarnem stanju, med drugim položaja treh rotorjev, togosti vzmeti in frekvenčnega razmerja. Postavljen je bil tudi model elektromagnetne sklopitve po algoritmu Runge-Kutta z adaptivno regulacijo in preučene so bile odvisnosti med stanjem sinhronizacije sistema in njegovimi elektromehanskimi sklopitvenimi lastnostmi. Končno je bil zasnovan tudi eksperimentalni prototip za potrditev teorije in numerične analize.

Povezovalne vzmeti z majhno togostjo  $k$  le malo vplivajo na sinhronizacijo sistema za ustvarjanje vibracij. Sinhrono stanje motorjev je vedno protifazno. S povečevanjem vrednosti  $k$  nad kritično vrednost se fazna razlika med posameznima dvema rotorjema postopoma stabilizira na ničli, sinhrono stanje sistema pa tako preide iz protifaznega v sofaznega. Dovolj toge povezovalne vzmeti omogočajo praktično ničelno fazno razliko med rotorji v stacionarnem obratovalnem stanju.

Eksperimentalne možnosti so omejene, zato je bila za validacijo rezultatov numerične analize in simulacij uporabljena strategija s preskusi sinhronizacije in dinamičnih lastnosti dveh sovrtečih se rotorjev, povezanih z vzmetjo. Fazna sinhronizacija dveh sovrtečih se rotorjev je preprosto uresničljiva z dovolj togo vzmetjo.

Za izboljšanje amplitude in učinkovitosti velikih in težkih vibracijskih sit, ki se uporabljajo pri vrtnju naftnih vrtin, je podan predlog sistema za ustvarjanje vibracij, ki ga sestavljajo trije sovrteči se rotorji, povezani z vzmetmi.

**Ključne besede:** sinhronizacija, dinamične lastnosti, sinhrono stanje, kriterij stabilnosti, vzmeti, vibracijsko sito za vrtno tekočino

# Elektrohidravlični pogon aktivno obremenjene dvigalne naprave z variabilnim razmerjem

Andrzej Kosucki<sup>1</sup> – Łukasz Stawiński<sup>1</sup> – Adrian Morawiec<sup>1</sup> – Jarosław Goszczak<sup>2</sup>

<sup>1</sup> Tehniška univerza v Lodžu, Inštitut za obdelovalne stroje in proizvodni inženiring, Poljska

<sup>2</sup> Tehniška univerza v Lodžu, Oddelek za vozila in osnove konstruiranja strojev, Poljska

Hidravlični sistemi, ki jih oskrbujejo črpalke z nespremenljivo iztisinino, gnane s frekvenčno krmiljenimi elektromotorji, lahko zamenjajo konvencionalne sisteme z dušilnimi elementi, saj omogočajo krmiljenje hitrosti hidravličnih aktuatorjev neodvisno od velikosti in smeri delovanja obremenitev. Hidravlični bagri, dvigala, kolesni nakladalniki, razni viličarji, škarjasta dvigala ter drugi mobilni in stacionarni stroji uporabljajo za premikanje bremen dvigalne sisteme s hidravličnimi valji. Za spuščanje bremen običajno izkoriščajo silo teže, krmilijo pa ga z dušenjem pretoka. Krmiljenje spuščanja z dušenjem v hidravličnih sistemih je težavna naloga (hitrost je odvisna od obremenitve). Sistemi s črpalkami s spremenljivo iztisinino ali s proporcionalnimi ventili so dragi, zaradi velikosti črpalk (od 8 cm<sup>3</sup>) pa se uporabljajo samo v strojih z veliko močjo.

Avtorji so razvili preprost hidravlični sistem s frekvenčnim pretvornikom, ki omogoča popoln nadzor nad hitrostjo hidravličnega valja oz. platforme dvigala med spuščanjem (in dviganjem) bremena. V primerjavi z običajno rešitvijo oz. dušenjem z volumetričnim krmiljenjem je uporabljen popolnoma drugačen pristop h krmiljenju. Ta je ekonomsko vzdržen, zmanjšuje pa tudi pojav porasta temperature, ki je značilen za pogone z dušenjem.

Prototopni sistem je bil prigraden na škarjasto dvigalo s kompleksno geometrijo, iz katere izhaja variabilno razmerje  $i$  oz. variabilna hitrost platforme pri konstantni hitrosti hidravličnega valja. Taka konstrukcija je povezana tudi s spremenljivo silo na valj, ki je funkcija dvižne višine (oz. giba aktuatorja).

Na prototipu škarjastega dvigala sta bili opravljeni dve skupini preizkusov:

1. Primerjava izračunanih in izmerjenih hitrosti.
2. Preizkus vpliva obremenitev na vzdrževanje nastavljenih hitrosti.

V obeh skupinah sta bili ločeno preverjeni hitrosti hidravličnega valja in platforme škarjastega dvigala. Obe hitrosti naj bi bili enaki nastavljeni, neodvisno od obremenitve. Povprečna razlika med dejansko in nastavljeno hitrostjo valja je znašala 3 % (največ 6 %), med dejansko in nastavljeno hitrostjo platforme pa 6 % (največ 10 %).

Predstavljena je tudi primerjava energijskih učinkovitosti klasičnega sistema, novega pogona z rekuperacijo električne energije in novega pogona brez nje. Pri sistemu s funkcijo rekuperacije se je pri prazni oz. manj obremenjeni platformi zmanjšala raba energije (od 20 % do 87 %), pri maksimalni obremenitvi pa je bila dosežena prava rekuperacija.

Predlagani sistem za krmiljenje spuščanja hidravličnega valja lahko vzdržuje nastavljeno hitrost z visoko točnostjo. Uporabljeni način krmiljenja poenostavlja zgradbo hidravličnega sistema, saj med drugim odpadeta dušilni in potni ventil.

Sistem ponuja več pomembnih prednosti v primerjavi z drugimi metodami krmiljenja hitrosti in pozicioniranja pri spuščanju bremen, kot so preprosta zgradba, nizka cena ter možnost izbire črpalke poljubne velikosti in tipa.

Z zveznim nastavljanjem hitrosti motorja črpalke je mogoče omejiti nezaželene pojave med pospeševanjem, kot so vibracije in preobremenitve.

Predstavljena rešitev tako širi nabor možnosti za krmiljenje pasivno in aktivno obremenjenih hidravličnih sistemov.

**Ključne besede:** hidravlični pogoni, črpalka z nastavljivo hitrostjo, naprava z variabilnim razmerjem, dvigalni sistem

# Uporaba algoritmov MCDM pri izbiri fazno spremenljivih snovi v prenosnikih toplote sistemov za shranjevanje toplote

Paul Gregory Felix\* – Velavan Rajagopal – Kannan Kumaresan

Tehniški kolidž PSG, Oddelek za strojništvo, Indija

Fazno spremenljive snovi (PCM) so nepogrešljive pri upravljanju toplote. To so snovi, ki akumulirajo in oddajajo latentno toploto fazne spremembe. Sistemi za shranjevanje toplote (TES) na osnovi PCM omogočajo izkoriščanje sončne energije za kuhanje na pari podnevi in v delu dneva, ko sonca ni na nebu. Parabolični kolektorji so solarni toplotni sistemi, ki omogočajo ustvarjanje pare s sončno energijo in istočasno skladiščenje energije v snovi PCM v prenosniku toplote TES. V času, ko sonca ni, je akumulirano energijo nato mogoče uporabiti za pripravo pare za kuhanje. Koncept tehnologije je sicer potrjen, toda učinkovitost sistema je odvisna od vrste fazno spremenljive snovi v prenosniku toplote TES. Potrebna je torej izbira ustrezne fazno spremenljive snovi, saj ima vsaka svoje značilne termofizikalne lastnosti. Zaradi neustrezne fazno spremenljive snovi se lahko poveča kompleksnost pri projektiranju prenosnika toplote. Obstaja torej potreba po postopku za izbiro ustrezne snovi PCM za aplikacijo kuhanje na pari.

Večkriterijsko odločanje (MCDM) je primeren protokol za izbiranje na podlagi subjektivne ocene alternativ. Na voljo so različni algoritmi MCDM in tudi več tehnik za strateško ocenjevanje uteži kriterijev, vključenih v analize. Pregled literature je pokazal, da je pomanjkljivost analize MCDM uporaba zgolj subjektivnih ali zgolj objektivnih tehnik ocenjevanja uteži. To vrzel bo mogoče zapolniti s pričujočo raziskavo. V njej je bilo uporabljenih 11 različnih algoritmov MCDM v kombinaciji s tremi različnimi tehnikami za subjektivno in objektivno ocenjevanje uteži. Analizirani so bili torej rezultati 33 različnih kombinacij algoritmov in fazno spremenljive snovi so bile rangirane po rezultatih za vsak primer posebej. Rezultati so bili nato za validacijo zanesljivosti obdelani še v trifazni študiji s Pearsonovim koeficientom korelacije.

V študiji je bilo zajetih šest alternativnih snovi PCM in šest termofizikalnih lastnosti oz. kriterijev za ocenjevanje. V skupino koristnih kriterijev so bili uvrščeni tališče, talilna toplota, gostota in toplotna prevodnost, za nekoristni kriterij pa je bila izbrana specifična toplota. Za objektivno ocenjevanje uteži sta bili izbrani entropijska metoda uteževanja (EWM) in metoda pomena kriterija z medkriterijsko korelacijo (CRITIC), za subjektivno ocenjevanje pa tehnika analitično-hierarhičnega procesa (AHP). Eritritol je bil po vseh 33 algoritmih izbran kot najprimernejša fazno spremenljiva snov za namene kuhanja na pari. V 28 od 33 algoritmov je drugo mesto zasedla snov  $MgCl_2 \cdot 6H_2O$  (MCHH). Opažena je bila jasna ločnica med funkcionalnostjo subjektivnih in objektivnih metod ocenjevanja uteži. Zanesljivost rezultatov je bila validirana s trifazno študijo s Pearsonovim koeficientom korelacije. V prvi fazi so bile upoštewane vse snovi PCM, vrednost večine koeficientov korelacije pa je presegla 0,5. V drugi fazi je bilo opravljeno rangiranje snovi po frekvencah in po omejitvi samo na snovi PCM iz prvega, drugega in tretjega ranga pa je bila ugotovljena močnejša korelacija kot v prvi fazi. V tretjo fazo so se nato uvrstile le snovi PCM iz prvega in drugega ranga. Korelacija je bila še močnejša, s tem pa je bila zanesljivost rezultatov dokončno potrjena. Novost raziskovalnega dela je v metodologiji, ki uporablja kombinacijo več algoritmov in ne zgolj enega. Predstavljeno metodologijo bo pozneje mogoče še razširiti za postopke izbire snovi za poljubno aplikacijo.

**Ključne besede:** eritritol, latentna toplota, večkriterijsko odločanje, fazno spremenljive snovi, kuhanje na pari, shranjevanje toplote

# Guide for Authors

All manuscripts must be in English. Pages should be numbered sequentially. The manuscript should be composed in accordance with the Article Template given above. The maximum length of contributions is 12 pages (approx. 5000 words). Longer contributions will only be accepted if authors provide justification in a cover letter. For full instructions see the Information for Authors section on the journal's website: <http://en.sv-jme.eu>.

## SUBMISSION:

Submission to SV-JME is made with the implicit understanding that neither the manuscript nor the essence of its content has been published previously either in whole or in part and that it is not being considered for publication elsewhere. All the listed authors should have agreed on the content and the corresponding (submitting) author is responsible for having ensured that this agreement has been reached. The acceptance of an article is based entirely on its scientific merit, as judged by peer review. Scientific articles comprising simulations only will not be accepted for publication; simulations must be accompanied by experimental results carried out to confirm or deny the accuracy of the simulation. Every manuscript submitted to the SV-JME undergoes a peer-review process.

The authors are kindly invited to submit the paper through our web site: <http://ojs.sv-jme.eu>. The Author is able to track the submission through the editorial process - as well as participate in the copyediting and proofreading of submissions accepted for publication - by logging in, and using the username and password provided.

## SUBMISSION CONTENT:

The typical submission material consists of:

- A **manuscript** (A PDF file, with title, all authors with affiliations, abstract, keywords, highlights, inserted figures and tables and references),
  - Supplementary files:
    - a **manuscript** in a WORD file format
    - a **cover letter** (please see instructions for composing the cover letter)
    - a ZIP file containing **figures** in high resolution in one of the graphical formats (please see instructions for preparing the figure files)
    - possible **appendices** (optional), cover materials, video materials, etc.
- Incomplete or improperly prepared submissions will be rejected with explanatory comments provided. In this case we will kindly ask the authors to carefully read the Information for Authors and to resubmit their manuscripts taking into consideration our comments.

## COVER LETTER INSTRUCTIONS:

Please add a **cover letter** stating the following information about the submitted paper:

1. Paper **title**, list of **authors** and their **affiliations**. **One** corresponding author should be provided.
2. **Type of paper**: original scientific paper (1.01), review scientific paper (1.02) or short scientific paper (1.03).
3. A **declaration** that neither the manuscript nor the essence of its content has been published in whole or in part previously and that it is not being considered for publication elsewhere.
4. State the **value of the paper** or its practical, theoretical and scientific implications. What is new in the paper with respect to the state-of-the-art in the published papers? Do not repeat the content of your abstract for this purpose.
5. We kindly ask you to suggest at least two **reviewers** for your paper and give us their names, their full affiliation and contact information, and their scientific research interest. The suggested reviewers should have at least two relevant references (with an impact factor) to the scientific field concerned; they should not be from the same country as the authors and should have no close connection with the authors.

## FORMAT OF THE MANUSCRIPT:

The manuscript should be composed in accordance with the Article Template. The manuscript should be written in the following format:

- A **Title** that adequately describes the content of the manuscript.
- A list of **Authors** and their **affiliations**.
- An **Abstract** that should not exceed 250 words. The Abstract should state the principal objectives and the scope of the investigation, as well as the methodology employed. It should summarize the results and state the principal conclusions.
- 4 to 6 significant **key words** should follow the abstract to aid indexing.
- 4 to 6 **highlights**; a short collection of bullet points that convey the core findings and provide readers with a quick textual overview of the article. These four to six bullet points should describe the essence of the research (e.g. results or conclusions) and highlight what is distinctive about it.
- An **Introduction** that should provide a review of recent literature and sufficient background information to allow the results of the article to be understood and evaluated.
- A **Methods** section detailing the theoretical or experimental methods used.
- An **Experimental section** that should provide details of the experimental set-up and the methods used to obtain the results.
- A **Results** section that should clearly and concisely present the data, using figures and tables where appropriate.
- A **Discussion** section that should describe the relationships and generalizations shown by the results and discuss the significance of the results, making comparisons with previously published work. (It may be appropriate to combine the Results and Discussion sections into a single section to improve clarity.)
- A **Conclusions** section that should present one or more conclusions drawn from the results and subsequent discussion and should not duplicate the Abstract.
- **Acknowledgement** (optional) of collaboration or preparation assistance may be included. Please note the source of funding for the research.
- **Nomenclature** (optional). Papers with many symbols should have a nomenclature that defines all symbols with units, inserted above the references. If one is used, it must contain all the symbols used in the manuscript and the definitions should not be repeated in the text. In all cases, identify the symbols used if they are not widely recognized in the profession. Define acronyms in the text, not in the nomenclature.
- **References** must be cited consecutively in the text using square brackets [1] and collected together in a reference list at the end of the manuscript.
- **Appendix(-ies)** if any.

## SPECIAL NOTES

**Units:** The SI system of units for nomenclature, symbols and abbreviations should be followed closely. Symbols for physical quantities in the text should be written in italics (e.g.  $v$ ,  $T$ ,  $n$ , etc.). Symbols for units that consist of letters should be in plain text (e.g.  $\text{ms}^{-1}$ , K, min, mm, etc.). Please also see: <http://physics.nist.gov/cuu/pdf/sp811.pdf>.

**Abbreviations** should be spelt out in full on first appearance followed by the abbreviation in parentheses, e.g. variable time geometry (VTG). The meaning of symbols and units belonging to symbols should be explained in each case or cited in a **nomenclature** section at the end of the manuscript before the References.

**Figures** (figures, graphs, illustrations digital images, photographs) must be cited in consecutive numerical order in the text and referred to in both the text and the captions as Fig. 1, Fig. 2, etc. Figures should be prepared without borders and on white grounding and should be sent separately in their original formats. If a figure is composed of several parts, please mark each part with a), b), c), etc. and provide an explanation for each part in Figure caption. The caption should be self-explanatory. Letters and numbers should be readable (Arial or Times New Roman, min 6 pt with equal sizes and fonts in all figures). Graphics (submitted as supplementary files) may be exported in resolution good enough for printing (min. 300 dpi) in any common format, e.g. TIFF, BMP or JPG, PDF and should be named Fig1.jpg, Fig2.tif, etc. However, graphs and line drawings should be prepared as vector images, e.g. CDR, AI. Multi-curve graphs should have individual curves marked with a symbol or otherwise provide distinguishing differences using, for example, different thicknesses or dashing.

**Tables** should carry separate titles and must be numbered in consecutive numerical order in the text and referred to in both the text and the captions as Table 1, Table 2, etc. In addition to the physical quantities, such as  $t$  (in italics), the units [s] (normal text) should be added in square brackets. Tables should not duplicate data found elsewhere in the manuscript. Tables should be prepared using a table editor and not inserted as a graphic.

## REFERENCES:

A reference list must be included using the following information as a guide. Only cited text references are to be included. Each reference is to be referred to in the text by a number enclosed in a square bracket (i.e. [3] or [2] to [4] for more references; do not combine more than 3 references, explain each). No reference to the author is necessary.

References must be numbered and ordered according to where they are first mentioned in the paper, not alphabetically. All references must be complete and accurate. Please add DOI code when available. Examples follow.

## Journal Papers:

Surname 1, Initials, Surname 2, Initials (year). Title. Journal, volume, number, pages, DOI code.

- [1] Hackenschmidt, R., Alber-Laukant, B., Rieg, F. (2010). Simulating nonlinear materials under centrifugal forces by using intelligent cross-linked simulations. *Strojniški vestnik - Journal of Mechanical Engineering*, vol. 57, no. 7-8, p. 531-538, DOI:10.5545/sv-jme.2011.013.

Journal titles should not be abbreviated. Note that journal title is set in italics.

## Books:

Surname 1, Initials, Surname 2, Initials (year). Title. Publisher, place of publication.

- [2] Groover, M.P. (2007). *Fundamentals of Modern Manufacturing*. John Wiley & Sons, Hoboken.

Note that the title of the book is italicized.

## Chapters in Books:

Surname 1, Initials, Surname 2, Initials (year). Chapter title. Editor(s) of book, book title. Publisher, place of publication, pages.

- [3] Carbone, G., Ceccarelli, M. (2005). Legged robotic systems. Kordić, V., Lazinica, A., Merdan, M. (Eds.), *Cutting Edge Robotics*. Pro literatur Verlag, Mammendorf, p. 553-576.

## Proceedings Papers:

Surname 1, Initials, Surname 2, Initials (year). Paper title. Proceedings title, pages.

- [4] Štefanič, N., Martinčević-Mikić, S., Tošanović, N. (2009). Applied lean system in process industry. *MOTSP Conference Proceedings*, p. 422-427.

## Standards:

Standard-Code (year). Title. Organisation. Place.

- [5] ISO/DIS 16000-6.2:2002. *Indoor Air - Part 6: Determination of Volatile Organic Compounds in Indoor and Chamber Air by Active Sampling on TENAX TA Sorbent, Thermal Desorption and Gas Chromatography using MSD/FID*. International Organization for Standardization. Geneva.

## WWW pages:

Surname, Initials or Company name. Title, from <http://address>, date of access.

- [6] Rockwell Automation. Arena, from <http://www.arenasimulation.com>, accessed on 2009-09-07.

## EXTENDED ABSTRACT:

When the paper is accepted for publishing, the authors will be requested to send an **extended abstract** (approx. one A4 page or 3500 to 4000 characters or approx. 600 words). The instruction for composing the extended abstract are published on-line: <http://www.sv-jme.eu/information-for-authors/>.

## COPYRIGHT:

Authors submitting a manuscript do so on the understanding that the work has not been published before, is not being considered for publication elsewhere and has been read and approved by all authors. The submission of the manuscript by the authors means that the authors automatically agree to transfer copyright to SV-JME when the manuscript is accepted for publication. All accepted manuscripts must be accompanied by a Copyright Transfer Agreement, which should be sent to the editor. The work should be original work by the authors and not be published elsewhere in any language without the written consent of the publisher. The proof will be sent to the author showing the final layout of the article. Proof correction must be minimal and executed quickly. Thus it is essential that manuscripts are accurate when submitted. Authors can track the status of their accepted articles on <http://en.sv-jme.eu/>.

## PUBLICATION FEE:

Authors will be asked to pay a publication fee for each article prior to the article appearing in the journal. However, this fee only needs to be paid after the article has been accepted for publishing. The fee is 380 EUR (for articles with maximum of 6 pages), 470 EUR (for articles with maximum of 10 pages), plus 50 EUR for each additional page. The additional cost for a color page is 90.00 EUR (only for a journal hard copy; optional upon author's request). These fees do not include tax.

Strojniški vestnik - Journal of Mechanical Engineering  
Aškerčeva 6, 1000 Ljubljana, Slovenia, e-mail: [info@sv-jme.eu](mailto:info@sv-jme.eu)



<http://www.sv-jme.eu>

# Contents

## Papers

- 547 Duraisivam Saminatharaja, Suresh Periyakgounder, Mahalingam Selvaraj, Jamuna Elangandhi:  
**Performance Study of EDM Process Parameters Using TiC/ZrSiO<sub>4</sub> Particulate-Reinforced Copper Composite Electrode**
- 557 Changbin Dong, Yongping Liu, Gang Zhao:  
**A Method for Calculating Elliptic Gear Transmission Efficiency Based on Transmission Experiment**
- 570 Govindaraj Periasamy, Senthilkumar Mouleeswaran, Prabhu Raja Venugopal, Chellapandi Perumal:  
**Investigation of Hydrodynamic Flow Characteristics in Helical Coils with Ovality and Wrinkles**
- 580 Mingjun Du, Yongjun Hou, Tong Tang, Lian Tang, Jialong Wang, Hongbo Gao:  
**Synchronization and Stability of a Three Co-Rotating Rotor System Coupled with Springs in a Non-Resonance System**
- 599 Andrzej Kosucki, Łukasz Stawiński, Adrian Morawiec, Jarostaw Goszczak:  
**Electro-Hydraulic Drive of the Variable Ratio Lifting Device under Active Load**
- 611 Paul Gregory Felix, Velavan Rajagopal, Kannan Kumaresan:  
**Applicability of MCDM Algorithms for the Selection of Phase Change Materials for Thermal Energy Storage Heat Exchangers**